Generation of discrete frequency tones by the flow around an aerofoil

Alan McAlpine

School of Mathematics
University of Bristol

A thesis submitted to the University of Bristol in accordance
with the requirements of the degree of Doctor of Philosophy
in the Faculty of Science

September 1997

Abstract

Tonal noise, the self-induced discrete frequency noise generated by aerofoils, is investigated. It is heard from an aerofoil placed in streams at low Mach number flows when inclined at a small angle to the stream. The tones are heard as a piercing whistle, commonly up to 30 dB above the background noise level. The work is motivated by the occurrence of tonal noise from rotors, fans and recently wind-turbines. Previous authors have attributed tonal noise to a feedback loop consisting of a coupling between laminar boundary-layer instability waves and sound waves propagating in the free stream. The frequency has been predicted by use of various methods based on this model.

In this thesis a review of wind-tunnel results obtained by Dr. E.C. Nash at the University of Bristol is presented. Boundary-layer measurements show the presence of tonal noise is closely related to the existence of a region of separated flow close to the trailing edge of the aerofoil. Highly amplified boundary-layer instability waves were observed close to the trailing edge of the aerofoil at the frequency of the tone.

A comprehensive analysis of the linear stability of the boundary-layer flow over the aerofoil is presented. The growth of boundary-layer instability waves over the aerofoil is calculated. The growth rates of the waves were obtained by solving the Orr–Sommerfeld problem at several stations on the aerofoil. The Falkner–Skan boundary layers were found to be a suitable form of velocity profiles to incorporate the adverse pressure gradients experienced by the flow over an aerofoil. The amplification of the instability waves is shown to be controlled almost entirely by the region of separated flow close to the trailing edge. The calculated frequency of the linear modes with maximum amplification over the aerofoil is found to be close to the observed frequency of the acoustic tone.

A weakly nonlinear stability analysis was also performed and this appears to be a suitable description of the boundary-layer instability waves. The results indicate that the frequency of the tones may commonly be predicted to within 10% by using weakly nonlinear stability theory.

The generation of sound by diffraction of the boundary-layer instability waves at the trailing edge of the aerofoil is also discussed as well as the proposed feedback models. A modified feedback model is proposed, being based on the experimental and theoretical results.

Acknowledgements

I would like to thank Professor Philip Drazin for his guidance during this project. I am grateful for his suggestions, encouragement and careful reading of this manuscript during its preparation. In particular, I have benefitted from his experience and the insight which he was able to convey into the problem.

I would also like to thank Dr. Emma Nash for her contribution to this project. The experimental results presented in this thesis were obtained by Dr. Nash and I would like to thank her for these, and for the many discussions we had over the course of this work.

I am also grateful for the help and suggestions I received from Professor Martin Lowson.

During the project I have received help and guidance relating to the computational methods from Dr. Tony Davey. His advice and encouragement is also gratefully acknowledged. I also received computer codes from Dr. Alison Hooper and Professor Mike Gaster which were helpful during the initial work on this project.

Further I would like to acknowledge the help and suggestions from several other people: Dr. Colm Caulfield, Professor Howell Peregrine and Dr. Maria Zaturska.

I would like to thank my family, in particular my wife Rachel, my parents and my brother Neil for their continuing support and encouragement.

Finally, I acknowledge the financial support of the EPSRC.

Author's declaration

The work described in this dissertation was carried out in the School of Mathematics, University of Bristol and has not been submitted for any other degree or diploma of any examining body. All the material described herein is the original work of the author, except where otherwise acknowledged.

A. McAlpine

Contents

List of Figures

List of Tables

Chapter 1

Introduction

The majority of this thesis describes an experimental and theoretical investigation into the generation of noise of discrete frequency (or tonal noise) by aerofoils. The work was conducted at the University of Bristol as a joint project between the Department of Aerospace Engineering and the School of Mathematics. Wind-tunnel experiments were performed in the Aerospace Engineering Laboratory by Dr. E.C. Nash with advice from Prof. M.V. Lowson.

Chapter 2 briefly describes the experimental work undertaken by Dr. Nash and presents a selection of the wind-tunnel results obtained. A complete set of experimental results together with further details of the experimental procedures used is in the Ph.D. thesis by Dr. Nash [33].

This chapter introduces the phenomenon of aerofoil tonal noise and reviews the literature on the subject. Chapters 3 and 4 model the linear and weakly nonlinear stability of the flow over the aerofoil. Chapter 5 describes a procedure to calculate the resultant sound field using the Wiener–Hopf technique and discusses the conclusions of the work.

As mentioned, all the wind-tunnel experiments were performed by Dr. Nash. I carried out all the theoretical calculations in this thesis with advice from Prof. P.G. Drazin at the School of Mathematics. However, analysis of the experimental and theoretical results, and subsequent conclusions reached, were obtained after many discussions between myself and Dr. Nash over the duration of the project. I believe that conducting the theoretical investigation in parallel with the experimental investigation has led to a comprehensive study on the phenomenon of tonal noise from aerofoils.

Chapter 6 is a self-contained chapter investigating the temporal stability of Jeffery–Hamel flow. This work, although unrelated to the study of tonal noise, was aided by the experience I had gained from the linear stability calculations already conducted for the flow around an aerofoil (see Chapter 3). Chapter 6 is a joint piece of work with Prof. Drazin.

1.1 Introduction to tonal noise

This thesis investigates the phenomenon of self-induced generation of noise of *discrete frequency* by aerofoils. The interaction of the motion of the aerofoil with air passing above and below it leads to radiation of self-induced noise.

Typically any solid object moving through air, or indeed, air moving around a stationary object, may radiate broadband noise. A common example is the ‘howling’ heard on a windy day as air moves fast around buildings. Broadband noise is characterized by its frequency spectrum. The spectrum shows a seemingly random ‘broad band’ of frequencies all at a similar intensity (i.e. decibel dB). To a listener no single note or tone is distinguishable.

The noise radiated from aerofoils is at certain flow conditions a piercing whistle which is a discrete frequency, typically between 20 and 40 dB above the background, broadband level. This tone is usually the dominant sound from the aerofoil. This phenomenon is thus often referred to as ‘tonal noise’. Another characteristic of tonal noise is that it lies in the receptivity range of human hearing (approximately 20 to $20,000\,\mathrm{Hz}$). The tones detected in the experiments conducted at Bristol were typically between 1000 and 2000 Hz. In fact they were audible in the laboratory even above all the extraneous noise sources (e.g. wind-tunnel fans and motors).

The occurrence of tonal noise is commonly associated with gliders and small, fixed-wing aircraft. The occurrence of tonal noise on larger, commercial aircraft is not expected because it is associated with laminar flow over aircraft wings. Laminar flow is only maintained for moderate Reynolds numbers and typically these are exceeded by commercial aircraft. Of course for commercial aircraft the engine noise would be the dominant noise source even if tonal noise were present.

Perhaps of more interest is the tonal noise of rotors and fans. Several papers investigating tonal noise were motivated by the excessive discrete frequency noise of fans, (see §1.3). A rotor or fan consists of several aerofoils aligned about a central rotating axis. As in the case of fixed aerofoils, tonal noise from rotors and fans has only been reported for moderate tip velocities.

The problem of tonal noise from rotors and fans is more complicated than for a fixed aerofoil because each blade in a rotor or fan passes through the wake of its neighbouring blade during rotation. The majority of the previous research into tonal noise has investigated tones from a single, fixed aerofoil to simplify the problem.

Having established the occurrence of tonal noise in practical applications there are two important motives to study this problem.

Firstly, tonal noise is an example of resonance. Previous papers attribute the mechanism to an aero-acoustic resonance, that is a resonance between the hydrodynamic and acoustic fields around the aerofoil. The most common resonances are usually mechanical and may lead to fatigue or excessive stress over and above 'normal' working levels. Resonance is worth investigation to be able to predict when it may occur and, if necessary, may be prevented.

Skin friction and drag account for approximately half the resistance an aeroplane must overcome in flight. At high Reynolds numbers small disturbances in the aerofoil boundary layers grow and interact with each other which lead to turbulent boundary layers. In a turbulent boundary layer the faster flowing fluid above the layer is forced onto the aerofoil surface and may curl back on itself thereby increasing the frictional forces. Aeronautical engineers struggle to reduce drag by just 1%. Reducing drag would have the affect of decreasing the fuel consumption and increasing aircraft efficiency.

An ideal to achieve would be laminar flow over all aerodynamic surfaces. This is an active research area where aeronautical engineers are attempting to delay the transition from laminar to turbulent flow on aerofoils. (e.g. The New Scientist Jan 1997 reports on the attempts to use compliant surfaces to mimic the skin of sharks and dolphins. Sharks and dolphins swim up to speeds which *appear* impossible to obtain from their power output. They experience less drag than any man-made body. Compliant surfaces are being developed to try and artificially reduce the energy transfer to boundary-layer eddies to delay the transition to turbulence.)

British Aerospace Airbus Ltd are currently developing 'laminar-flow wing technology' to keep airflow as laminar as possible. They are developing 'Hybrid laminar flow control (HLFC)' where suction through tiny holes in the wings reduces drag.

As mentioned already, tonal noise depends on laminar flow over the aerofoil surface. The dependence on laminar flow is described in Chapter 2. Improvements in the aerodynamic efficiency of surfaces may lead to flow conditions where tonal noise is more prevalent. Preventing transition from laminar to turbulent flow on aerodynamic surfaces may increase the likelihood of tonal noise being heard at much higher flow velocities. It would seem unlikely that the benefits in drag reduction would be outweighed by the increase in tonal noise. However, knowledge of the effect of this resonance mechanism on the skin friction on the aerofoil surface, aerofoil vibration and the noise output may be required.

One solution employed on fans is to 'trip' the flow over the aerofoil blades. This ensures turbulent flow over the blades and destroys any tonal noise. This solution is highly undesirable for most practical applications as the loss in aerodynamic efficiency would greatly outweigh the reduction in noise output.

As well as to understand resonance, the study of tonal noise is also motivated by the need to predict the frequency and intensity of the tones. Disregarding the effects on aerodynamic efficiency still leaves the environmental impact of tonal noise.

One recent example of this was the installation of fans for the channel tunnel. They had to be insulated to reduce the noise output heard at the ends of the tunnel.

An ongoing topical example is wind-turbines. The wind energy industry in the UK is growing rapidly and by the end of 1995 there were twenty-nine wind farms in the UK with thirteen more under construction. The Government aims to use renewable energy sources to represent one fifth of the total carbon savings by the year 2000. In 1995 wind energy led to a representative saving of 82000 tonnes of carbon.

Tonal noise is heard on wind-turbines and this is a factor which may limit the number of turbines which may be placed together. It may be argued that wind farms are usually sited in open, exposed areas where strong winds are prevalent. These areas are generally sparsely populated and hence tonal noise would have a low environmental impact. However with demand for alternative energy sources increasing, the environmental impact of wind farms is increasingly important.

In February 1997 it was reported (BBC Radio 5) that research is being undertaken to investigate the possibility of floating wind-turbines on the ocean. This would have a much lower environmental impact and the wind farms would presumably be able to site many more turbines together.

It should be noted that mechanical noise (e.g. from bearings etc) is also a strong source of noise in wind-turbines.

The aims of this research are to understand the mechanism of tonal noise with a view to prediction and possible reduction of tonal noise.

1.2 Examples of self-induced noise mechanisms

In 1989, Brooks et al. [7] completed an extensive experimental and theoretical investigation into self-induced noise mechanisms from different aerofoil sections. They were motivated by broadband helicopter noise, wind-turbine noise and airframe noise. The mechanisms investigated were all for subsonic flow and the aim was to predict the noise generation using semi-empirical scaling laws, (i.e. scaling laws for the sound level based on parameters such as the Reynolds number, Mach number and flow geometry).

1.2.1 Turbulent boundary layer — trailing edge noise

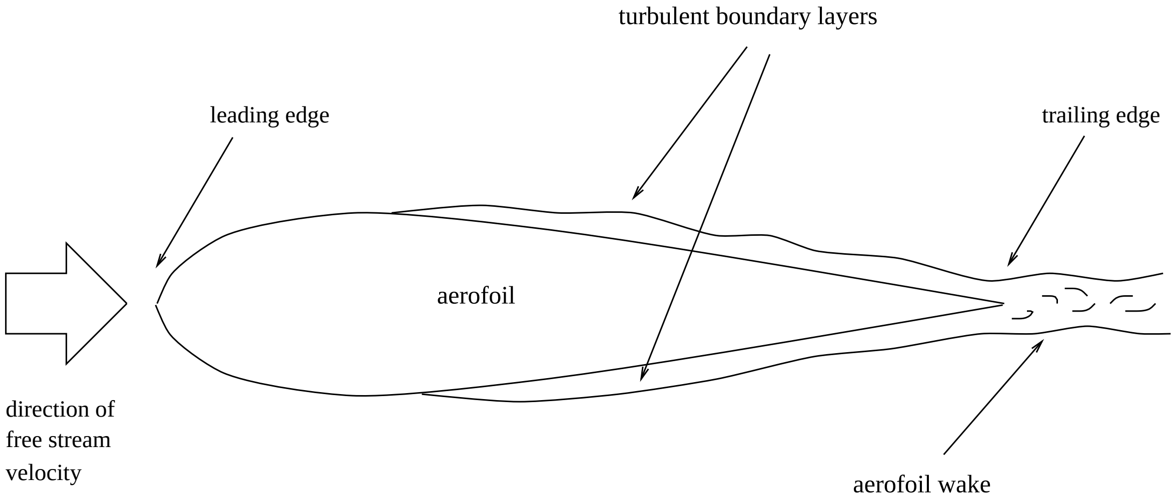

Figure 1.1: Turbulent boundary layer — trailing edge noise

For high Reynolds numbers, turbulent boundary layers develop over a large extent of both the suction (top) and pressure (underneath) surfaces of an aerofoil. Unless otherwise specified, the Reynolds number for the flow past an aerofoil section is taken to be $R = U_\infty c/\nu$, where U_∞ is the free-stream velocity, c the chord length of the aerofoil and ν the kinematic viscosity of air, $\approx 1.5 \times 10^{-5}\,\mathrm{m^2 s^{-1}}$. Broadband noise is generated through the interaction of the turbulent boundary layers with the trailing edge of the aerofoil. Scaling laws for the trailing edge noise are then sought by the analysis of Ffowcs-Williams & Hall [17].

Ffowcs-Williams & Hall investigated the effect on aerodynamic sound generation by turbulent flow in the presence of a rigid, half-plane. The presence of the edge of the half-plane was found to increase the radiated noise from the fluid at low Mach numbers.

Lighthill (1951), in his pioneering work on aerodynamic noise defined the source of sound to be the difference between the *exact* statements of mass and momentum conservation and the *approximate* equations satisfied by acoustical motion. Acoustic pressure p' and density ρ' perturbations satisfy linearized equations of motion as they are small with respect to mean levels (p and ρ respectively). Lighthill's equation is

$$\frac{\partial^2 \rho'}{\partial t^2} - a_0^2 \nabla^2 \rho' = \frac{\partial^2 T_{ij}}{\partial x_i \partial x_j} , \tag{1.1}$$

where $T_{ij} = \rho v_i v_j + \sigma_{ij} - a_0^2 \rho' \delta_{ij}$ is Lighthill's stress tensor. Note that a_0 is the speed of sound, v_i the ith component of velocity and $-\sigma_{ij} = -p'\delta_{ij} + \mu(\partial v_i/\partial x_j + \partial v_j/\partial x_i) - \frac{2}{3}\mu \partial v_i/\partial x_i \delta_{ij}$ is the stress tensor for a compressible fluid. No approximation is made in (1.1). For linear, inviscid flow T_{ij} is zero to first order. However, in turbulent flow T_{ij} does not vanish and areas of turbulence in free space generate sound as a quadrupole distribution.

Ffowcs-Williams & Hall considered, (for Reynolds numbers $\gg 1$), the potential field radiated by a distribution of quadrupoles situated close to the sharp edge of a half-plane. In cylindrical polar coordinates the edge of the half-plane is taken as $r = 0$, i.e. the z-axis, with the half-plane situated on $\theta = 0$. This introduces the boundary condition that the normal velocity is zero on $\theta = 0$.

The solution is sought by taking the Fourier transform in time of (1.1) and then using a Green's function (with the half-plane geometry). Sound intensity I is defined to be the rate at which acoustic energy crosses unit area in space. The intensity of the sound is considered at locations far away from the half-plane edge (that is $kr \gg 1$ where $k = 2\pi/\lambda_{ac}$ is the wave number of the respective acoustic wave with wavelength λ_{ac}), due to turbulent eddies in the flow near the edge. The turbulent eddies are taken to be cylindrical regions of the turbulence over which the velocities are highly correlated. The mean location of the eddy cores is taken as $\bar{r_0}$ and if $2k\bar{r_0} \ll 1$ then the sound output due to the quadrupole sources increases by a factor of $1/(k\bar{r_0})^3$ as a result of the half-plane edge. The intensity of the sound also has directional dependence $\cos^2\theta/2$.

The analysis concludes that for a single eddy in the vicinity of the half-plane edge the intensity is given by the following scaling law,

$$I \sim \rho U^3 \left(\frac{U}{a_0}\right)^2 \frac{\delta^2}{d^2} , \tag{1.2}$$

where U is the characteristic velocity scale, δ the radius of the eddy and d the distance from the eddy to an observer in the far-field. Lighthill's celebrated result that free turbulence generates sound with intensity increasing by U^8 was derived from dimensional analysis of (1.1). Compared with (1.2) the scaling law for a turbulent eddy in free space (or an infinite plane) radiates sound with intensity,

$$I \sim \rho U^3 \left(\frac{U}{a_0}\right)^5 \frac{\delta^2}{d^2}\,. \tag{1.3}$$

Recalling that the scaling laws (1.2), (1.3) are derived for low Mach number flows, (that is $M = U/a_0 \ll 1$), then Ffowcs-Williams & Hall have shown that diffraction at the sharp edge of a half-plane increases the scattered intensity of the aerodynamic sound generation by a turbulent flow.

1.2.2 Separation — stall noise

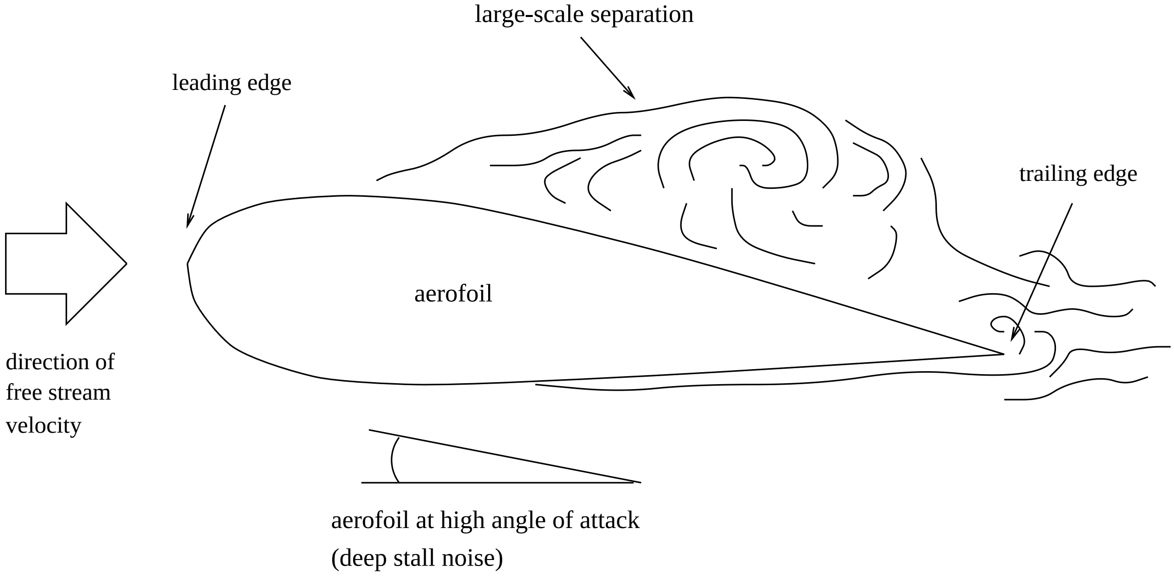

Figure 1.2: Separation — stall noise

With the aerofoil at high angles of attack, large-scale flow separation will occur on the suction surface of the aerofoil. This is also known as ‘deep stall’ when the aerofoil lift drastically reduces (possibly to a critical level for an aircraft in flight). The aerofoil radiates low-frequency noise from the whole chord, not just the trailing edge. The wavelength of the low-frequency noise will be large compared with the aerofoil chord length and the aerofoil will in effect be a compact sound source (i.e.

$\lambda_{ac} \gg c$). The high angle of attack makes the aerofoil in effect a bluff body with respect to the oncoming free-stream flow.

Bluff bodies in a uniform flow, such as cylinders, often shed periodic wakes which have the same frequency as the resultant acoustic tones. One well known example of this phenomenon are 'Aeolian' tones — the discrete frequency tones heard from wires in a uniform flow. Strouhal observed that the frequency of the Aeolian tones was proportional to U_∞ and $1/d$ where U_∞ is the free-stream velocity and d the diameter of the wire.

Over a range of free-stream velocities the Strouhal number, $St = fd/U_\infty$ is found for some bluff bodies to be relatively constant. The frequency f of the radiated acoustic tones may then be easily predicted.

1.2.3 Laminar boundary layer — vortex-shedding noise

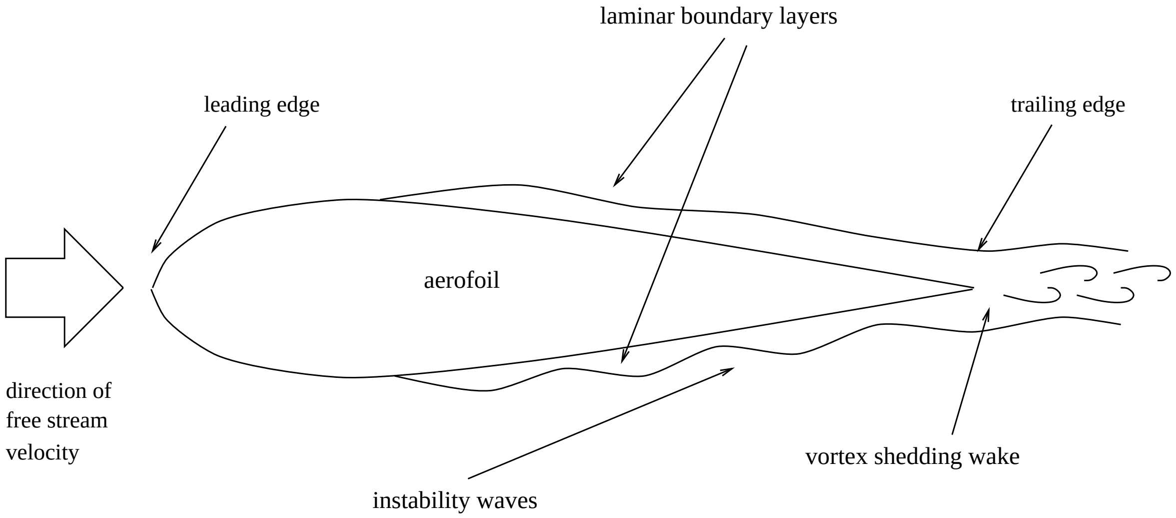

Figure 1.3: Laminar boundary layer — vortex-shedding noise

For lower Reynolds numbers than in §1.2.1 a laminar boundary layer may be maintained along one surface of the aerofoil. Boundary-layer instabilities propagating along the aerofoil grow towards the trailing edge where they roll up (see §5.2) and vortices are shed into the aerofoil wake. In §1.3 previous authors suggest that the boundary-layer instability waves 'couple' with acoustic waves generated at the trailing edge to form 'feedback' loops resulting in a noise spectrum of discrete tones.

At non-zero angles of attack, then trailing edge noise may be generated due to the shedding of turbulent vorticity into the wake as the flow on the suction surface separates close to the trailing edge. (As R increases and the angle of attack rises this separation on the suction surface grows and may lead to the conditions described in §1.2.2.)

The tonal noise described in the introduction §1.1 is believed to be the phenomenon referred to here by Brooks et al. as laminar boundary layer — vortex shedding noise. The papers reviewed in §1.3 all describe aerodynamic noise generation which is described loosely by this mechanism of self-induced noise.

1.2.4 Tip vortex formation noise

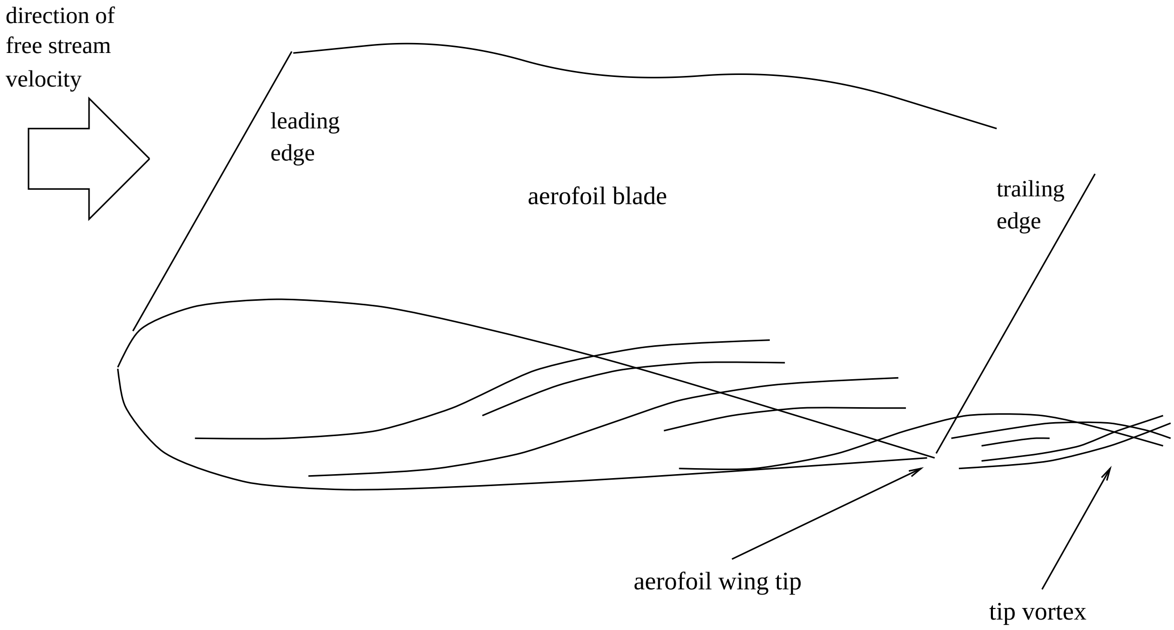

Figure 1.4: Tip vortex formation noise

In flight the flow over the aerofoil wing leads to a vortex with a central, viscous, turbulent core, shed from each tip. The mechanism of noise generated by these 'tip vortices' is taken to be the propagation of the turbulence over the trailing edge (see §1.2.1). Prediction models have previously been proposed by using data taken from delta wings. Delta wings are triangular shaped wings which have two, highly correlated vortex structures shed into the wake. These vortices are assumed to approximate the tip vortices from more traditional wings.

Tip vortex noise may be avoided in wind-tunnel experiments by having the aerofoil profile span the entire working section of the wind-tunnel (as was the case at Bristol).

1.2.5 Trailing edge bluntness — vortex-shedding noise

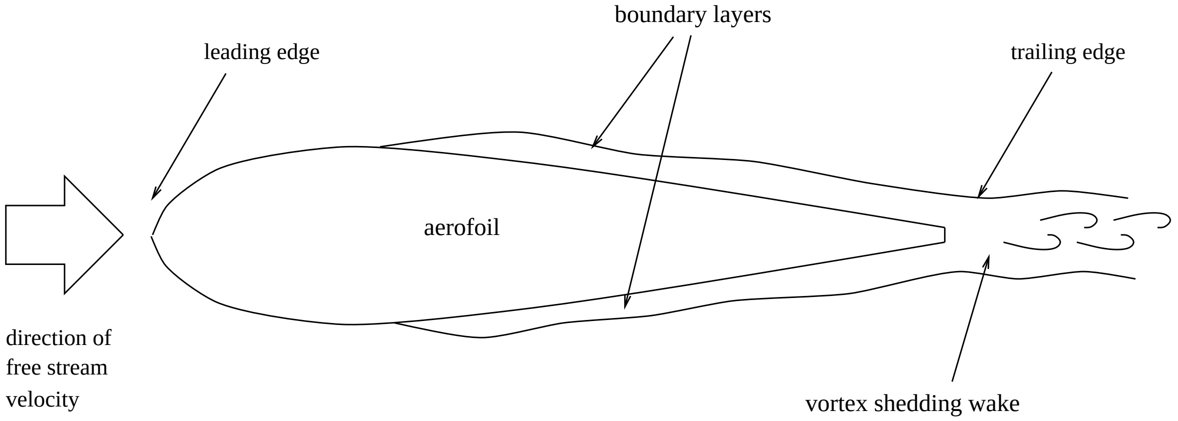

Figure 1.5: Trailing edge bluntness — vortex-shedding noise

Blunt trailing edges on aerofoils also lead to vortex shedding in the wake as the flow separates after the trailing edge. The noise mechanism will then be similar to that for bluff bodies in a uniform flow (see §1.2.2).

For many aerofoil designs the trailing edge will be ‘sharp’, and even for ‘blunt’ trailing edges, the thickness is often small compared with the boundary-layer thickness at the trailing edge.

All the aerofoils used at Bristol University and those discussed from previous papers had ‘sharp’ trailing edges.

1.3 Review of past literature

The first comprehensive paper dedicated to the tonal noise generated by isolated aerofoils is believed to be that of Paterson et al. ([16], (1973)). The authors were motivated by the noise from helicopter rotors and propellers but simplified the study to a stationary, isolated aerofoil in a uniform stream. They believed that vortex shedding noise dominated other sources such as the turbulent boundary layer and wake fluctuations.

Initial tests were conducted in a low-turbulence, open-jet wind-tunnel on NACA 0012 and NACA 0018 aerofoil sections, (see §2.1 for details of NACA aerofoil specifications). At moderate Reynolds numbers ($R \approx 10^5$), and low angles of attack, the resultant acoustic spectrum was found to exhibit a discrete frequency between 20 and 30 dB above the background, broadband level. At higher R with turbulent boundary layers on both sides of the aerofoil, the discrete tones were no longer detected.

A hot-wire placed in the aerofoil wake, downstream of the trailing edge, revealed large wake fluctuations at the same frequency as the discrete acoustic tone. The presence of the tone was associated with a laminar boundary layer on the pressure surface of the aerofoil. The laminar boundary layer also oscillated at the same frequency as the acoustic tone. A boundary-layer trip strip was found to have no effect on the tonal noise when placed at various stations on the suction surface. The low angles of attack were believed to be necessary to maintain a laminar boundary layer along the whole extent of the pressure surface.

The noise measured qualitatively resembled the vortex shedding noise associated with bluff bodies. Paterson et al. formed a Strouhal number

$$St = \frac{2f\delta}{U_\infty}\,, \tag{1.4}$$

where δ was the boundary-layer thickness at the trailing edge. Previous experimental work had shown that for a bluff body, $St \approx 0.2$. The boundary-layer thickness δ was approximated by using boundary layer theory for the flow over a flat plate, namely the Blasius boundary layer. Using (1.4), this resulted in a scaling law for the dominant frequency f,

$$f \approx 0.02\frac{U_\infty^{3/2}}{(c\nu)^{1/2}}\,. \tag{1.5}$$

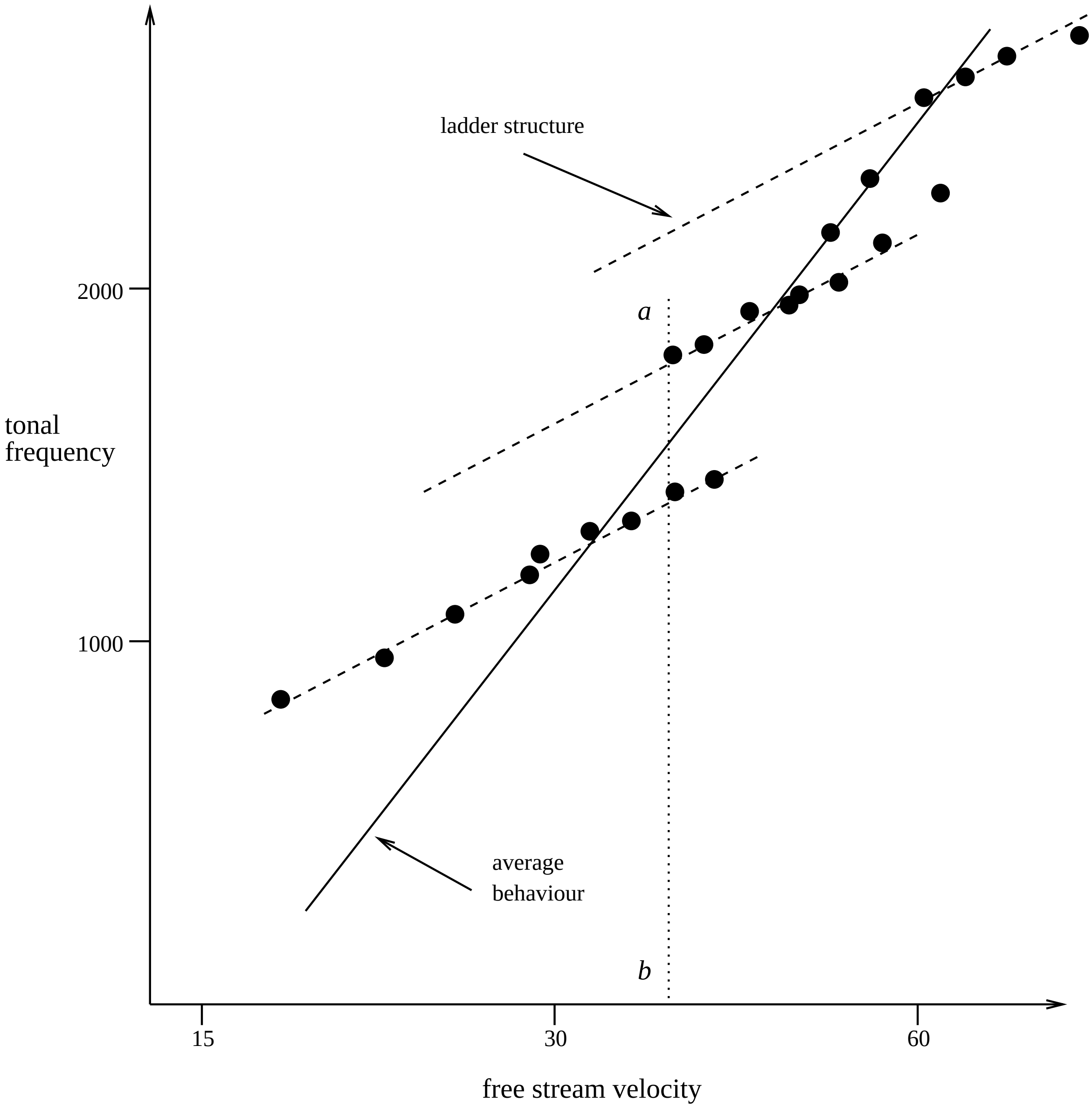

Figure 1.6: Sketch of dominant discrete frequency tones against U_∞ for angle of attack 4°, (taken from Paterson et al. [16]).

Figure 1.6 is a sketch taken from Paterson et al. showing the variation of the dominant discrete frequency tones with the free-stream velocity U_∞. The overall trend of the discrete frequencies matches the $U_\infty^{3/2}$ dependence but for local variations in U_∞ the frequencies follow curves proportional to $U_\infty^{0.8}$. At intermittently spaced free-stream velocities the frequency tones ‘jumped’ up to higher $U_\infty^{0.8}$ curves. The authors were unable to offer an explanation to the ‘ladder-like’ structure with ‘rungs’ of curves proportional to $U_\infty^{0.8}$ followed by the discrete tones, or to the existence of multiple tones at some free-stream velocities (such as on the line ab in figure 1.6).

Paterson et al. also demonstrated experimentally that the location of the sound source was very near the trailing edge of the aerofoil.

In 1974, Tam [42] argued that the discrete tones were not related to vortex shedding as first suggested. He suggested that, as an aerofoil was streamlined this was a poor approximation to a bluff body which vortex shedding noise was commonly associated with. He believed that the aerofoil wake would only roll-up into a vortex street far downstream of the aerofoil, but the noise source had been shown to be located near to the trailing edge. Further, he argued that vortex shedding did not adequately explain the sudden jumps in the discrete frequency tones (with increases in U_∞).

The following tonal noise characteristics revealed by the experimental results presented in Paterson et al. are as follows:

- Tonal noise arises on a laminar boundary layer on the pressure surface of the aerofoil.
- Frequencies of tonal noise follow (locally) curves proportional to $U_\infty^{0.8}$ and suddenly jump to higher curves as U_∞ increases.
- Frequencies of tonal noise are overall proportional to $U_\infty^{3/2}$.
- The source of the tonal noise is near the trailing edge.

Tam proposed that tonal noise is generated by a self-excited feedback loop between the trailing edge and a point in the wake nearby. Boundary-layer instabilities propagating into the wake would grow, causing the wake to vibrate laterally. These vibrations would emit an acoustic wave at some point close to the trailing edge which coupled with the instabilities propagating into the wake over the trailing edge — thus completing the loop.

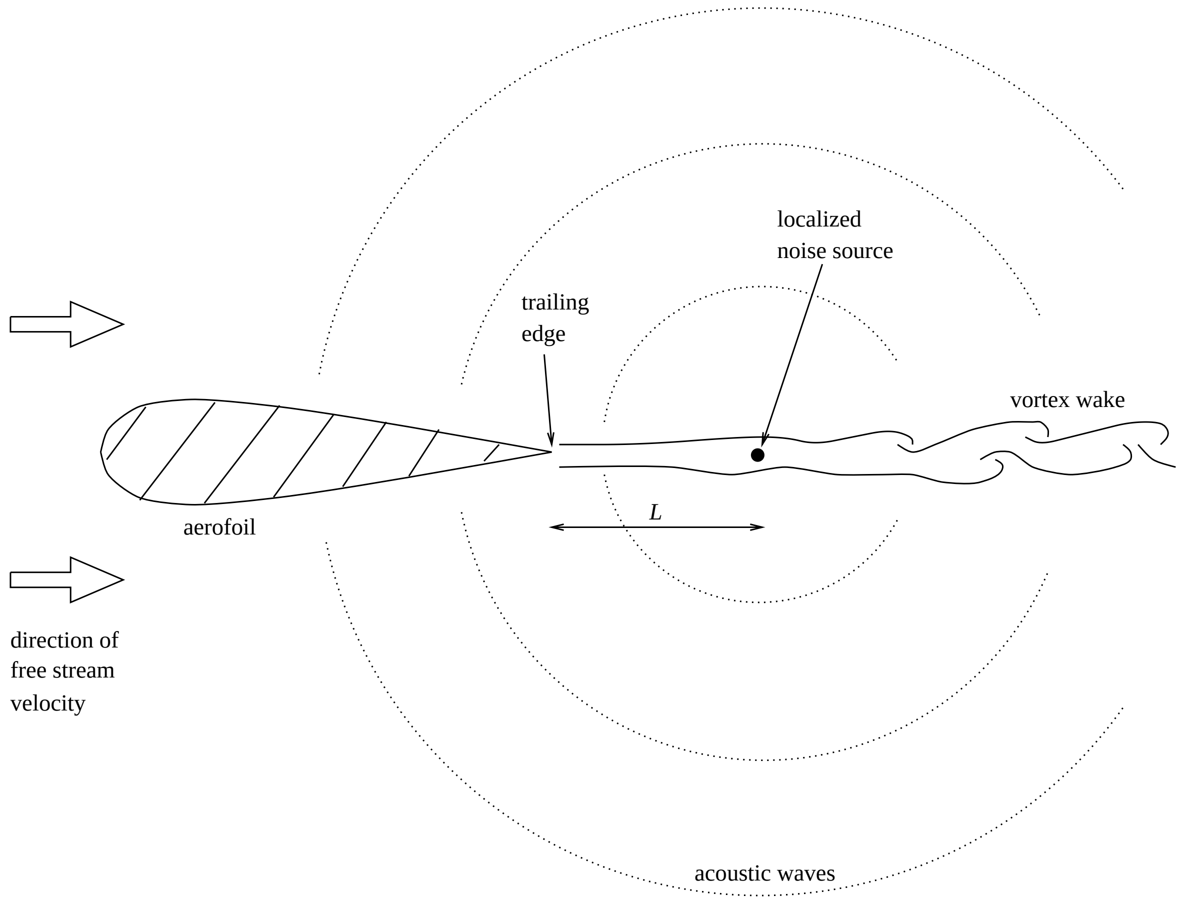

Figure 1.7: Sketch of feedback loop for tonal noise from aerofoils, (taken from Tam [42]).

Approximating the stability characteristics of an aerofoil to those of a flat plate, Tam claimed that the experimental data points were located inside the neutral stability curve of a flat plate, i.e. the unstable region. Using hydrodynamic stability theory, Tam proceeded to represent the hydrodynamic and acoustic disturbances in normal modes form. Then,

$$\text{wake disturbance phase change} = \frac{2\pi f L}{c_r}, \tag{1.6}$$

$$\text{acoustic disturbance phase change} = \frac{2\pi f L}{a_0}, \tag{1.7}$$

where L is the distance between the trailing edge and the sound source, and c_r is the phase velocity of the hydrodynamic instability in the wake. The total phase change around the loop is thus $2\pi f L(1/c_r + 1/a_0)$ and for reinforcement to occur this should be an integral multiple of 2π. This gave an expression for the tonal frequencies,

$$f = \frac{n}{L(1/c_r + 1/a_0)} \, , \tag{1.8}$$

which on varying the integer n would lead to a 'ladder-like' structure. (Each rung on the ladder would be for a different integer value n.) Tam concluded that he believed only the free-stream velocity U_∞ and the angle of attack of the aerofoil would influence the feedback loop distance L and the phase velocity c_r of the hydrodynamic instabilities.

Wright ([44], 1976) investigated acoustic output from propellers, helicopter rotors and fans. The tip speeds for all the blades were always subsonic. He considered both discrete and broadband radiated noise and described a process for the generation of laminar boundary-layer noise through an aerodynamic-acoustic feedback loop (hereafter referred to as an aero-acoustic loop).

The feedback mechanism is assumed on the basis that a laminar boundary layer extends over at least one surface of the aerofoil blade. Aerodynamic disturbances were assumed to originate from a source point upstream of the trailing edge, the trailing edge being the radiation point of the sound. The aerodynamic disturbances (or boundary-layer waves) induced a fluctuating pressure distribution on the aerofoil surface which, on interacting with the sharp, trailing edge, generated acoustic waves which were assumed to act as a dipole source. The acoustic waves radiate upstream and constructively reinforce the original disturbance, thus completing the aero-acoustic feedback loop.

The loop will be maintained if the acoustic waves have appropriate phase and magnitude to couple with the boundary-layer disturbances at the source.

Wright then proceeded to calculate the tonal frequencies by the method used by Tam. Once again he assumed that for resonance to occur the total phase around the loop must be $2\pi n$ where $n \in \mathbb{N}$. Wright obtained a slightly different expression for f than (1.8) by assuming that the relative velocity of the acoustic waves upstream would be $a_0 - U_\infty$. Hence,

$$f = \frac{nc_r}{L}\left(\frac{a_0 - U_\infty}{a_0 - U_\infty + c_r}\right) , \tag{1.9}$$

where now c_r is taken to be the phase velocity of the boundary-layer instability wave.

Wright concluded that the laminar boundary-layer noise was most common for $10^5 < R < 10^6$. He suggested that for $R < 10^5$ the 'gain' around the feedback loop was not sufficient to sustain the boundary-layer disturbances and for $R > 10^6$ the flow would no longer be laminar over the entire aerofoil.

Longhouse ([28], 1977) also conducted tests on low tip speed axial flow fans to attempt to determine the noise source mechanisms. He separated the noise mechanisms into two categories, namely rotational and non-rotational. The rotational noise sources involve interactions between the rotating blades of the axial fans and the blade wakes. The non-rotational noise source mechanisms were assumed to be those already discussed by Brooks et al. [7], i.e. fixed blade problems.

Longhouse assumed that vortex shedding noise (as described by Paterson et al.) was a result of fluctuating pressures in the laminar boundary layer. He suppressed the majority of the tonal noise by placing serrations on all the blades except for a small spanwise region on one blade. The results from the axial fan were then comparable to those from a single (two-dimensional) aerofoil profile, although the blade was not stationary. He based his feedback model on those already formulated by Tam and Wright. If the phase conditions were met then the feedback loop becomes 'locked-in' to the vortex shedding frequency and the noise is characterized by a sharp peak in the acoustic spectrum. He noted that the source point of the boundary-layer instability waves should occur far enough upstream of the trailing edge to allow the instability waves to have time to develop.

Longhouse reported narrow peaks in the acoustic frequency spectrum up to 20 dB above the background levels. He believed that Tam's approach is correct but the hypothesis of feedback through the wake instability was discounted because experiments revealed that the wake became turbulent close to the trailing edge. There would therefore not be any coherent wake instability. (The experiments of Longhouse on axial flow fans were different from those of Tam for a single, stationary aerofoil — however the authors believed the tonal noise mechanism was essentially the same for both examples.)

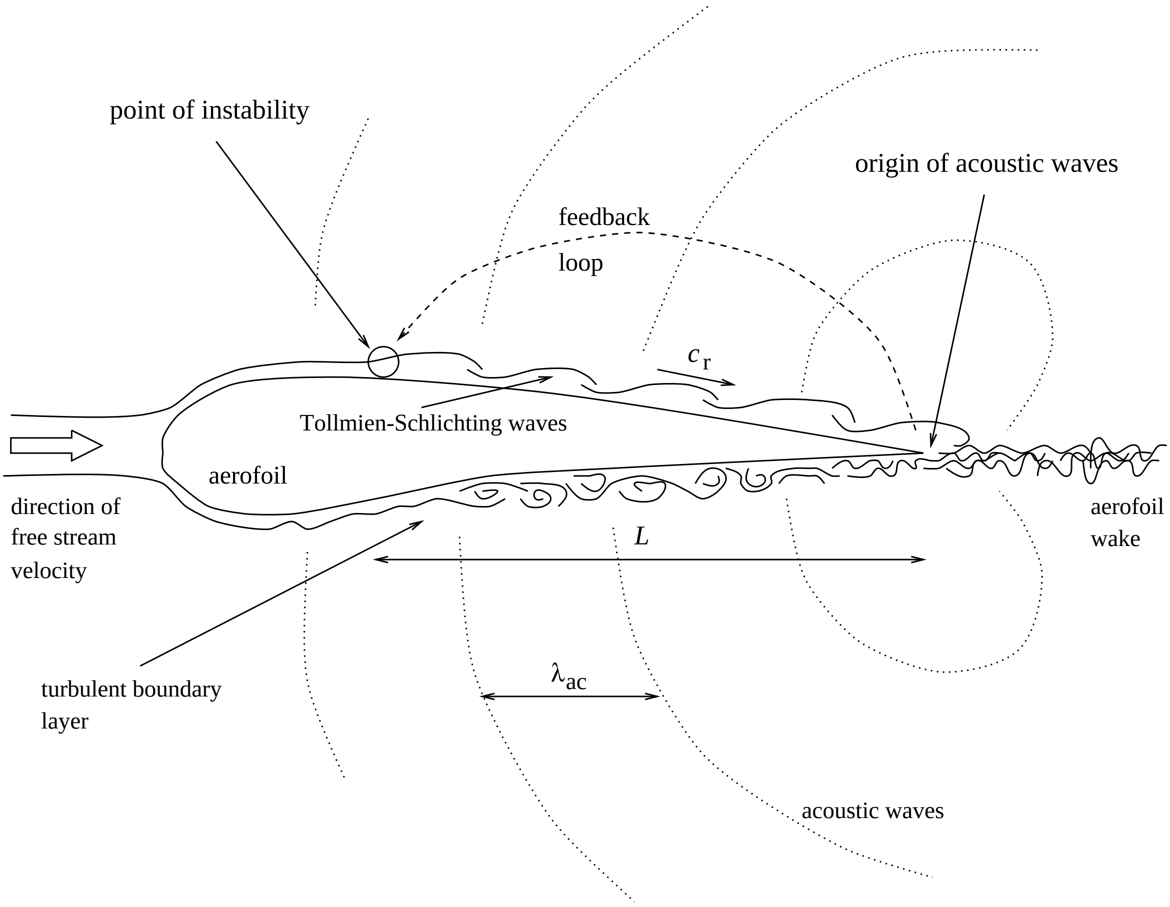

Figure 1.8: Sketch of feedback loop for tonal noise from aerofoils, (taken from Longhouse [28]).

Figure 1.8 is a schematic of the feedback loop proposed independently by Wright and Longhouse (taken from Longhouse).

Longhouse expressed the frequency (1.9) by Wright, in terms of the Strouhal number $St = fc/U_\infty$, the Mach number $M = U_\infty/a_0$ and the ratios $\alpha = c_r/U_\infty$, $\beta = L/c$. Then the integer n of 2π phase changes around the feedback loop is written as

$$n = St \left[\frac{1 - M(1-\alpha)}{\alpha(1-M)} \right] \beta \,. \tag{1.10}$$

The values of α and β were then estimated as ≈ 0.5 but Longhouse noted that the program used had predicted flow separation between 65–80% chord. Longhouse did not take into account the flow separation. He did, however, note that separation on the aerofoil surface (as numerically predicted) was probably quite likely and that this may in turn affect the stability characteristics and the tonal noise levels.

Fink ([18], 1978) developed the feedback model proposed by the previous authors. He assumed the aerodynamic disturbances were specifically Tollmien–Schlichting waves (hereafter referred to as T–S waves, see Chapter 3 for further details). His revised analysis followed the formulation of Wright (1.8), (1.9) and Longhouse (1.10), with now

$$\frac{f}{n} = \left(\frac{U_\infty}{c}\right)\left(\frac{c_r}{U_\infty}\right)\left(\frac{c}{L}\right)\left(\frac{1-M}{(1-M(1-c_r/U_\infty))}\right) . \tag{1.11}$$

Fink then proceeded to use the stability characteristics of the flow over a flat plate, namely the Blasius boundary layer, to model the stability of the laminar flow over one surface of the aerofoil. He assumed that a ‘thin’ aerofoil may be modelled by a flat plate to a first approximation. Then the tonal frequency was assumed to be close to the frequency of T–S waves with maximum amplitude at the trailing edge.

Fink suggested that the Reynolds number $R_{\delta^\star}$ at the trailing edge determines the frequency of the T–S wave with maximum amplitude and the length L of the feedback region. Note the Reynolds number $R_{\delta^\star} = U_\infty \delta^\star/\nu$ where the characteristic length scale is $\delta^\star$, the boundary-layer displacement thickness, (see §3.2.2). Figure 1.9 taken from Fink demonstrates how the maximum frequency is taken to be the frequency on the upper branch of the neutral curve for $R_{\delta^\star}$ at the trailing edge. L may then be predicted by assuming the feedback starts at the point indicated on the lower branch. Then from the source point to the trailing edge T–S waves at that frequency will be unstable and grow as they propagate over the aerofoil. The phase velocity c_r of the T–S wave is taken as the ‘average’ over the feedback region, although Fink demonstrates that the change in c_r over the feedback region will be small.

The number of phase cycles n around the loop changes discontinuously. ‘Jumps’ in the number of phase cycles appear to occur when the tonal frequencies have acoustic wavelengths λ_{ac} such that an integral number of half-wavelengths are equal to the aerofoil chord, i.e. $i\lambda_{ac}/2 = c$, where $i \in \mathbb{N}$. Figure 1.10 demonstrates a scheme to

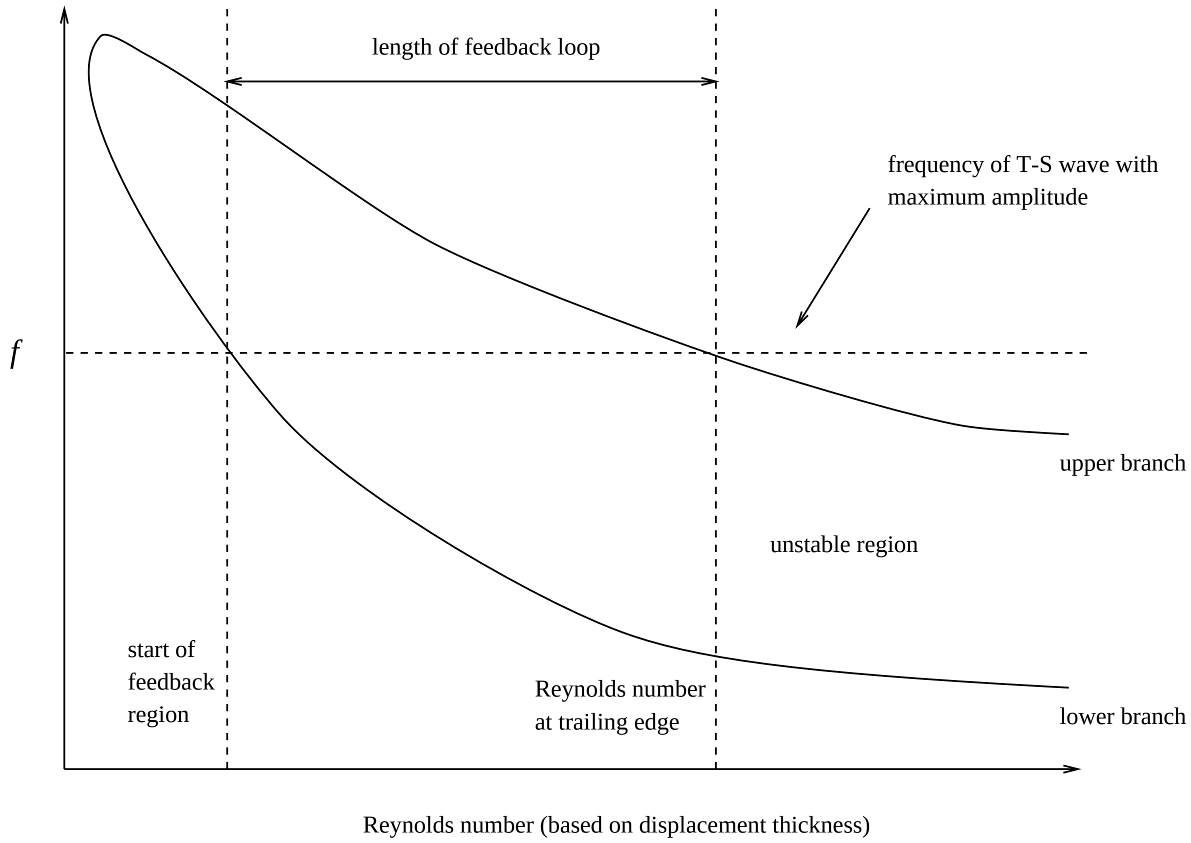

Figure 1.9: Sketch of neutral stability curve for the Blasius boundary layer, (taken from Fink [18]).

predict the tonal frequencies and location of the 'jumps'.

The tonal frequencies f will tend to follow the curves of constant phase shown in figure 1.10. (These curves are close to the upper branch of the neutral stability curve which was used previously to predict values of c_r and L to insert into equation (1.11).) 'Jumps' in the phase appear to occur when the free-stream velocity U_∞ corresponds to a tonal frequency on the upper branch of the neutral curve with wavelength λ_{ac} such that $i\lambda_{ac}/2 = c$. The frequency 'jumps' to a curve of constant phase just above the upper branch. Fink also assumes that for low U_∞ when $\lambda_{ac}/2 > c$ the tonal frequencies will remain close to the upper branch.

Fink's prediction method only appears to agree qualitatively with data of other authors such as Paterson et al. He was the only author to attempt to predict when the frequency jumps occur, although it is unclear why he predicts jumps to occur when

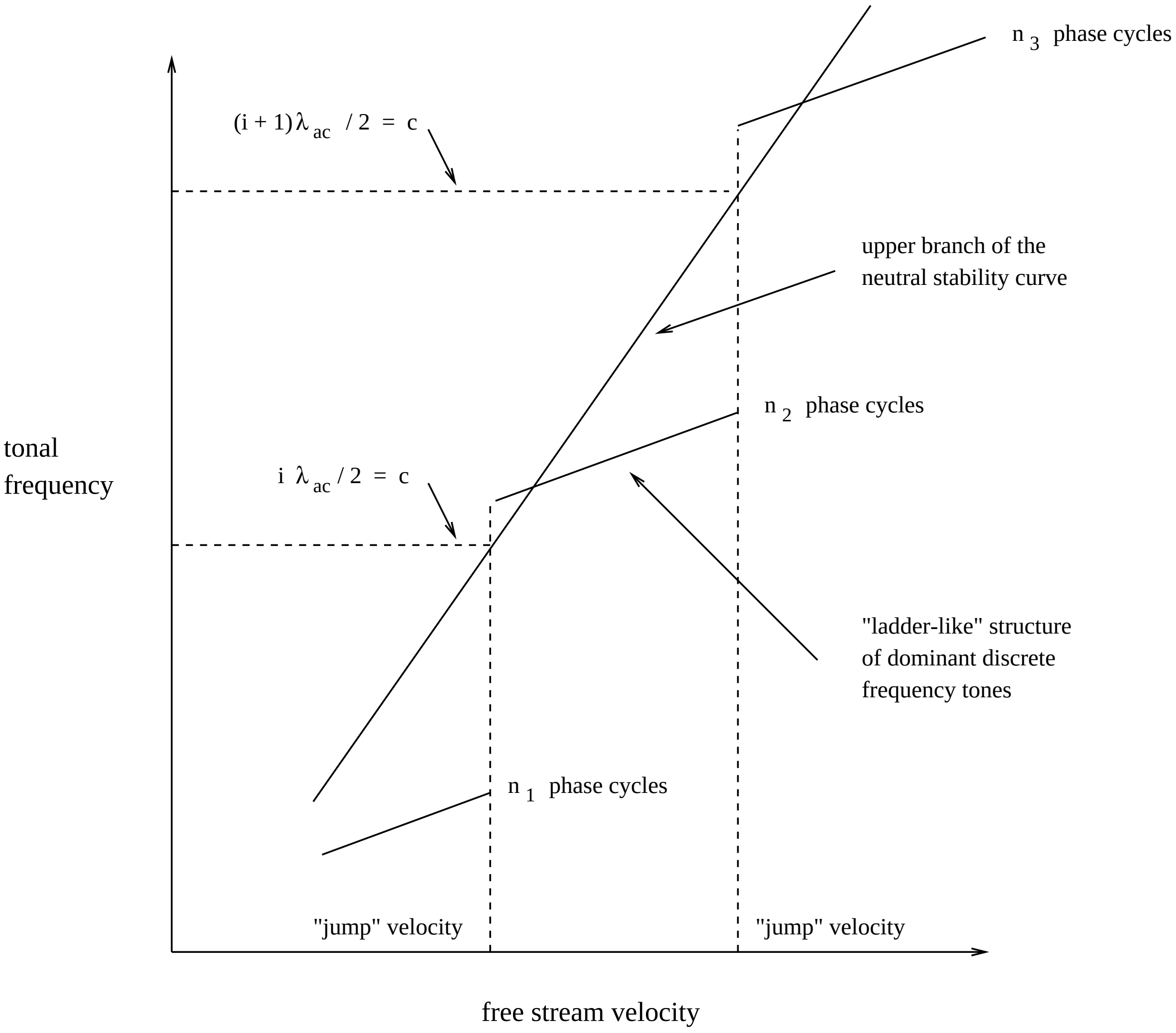

Figure 1.10: Sketch of frequency prediction scheme, (taken from Fink [18]).

an integral number of acoustic half-wavelengths fit across the chord. In my opinion the agreement between the prediction model and experimental data shown by Fink is questionable.

Arbey & Bataille ([3], 1983) recognized that the feedback mechanisms described by the previous authors held merit but found Fink's prediction method unconvincing. From results of typical spectra of the radiated noise, Arbey & Bataille concluded that there were two contributions to the noise spectrum, a broadband contribution around frequency f_b and a set of regularly spaced discrete frequencies f_n. It should be noted that the noise frequency spectra presented in Arbey & Bataille reveal many discrete peaks in the spectrum and do not resemble those originally presented by Paterson et al. However, tonal noise was heard in both cases and Arbey & Bataille compared their results with those of Paterson et al.

Arbey & Bataille attribute the broadband noise to diffraction of T–S waves at the trailing edge of the aerofoil. The discrete peaks are tones superimposed on the broadband noise spectrum generated by a feedback mechanism (taken to be the aero-acoustic feedback loop described previously).

Experimental results revealed that the Strouhal number for the broadband noise was approximately constant,

$$St_b = \frac{f_b \delta}{U_\infty} \approx 0.048 \pm 0.003\,. \tag{1.12}$$

Calculation of the boundary-layer thickness, δ, gave the following relationship for the broadband noise,

$$f_b = 0.011 U_\infty^{3/2} (c\nu)^{-1/2}\,, \tag{1.13}$$

which coincided with the average law (1.5) for tonal frequencies from Paterson et al.

They also found a Strouhal number for the discrete frequencies f_n,

$$St_n = \frac{f_n L}{C_1 U_\infty^m}\,, \tag{1.14}$$

where $C_1 \approx 0.89 \pm 0.05$ and $m \approx 0.85 \pm 0.01$. They believed (1.14) accounted for the $U_\infty^{0.8}$ behaviour followed for small variations in U_∞ by the discrete frequencies, also described by Paterson et al.

From (1.13) and (1.14), f_b increased roughly twice as quickly as f_n. Unlike f_b and f_n, the dominant discrete frequency, say $f_{n\,max}$, was a discontinuous function of U_∞. Arbey & Bataille suggested 'jumps' in the dominant tonal frequency occurred when f_b coincided with the discrete frequencies f_n, f_{n+1}, $f_{n+2}\,, \ldots$ as U_∞ was slowly increased.

The experimental work by Arbey & Bataille offers a link between the $\sim U_\infty^{3/2}$ and $\sim U_\infty^{0.8}$ power laws in Paterson et al. with the aero-acoustic feedback mechanisms described in later papers.

1.4 Initial work conducted at the University of Bristol

§1.3 describes in chronological order the study of tonal noise since the 1970's. The study of tonal noise conducted at the University of Bristol initially had several aims.

Firstly, the occurrence of tonal noise had only previously been reported in open-jet wind-tunnels. Tonal noise in closed wind-tunnels is usually attributed to acoustic resonances between the tunnel walls, known as Parker modes (§2.2.2). The initial experimental investigation was carried out to see if the tonal noise characteristics of aerofoils in open-jet wind-tunnels was also present in closed wind-tunnels.

A private communication between Prof. S.P. Fiddes (Dept. of Aerospace Engineering, University of Bristol) and Dr. E.C. Nash had indicated that the comment made by Longhouse [28] regarding flow separation on the aerofoil deserved further investigation. Numerical results from a boundary layer prediction code written by Prof. Fiddes had indicated the existence of a region of separated flow, near the trailing edge, on the pressure surface of a NACA 0012 aerofoil, for the flow conditions where tonal noise was predicted.

Assuming tonal noise was also detectable in a closed wind-tunnel then the aim was to investigate the tonal noise mechanism, in particular the boundary layer over the aerofoil, in the hope of providing a more complete description of the mechanism of tonal noise.

A note on the work of Hersh & Hayden (1971) and Longhouse (1977)

In §1.3 the papers reviewed *all* assumed that a laminar boundary layer extends to the trailing edge on at least one surface of the aerofoil for the existence of tonal noise. Longhouse [28] was the only author to mention the possibility of flow separation on the aerofoil although he did not pursue this any further.

However the flow separation on a NACA 0012 aerofoil had been reported in 1971 by Hersh & Hayden [23] when investigating sound radiation from lifting surfaces. (The paper was not specifically an investigation of tonal noise and hence is not reviewed in §1.3.)

In their study, one of the blades used by Hersh & Hayden was the NACA 0012 aerofoil and they report that 'loud, distinct tones' were heard when the flow over the surfaces corresponded to 'predominantly laminar boundary layers'. For $R < 0.33 \times 10^6$ the NACA 0012 aerofoil was observed to have laminar trailing edge separation. They attributed the tones to trailing edge vortex shedding noise and noted that placing serrations on the leading edge removed the distinct tones. The serrations generated vortices which propagated over the aerofoil destroying the character of the laminar boundary layer and the separation. The dependence of the noise on the trailing edge separation was not developed further.

1.4.1 Review of recent literature

Initial results from the investigation at the University of Bristol were presented by Lowson et al. [29] in 1994. Tonal noise was found to be present in a closed wind-tunnel and was found to occur in roughly the same flow conditions as those of Paterson et al. [16]. This is believed to be the first time that 'laminar boundary-layer noise' has been heard in a closed wind-tunnel. (Problems associated with testing in a closed wind-tunnel are discussed in detail in §2.2.)

Results initially from a NACA 23015 aerofoil section indicated a laminar separation bubble on the pressure surface of the aerofoil at the free-stream velocities where tonal noise was heard. Small changes of only 1° may eliminate the tones. Tones were also heard up to 40 dB above the background level from a NACA 0012 aerofoil but the results are difficult to interpret owing to many spurious frequencies.

The length of the laminar separation bubble was found to reduce as R increased and it was also shown that placing a trip strip inside the bubble may not eliminate the tones. T–S waves were assumed to be present initially in the boundary layer and it was expected that the separated laminar shear layer would strongly amplify them. This amplification stops on boundary-layer transition (along with the tones), and hence the noise level is expected to be a ‘function of the bubble length’.

Lowson et al. also showed that a leading edge bubble on the suction surface which may occur was not related to this mechanism.

Nash & Lowson ([34], 1995) described the steps taken to eliminate the numerous spurious frequencies which were detected during the experiments in a closed wind-tunnel. Having established that the tonal frequencies were controlled by the flow separation region, boundary-layer measurements using both hot-wire techniques and a Laser Doppler Anenmometer (LDA) were conducted. Nash & Lowson demonstrated that hot-wire measuring techniques were seen to alter the basic flow, (only in the region of the laminar separation bubble).

The paper presented LDA boundary-layer velocity profiles, rms boundary-layer profiles and streamwise time series plots for the boundary layer. These revealed large fluctuations around the separation bubble, fluctuations at the frequency of the tonal noise. The paper concludes that the fluctuations were amplified T–S waves which were shown to correspond directly to the tonal noise. (A review of the experimental procedures and results is presented in Chapter 2).

1.5 Review of laminar boundary-layer separation and instability

The dependence of the tonal noise on a region of separated flow close to the trailing edge on the pressure surface has been shown by Lowson et al. [29]. A review of laminar boundary-layer separation and its associated instability was undertaken by Dovgal et al. [14] in 1994.

A separation bubble is defined as the region of recirculating flow between the flow separation and re-attachment points on the surface of a rigid body. Flow separation is commonly caused by adverse pressure gradients. Separation bubbles are usually very small, often less than one boundary-layer thickness high. However, experimental observations reveal that separated flows become unstable at relatively low Reynolds numbers. A model of a separation bubble is sketched in figure 1.11.

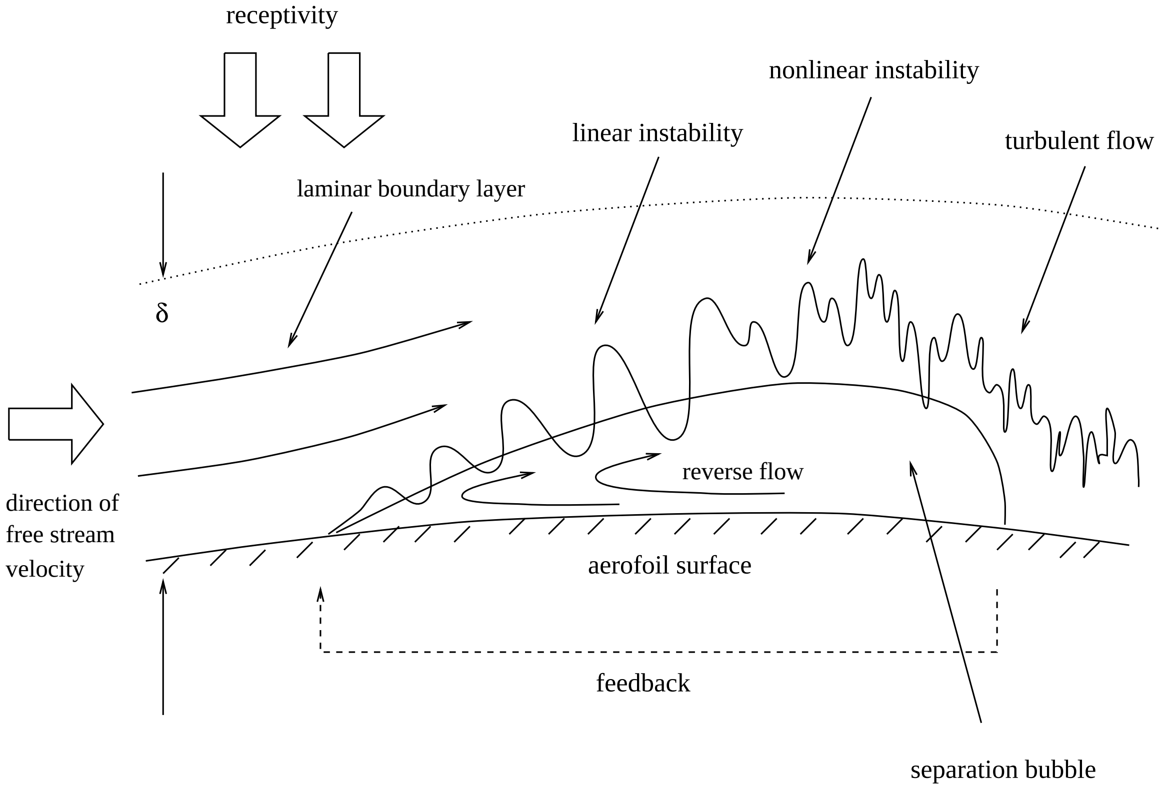

Figure 1.11: Sketch of laminar separation bubble, (taken from Dovgal et al. [14]).

Again experiments reveal that a separation bubble induces boundary-layer transition at or close to the point of re-attachment. The transition originates from the convective streamwise growth of initially small-amplitude disturbances. Strong growth occurs just upstream of the separation bubble and nonlinear interactions of now finite-amplitude disturbances over the separation bubble lead quickly to transition.

Boundary-layer receptivity is the mechanism through which external oscillations (such as background turbulence or sound waves) excite small-amplitude disturbances in the boundary layer. If the layer is unstable then these disturbances will grow as they propagate in a streamwise direction. The mean velocity profiles of a separated flow appear more receptive to external influence than those with weaker pressure gradients, such as the Blasius boundary layer.

Laminar separated flows may be shown to be unstable because they have an inflexion point in their profile away from the boundary surface. Rayleigh showed that all profiles with an inflexion point are unstable as $R \rightarrow \infty$. Thus instability through an inflexional profile is largely governed by inviscid dynamics. The mechanisms of inflexional instabilities are discussed in more detail in §3.5.1. The disturbances in a separation bubble surprisingly appear linear until their amplitude is about 1% of the free-stream velocity U_∞. The growth of disturbances may be considered locally by modelling the front of the bubble as a shear layer. This is reasonable because the instability is no longer governed by the viscous effects of the no slip condition on the boundary surface. The frequency spectrum of the disturbances in the nonlinear regime is largely governed by the spectrum from the linear growth. The main mechanism of nonlinear breakdown is through the generation of harmonics by the fundamentally growing wave.

Experiments also indicate that the growth of streamwise perturbations may lead to the disturbances distorting the mean-flow. If the amplitude of the disturbances is above about 1% on re-attachment of the flow then typically the nonlinear waves generate a distortion of the mean-flow which spreads upstream over the entire separation bubble. The weakly nonlinear stability analysis conducted in Chapter 4 includes a 'mean-flow distortion' term in the formulation to take account of the fact that finite-amplitude disturbances may alter the mean-flow.

The frequency spectra of separation bubbles will typically contain a broadband long-wave at low frequencies. This is due to a phenomenon called 'flapping', the transverse (vertical) oscillations of the bubble.

Experiments also show that the boundary-layer disturbances in a bubble will typically have three amplitude peaks as you move vertically up from the boundary surface. This characteristic of the instabilities in separation bubbles is confirmed both experimentally and through numerical calculations in Chapters 2 and 3 respectively.

The experimental results now presented in Chapter 2 clearly show the existence of a laminar separation bubble on the pressure surface of the aerofoil, and how the flow separation is an integral feature of the tonal noise mechanism.

Chapter 2

Experimental set-up and results

Wind-tunnel experiments investigating tonal noise were conducted at the Department of Aerospace Engineering Laboratory, University of Bristol, by Dr. E.C. Nash with advice from Prof. M.V. Lowson. This chapter briefly reviews the experiment and presents detailed results for several cases where tonal noise was heard. For a complete summary of the results the reader is referred to Nash [33], from which the results in this chapter are taken.

2.1 Aerofoil profiles

The majority of the experimental results were obtained using the NACA 0012 aerofoil profile. The specifications of the family of NACA aerofoils are described briefly in Anderson ([2], pp. 249–251). Several previous papers (e.g. Paterson et al. [16], Fink [18]) present results for the NACA 0012 aerofoil and hence this profile was chosen in the hope that the results would be comparable. The generation of tonal noise was not restricted to one aerofoil profile, and brief results are presented for the FX79 W151 aerofoil.

The NACA 0012 aerofoil is a symmetric profile with a ratio of maximum thickness to chord length of 12%. The NACA 0012 aerofoil constructed for this investigation spanned the width of the wind-tunnel (1000 mm), had chord length 300 mm, maximum thickness 36 mm and a sharp trailing edge. The FX79 W151 aerofoil is an asymmetric profile which is an example of a two-dimensional cross-section taken from a wind-turbine blade, (hence is of particular relevance to this problem as mentioned in §1.1). The FX79 W151 profile also had a span of 1000 mm, chord length 230 mm and a sharp trailing edge. Schematics of the two aerofoil profiles are shown in figure 2.1. Figure 2.1 also shows the three Cartesian coordinates (x, y, z) which are referred to as the streamwise (or chordwise), spanwise and transverse directions respectively.

2.2 Acoustic investigation

2.2.1 Preliminary set-up

Previous experimental studies have all used open-jet wind-tunnels to simulate an open environment. The aim is to eradicate any acoustic reflections due to nearby solid surfaces. For this investigation however all the experiments were conducted in a closed working section, closed-loop, low-turbulence wind-tunnel. The aerofoils used completely spanned the working section which had glass panels on both sides. Typically, the wind-tunnel was driven for velocities from $10\,\mathrm{ms}^{-1}$ up to $70\,\mathrm{ms}^{-1}$. Background acoustic measurements were taken in the empty tunnel so any spurious frequencies would be discounted. For velocities up to $30\,\mathrm{ms}^{-1}$ discrete frequencies at 600 Hz and 900 Hz were caused by the motor.

The aerofoil was mounted horizontally across the wind-tunnel working section and fixed at the required angle of incidence to the horizontal. The aerofoil was fixed at small negative angles of incidence so that the pressure surface would then be the top surface. This was performed to facilitate access to the pressure surface for future boundary-layer measurements.

All acoustic measurements were taken with a Brüel and Kjær (B&K) half-inch, condenser microphone, (type 4134), which was shielded by a polished nose cone to reduce the picking up of background wind noise. The microphone was mounted 150 mm above the trailing edge of each aerofoil and at midspan of the wind-tunnel. For the

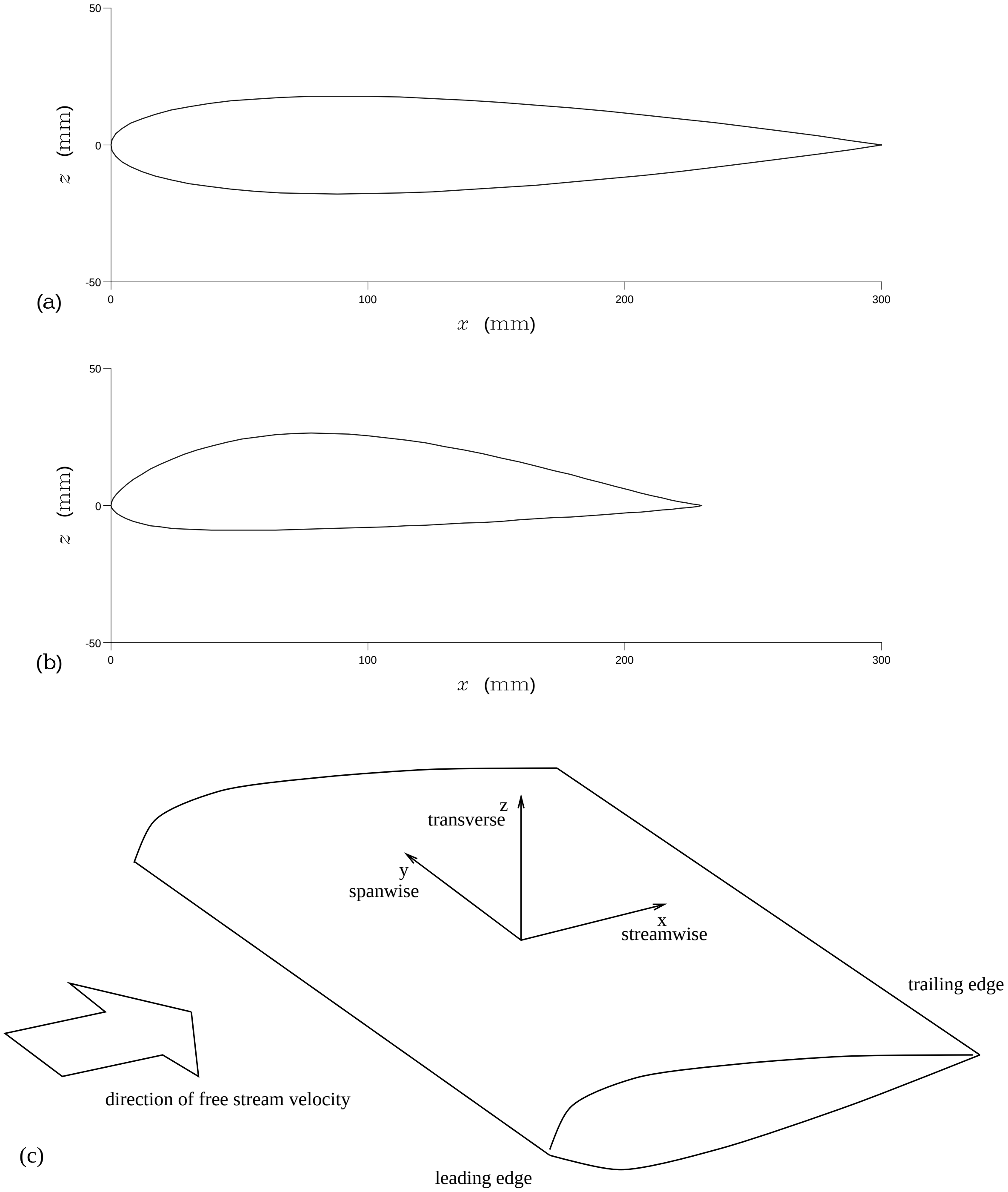

Figure 2.1: Aerofoil schematics: (a) NACA 0012, (b) FX79 W151 and (c) set-up and nomenclature.

NACA 0012 it was situated 100 mm and for the FX79 W151 135 mm downstream of their respective trailing edges. The microphone had a frequency range of 4 to

$20,000\,\mathrm{Hz}$.

2.2.2 A note on Parker modes

The main disadvantage of testing aero-acoustic effects in a closed wind-tunnel is the generation of unwanted acoustic resonances between the solid walls of the wind-tunnel.

The shedding of periodic wakes is commonly associated with mechanical vibrations when the shedding frequency becomes close to any natural frequencies of oscillation. The collapse of the Tacoma Narrows bridge in 1940 is possibly the most infamous example of this phenomenon. Mechanical vibrations of the aerofoils is discussed briefly in §2.2.5.

In 1966 however, Parker [37] & [38], investigated the connection between wake shedding and acoustic resonances. Initially, the tests were conducted over a cascade of flat plates in a wind-tunnel. Discrete acoustic resonant frequencies were detected in the tunnel over a range of free-stream flow velocities. The frequencies became 'locked' and were locally invariant to small changes in the free-stream velocity before 'jumping' to higher levels. The frequencies were dependent on the configuration of the system. The number of plates, the plate chord length and the distance between the plates are all factors which controlled the resonant frequencies. If the natural wake shedding frequency had wavelength greater than twice the plate separation, then the dimensions of the wind-tunnel controlled the frequency. The wavelengths of low frequency resonances become more comparable with the wind-tunnel dimensions and their behaviour gradually becomes independent of the plates in the tunnel.

Wind-tunnel traverses revealed pressure nodes both up- and downstream of the plates (in the plane of each plate). On increasing the distance between the plates, pressure nodes were also detected midway between, and normal to, the plates. Parker characterized the different patterns as α, β, γ, and δ modes.

In 1989, Parker & Stoneman [39] reviewed the research conducted since 1966 on closed flow systems where acoustic resonances were excited by vortex shedding from solid bodies in the flow. For a single flat plate in a wind-tunnel, the simplest acoustic mode which exists is the Parker β-mode which has a single pressure node in the plane of the flat plate. The Parker α-mode may also exist which has a further pressure node at approximately 50% chord normal to the flat plate. The more complicated Parker γ- and δ-modes only exist in a cascade of plates.

From experiments, in the flow over a bluff body (such as a plate or a cylinder) vortices are alternately shed from above and below the body. The vortex pairs being shed form a vortex street in the wake of the body. Over a wide range of Reynolds numbers it has been shown experimentally that the Strouhal number ($St = ft/U_\infty$ where f is the wake frequency, t the plate thickness and U_∞ the free-stream velocity) will remain approximately constant for a bluff body — close to 0.2.

As U_∞ increases, the wake frequency f approaches the first resonant frequency of the wind-tunnel duct. As this occurs the vortex shedding becomes highly correlated along the span of the plate as the frequency becomes 'locked' to the resonant frequency. Discrete frequency tones are generated. As U_∞ slowly increases the wake frequency remains 'locked' and therefore may not be predicted by assuming a constant Strouhal number.

The generation of discrete frequency tones in a closed wind-tunnel by the mechanism described by Parker modes is *not* the mechanism under investigation in this research. However Parker mode resonances (i.e. the Parker α- and β-modes) were likely to be observed from a single aerofoil mounted in a closed wind-tunnel. The occurrence of Parker modes was not a consideration in the previous studies already mentioned because they all used open-jet wind-tunnels.

2.2.3 Preliminary results

Preliminary experiments were performed to see if discrete frequency tones were observable in a closed wind-tunnel, loud enough to be heard above background noise levels. The limitations of a closed wind-tunnel were the main concern.

Resonant frequencies caused by standing waves between the tunnel walls and the aerofoil (i.e. Parker modes) will often be locally invariant to changes in U_∞, the free-stream wind-tunnel velocity. From Paterson et al. [16], the discrete frequency tones were overall proportional to $U_\infty^{0.5}$, with a local ‘ladder-type’ structure with ‘rungs’ proportional to $U_\infty^{0.8}$, see figure 1.6. The different dependence on U_∞ of Parker modes and those described by Paterson et al. allowed certain modes to be clearly identifiable.

The preliminary tests showed approximate agreement with the empirical expressions of Paterson et al., and many discrete tones were heard well above background noise levels. The background noise level was approximately 70 dB when the tunnel was driven at moderate free-stream velocities (less than $30\,\mathrm{ms}^{-1}$). The discrete tones detected were of the order of 100 dB — 30 dB higher than the background level. (A difference of x dB implies a change in the intensity of the sound of $10^{x/20}$. A difference of say 40 dB is actually a tone with intensity 100 times louder than the background level.)

The results were complicated by the existence of several discrete frequencies which were invariant over a range of free-stream velocities, and many tones did not fit the empirical expressions. Care was taken to compensate for this and modify the wind-tunnel to better approximate the anechoic conditions of an open-jet wind-tunnel.

2.2.4 The modified wind-tunnel

To attempt to approximate anechoic conditions, the floor and ceiling of the wind-tunnel test section were removed and replaced by boxes 500 mm deep containing acoustic foam. The foam absorbs the acoustic energy and greatly reduces acoustic reflections between the walls of the tunnel. Figure 2.2 is a schematic of the test section of the wind-tunnel. The boxes filled with acoustic foam are shown. The test section is octagonal and it was not practical to put acoustic foam on the inclined walls.

As reported by Paterson et al. [16], the tonal noise appeared to depend upon a laminar boundary layer on one side of the aerofoil. Placing a boundary-layer trip strip on the aerofoil at (say) 80% chord destroys the laminar boundary layer and also the tonal noise. A trip is a narrow, fine strip of material with a coarse texture, such as glass paper, which trips a laminar flow to a turbulent one. The strips used were made

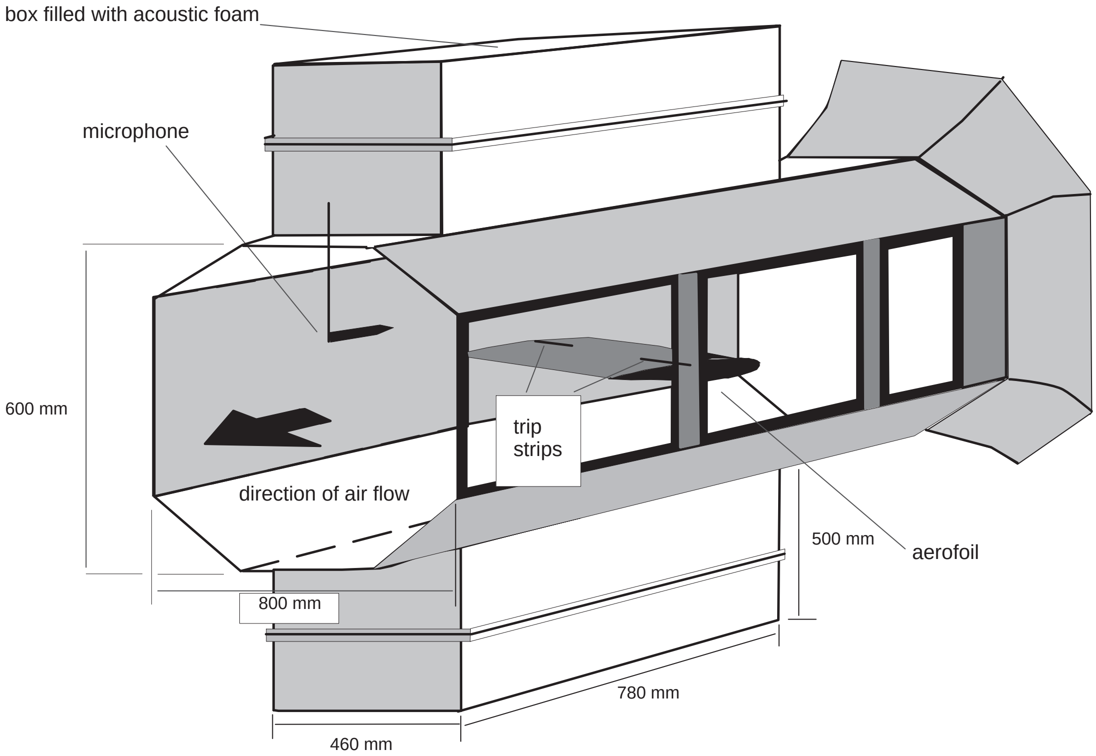

Figure 2.2: Wind-tunnel test section schematic

of glass paper, 3 mm wide and 0.6 mm high. Both the discrete tones and the acoustic resonances between the tunnel walls were successfully eliminated by placing a trip strip across the entire span of the aerofoil at 80% chord.

To further eliminate acoustic resonances between the tunnel walls, the flow was partially tripped at either end of the aerofoil for two reasons. Firstly, the partial trips should eliminate any acoustic resonances which may occur between the inclined walls of the test section (which were not lined with the acoustic foam). Secondly, the presence of multiple tones at one free-stream velocity were believed to be due to a loss of spanwise uniformity across the aerofoil (see Fink [18]). Both the aerofoils under investigation were two-dimensional, but boundary-layer instabilities are notoriously sensitive to changes in the boundary surface, and, partially tripping the flow would further increase the two-dimensionality of the experiment.

2.2.5 Results using the modified wind-tunnel

Placing the trip strip on the suction surface of the aerofoil did not affect the tones for all free-stream velocities. This confirmed that the tones were dependent on one surface of the aerofoil — namely the pressure surface. Placing the trip strip at 80% chord on the pressure surface destroyed the tonal noise for all free-stream velocities. In all the papers discussed in §1.3, the tones were assumed to be dependent on a laminar boundary layer extending until the trailing edge of the aerofoil. However in our experiment, tones were still heard if the trip strip was placed very close to the trailing edge on the pressure surface of the aerofoil. Commonly tones were still heard for a trip strip placed at 95% chord. This confirmed that the flow does *not* have to be laminar and attached at the trailing edge for tones to be heard.

It was possible to eliminate the tones again by moving the trip strip further upstream of the trailing edge. The reason for this surprising result was the existence of a small region of separated flow close to the trailing edge. Placing the trip strip *before* the flow separation will eliminate all the tones. Placing the trip strip *after* the flow separation does not eliminate the tones. This observation will be discussed in more detail in this chapter and Chapter 3.

In figure 2.3, the discrete frequency tones detected over a range of free-stream velocities, for four fixed angles of incidence, are plotted. The tones detected before the partial trips were placed on the aerofoil are denoted by $\circ$. The tones remaining after the introduction of the partial trips are denoted by $*$. Even without the partial trip strips the acoustic lining has successfully eliminated the majority of the Parker mode resonances. (Possibly an invariant frequency remains just less than 1000 Hz at -4° incidence.) With the partial trips included all spurious resonances appear to have been eliminated and the aerofoil is assumed to approximate anechoic conditions. The introduction of the partial trips has reduced the occurrence of multiple tones at one free-stream velocity. At most free-stream velocities only one discrete frequency is detected. The modified wind-tunnel set-up reduced the occurrence of Parker mode resonances and improved the two-dimensionality of the experiment. All the results presented shortly were obtained using the modified wind-tunnel.

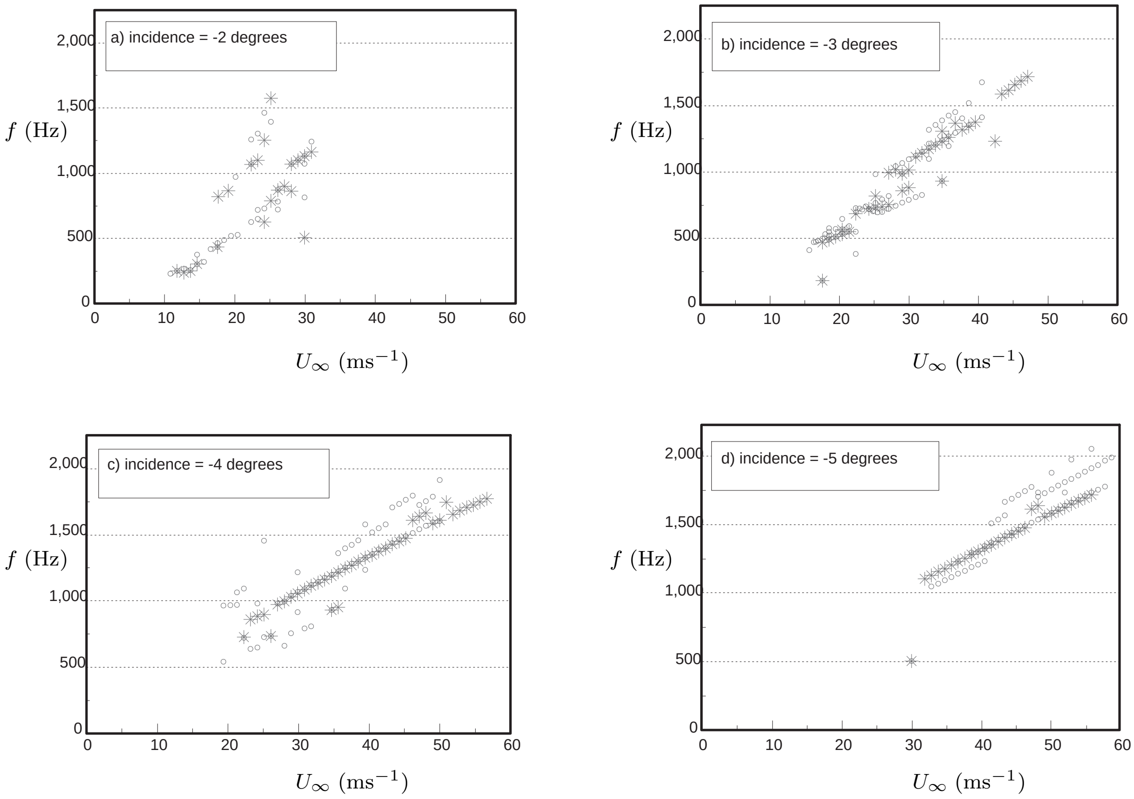

Figure 2.3: Comparison of discrete frequency tones detected from the NACA 0012 aerofoil with side trips ($*$), and without side trips ($\circ$).

The discrete frequency tones measured at $-4°$ and $-5°$ do not show the 'ladder-like' structure described by Paterson et al. [16]. However, the curves do fit the empirical expression $f \propto U_\infty^{0.8}$ very well. At each angle of incidence there is a lower and upper bound on U_∞ between which tonal noise is heard. The tones measured at $-3°$ possibly exhibit a 'ladder-like' structure. The behaviour is less clear for $-2°$ and the tones only occur for lower free-stream velocities.

The frequencies heard were found to be repeatable. Although the presence of frequency 'jumps' was questionable at these angles of incidence, the range of frequencies and their relation to U_∞ confirmed that the mechanism being studied was the same as reported previously in open-jet wind-tunnels.

Tests were also conducted to ensure that the tones were not due to mechanical vibrations of the aerofoils. Mechanical vibrations are common in most aspects of engineering and it was important to confirm that the tones were not due to mechanical vibrations at the natural resonant frequencies of the aerofoils.

The results of these tests showed clearly that any mechanical vibration was a result of the tonal noise and not vice versa. The aerofoil was shown to vibrate at exactly the frequency of the discrete tones but on eliminating the tones the vibration also was eliminated. The tones were eliminated by a trip strip which would have a negligible effect on the structural resonant frequencies of the aerofoil. The tones cause aerofoil vibrations which could lead to aerofoil fatigue (although these vibrations are very small — much less than one boundary-layer thickness).

2.3 Boundary layer investigation

This section describes the investigation of the boundary layer on the pressure surface of the two aerofoils.

2.3.1 The hot-wire and the laser doppler anemometer

Until recently the most common method of measuring boundary-layer and rms (root mean square) velocity profiles (see 2.3.2) was with a hot-wire anemometer. A hot-wire anemometer is a tiny strip of wire, (1.25 mm in length and approximately 0.005 mm in diameter), supported on a mount with a current passing through it. When placed in a flow the heat loss from the wire is dependent on the velocity of the flow perpendicular to the wire. The hot-wire is kept at the same temperature through a heating current supplied by an amplifier. The output from the amplifier changes to reflect changes in the temperature of the wire (or its resistance) as a result of changes in the flow around the wire. From the output of the amplifier, mean-velocity measurements are obtained. A hot-wire can only detect the magnitude of the flow and not the direction. It is also a flow intrusive method as the hot-wire and its mount have to be placed inside the flow.

The laser doppler anemometer (LDA) used at Bristol University was a *Dantec* three-component LDA consisting of two optic heads mounted on a fully automated traverse. Three pairs of beams transmitted from the optic heads focus on one point in the flow. The automated traverse allows the measuring volume to be positioned precisely. Typically measurements were taken starting from 0.05 mm above the aerofoil surface and with steps in the transverse direction of 0.05 mm. Three pairs of beams are used to take three-component measurements simultaneously.

Seeding particles are added to the flow downstream of the working section. The particles were oil droplets with a diameter of approximately 0.001 mm. They are added downstream of the working section to ensure the turbulence levels are as low as possible upstream of the aerofoil.

If there is a relative motion between the source of a transmitted wave and an observer, then the frequency of the transmitted wave will differ to the frequency as viewed by the observer, by the Doppler shift. A simple example is to consider two pulses of light emitted from a source located in a frame of reference which is moving relative to a rest frame. The time difference between the pulses measured by an observer in the rest frame will differ from those measured by an observer in the moving frame of reference. This is because the distance between the source and the observer in the rest frame will differ between the two pulses because there is a relative motion between the two frames.

When a seeding particle passes through the measuring volume, light is scattered and picked up by the optic heads. The relative speed of the seeding particle with the origin of each beam (in a pair) is different because the origins are slightly different. For each pair of beams two slightly different frequencies of light are detected because of the Doppler shift. The signals picked up by the receiving optic heads convert the scattered light into a voltage signal known as a 'burst'. A burst spectrum analyzer then converts the voltage frequency into a velocity. At any point 10,000 data points (or 'bursts') were taken. The LDA was run by a *Dantec* software package called *Burstware* which controlled the collection, processing and presentation of the data.

The LDA is able to measure both the magnitude and the direction of the flow in three-component directions simultaneously. It is also a non-intrusive device for measuring the flow.

2.3.2 Results obtained from the hot-wire and LDA

The hot-wire anemometer and the LDA both measure the mean- and rms velocity profiles. These are defined for n data points at a fixed station to be,

$$\text{mean velocity} \quad \bar{u} = \sum_{i=1}^{n} u_i/n \,, \tag{2.1}$$

$$\text{rms velocity} \quad \sigma = \sqrt{\sum_{i=1}^{n}(u_i - \bar{u})^2/n} \,. \tag{2.2}$$

The rms velocity profile is a measure of the deviation from the mean-velocity profile, and in this sense is a measure of the magnitude of the disturbances in the flow. The rms velocity profiles are analogous to the eigenfunctions presented in §3.5.1. As noted previously, the hot-wire only detects the magnitude of the velocity and hence $\bar{u} > 0$ everywhere.

It is only recently that spectral measurements have been taken by using a LDA. (The main difficulty is that very high data rates are required.) Advanced techniques for achieving these high data rates have been developed over the past few years at the Aerospace Engineering Laboratory at Bristol University. They found that the data rate should be around 10 times the maximum frequency to be measured, and have developed techniques to achieve this, even in the boundary layer.

The randomly arriving data may be plotted to show time series in each coordinate direction. The data is also re-sampled to produce ‘pseudo-equi-time-spaced data’ which is then suitable for FFT analysis, (Fast Fourier Transform), to produce frequency spectra.

Mean- and rms velocity profiles, time series and frequency spectra are all presented in this chapter.

2.3.3 Preliminary results of the hot-wire and LDA

Figure 2.4 compares the hot-wire results with the LDA results. The LDA results reveal that there is a region of reversed flow close to the trailing edge of the aerofoil. The hot-wire is unable to detect this, and perhaps more significantly, there is a large discrepancy between the boundary-layer profiles measured when the mean flow is positive. Nash [33] concluded that the discrepancy was due to the distortion of the flow through the introduction of the hot-wire, particularly in the region of reversed flow. This region is less than 1 mm in height and extremely sensitive. Nash found that three different hot-wires all disturbed the flow to an extent that they modified the reversed flow and the flow remained attached up to the trailing edge. This reduced the tonal output in most cases by around 50%. For the rest of the investigation Nash only used the LDA because the tonal noise mechanism was deemed too sensitive to be studied using a flow intrusive technique such as a hot-wire. The hot-wire was believed to affect the region of reversed flow close to the trailing edge of the aerofoil, which Nash & Lowson [34] had shown controlled the tonal noise (see §1.4.1).

2.3.4 Prediction methods

Chapter 3 describes how a linear stability analysis was conducted for the flow over the pressure surface of the aerofoil. To ascertain the development of the boundary layer, measurements were made at stations from approximately 30% chord until the trailing edge. At each station the boundary layer was characterized by two integral thicknesses — namely the displacement and momentum thickness. It was not practical because of time constraints to obtain a complete set of experimental results at each station on the pressure surface of the aerofoil.

Instead a prediction program supplied by Prof. S. Fiddes (Department of Aerospace Engineering, University of Bristol) was used to calculate the displacement and momentum thicknesses of the flow upstream of the separation point on the aerofoil. The prediction program requires the coordinates of the aerofoil, the angle of incidence and the Reynolds number of the flow as input parameters. The prediction method assumes a laminar attached boundary layer and also predicts the point of separation. It was found that this theoretical separation point was always upstream of the observed point of separation. This ensured that the flow was attached for all the stations where the prediction program was used to obtain the integral thicknesses.

A comparison between the predicted and experimentally measured displacement and momentum thicknesses was conducted, and the discrepancy was found to be less than 5% for stations before the separation point. Examples of the data obtained is shown in appendix A for cases 1, 2 and 3 (see table 2.1 for a list of cases). The spreadsheets in appendix A for cases 1, 2 and 3 indicate whether the data were obtained using the prediction program or experimentally.

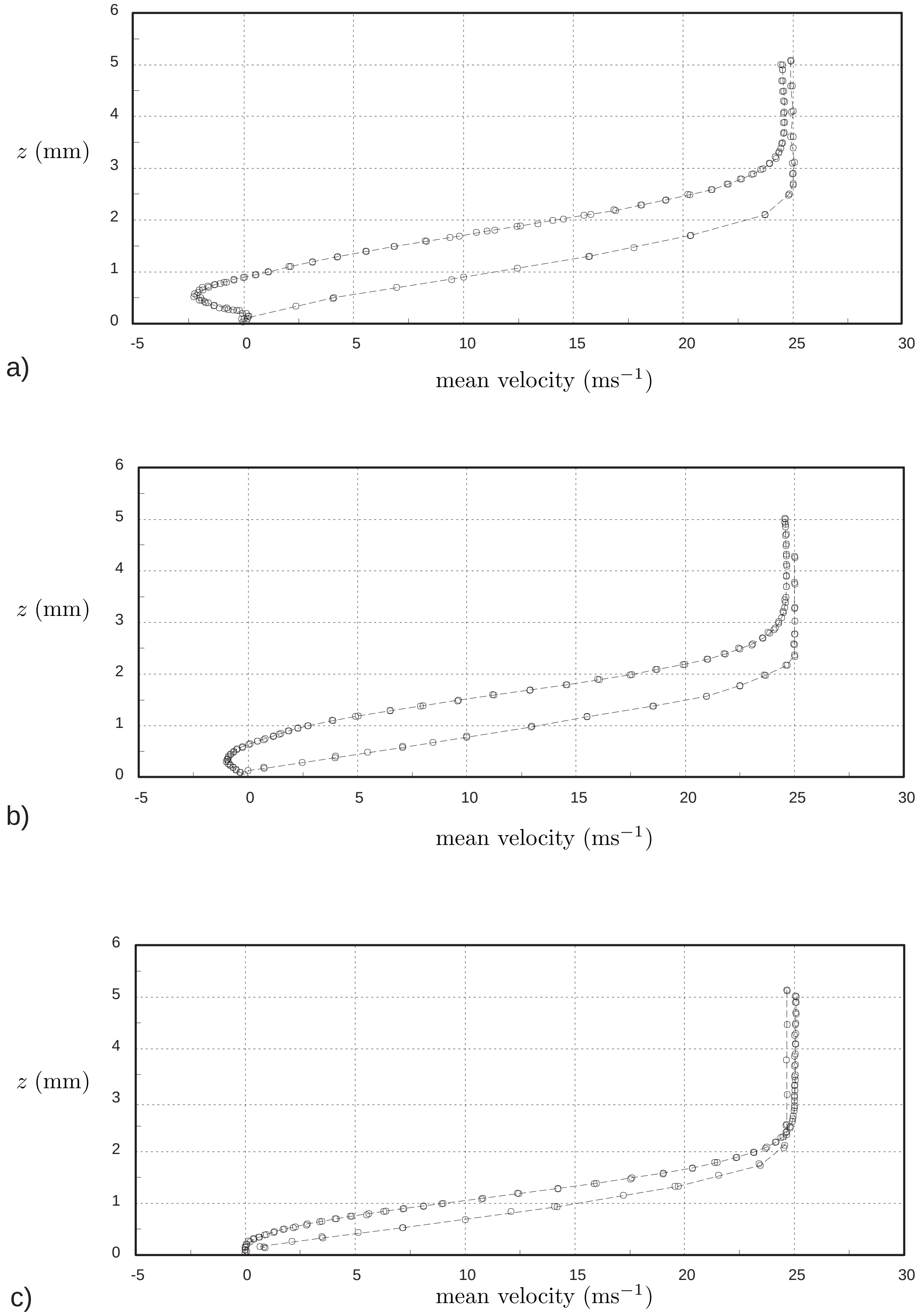

Figure 2.4: Comparison of mean-velocity profiles measured by the hot-wire anemometer and LDA. Measurements taken from the NACA 0012 aerofoil with $U_\infty = 30\,\text{ms}^{-1}$: (a) 5 mm, (b) 10 mm and (c) 25 mm, upstream of the trailing edge.

2.4 LDA experimental results

2.4.1 Cases investigated

Table 2.1 is a summary of the six test cases for which experimental data are presented in this section. In Chapter 3 the linear stability analysis conducted on each of these cases is presented. The experimental and theoretical results are then compared.

Case	Aerofoil	Angle	U_∞	Tone
1	NACA 0012	$-4°$	$30\,\mathrm{ms}^{-1}$	1048 Hz
2	NACA 0012	$-4°$	$38\,\mathrm{ms}^{-1}$	1280 Hz
3	NACA 0012	$-4°$	$44\,\mathrm{ms}^{-1}$	1420 Hz
4	FX79 W151	$-3°$	$30\,\mathrm{ms}^{-1}$	1192 Hz
5	NACA 0012	$-3°$	$8\,\mathrm{ms}^{-1}$	no tone
6	NACA 0012	$0°$	$17\,\mathrm{ms}^{-1}$	no tone

Table 2.1: Details of cases of tonal noise investigated.

Mean and rms boundary-layer profiles together with time series and frequency spectra plots were obtained for all the cases listed in table 2.1, using the LDA. A full set of results may be found in Nash [33]. A discussion of the experimental results for each case follows. All the data shown are for measurements in the streamwise direction.

2.4.2 Tonal cases: 1, 2, 3 and 4

Figure 2.5 shows the range of free-stream velocities over which tones were heard for the NACA 0012 aerofoil at $-4°$. Cases 1, 2 and 3 are shown on this graph, with U_∞ increasing with each case. For $20\,\mathrm{ms}^{-1} < U_\infty < 60\,\mathrm{ms}^{-1}$ discrete tones are heard. In §2.4.4 the behaviour of the tones as $U_\infty \to 60\,\mathrm{ms}^{-1}$ is discussed. As shown in figure 2.3, tones were heard for a range of small angles of incidence. Results for a low free-stream velocity where no tones are heard for the NACA 0012 aerofoil at $-3°$ are presented in §2.4.3. The behaviour of the flow around the aerofoil at low free-stream velocities, e.g. $U_\infty < 20\,\mathrm{ms}^{-1}$, is similar for all small angles of incidence.

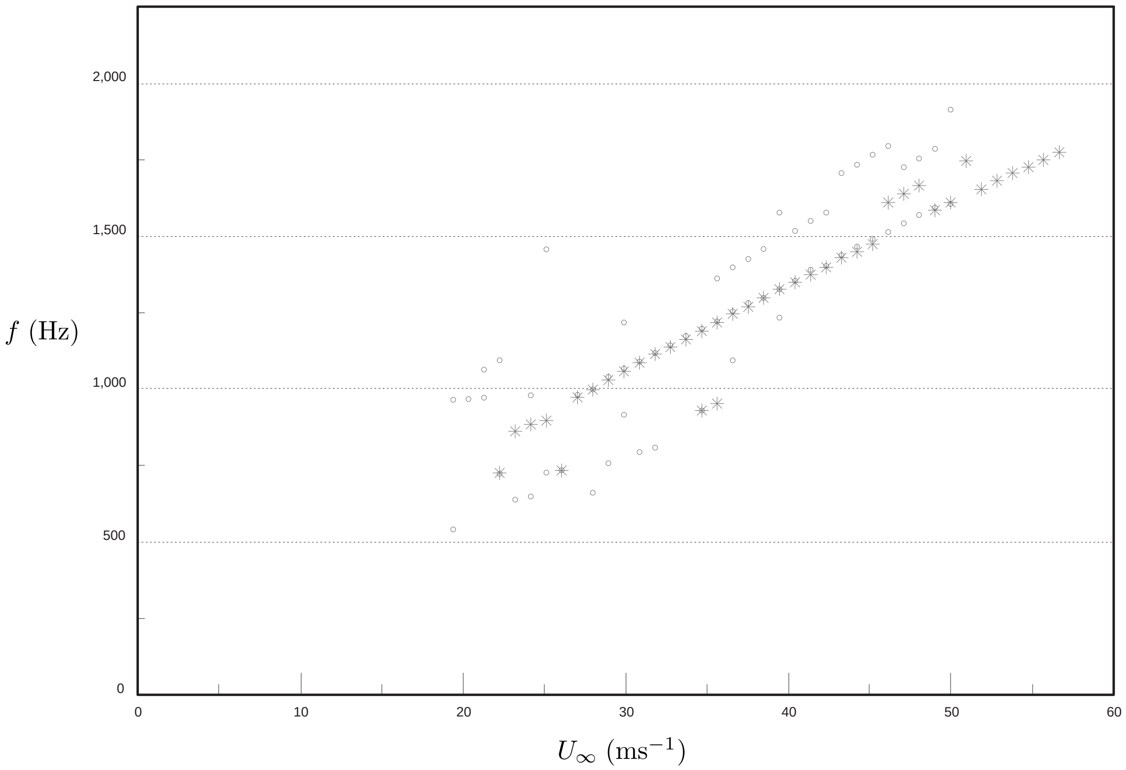

Figure 2.5: Discrete frequencies detected using the modified wind-tunnel ($*$), for NACA 0012 aerofoil at $-4°$.

The behaviour of the tones for $20\,\mathrm{ms}^{-1} < U_\infty < 30\,\mathrm{ms}^{-1}$ is unclear, but, for $30\,\mathrm{ms}^{-1} < U_\infty < 60\,\mathrm{ms}^{-1}$ the behaviour of the tones is very regular. To the eye the frequency depends almost linearly on the free-stream velocity and there may be a frequency 'jump' around $U_\infty \approx 46\,\mathrm{ms}^{-1}$. In Paterson et al. [16], an open-jet wind-tunnel was used with a NACA 0012 aerofoil with chord 9 in. At an angle of $-4°$ discrete tones were detectable between approximately $U_\infty = 100\,\mathrm{FPS}$ and $250\,\mathrm{FPS}$. The discrete frequencies were heard for Reynolds numbers between $R = 460,000$ and $1,160,000$. In figure 2.5 the range of Reynolds numbers over which tones are heard is $440,000 < R < 1,140,000$. The range of the Reynolds number over which discrete tones are heard is remarkably similar for the two separate experiments. In Paterson et al. there are three 'jumps' in the frequency over the prescribed range of the Reynolds number. In figure 2.5 there appears to be only one 'jump' in the frequency. However the results from Paterson et al. encompass the results for several angles of incidence. It is unclear from Paterson et al. as to whether the ‘jumps’ occur at the same frequencies for varying angles of incidence. This would seem unlikely and the three ‘jump’ frequencies marked in Paterson et al. are assumed to be the general trend observed by using data points from various angles of incidence. A ‘jump’ in frequency suggests that a feedback loop is present, and the jump occurs when there is a change of phase around the loop. However, in figure 2.5 the ‘jump’ at $U_\infty \approx 46\,\mathrm{ms}^{-1}$ is questionable because the tonal frequencies do not remain on the next ‘rung’ of the ‘ladder’. It is possible that this is an experimental error and all the tonal frequencies may depend almost linearly on the free-stream velocity.

Figure 2.6 shows the acoustic frequency spectra for the tonal cases 1, 2, 3 and 4. The background sound level is between 60 and 70 dB — the discrete tones are between 25 and 30 dB higher. There is also loud, low frequency, broadband noise (up to approximately 200 Hz) visible in each spectrum due to extraneous tunnel noise. Note again (see §2.2.1) that the acoustic spectra were obtained from a microphone placed 150 mm above, and between 100 and 135 mm downstream, of the trailing edge of each aerofoil. Hydrodynamic disturbances in the wake and boundary layer of the aerofoil decay exponentially in the free stream. The microphone was positioned far enough away from the aerofoil to be unaffected by the hydrodynamic disturbances propagating over the aerofoil and into the wake.

Figures 2.7, 2.8 show the mean- and rms velocity profiles for the flow from 35 mm to 2.5 mm upstream of the trailing edge. The characteristics exhibited by the profiles for case 1 are repeated for each tonal case.

Until 25 mm upstream of the trailing edge, the flow is attached and laminar. The rms profiles have one small peak (less than $1\,\mathrm{ms}^{-1}$) approximately midway through the boundary layer. At approximately 20 mm upstream of the trailing edge the boundary layer is on the verge of separating. All the mean-velocity profiles downstream of this point have a small component of reversed flow close to the aerofoil surface. The boundary layer is also thickening as it approaches the trailing edge, (approximately increasing from 2 mm to 3 mm after the point of separation).

The rms velocity profile distributions become much stronger approaching the trailing edge. After the flow separation the rms profiles have a triple-peaked structure. This structure is also observed in the eigenfunctions presented in §3.5.1. The rms velocities peak at 3 to 4 times the mean velocity close to the surface of the aerofoil. The rms is also significantly greater than the background rms free-stream level, up to approximately two boundary-layer thicknesses above the aerofoil. The rms profiles indicate the presence of large boundary-layer instability waves after the flow has separated.

Figure 2.9 shows a series of time series plots taken 5 mm upstream of the trailing edge moving through the boundary layer, normal to the aerofoil surface. Time series (a) was obtained 0.4 mm above the aerofoil surface and hence the mean velocity is close to $0\,\mathrm{ms}^{-1}$. The flow exhibits large fluctuations of the order of $\pm 5\,\mathrm{ms}^{-1}$. These large fluctuations close to the aerofoil surface correspond to the largest rms velocity peaks seen in figure 2.8. Although the flow is clearly fluctuating the time series does not exhibit any discernible regular structure.

At 1.55 mm above the surface of the aerofoil, time series (b) exhibits fluctuations of $\pm 3\,\mathrm{ms}^{-1}$ about a mean velocity of $\approx 15\,\mathrm{ms}^{-1}$. These correspond to the second smaller peak in the rms profiles. There is still no discernible regular structure.

Time series (c) is at 2.84 mm above the surface with mean velocity $29\,\mathrm{ms}^{-1}$. This is reasonably near the edge of the boundary layer which is typically taken to be where the mean velocity is measured to be 99% of the free-stream velocity. The fluctuations of $\pm 2\,\mathrm{ms}^{-1}$ correspond roughly to the third smallest peak in the rms profiles. The fluctuations now appear to have a regular structure. As a rough estimate, the oscillations appear to have a a period of $\approx 0.001\,\mathrm{s}$, implying a frequency of $\approx 1000\,\mathrm{Hz}$, a frequency close to 1048 Hz, the frequency of the tone.

Finally, time series (d) at 11.85 mm above the surface has a mean velocity between 29 and $30\,\mathrm{ms}^{-1}$ with small fluctuations all less than $\pm 1\,\mathrm{ms}^{-1}$. This also agrees with the rms profiles, which indicate that the magnitude of any fluctuations is close to the the background rms level in the free stream. Again there is no discernible regular structure.

In this chapter I will loosely describe any boundary-layer disturbances as Tollmien–Schlichting (T–S) waves. The mechanism of instability proposed by Tollmien and Schlichting is discussed in §3.5.1. The mechanisms of instability governing the development of boundary-layer waves propagating over the aerofoil is also discussed in §3.5.1.

The frequency spectra (a), (b), (c) and (d) in figure 2.10 are the respective spectra for the time series (a), (b), (c) and (d) in figure 2.9. For each time series the respective frequency spectrum reveals a discrete fundamental at 1048 Hz, the frequency of the tone. Frequency spectrum (a) at 0.4 mm above the surface reveals a discrete frequency, in the region of reversed flow.

In 2.10(b), 1.55 mm above the surface, the fundamental and two harmonics are detectable. The first harmonic has nearly the same amplitude as the fundamental. This suggests that close to the edge of the separation bubble the T–S waves exhibit nonlinearity.

Moving up to 2.84 mm above the aerofoil surface, the regular time series seen in figure 2.9(c) has a frequency spectrum 2.10(c) with the strongest fundamental observed throughout the boundary layer. The first harmonic is still detectable, although considerably weaker than at 1.55 mm above the surface. Above the separation bubble the T–S waves exhibit weak nonlinearity. The nonlinearity appears to reduce with increasing distance above the surface.

This is seen in 2.10(d) at 11.85 mm above the surface. The fundamental at 1048 Hz is still detectable but is reduced in intensity by approximately 50 dB. No harmonics are detectable above the background level. T–S waves decay exponentially moving in the z-direction outside of the boundary layer. Frequency spectrum (d) is over two boundary-layer thicknesses from the aerofoil surface and the decay in the fundamental mode is apparent.

Figure 2.11 shows the development of the T–S waves in the streamwise direction along the aerofoil. All the frequency spectra are taken at approximately half the boundary layer thickness. At 30 mm upstream of the trailing edge (a) there is no discrete frequency in the spectrum. This station is located upstream of the separation point and the T–S waves are broadband with no one single frequency dominating the others.

At 25 mm upstream of the trailing edge (b) a small discrete peak at 1048 Hz is detectable. The flow separates at approximately 20 mm upstream of the trailing edge, (cf. figure 2.7). A T–S wave at the frequency of the observed tone appears to be *selected* just before the flow separates. The *selected* mode is then amplified over and above all other frequencies such that on reaching the trailing edge it is the dominant frequency in the boundary layer. Figures 2.11(c) and (d) are 15 mm and 2.5 mm upstream of the trailing edge. By (d) the fundamental mode has been amplified to an intensity approximately 50 dB louder than the background broadband level. Again there is evidence of weak nonlinearity with two small harmonics detected.

In summary, the results presented in this section for case 1 reveal the existence of an amplified T–S wave at the *same* frequency as the tone. The majority of the growth of the instability appears to occur close to the trailing edge of the aerofoil where the flow has separated and there exists a small region of reversed flow. The growth of the single mode (over all other frequencies) appears to start just before the flow separates.

The mean boundary-layer and rms velocity profiles, together with the time series and frequency spectra for the tonal cases 2, 3 and 4 all exhibit the same characteristics as case 1.

The characteristics of the flow over an aerofoil where tonal noise is heard appear to be similar for different aerofoil profiles. Case 4 is an investigation of a discrete frequency of 1192 Hz heard from the FX79 W151 profile. Figure 2.12 is the frequency spectrum taken in the centre of the boundary layer at (a) 15 mm and (b) 0.5 mm upstream of the trailing edge. The spectra reveal discrete frequency peaks at 1192 Hz which have grown to roughly 50 dB above the background level by the trailing edge.

Figure 2.13 shows the coherence between the peak frequency in the boundary layer with the frequency of the tone, against the distance upstream of the trailing edge of the aerofoil. In all the tonal cases the coherence is only close to one for approximately the last 25 mm of the aerofoil. Before this region there are no dominant frequencies in the boundary layer and no single frequency appears to have been selected over the others.

Previous papers such as Fink [18] have described a feedback loop between T–S waves and acoustic waves (see §1.3). The start of the feedback loop is taken to be where the flow first becomes unstable, (a point close to the maximum thickness point on the aerofoil). The T–S wave grows as it propagates downstream. Acoustic waves travelling upstream from the trailing edge couple with the T–S waves at the start of the feedback loop. However, no discrete frequency is detectable in the boundary layer until close to the trailing edge. The majority of the amplification of the T–S waves is close to the trailing edge of the aerofoil. This is not consistent with the feedback mechanism described by Fink [18].

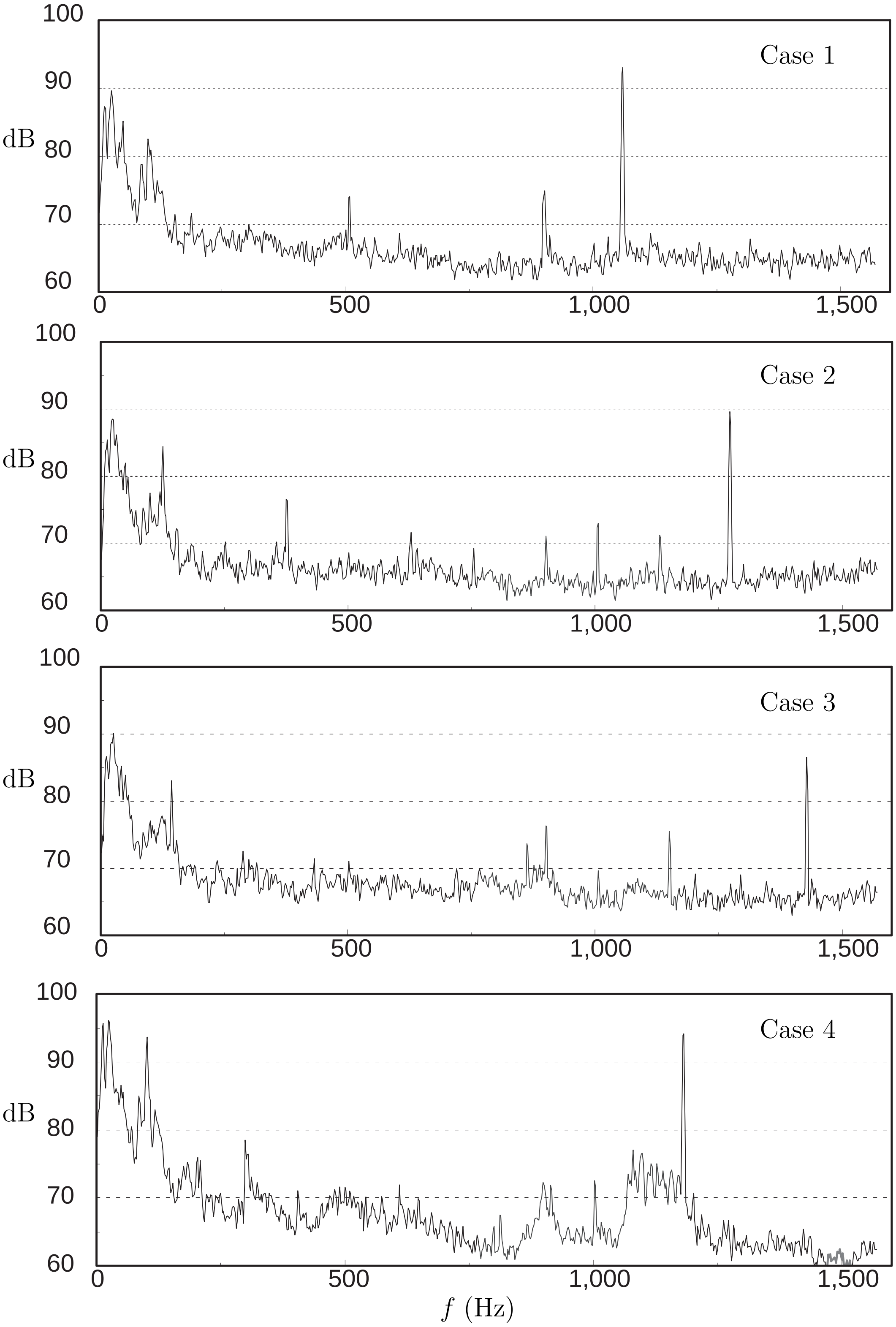

Figure 2.6: Acoustic frequency spectra for cases 1, 2, 3 and 4.

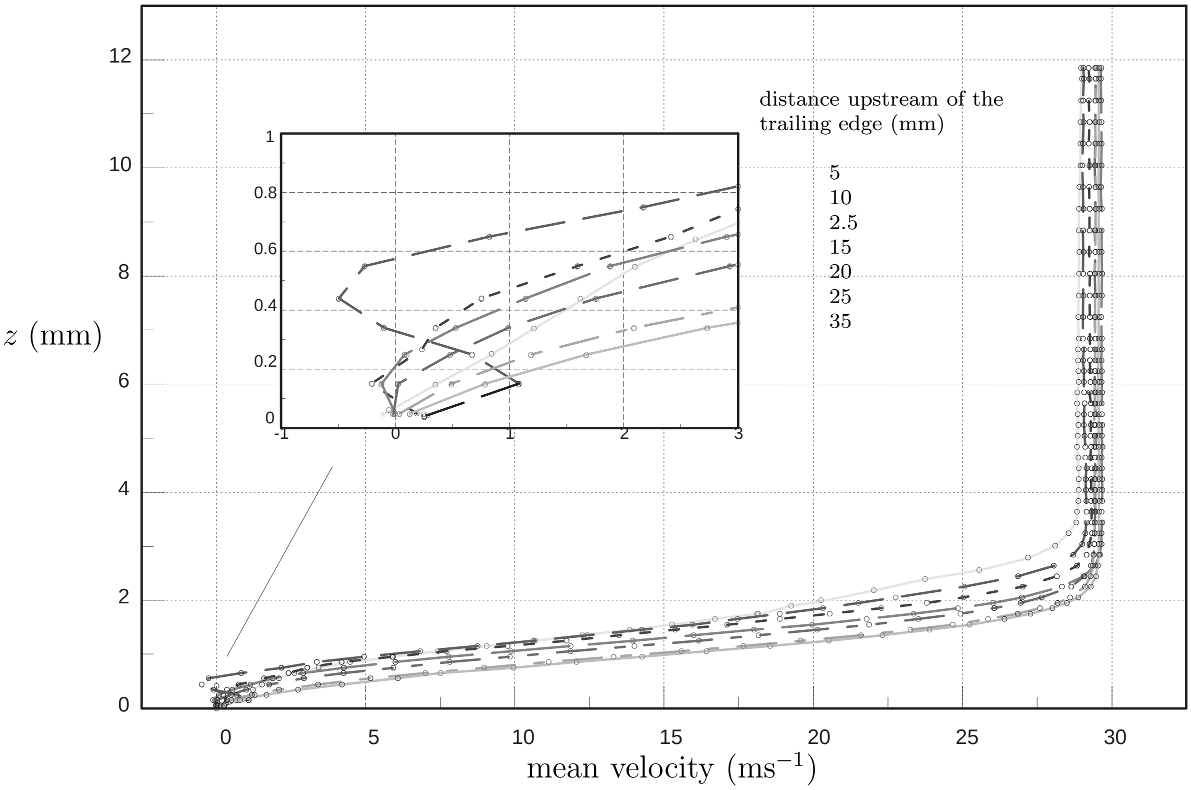

Figure 2.7: Mean boundary-layer velocity profiles for case 1.

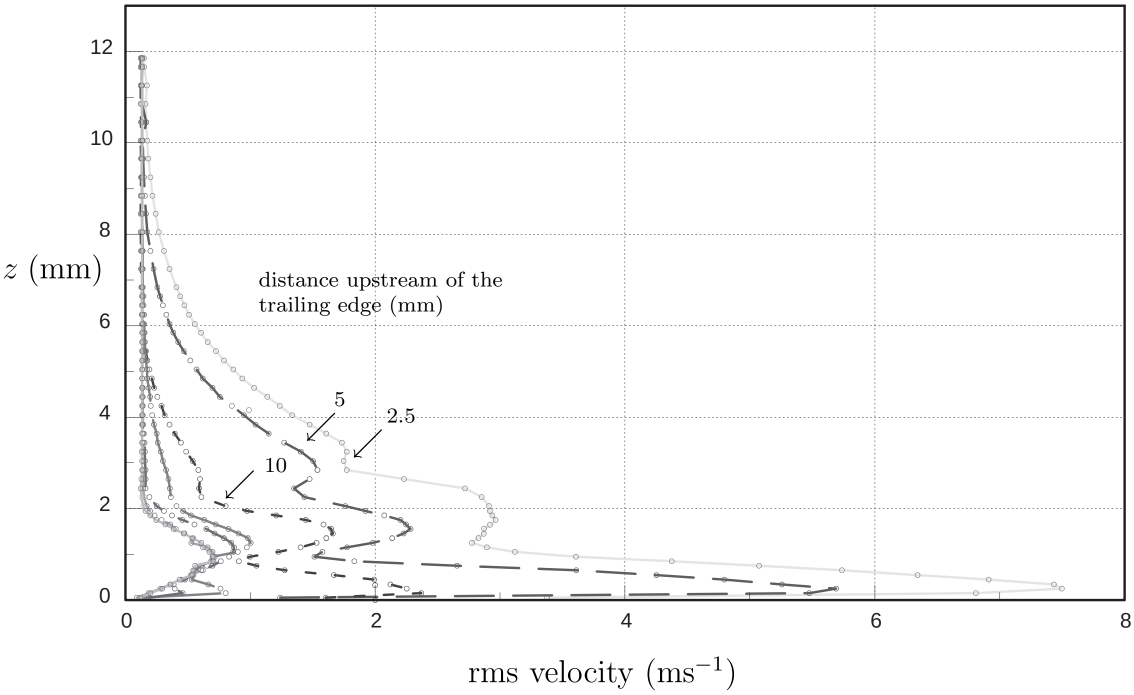

Figure 2.8: rms velocity profiles for case 1.

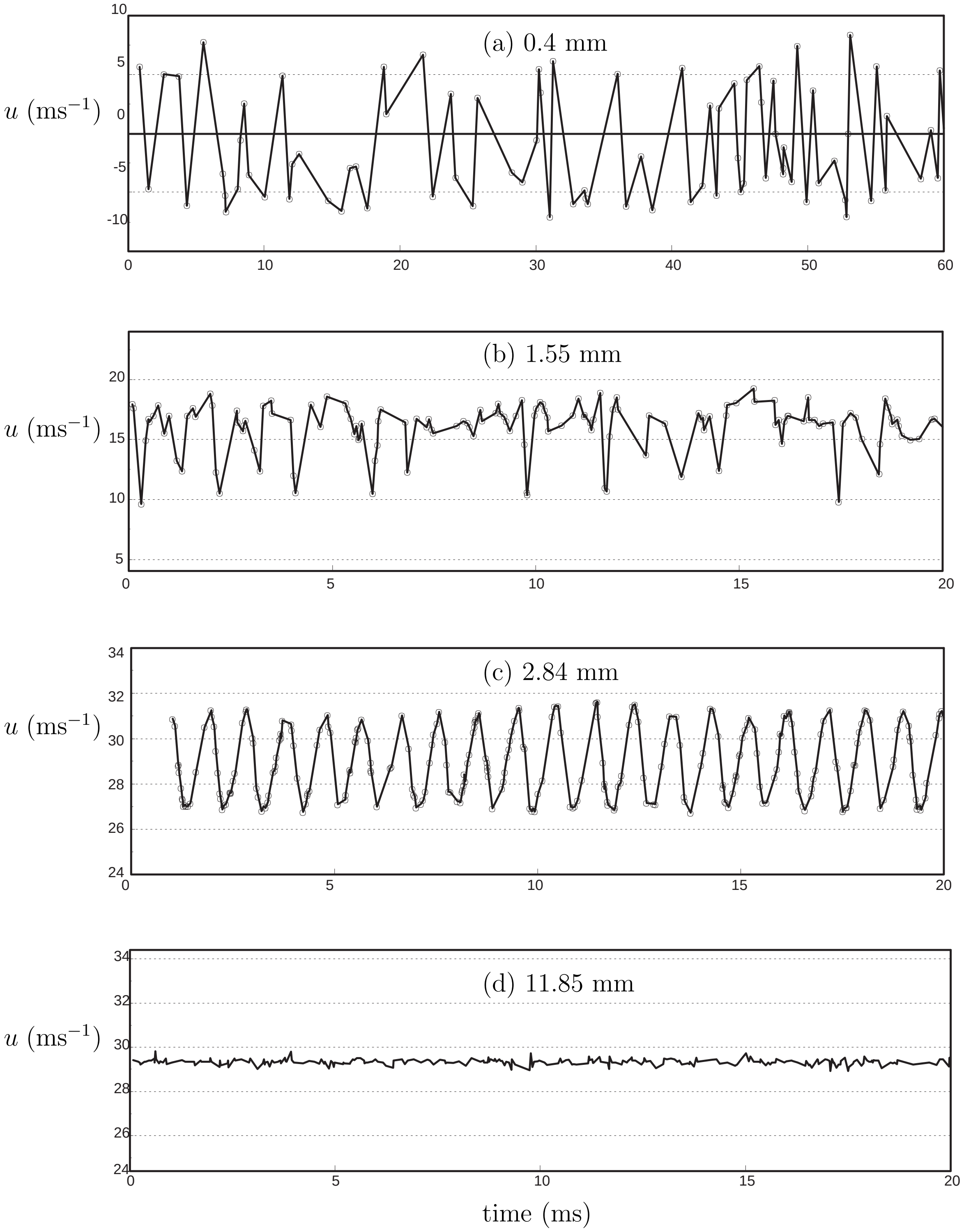

Figure 2.9: Time series taken through the boundary layer, 5 mm upstream of the trailing edge, for case 1.

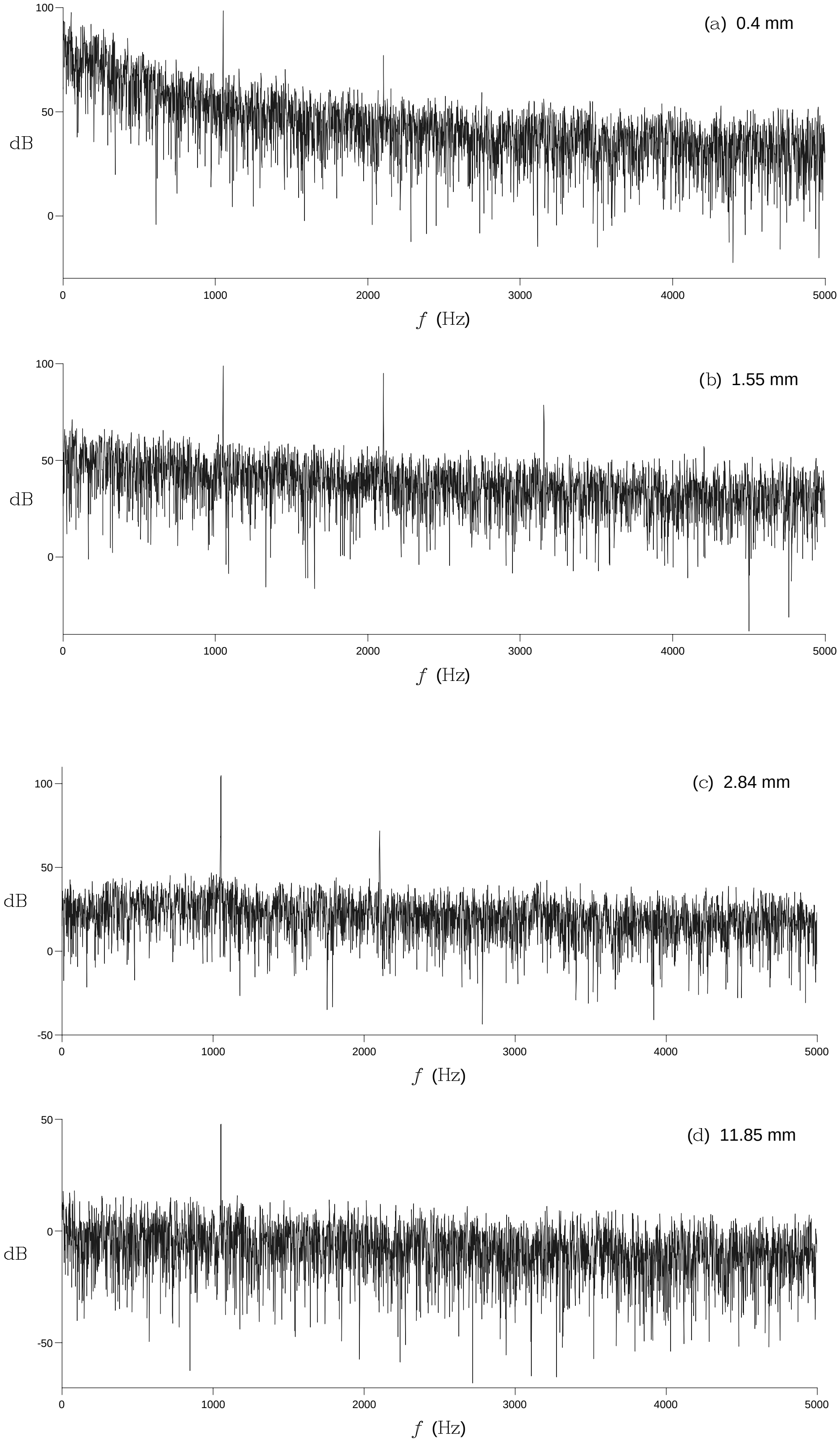

Figure 2.10: Frequency spectra taken through the boundary layer, 5 mm upstream of the trailing edge, for case 1.

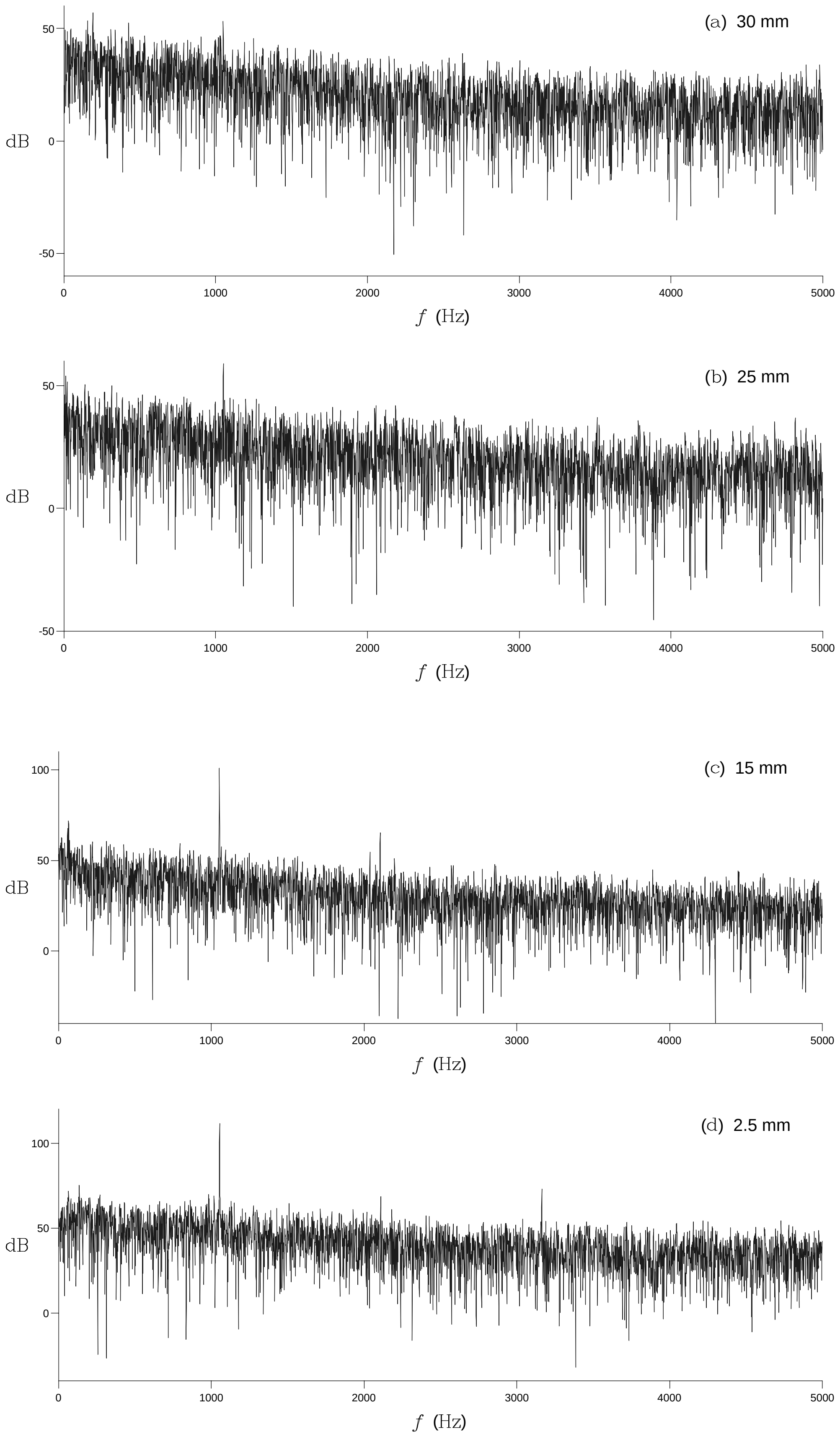

Figure 2.11: Frequency spectra taken in the centre of the boundary layer, at various stations upstream of the trailing edge, for case 1.

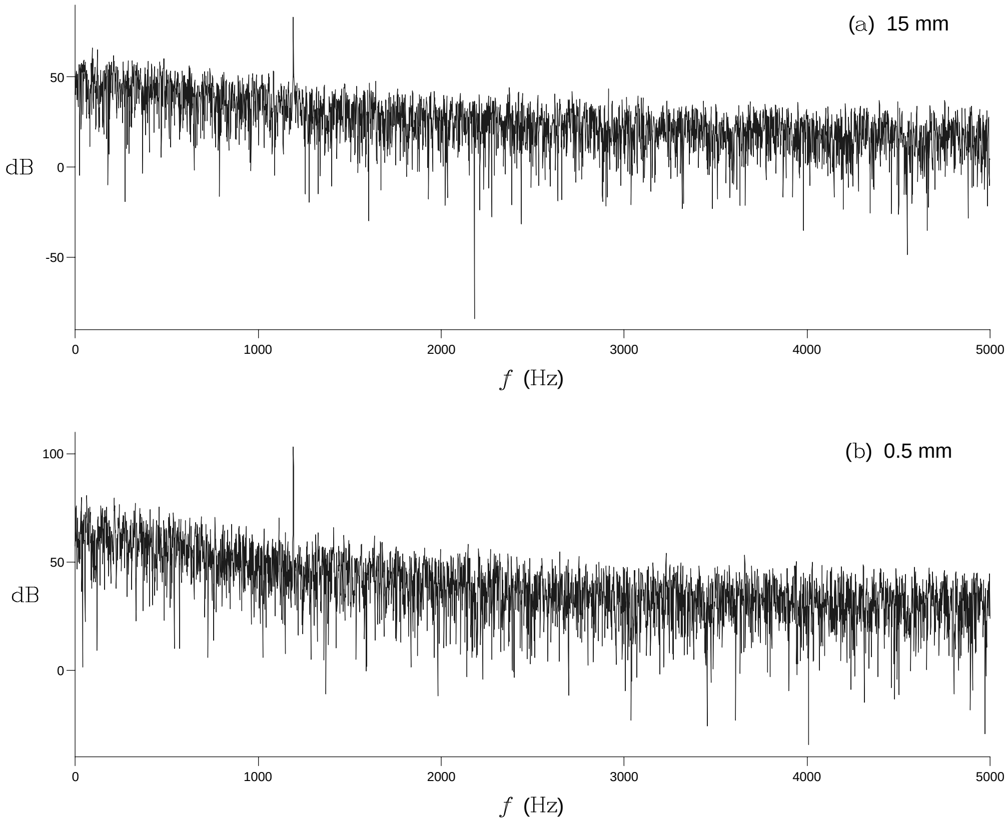

Figure 2.12: Frequency spectra taken at (a) 15 mm and (b) 0.5 mm upstream of the trailing edge, for case 4.

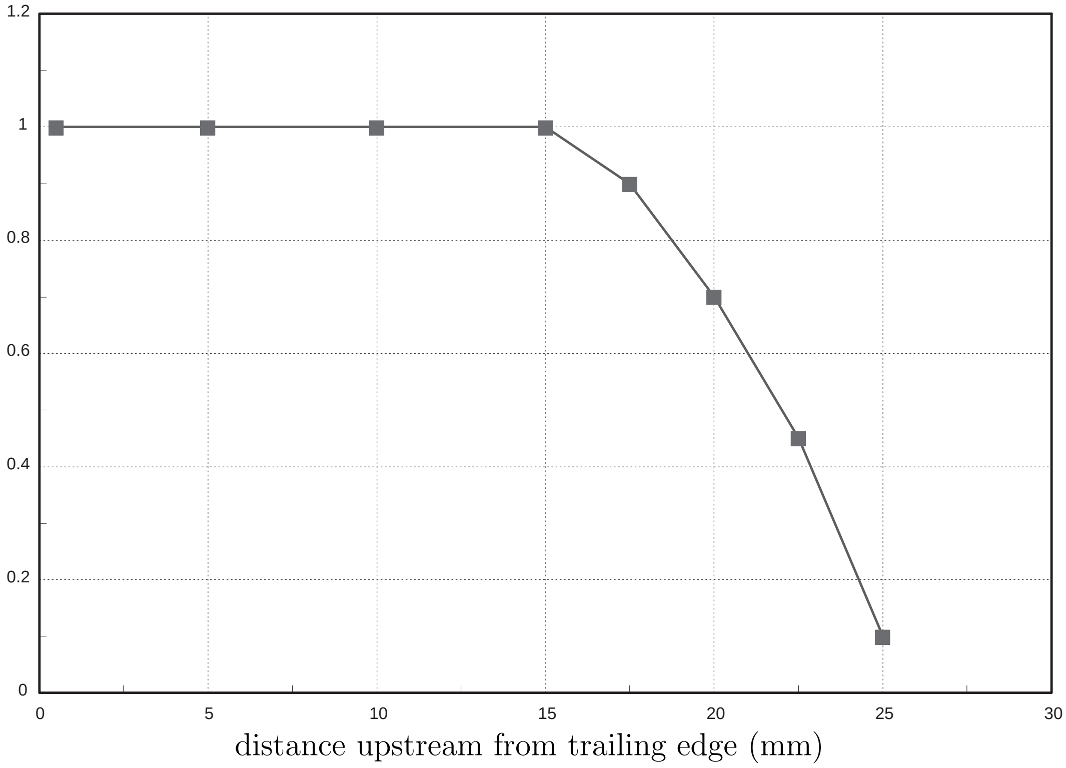

Figure 2.13: Coherence between frequencies for FX79 W151 aerofoil.

2.4.3 No-tone case 5

Figures 2.14 and 2.15 are the mean boundary-layer and rms velocity profiles from the NACA 0012 aerofoil for a low free-stream velocity, with no tones present. Figure 2.14 shows a substantial region of reversed flow of height approximately 2 mm over the NACA 0012 aerofoil. The flow separates approximately 55 mm upstream of the trailing edge and the boundary layer continues to grow steadily until the trailing edge where it is over 6 mm thick! This contrasts the tonal case presented in §2.4.2, (figures 2.7, 2.8), where separation occurred approximately 20 mm upstream of the trailing edge and the boundary layer thickness was only 2-3 mm.

The corresponding rms velocity profiles are also considerably different to the tonal case. There are two distinct differences. Firstly, the magnitude of the rms profiles for the no-tone case is very small compared with the tonal case. In figure 2.15 the peak rms value is less than $0.3\,\mathrm{ms}^{-1}$ compared with $\approx 8.0\,\mathrm{ms}^{-1}$ in the tonal case. Secondly, the rms profiles display a characteristic two-peaked profile in the boundary layer. In the tonal case the rms profiles in figure 2.8 displayed three-peaked profiles after the flow separation, also with considerably larger magnitudes.

There is no evidence in figures 2.14 and 2.15 of the large T–S waves associated with the flow separation that was seen in the tonal cases. At this relatively low free-stream velocity the boundary-layer separates further upstream of the trailing edge than in the tonal cases, and the region of reversed flow is both longer and thicker than before. However the rms velocity profiles have a two-peaked shape, similar to that seen *before* flow separation in the tonal case, (see figure 2.8). In the tonal case *after* flow separation, the flow becomes highly unstable with the existence of large T–S disturbances oscillating at the frequency of the tone. However in the no tone case *after* flow separation, the flow remains relatively stable (compared with the tonal cases), and no large T–S waves are detected. Although there is a large region of reversed flow, the boundary layer remains stable to small perturbations in the flow.

Figure 2.16 show frequency spectra taken in the centre of the boundary layer at (a) 35 mm and (b) 0.5 mm upstream of the trailing edge. They both display only broadband frequency showing no discrete frequency anywhere in the boundary layer. Together with the rms profiles, these figures show that there is no selective amplification of a single frequency in the boundary layer.

With a low free-stream velocity, there is no large, discrete frequency, T–S wave detected anywhere in the boundary layer and and hence no discrete tone is heard. Tonal noise is directly related to the existence of amplified T–S waves, at a single frequency.

In §3.5.2, the linear stability for case 5 is investigated. The lack of amplification of the T–S waves will be discussed. Stability of a flow usually depends on the Reynolds number and for low free-stream velocities (i.e. lower R) the flow would be expected to remain stable over a greater extent of the aerofoil. However, in the tonal case it has been shown that the flow is very unstable after the point of flow separation. In this case the flow separates further upstream of the trailing edge than in the tonal cases, but remains relatively stable over all the aerofoil. This is discussed further in §3.5.2.

2.4.4 No-tone case for high U_∞

Figure 2.3 showed the discrete frequency tones heard from the NACA 0012 aerofoil for various small angles of incidence. At $-3°$, discrete tones were detected for $16\,\mathrm{ms}^{-1} < U_\infty < 48\,\mathrm{ms}^{-1}$. The results in the previous section were for a low free-stream velocity where no tones were heard. At each angle of incidence there is a lower and upper bound outside of which no tones are heard. Figures 2.18, 2.19 are the mean boundary-layer and rms velocity profiles taken over the NACA 0012 aerofoil, at $-3°$, for $U_\infty = 47\,\mathrm{ms}^{-1}$. At $U_\infty = 47\,\mathrm{ms}^{-1}$ there is a discrete tone at 1708 Hz, and this was the highest free-stream velocity where a discrete tone was detected.

The mean boundary-layer profiles at 30 mm and 25 mm upstream of the trailing edge have no reversed flow. It was found that none of the mean profiles had any reversed flow. However, velocity histograms clearly showed there was still some reversed flow present. (At each station a velocity histogram was obtained. This was a histogram of velocity against the number of observations. Recall that at each station approximately

10,000 data points were taken. Mean-velocity profiles may be constructed from these velocity histograms.) Although the mean-velocity profiles do not have reversed flow, the rms profiles at 30 mm and 25 mm have a three-peaked shape and they are a comparable magnitude to the rms profiles in figure 2.8. The high rms values indicate the presence of large T–S disturbances.

At 0.5 mm upstream of the trailing edge the boundary layer is approaching the shape of a turbulent boundary-layer profile. In a turbulent boundary layer the velocities close to the boundary are higher than in a laminar layer. As a result a turbulent boundary-layer profile will have a 'flatter' shape close to the boundary surface than in a laminar boundary layer. Also the momentum diffusion from the boundary layer into the free stream will be greater in a turbulent boundary layer. As a result the mean velocity will approach the free-stream velocity higher above the boundary surface than in a laminar boundary layer. The rms velocity profile at 0.5 mm has a peak close to the boundary of approximately 7 ms^{-1}. Although it has lost the expected third (smallest) peak seen in figure 2.8, the dramatic increase in the magnitude of the boundary-layer disturbances from those 30 mm and 25 mm upstream of the trailing edge indicates the large growth of the T–S waves.

A turbulent boundary layer at the trailing edge would be expected to destroy the tonal noise mechanism. Indeed the tones have been shown to be independent of the turbulent boundary layer on the suction surface of the aerofoil. For a low free-stream velocity, the flow separates far upstream of the trailing edge and the region of reversed flow extends until the trailing edge, up to approximately 2 mm above the aerofoil surface. For the tonal cases at higher free-stream velocities the flow separates closer to the trailing edge, and the region of reversed flow is approximately 0.5 mm high. Increasing the free-stream velocity compresses the region of reversed flow and moves this region closer to the trailing edge.

The tonal noise mechanism is dependent on the existence of a large T–S wave at the same frequency. The majority of the amplification of this wave occurs after the flow has separated. For $U_\infty > 48\,\mathrm{ms}^{-1}$ there will be no large T–S wave detectable at the trailing edge of the aerofoil, and hence no tone generated.

The velocity profile 0.5 mm from the trailing edge in figure 2.18 shows that the boundary layer is becoming turbulent. A fully developed turbulent boundary layer would destroy any discrete frequency structures generated upstream of the transition point. For $U_\infty > 48\,\mathrm{ms}^{-1}$ it is proposed that there is a fully developed turbulent boundary layer at the aerofoil trailing edge, which destroys any regular structure in the boundary layer. Increasing the free-stream velocity will make the flow more unstable to small perturbations in the flow. Also, the increase in U_∞ compresses the region of reversed flow. At high enough free-stream velocities the region of reversed flow will be very thin and the boundary layer will re-attach *before* the trailing edge. The flow propagating over the region of reversed flow will be very unstable and transition to a turbulent boundary layer will occur on or shortly after re-attachment.

The increase of the free-stream velocity leads to transition to turbulence before the trailing edge because the region of reversed flow is compressed. The process is gradual. The onset of turbulence has to be far enough upstream of the trailing edge to have sufficient distance to destroy the large T–S waves. In figure 2.18 the boundary layer 0.5 mm upstream of the trailing edge has a turbulent profile but the rms profile suggests the T–S wave is still detectable. It is assumed that the flow re-attaches close enough to the trailing edge in this case such that the T–S wave remains detectable at the trailing edge — leading to the tone. This free-stream velocity represents an upper bound for the discrete tones, and higher velocities lead to turbulent re-attachment further upstream of the trailing edge, which in turn destroys the coherence of the boundary layer near the trailing edge.

Finally note that although no mean reversed flow was found when $U_\infty = 47\,\mathrm{ms}^{-1}$, the discussion is believed to be correct. I have assumed so far that the majority of the amplification of the T–S waves occurs after the flow has separated. However, in this example the region of reversed flow is assumed to be very thin, that is thin enough to be undetectable by the LDA. It will be shown in §3.5.1 that the amplification depends on the location of the inflexion point of the mean-velocity profile. It is shown that the largest amplification of boundary-layer waves occurs for profiles with the inflexion point far away from the boundary surface. This is directly related to the separated profiles as their inflexion points are located further away from the boundary surface than those of attached profiles.

2.4.5 No-tone case 6

When the aerofoil is positioned at 0° incidence with respect to the free-stream flow then *no* discrete tones were heard for any free-stream velocities. Tonal noise is only detected for small angles of incidence and, (recall figure 2.3), for the NACA 0012 aerofoil discrete tonal noise was only detected in the range $[-2^\circ, -5^\circ]$.

The lower and upper bounds of free-stream velocity outside of which no tones are detected have different physical reasons preventing the generation of tonal noise. Similarly the lower and upper bounds on the angle of incidence have different mechanisms associated with them, although they are both related to the pressure gradients over the aerofoil. The results for case 6 are presented for a zero angle of attack. (Note that this also means the system is symmetric about $z = 0$. No tones are detected, hence the tonal noise mechanism is not present on either aerofoil surface.)

Figures 2.20, 2.21 are the mean boundary-layer and rms velocity profiles for case 6. For case 6 a region of reversed flow exists from approximately 75 mm to 40 mm upstream of the trailing edge. At 0.5 mm upstream of the trailing edge there is a fully developed turbulent boundary layer. The boundary layer is assumed to be a fully developed turbulent boundary layer when compared with the profiles at 0.5 mm seen in figures 2.18 and 2.19. In figure 2.19 the rms profile has the characteristic shape of those associated with the presence of large T–S instability waves, decaying outside of the boundary layer. The rms profile in figure 2.21 at 0.5 mm upstream of the trailing edge is also a fully developed turbulent profile. There are no distinct peaks in the boundary layer, and the magnitude remains relatively large moving upwards out of the boundary layer compared with any of the rms profiles presented so far. The large rms is due to the increased momentum diffusion from the boundary layer to the free stream seen in a fully developed turbulent boundary layer.

The rms velocity profiles further upstream have the characteristic three-peaked shape seen previously, which suggest large T–S instabilities around the region of reversed flow. There are no tones present because the flow has re-attached approximately 40 mm upstream of the trailing edge and the flow is fully turbulent by the trailing edge.

Figure 2.17 shows frequency spectra taken in the centre of the boundary layer (a) 50 mm and (b) 0.5 mm upstream of the trailing edge. These demonstrate how the onset of turbulence destroys the discrete frequency T–S waves by the trailing edge. Upstream (around the region of reversed flow) there is a discrete frequency in the boundary layer of 542 Hz, approximately 40 dB above the broadband background level. By the trailing edge this has been destroyed and the frequency spectrum is broadband. The onset of turbulence has destroyed the coherent boundary-layer structure by the trailing edge.

For this case $U_\infty = 16.6\,\mathrm{ms}^{-1}$ which is considerably less than $U_\infty = 48\,\mathrm{ms}^{-1}$ discussed in §2.4.4. The onset of turbulent flow is the physical mechanism which destroys the coherent structure in the boundary layer in both these cases. However the mechanisms governing the onset of turbulence are different. For a high free-stream velocity the onset of turbulence may be thought in terms of primarily a Reynolds number based phenomenon. Increasing the free-stream velocity (and hence R) reduces the stability of the flow around the aerofoil. The boundary layer transition point may be thought of as a function of R.

In case 6 the free-stream velocity (and hence R) is much lower and the onset of turbulence is controlled by the pressure gradients close to the trailing edge of the aerofoil. The pressure gradients around the aerofoil are related locally to the curvature of the profile. There are strong pressure gradients around the blunt leading edge where the curvature is high. The angle of incidence of the aerofoil alters the local curvature of the aerofoil surface with respect to the free stream. The area of interest (for all cases) is approximately the final 25% of the chord. The tonal noise mechanism depends on the amplification of T–S waves over the region of reversed flow close to the trailing edge. In case 6 the flow separates further upstream of the trailing edge than in the tonal cases. The large amplification of the T–S waves does occur *but* further upstream of the trailing edge. The flow re-attaches significantly upstream of the trailing edge and becomes turbulent. The point of separation is determined by the pressure gradients.

Ideally separation should occur close to the trailing edge — approximately 20 mm upstream in most cases.

Figure 2.22 is a schematic showing the location of the reversed flow over the aerofoil for (a) 0°, (b) between $[-2^\circ, -5^\circ]$ and (c) $< -5^\circ$. In (a) the local curvature close to the trailing edge is greater than in (b) for the aerofoil inclined at a small angle. The adverse pressure gradient close to the trailing edge will be stronger in (a) than in (b), causing separation further upstream of the trailing edge. As discussed, the ideal situation for the generation of tones is (b). In (c) the angle of incidence has been decreased so that it is $< -5^\circ$ and eventually there will be *no* adverse pressure gradient on the aerofoil pressure surface. Therefore amplification of the T–S waves will not be large and no discrete tone is generated.

In summary, the existence of the tones depends on the existence of a region of reversed flow close to the trailing edge of the aerofoil, and that only occurs for a small range of angles of incidence.

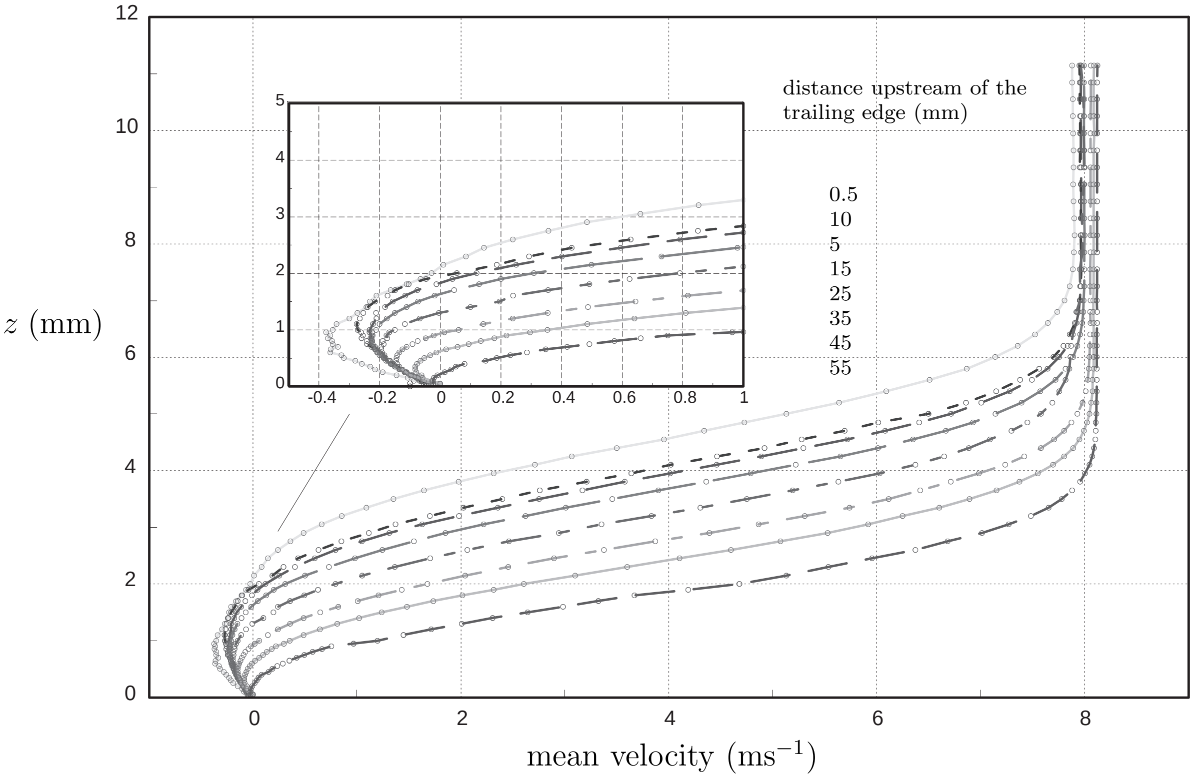

Figure 2.14: Mean boundary-layer velocity profiles for case 5.

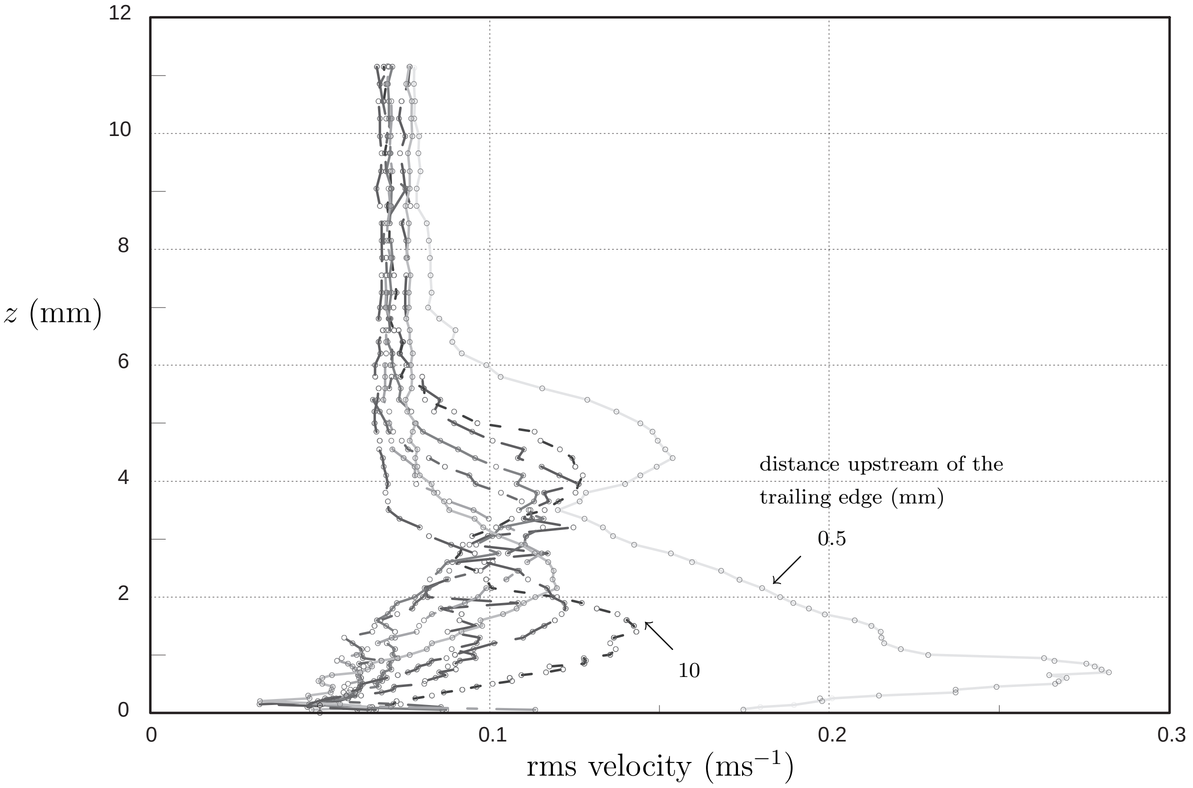

Figure 2.15: rms velocity profiles for case 5.

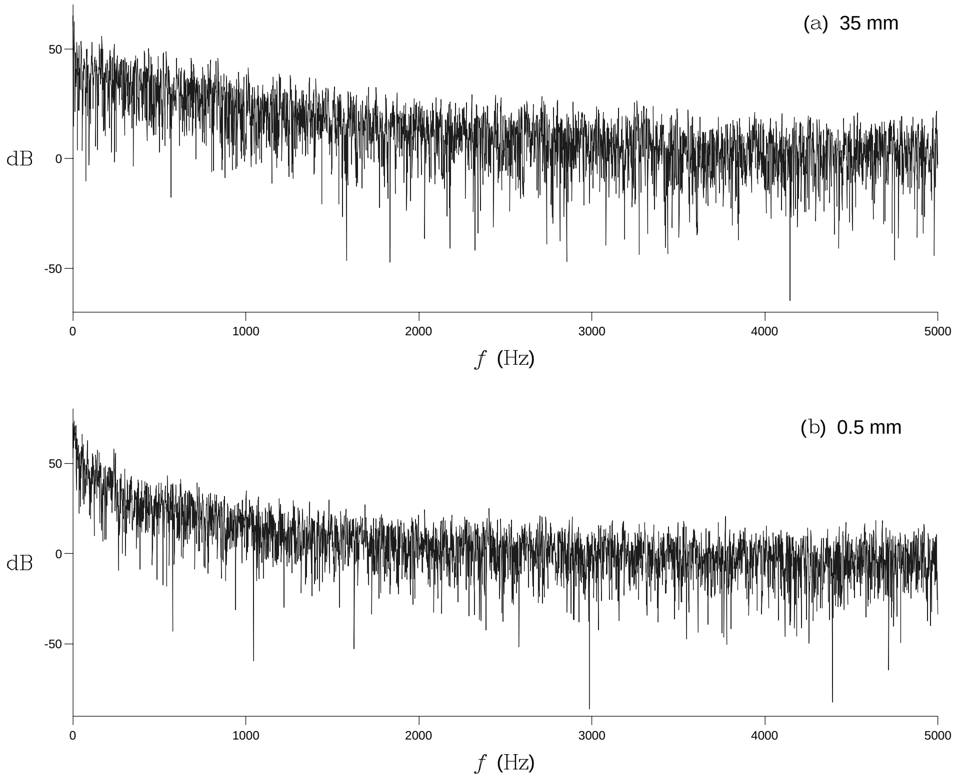

Figure 2.16: Frequency spectra taken at (a) 35mm and (b) 0.5mm upstream of the trailing edge, for case 5.

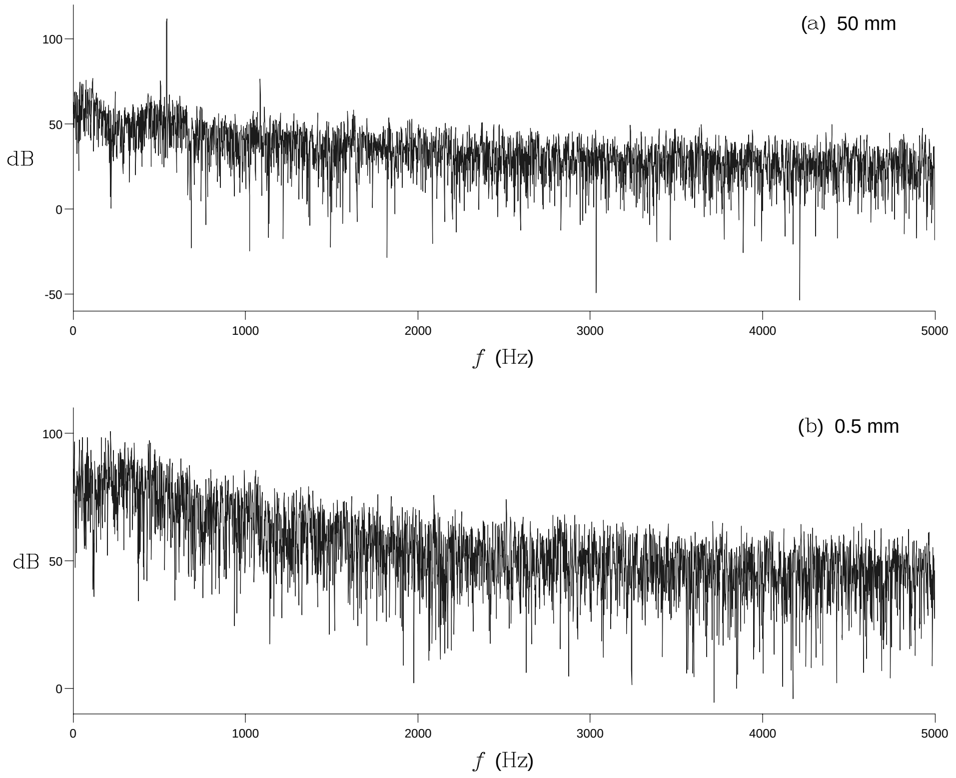

Figure 2.17: Frequency spectra taken at (a) 50 mm and (b) 0.5 mm upstream of the trailing edge, for case 6.

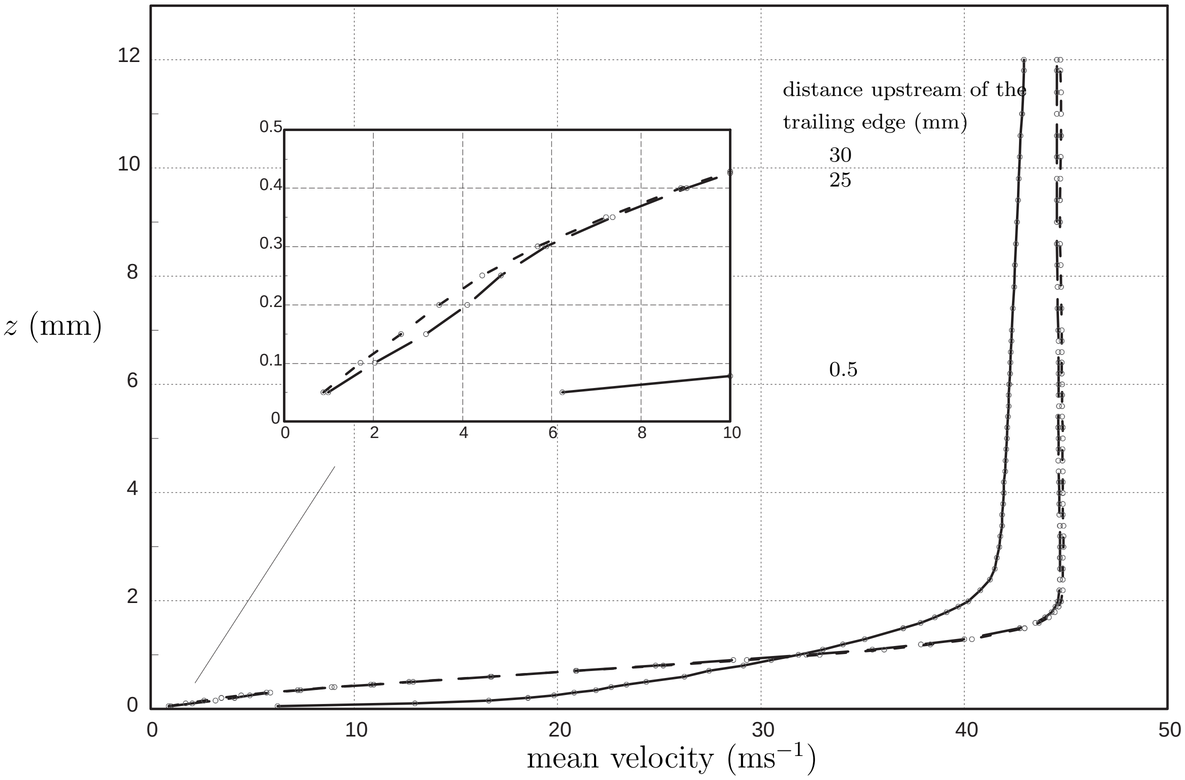

Figure 2.18: Mean boundary-layer velocity profiles for $U_\infty = 47\,\mathrm{ms}^{-1}$.

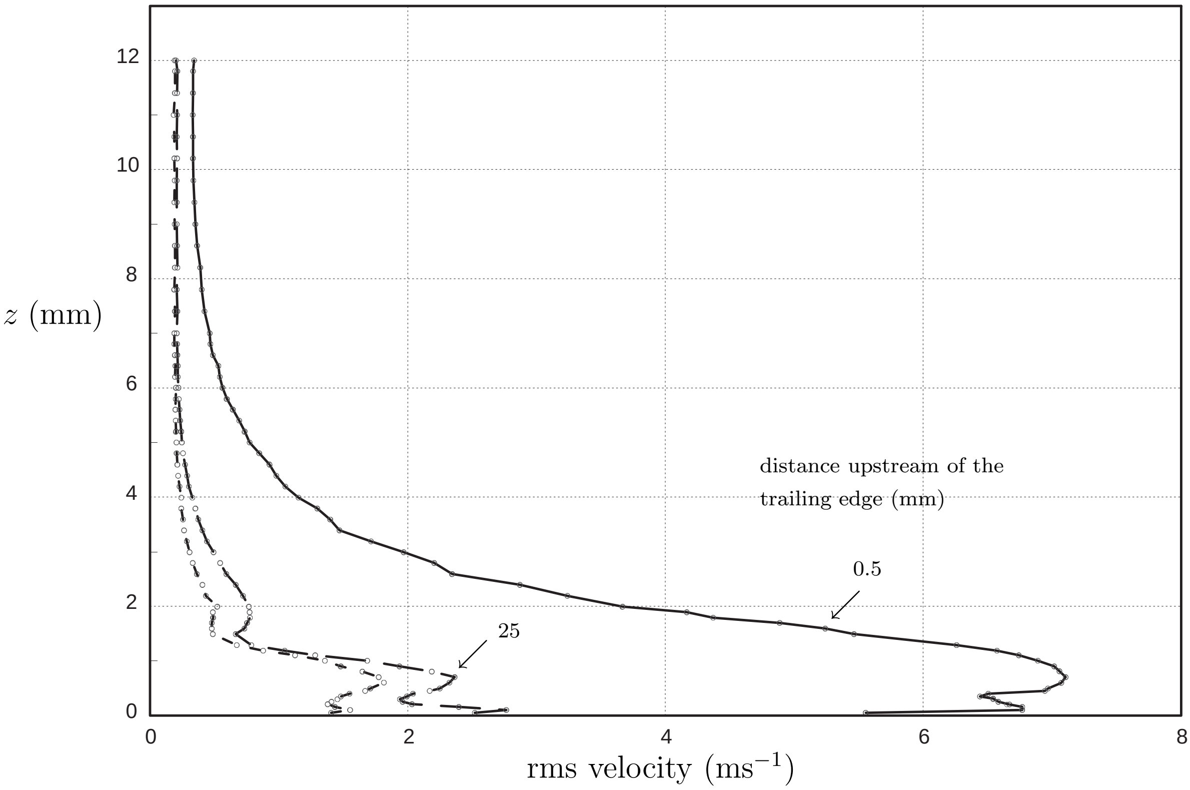

Figure 2.19: rms velocity profiles for $U_\infty = 47\,\mathrm{ms}^{-1}$.

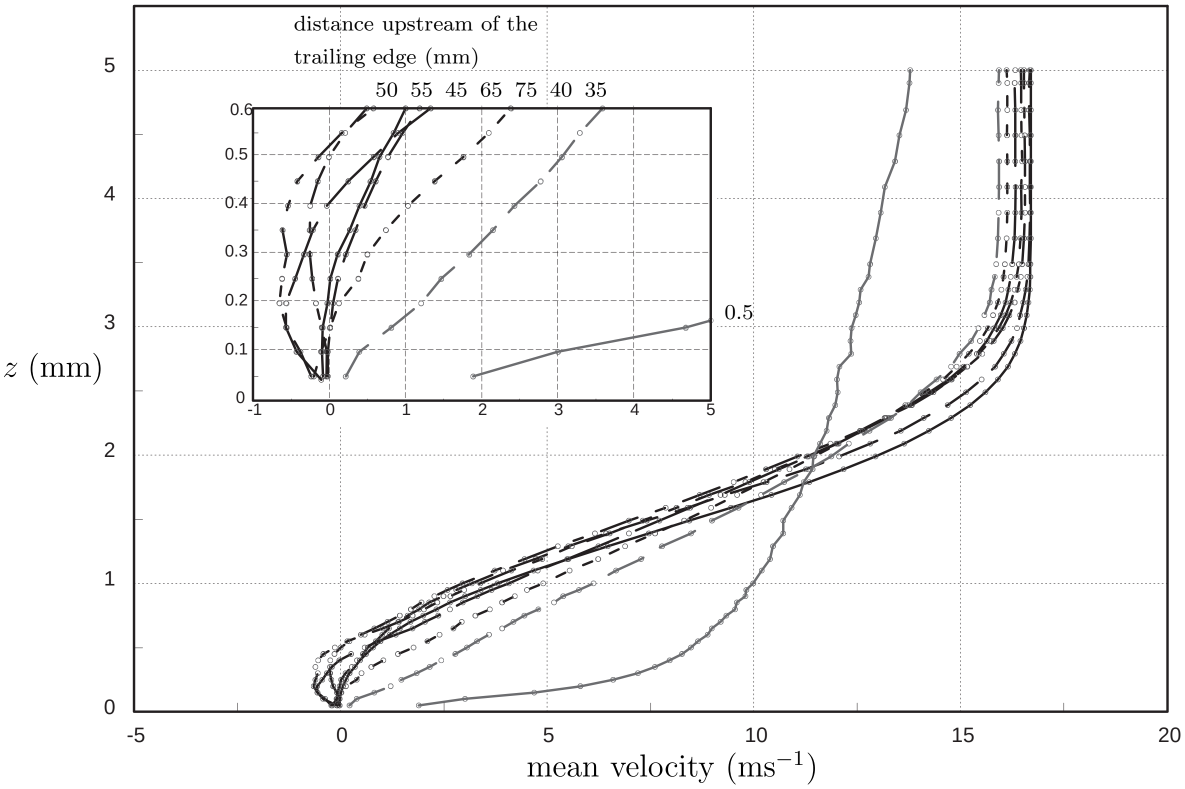

Figure 2.20: Mean boundary-layer velocity profiles for case 6.

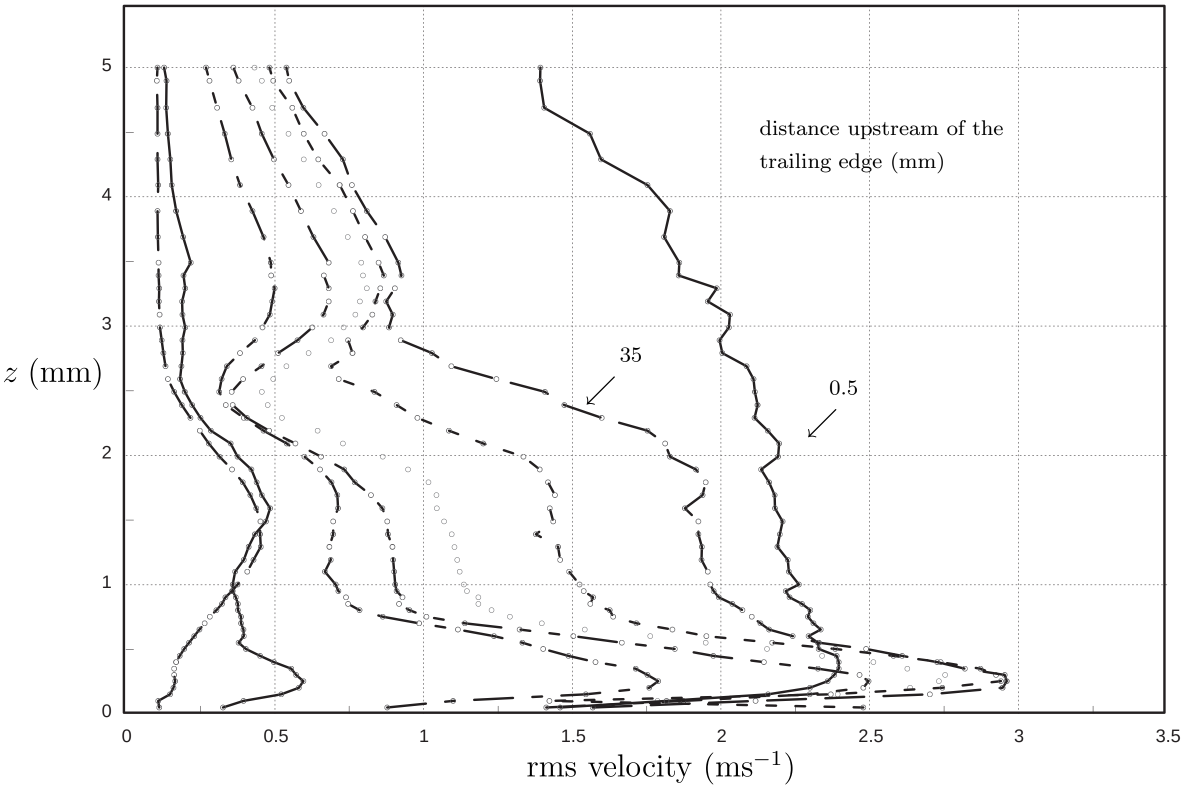

Figure 2.21: rms velocity profiles for case 6.

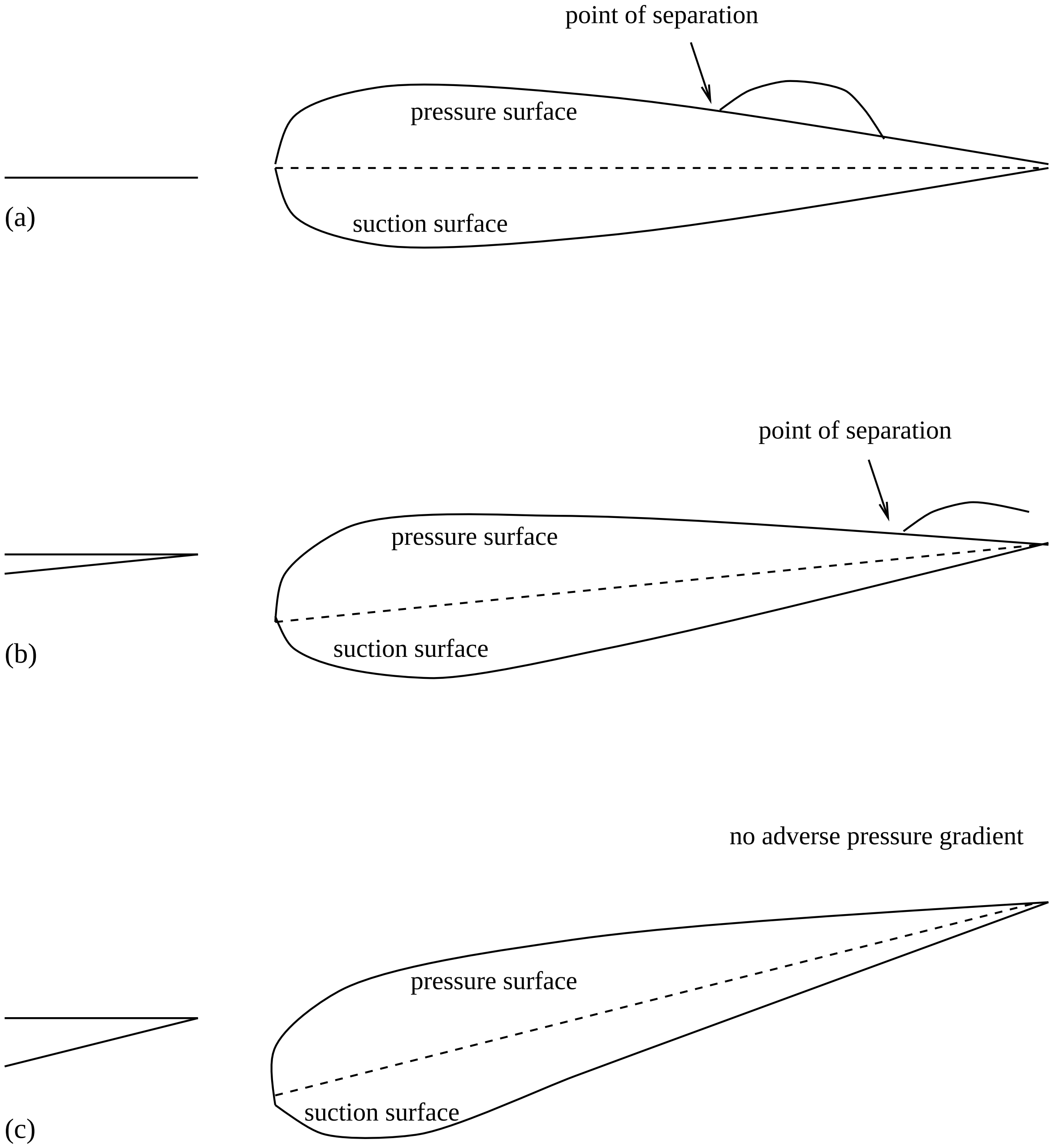

Figure 2.22: Schematic showing the location of reversed flow over the aerofoil.

2.5 Flow visualization

2.5.1 Experimental procedure

There are several ways to introduce smoke filaments into a wind-tunnel, but, these often involve inserting a probe upstream of the leading edge from which smoke is emitted. One such method was attempted but no acoustic tones were heard at the flow conditions of case 1. As in the case of the hot-wire anemometer, the introduction of the probe was assumed to alter the flow, preventing the separation close to the trailing edge.

The method used is known as the 'titanium tetrachloride method'. Titanium tetrachloride ($TiCl_4$) reacts with air to form a white smoke which is easily visible. The fumes consist of titanium oxide and hydrogen chloride and the presence of hydrochloric acid in the fumes limits the number of experiments which may be conducted due to the corrosiveness of the acid. (As the method is corrosive only tests for case 1 were conducted.) At room temperature $TiCl_4$ is a liquid and a few drops were placed on the aerofoil at 70% chord. Once the $TiCl_4$ is in place then the method is non-intrusive. At $U_\infty = 30\,\mathrm{ms}^{-1}$ an acoustic tone at 1048 Hz was heard, indicating that the phenomenon had not been affected by the $TiCl_4$.

A laser light sheet was used to illuminate the flow. To observe the characteristics the light was strobed using a 60 slit strobe disc. For this case the disc was driven by a motor operating at 1048 rpm. Any oscillations at a frequency of 1048 Hz would thus appear frozen. The observed flow was recorded by a video camera, and, still images were recovered of the wake and trailing edge using a frame-grabber.

2.5.2 Flow visualization pictures

Figure 2.23 shows approximately the final 35 mm of the NACA 0012 aerofoil pressure surface and the beginning of the aerofoil wake. At least one wavelength of a T–S wave is visible, with a wavelength of approximately 10 mm. Approximately 20 mm from the trailing edge the flow separates and the free shear layer over the region of reversed

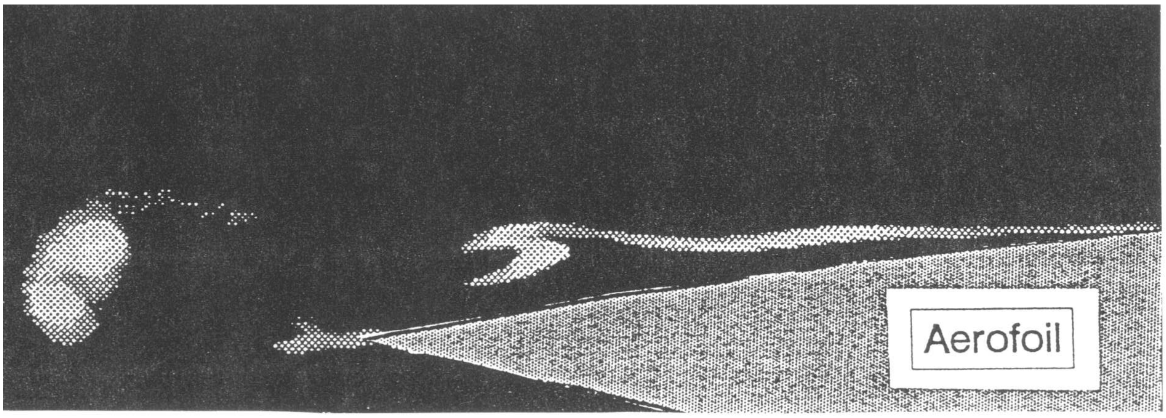

Figure 2.23: Flow visualization of the trailing edge of the aerofoil.

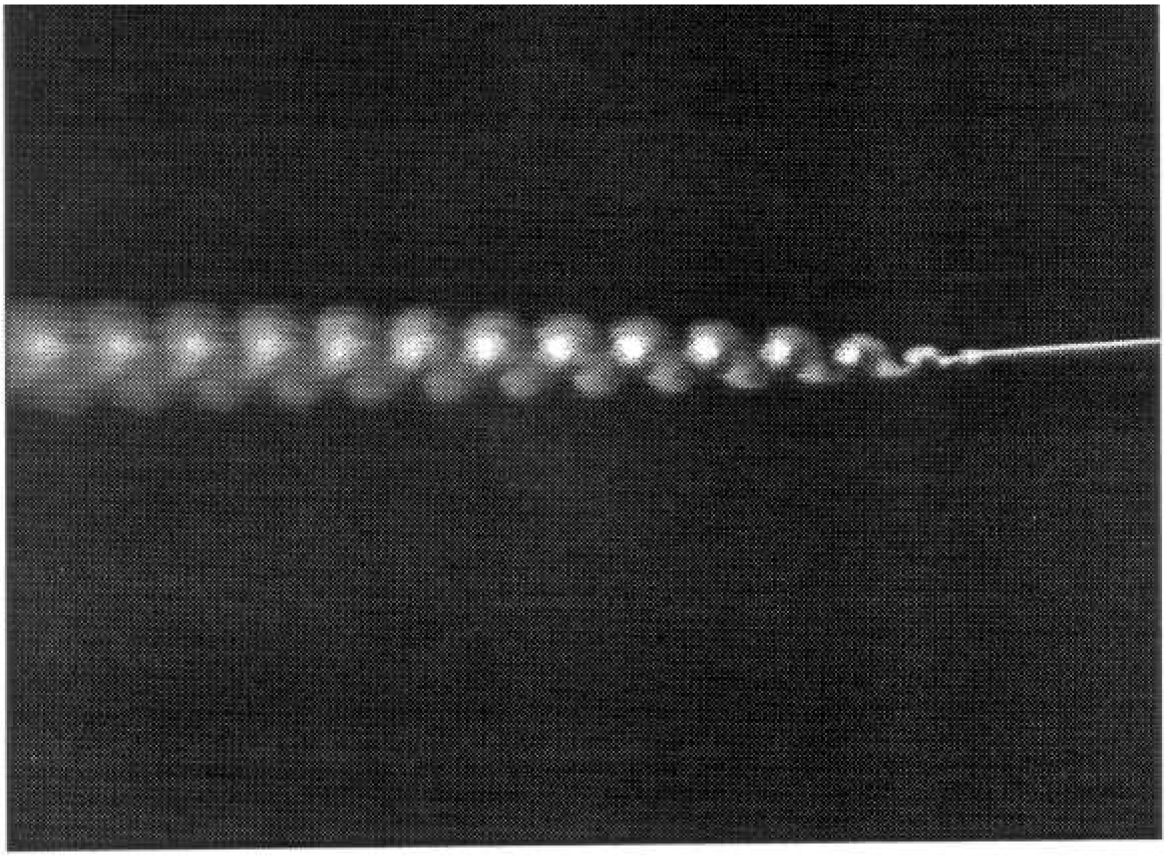

Figure 2.24: Flow visualization of the wake of the aerofoil.

flow is visible. The T–S wave rolls up into a vortex as it passes over the trailing edge, which is then shed into the aerofoil wake. Figure 2.23 further confirms the existence of an amplified T–S wave *at the frequency of the tone* propagating up to the aerofoil trailing edge.

Figure 2.24 is a flow visualization of the aerofoil wake. Approximately 300 mm of the wake is shown. Again the light source is strobed at 1048 Hz and the video image (from which this picture was taken) was *steady*. In the wake there is a vortex street with vortices being shed alternately from the pressure and suction surfaces of the aerofoil.

Probably the most common example of vortex shedding is the *von Kármán vortex street* for the flow past a cylinder. Increasing the Reynolds number of the flow around a cylinder results initially in two symmetric eddies forming behind the cylinder as a result of flow separation. As the Reynolds number increases the eddies grow in size until at some critical Reynolds number instabilities in the wake affect the two eddies. At this point the symmetry of the system is destroyed and the eddies oscillate in a lateral sense shedding vorticity alternately from either side of the cylinder. The resulting vortex structure is remarkably organized and characterized by a discrete frequency, say n Hz, resulting from $2n$ vortices shed per second alternately from above and below the cylinder.

A von Kármán vortex street is typically observed behind a bluff body. However an aerofoil is not a good approximation of a bluff body (such as a cylinder) because it is streamlined. Hence Tam [42] assumed the wake only rolled up into a vortex street far downstream of the trailing edge. However, the closeness of the flow separation to the trailing edge ensures that vorticity is shed into the wake at the trailing edge.

The other difference between the vortex street shed by the aerofoil and the von Kármán vortex street in the wake of a cylinder is that initially the flow around the cylinder is symmetrical about the centre line. There is a region of separated flow on either side of the cylinder which oscillates laterally when the symmetry is broken, shedding vorticity. The flow around the aerofoil is not symmetric. Boundary-layer transition occurs further upstream of the trailing edge on the suction surface of the aerofoil. Although no results are presented, it is assumed that at the trailing edge on the suction surface the boundary layer is turbulent with only a broadband frequency. Presumably the wake is dominated by the T–S wave on the pressure surface of the aerofoil which controls the frequency with which vorticity is shed from the aerofoil surfaces.

No $TiCl_4$ was placed on the suction surface of the aerofoil. The vortices shed from the suction surface of the aerofoil are only visible after the entrainment of the smoke particles in the wake. Hence only the aerofoil pressure surface is visible at the far right of figure 2.24. As a result, the vortices shed from the pressure surface appear more clearly in figure 2.24, particularly at the vortex cores where the smoke particles are concentrated.

The regular structure of the vortex street (i.e. the steadiness of the image when strobed at 1048 Hz), together with the boundary-layer structure on the pressure surface of the aerofoil, account for the discrete (narrow band) nature of the acoustic tone.

2.6 Flow field around the aerofoil

All the frequency spectra shown have been taken in or close to the boundary layer. In figure 2.10 the frequency spectrum is shown for case 1, 5 mm upstream of the trailing edge of the aerofoil. Figures 2.10(a), (b), (c) and (d) show how the spectrum changes on upwards through the boundary layer. The peak frequency in 2.10(d) is approximately 50 dB compared with approximately 100 dB in 2.10(a), (b) and (c). Figures 2.10(a), (b) and (c) taken at 0.4 mm, 1.55 mm and 2.84 mm above the aerofoil surface have much stronger peaks because the stations are all located inside the boundary layer. Figure 2.10(d) at 11.85 mm above the aerofoil surface is outside the boundary layer and the peak has decreased in intensity by 50 dB. This is consistent with linear stability theory for boundary-layer flows, which shows that boundary-layer disturbances decay exponentially outside of the boundary layer.

For case 1 the flow in the free stream outside the boundary layer was investigated on both sides of the aerofoil. The frequency spectrum of the free stream was analyzed and found to *still* contain a discrete frequency above background levels in some places up to 100 mm above or below the aerofoil. The discrete frequency was fixed everywhere at 1048 Hz, the frequency of the tone for this case.

The flow around the aerofoil was investigated to find where this discrete frequency was detectable. Figure 2.25 is a contour plot of the amplitude of the discrete frequency at 1048 Hz of the streamwise velocity around the aerofoil. The contour labels are the intensity of the peak frequency above the background level, measured in decibels. (Note that the background level is variable and is itself much higher in the boundary layer — see figure 2.10 for example.) Figure 2.25 shows that peak frequencies are detectable up to 150 mm upstream of the trailing edge (50% of chord length) on either side of the aerofoil. Downstream of this point there is a large region on either side of the aerofoil up to approximately 100 mm away from either surface where peak frequencies are still detectable in the free stream. The contour pattern appears approximately symmetrical about the aerofoil.

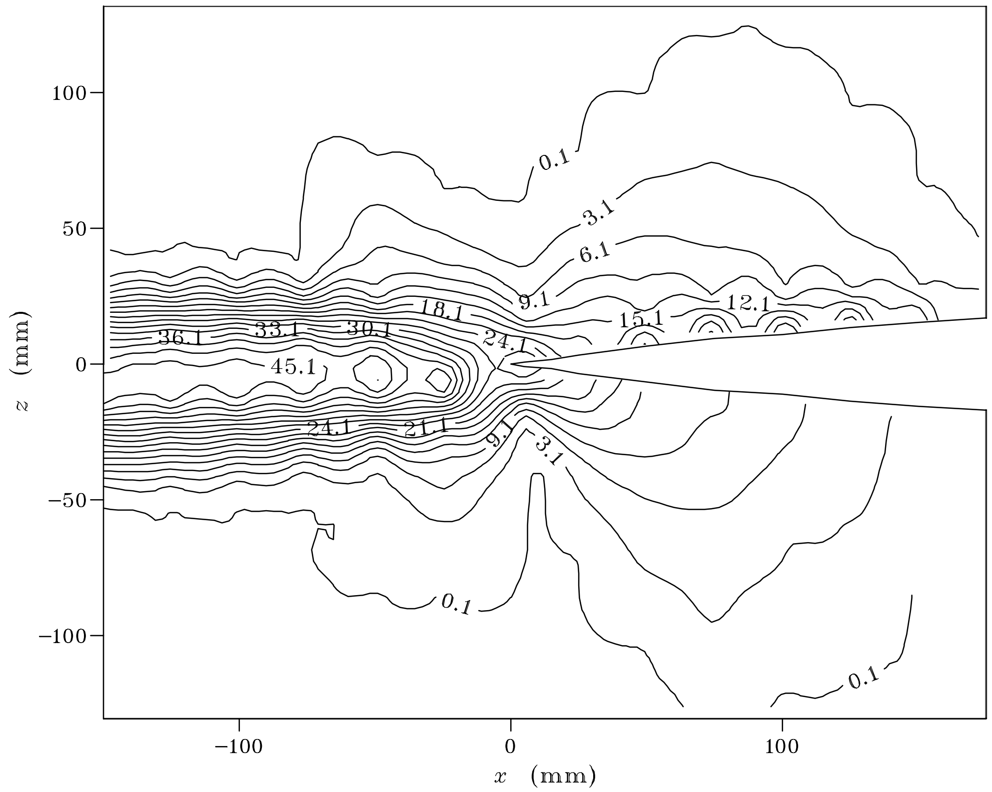

Figure 2.25: Contour plot of the streamwise peak frequency, for case 1.

Downstream of the trailing edge the contour lines are closely packed together and a peak frequency is only detectable up to approximately 50 mm above and below the centre line of the aerofoil ($z = 0$).

On the suction surface the peak frequencies were undetectable within 5 mm of the aerofoil surface due to the turbulent boundary layer. The wave-like pattern on the suction surface of figure 2.25 has no physical significance and is caused by the interpolation routine. (Note that in figure 2.25 the suction surface is now the top surface.)

The contour plot appears to show the presence of a large, oscillating, hydrodynamic field around the aerofoil, together with the aerofoil wake. From figure 2.24, 150 mm downstream of the trailing edge the vortex wake is between 20 and 30 mm wide. Similarly to T–S waves, outside of the wake the disturbances would decay very rapidly. The contour lines are thinly spaced and roughly aligned parallel with the aerofoil wake from approximately 50 mm downstream of the trailing edge. At 100 mm downstream of the trailing edge, plotting $\ln \mathrm{dB}$ against z shows a linear relationship on the pressure and suction sides of the wake. This shows that the decay of the peak frequencies in the wake is exponential — consistent with the linear theory of the unstable hydrodynamic wake of an aerofoil.

The contour pattern around the aerofoil (excluding the wake) is believed to be the hydrodynamic field resulting from the diffraction of the T–S wave at the trailing edge of the aerofoil. In §5.1 the diffraction of a T–S wave at the edge of a semi-infinite plate is calculated analytically using the Wiener–Hopf technique, after the method of Aizin [1]. The diffraction results in an oscillating hydrodynamic field close to the plate, and a sound field at the frequency of the T–S wave further away from the plate. The field is believed to be due to the interaction of the T–S wave and the trailing edge because the contour pattern appears to have a radial form centred at the trailing edge. This is a characteristic of a field scattered at an edge. Without the trailing edge (i.e. assume an infinitely long aerofoil) the T–S disturbances would decay exponentially with distance z, and the contour pattern would be similar to that seen in the wake.

On disregarding the shape of the field, the contour pattern is *not* consistent with solely the decay of T–S waves for several reasons.

The amplitude A of T–S disturbances is found to be proportional to $\exp(-\alpha z)$ outside of the boundary layer (cf. §3.4.2), where α is the wavenumber. For case 1 the wavelength of an unstable wave is $\approx 10\,\mathrm{mm}$. Then $\alpha = 2\pi/0.01 \approx 630\,\mathrm{mm}^{-1}$. The amplitude A outside of the boundary layer is thus proportional to $\exp(-630z)$. Recall that the amplitude of an oscillation is related to its dB level by,

$$\mathrm{dB} = 20\log_{10}\frac{A}{\mathrm{constant}}\,. \tag{2.3}$$

From figure 2.10(d), at 11.85 mm above the aerofoil surface the peak frequency was 50 dB, 45 dB above the background level of 5 dB. From (2.3) the amplitude A will be,

$$A = \mathrm{constant} \times 10^{50/20} \approx \mathrm{constant} \times 320\,. \tag{2.4}$$

Assume without loss of generality that for a background level of 5 dB then $A = 1$. Then the constant is ≈ 0.56. The amplitude at $z = 11.85\,\mathrm{mm}$ will be $A \approx 180$. Hence the amplitude of a T–S wave outside of the boundary layer for case 1 may be approximated by $A \approx 3 \times 10^5 \exp(-630z)$. Then at $z = 20\,\mathrm{mm}$, $A \approx 1$.

This rough calculation shows that for case 1 the amplitude of the T–S wave will have decayed to the background level by $z = 20\,\mathrm{mm}$. (That is five boundary-layer thicknesses above the aerofoil surface.) In figure 2.25 the peak frequencies remain above background levels until 100 mm above the aerofoil, that is twenty-five boundary-layer thicknesses and therefore very unlikely to be decaying T–S waves.

Further, from the frequency spectra in figure 2.11, there is no discrete peak detectable in the boundary layer until approximately 25 mm upstream of the trailing edge. Further upstream than this, the frequency spectra show only broadbands and it is assumed that no discrete frequency has undergone amplification. However a discrete frequency is detectable up to approximately 100 mm above and below the aerofoil, up to roughly 75 mm upstream of the trailing edge. At 75 mm upstream of the trailing edge, the frequency 1048 Hz has not been amplified above the broadband level. Thus the presence of a peak frequency, many boundary-layer thicknesses away, may not be due to a T–S wave at 1048 Hz. In fact *if* the contour pattern was due entirely to boundary-layer disturbances then it would be more localized around the trailing edge.

Finally the contour pattern is not solely attributed to decaying T–S instabilities because the pattern is reasonably symmetric about the aerofoil. It is assumed that transition to turbulence occurs earlier on the suction surface than on the pressure surface, and a discrete frequency is only detectable in the pressure surface boundary layer. Assuming this asymmetry, then a plot of the intensity of the T–S disturbances would also be asymmetric.

It is concluded that there is compelling evidence to suggest that the interaction, between boundary-layer disturbances and the trailing edge, generates an oscillating hydrodynamic field around the aerofoil. The flow-field oscillates at the same frequency as the T–S waves.

Chapter 3

Linear stability analysis

One of the aims of this study of tonal noise was to compare experimental and theoretical results. The experimental results presented in Chapter 2 were obtained using sophisticated measuring techniques and give a broad range of information about the flow over the aerofoil, in particular the boundary layer.

Time series plots and frequency spectra taken in the boundary layer over the aerofoil established that the presence of tonal noise is directly related to the presence of boundary-layer instability waves at the same frequency as the acoustic tones. The boundary-layer instability waves are loosely referred to as T–S waves.

Linear stability analysis models the development of infinitesimal perturbations of a laminar flow (such as a boundary layer). If the flow is unstable then transition from a laminar to a turbulent flow may eventually occur. During this transition the development of the flow may be broadly modelled in turn by linear, weakly nonlinear and strongly nonlinear stability analysis.

Linear stability analysis assumes that the amplitude of all the perturbations is *infinitesimal*. Any disturbance may then be expressed as a superposition of individual modes, each with a different wavelength. There will be no interaction between the modes and hence the stability of the flow may be considered by looking at the individual modes separately.

If the flow remains unstable then energy is continually transferred from the background flow to the perturbations. Eventually the amplitude of the perturbations will no longer be infinitesimal and there will be interactions between the modes. Weakly nonlinear stability analysis describes a flow with mild interactions between the perturbations. When the interactions become stronger a full nonlinear stability analysis is required to model the subsequent development.

The majority of the frequency spectra presented in Chapter 2 show a fundamental mode (at the frequency of the acoustic tone) with one or more harmonics visible above the background broadband level. The amplitude of the harmonics is generally much less than that of the fundamental. Harmonics are generated by nonlinear interactions between the perturbations. The majority of the harmonics are weak compared with the fundamental modes and this suggests that the flow is weakly nonlinear.

This chapter describes the linear stability analysis for the flow over the aerofoil for the cases 1 to 6 in Chapter 2.

3.1 Introduction to hydrodynamic stability

If a flow is perturbed then the perturbation may grow, decay or persist at a similar amplitude. This behaviour may be described more formally in a Liapounov sense where the magnitude of the difference between the basic state and the present state for the velocity and pressure fields is compared to the initial difference. Considering the limit as $t \to \infty$ then a flow will be deemed asymptotically stable if all perturbations decay to zero, neutrally stable if one or more perturbations persist at a similar amplitude and unstable if any perturbation becomes unbounded in the limit.

An instability may occur when there is a disturbance to the equilibrium of a fluid between the inertia, viscous and external stresses. External forces may include buoyancy (due to variable density of the fluid), surface tension and rotational forces.

Common examples of hydrodynamic instabilities are ‘Kelvin–Helmholtz billows’. Two fluids moving with different velocities (and possibly having different densities) move over each other and the interface becomes unstable, rolling up into ‘billows’.

This phenomenon may sometimes be observed in the atmosphere. Also a swirling flow where the circulation is greater as you move towards the centre of rotation may result in an overturning instability as the centrifugal force throws the fluid outwards. Couette flow between two cylinders (Taylor–Couette flow) when the circulation of the inner cylinder is greater than the outer results in steady Taylor vortices regularly spaced in an axial sense between the cylinders.

Viscosity has different effects on the perturbations of a fluid. Intuitively viscosity would dissipate the energy of a disturbance and hence stabilize the flow (particularly for very viscous fluids). However, viscosity also diffuses momentum and this may lead to instability.

Boundaries may also affect the stability of a fluid. They may act as a constraint to instability growth. However for viscous fluids there is no slip on the boundary and hence vorticity will be distributed close to the boundary. This may increase momentum diffusion into the outer flow leading to instability.

The classical approach (most widely used up until the 1960's) is to perform a linear stability analysis by perturbing the basic flow, and then linearizing the equations of motion for small perturbations. This approach may then be extended by also taking into account the leading nonlinear terms of the equations, resulting in the weakly nonlinear theory. This has been extensively developed over the last 40 years (see Chapter 4). Hydrodynamic stability is studied by both experimental and numerical modelling.

3.1.1 Inviscid stability theory

Consider a steady, bounded and parallel basic flow

$$\mathbf{u} = (U(z), 0, 0)\,, \tag{3.1}$$

and appropriate boundary conditions which satisfy the Euler and continuity equations,

$$\begin{aligned} \mathbf{u}_t + (\mathbf{u}.\nabla)\mathbf{u} &= -\nabla p\,, && (3.2)\\ \nabla.\mathbf{u} &= 0\,. && (3.3) \end{aligned}$$

Assume that there is a small disturbance of the basic flow such that the perturbed velocity field will be

$$\mathbf{u} = (U + u', v', w')\,, \tag{3.4}$$

with a corresponding perturbation p' of the pressure field. Now substitute (3.4) into (3.2), (3.3) and linearize the resulting equations.

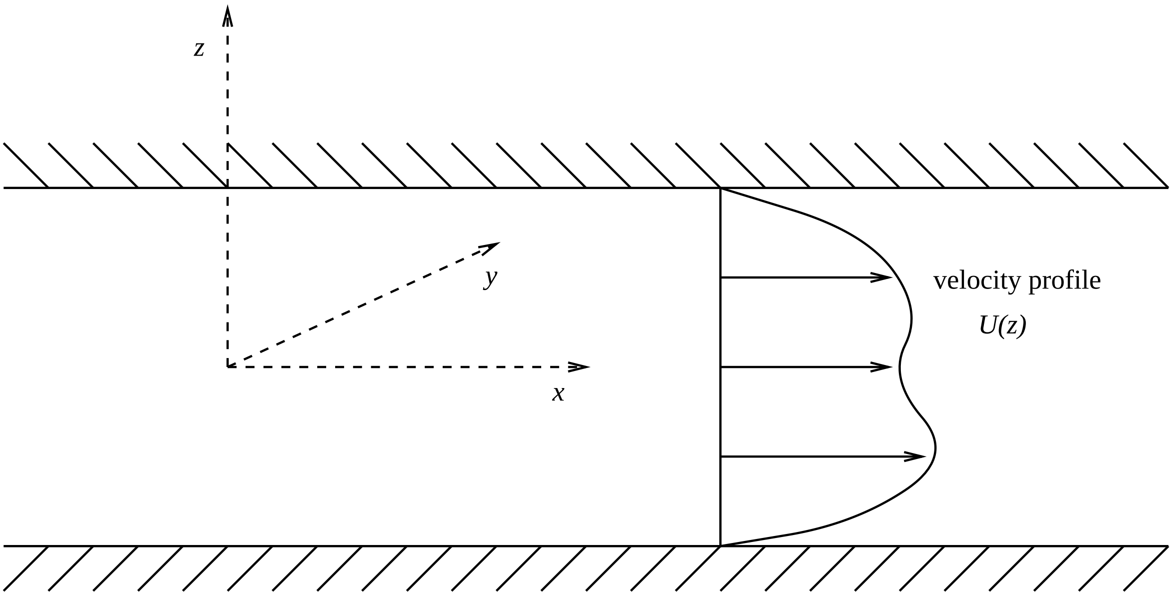

Figure 3.1: Basic set-up

Method of normal modes

The method of normal modes separates a solution into its individual wave components. The whole solution may then be expressed as a superposition of these components. If the basic flow is invariant under a translation (or rotation) with respect to a space coordinate then that coordinate may be separated from the others. Also if the basic flow is steady then the time dependence may also be separated.

Consider the basic flow in figure 3.1. Using the method of normal modes write

$$\{u', v', w', p'\} = \{\hat{u}(z), \hat{v}(z), \hat{w}(z), \hat{p}(z)\}\, e^{i\alpha(x-ct)+i\beta y}\,, \tag{3.5}$$

where by definition we implicitly take the physical values to be the real parts of the quantities in (3.5). Note that α and β are the wavenumbers in the x and y directions respectively.

The method of normal modes may be justified by taking Fourier transforms with respect to x and y and a Laplace transform with respect to t. As the variables x, y and t only appear indirectly as differential operators $\partial/\partial x, \partial/\partial y$ and $\partial/\partial t$ in the linearized Euler and continuity equations then taking Fourier and Laplace transforms results in a set of ordinary differential equations. These may then be solved and after carrying out Fourier and Laplace inversions the solution would be the same as writing the linear superposition of the complete set of normal modes.

The wave speed c in (3.5) may be complex $c_r + ic_i$ and then the modes are waves travelling in the $(\alpha, \beta, 0)$ direction with phase speed $\alpha c_r/\sqrt{(\alpha^2+\beta^2)}$. The modes will be stable if the growth rate $\alpha c_i \leq 0$, unstable if $\alpha c_i > 0$ and neutrally stable when $\alpha c_i = 0$.

Squire's theorem

Using a transformation by Squire (1933) the three-dimensional problem may be reduced to an equivalent two-dimensional one:

$$\tilde{\alpha} = \sqrt{\alpha^2+\beta^2}\,, \quad \tilde{\alpha}\tilde{u} = \alpha\hat{u} + \beta\hat{v}\,, \quad \tilde{p}/\tilde{\alpha} = \hat{p}/\alpha\,. \tag{3.6}$$

The set of ordinary differential equations is the same as the previous set with $\beta = \hat{v} = 0$. The solution of the two-dimensional problem may be sought and then using Squire's transformation the three-dimensional solution is easily found. The two-dimensional disturbance will have growth rate $\tilde{\alpha}c_i > \alpha c_i$ for $\beta \neq 0$, which is the basis of Squire's theorem for an inviscid fluid;

'to each unstable three-dimensional disturbance there corresponds a more unstable two-dimensional one'.

Considering two-dimensional disturbances allows the introduction of a perturbation stream function ψ' such that

$$u' = \frac{\partial \psi'}{\partial z} \text{ and } w' = -\frac{\partial \psi'}{\partial x}\,, \tag{3.7}$$

where

$$\psi'(x,z,t) = \phi(z)e^{i\alpha(x-ct)} \,. \tag{3.8}$$

Rayleigh theory

Substituting the perturbation stream function (3.8) into the (two-dimensional) linearized Euler and continuity equations (3.2), (3.3) and combining these will lead to Rayleigh's stability equation,

$$(U-c)(\phi'' - \alpha^2\phi) - U''\phi = 0 \,. \tag{3.9}$$

The Rayleigh stability equation describes the development of infinitesimal inviscid disturbances and is a second-order eigenvalue problem for eigenvalues c with corresponding eigenfunctions $\phi(z)$.

For a fixed wavenumber α assume the flow is unstable. Then there will be an eigenvalue for which $c_i > 0$. If $(U-c) \neq 0$ then it may be shown that

$$c_i \int_{z_1}^{z_2} \frac{U''|\phi|^2}{|U-c|^2} dz = 0 \,, \tag{3.10}$$

where $\phi(z_1) = \phi(z_2) = 0$. For (3.10) to hold then U'' will change sign in the interval (z_1, z_2) and the basic velocity profile will have an inflexion point $U'' = 0$. This result is known as Rayleigh's inflexion-point theorem;

'a necessary condition for instability is that the basic velocity profile should have an inflexion point'.

It should be noted that this is not a sufficient condition for a bounded, parallel flow.

3.1.2 Viscous stability theory — The Orr–Sommerfeld equation

Now consider a steady, bounded and parallel flow satisfying the Navier–Stokes and continuity equations,

$$\begin{aligned} \mathbf{u}_t + (\mathbf{u}.\nabla)\mathbf{u} &= -\nabla p + R^{-1}\nabla^2\mathbf{u} \,, && (3.11) \\ \nabla.\mathbf{u} &= 0 \,, && (3.12) \end{aligned}$$

where the Reynolds number $R = UL/\nu$ for a flow with characteristic velocity and length scales U and L respectively. Follow the same procedure as for inviscid fluid and perturb the basic velocity profile and linearize (3.11), (3.12). Invoke the method of normal modes and note that Squire's transformation holds with the extra condition that $\tilde{\alpha}\tilde{R} = \alpha R$. Again consider the two-dimensional perturbation stream function (3.8) and then combine the linearized equations into the eigenvalue relation $\mathcal{F}(\alpha, c, R) = 0$. The eigenvalue relation $\mathcal{F}(\alpha, c, R) = 0$ describes the development of the flow to infinitesimal viscous disturbances and is called the Orr–Sommerfeld equation,

$$\left(D^2 - \alpha^2\right)^2 \phi = i\alpha R \left\{(U - c)\left(D^2 - \alpha^2\right) - U''\right\} \phi \,, \tag{3.13}$$

where $D = \mathrm{d}/\mathrm{d}z$. The Orr–Sommerfeld equation (3.13) is a fourth-order eigenvalue problem. As the Reynolds number $R \to \infty$ it reduces to the Rayleigh stability equation (3.9) for inviscid flow.

The Orr–Sommerfeld equation may be solved for fixed (R, α) to determine the eigenvalue c at any point in the (R, α)-plane to investigate the stability of the flow. Following the definitions of stable, neutrally stable and unstable modes given in §3.1.1, curves of neutral stability may be plotted in the (R, α)-plane on which $\alpha c_i = 0$. If for neighbouring values of (R, α), $\alpha c_i > 0$ then these curves are also known as marginal stability curves (as they are located at the 'margin' of stability). For all the flows investigated in this chapter the marginal and neutral stability curves coincide. The marginal stability curves separate the (R, α)-plane into stable and unstable regions.

Figure 3.2 is a sketch of a marginal stability curve which may be calculated for a bounded, parallel flow, such as plane Poiseuille flow. Now define the critical Reynolds number R_c such that $\forall\, R < R_c$ the flow is stable for all modes and for $R > R_c$ at least one mode is unstable..

The extra condition $\tilde{\alpha}\tilde{R} = \alpha R$ required for Squire's transformation (for viscous fluid) implies that $\tilde{R} \leq R$. Squire's theorem for a viscous fluid may be written as;

'to obtain the minimum critical Reynolds number it is sufficient to consider only two-dimensional disturbances'.

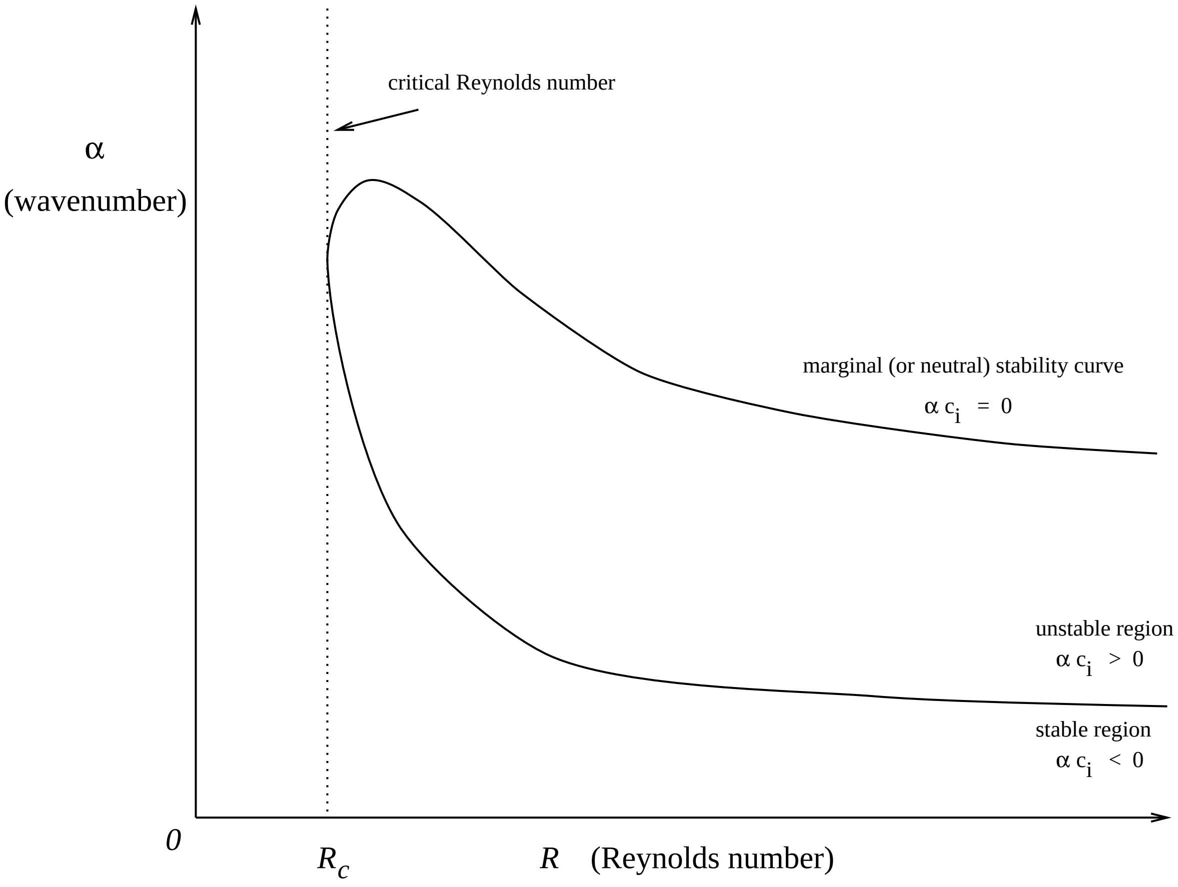

Figure 3.2: Schematic of a marginal (or neutral) stability curve (such as for plane Poiseuille flow).

3.1.3 Spatial and temporal modes

The theory described so far has only considered the development of small disturbances in time — temporal stability analysis. This method of modelling assumes knowledge of the physical quantities at some arbitrary point in time, say $t = 0$, and then follows the development of the flow with increasing time. If the physical quantities remain bounded for all time then the disturbance is deemed to be stable. This approach is the familiar initial value problem.

Temporal mode analysis has been observed experimentally to be a poor model for some physical situations. Landau and Lifshitz (1959) proposed modes which grew or decayed with distance downstream and oscillated sinusoidally with time. Spatially growing or decaying modes are observed if the flow is forced at some fixed, real frequency with constant amplitude. A simple example of this is the introduction of a loudspeaker or an oscillating ribbon vibrating with a constant frequency, (say ω). If the group velocity is in the direction of the flow (ensuring that the energy of the disturbance will propagate in the same sense as the basic flow), then after a finite time the observed flow will have disturbances with amplitude varying with distance downstream, oscillating with fixed real frequency ω.

This model suggests modes which vary with distance downstream of the form $e^{i\alpha x}$ where $\alpha \in \mathbb{C}$. Spatial modes take the form

$$\phi(z)e^{i(\alpha_r x-\omega t)}e^{-\alpha_i x}\,, \tag{3.14}$$

where $\alpha = \alpha_r + i\alpha_i$. They grow or decay with increasing x unless $\alpha_i = 0$ when they coincide with neutral temporal modes. Spatial modes have wavelength $2\pi/\alpha_r$ and growth rate $-\alpha_i$.

For a solution to be valid we require that all disturbances have decayed away as $x \to \pm\infty$. This situation is also obviously physically realistic. After a finite time the disturbance will be bounded as $x \to \pm\infty$ because the disturbance energy is propagated at its group velocity.

In many situations, after some time has passed, it appears that spatial modes more realistically model the development of the flow to small disturbances. So far the theory has been developed specifically for bounded, parallel flows but in practice this may be extended to include flows which are quasi-parallel and also unbounded (§3.3). Spatial modes appear to model the stability of shear layers, jets and (of particular interest for this problem) boundary layers.

3.2 Boundary layer theory

In 1904 Prandtl noted how the flow of a slightly viscous fluid may be divided into two regions. Flow in the presence of a boundary will appear inviscid up until a relatively close point near the boundary surface. Viscous effects will only be significant in this small region close to the boundary surface. The boundary conditions for a viscous fluid will be zero velocity on the boundary, that is no slip as well as the usual no penetration condition for an impermeable material.

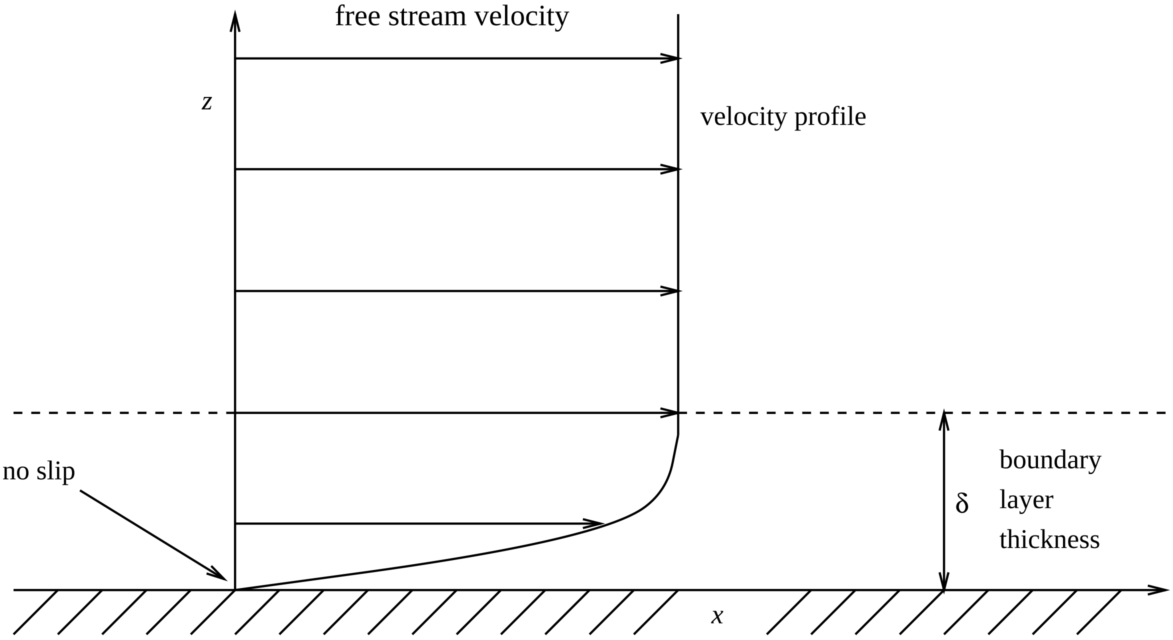

Figure 3.3: Schematic of a boundary layer over a flat plate

Consider figure 3.3 where U_∞ is the free-stream velocity (or outer velocity). The viscous no slip boundary condition forces a rapid change in the u velocity component from U_∞ to 0 in a small z distance δ. The basic assumption

$$\left|\frac{\partial u}{\partial z}\right| \gg \left|\frac{\partial u}{\partial x}\right| , \tag{3.15}$$

assumes that the u velocity changes much more rapidly with z than with x close to the boundary. Intuitively (3.15) implies that the characteristic length scale $L \gg \delta$. Rescaling the Navier–Stokes and continuity equations (3.11), (3.12) reveals that viscosity is significant over a distance

$$\delta \sim \frac{1}{\sqrt{R}} , \tag{3.16}$$

where the flow satisfies the boundary-layer equations:

$$\begin{aligned} uu_x + wu_z &= U_\infty U_{\infty x} + \nu u_{zz} , & (3.17) \\ u_x + w_z &= 0 . & (3.18) \end{aligned}$$

For the flow over a flat plate the free-stream velocity U_∞ is constant and $U_{\infty x} = 0$ in equation (3.17). However the flow past a curved surface will form a boundary-layer profile similar to the profile in figure 3.3, for boundaries of low curvature. The only difference is that the free-stream velocity is now $U_\infty = U_\infty(x)$. Using Bernoulli's relation, if $U_\infty = U_\infty(x)$ then

$$p + \tfrac{1}{2}\rho U_\infty^2 = \text{Const.}\,, \tag{3.19}$$

and

$$-p_x/\rho = U_\infty U_{\infty x}\,. \tag{3.20}$$

Note that from (3.20), the term $U_\infty U_{\infty x}$ in equation (3.17) is the pressure gradient.

3.2.1 The Falkner–Skan boundary layer

Consider a free stream with velocity $U_\infty \propto x^m$ which from inviscid theory may be shown to represent the flow around a wedge of semi-angle $\pi m/(m+1)$. Taking the x coordinate in a direction parallel to a face of the wedge enables this problem to be considered as the development of the flow over a rigid plate with (if $m \neq 0$) a non-zero pressure gradient. If $m = 0$ the problem is reduced to the flow over a flat plate.

The boundary layer over a plate with a leading edge will become thicker with distance x downstream as the layers of fluid closest to the plate gradually slow down layers further away. Introduce the similarity variable

$$\eta = \frac{z}{g(x)}\,, \tag{3.21}$$

where the function $g(x)$ compensates for the stretching of the boundary-layer profile by the gradual thickening of the boundary layer. The boundary-layer velocity profile may then be expressed as $u(\eta)$ which is independent of position. If $g(x)$ is known then $u(z)$ may easily be found for any x. Next consider a similarity solution

$$\psi = F(x) f(\eta)\,, \tag{3.22}$$

which satisfies the continuity equation (3.18) by choosing $F(x) = U_\infty(x)g(x)$. Then on substituting (3.22) into the boundary-layer equation (3.17), (3.17) reduces to:

$$f'^2 - ff'' - \frac{U_\infty}{U'_\infty}\frac{g'}{g} ff'' = 1 + \frac{\nu}{U'_\infty g^2} f'''\,, \tag{3.23}$$

where a prime denotes differentiation with respect to η. A similarity solution will exist if (3.23) is only dependent on the similarity variable η. This occurs when $U_\infty(x)$ satisfies

$$\frac{U_\infty U_\infty''}{U_\infty'^2} = \text{Const.}\,, \tag{3.24}$$

which will be for free streams of the form $U_\infty \propto x^m$ or $U_\infty \propto e^{mx}$.

If $U_\infty = Ax^m$, then (3.23) reduces to the Falkner–Skan boundary-layer equation,

$$f''' + ff'' + \beta(1 - f'^2) = 0\,, \tag{3.25}$$

$$f(0) = f'(0) = 0 \quad , \quad f'(\infty) = 1\,, \tag{3.26}$$

where $\beta = 2m/(m+1)$. The stretching function $g(x)$ is found to be

$$g(x) = \sqrt{\frac{2}{(m+1)}\frac{\nu x}{U_\infty}}\,, \tag{3.27}$$

and hence the boundary-layer thickness δ grows like $(\nu x/U_\infty)^{\frac{1}{2}}$ with distance x downstream. The boundary-layer velocity is given by

$$u/U_\infty = f'(\eta)\,, \tag{3.28}$$

from (3.22).

The flow over a flat plate with zero pressure gradient (i.e. constant free-stream velocity) is known as the Blasius boundary layer and this is just a special case of the Falkner–Skan boundary layer when $\beta = m = 0$. The Falkner–Skan equation (3.25) reduces to the Blasius equation

$$f''' + ff'' = 0\,, \tag{3.29}$$

with the same boundary and matching conditions (3.26) as β (or m) → 0.

Falkner–Skan boundary-layer velocity profiles

On varying the parameter β (or m) which is associated with the pressure gradient in the free stream, the solution of the Falkner–Skan problem (3.25), (3.26) will give the boundary layer for the flow over a rigid plate inclined at an angle of $\pi\beta/2$.

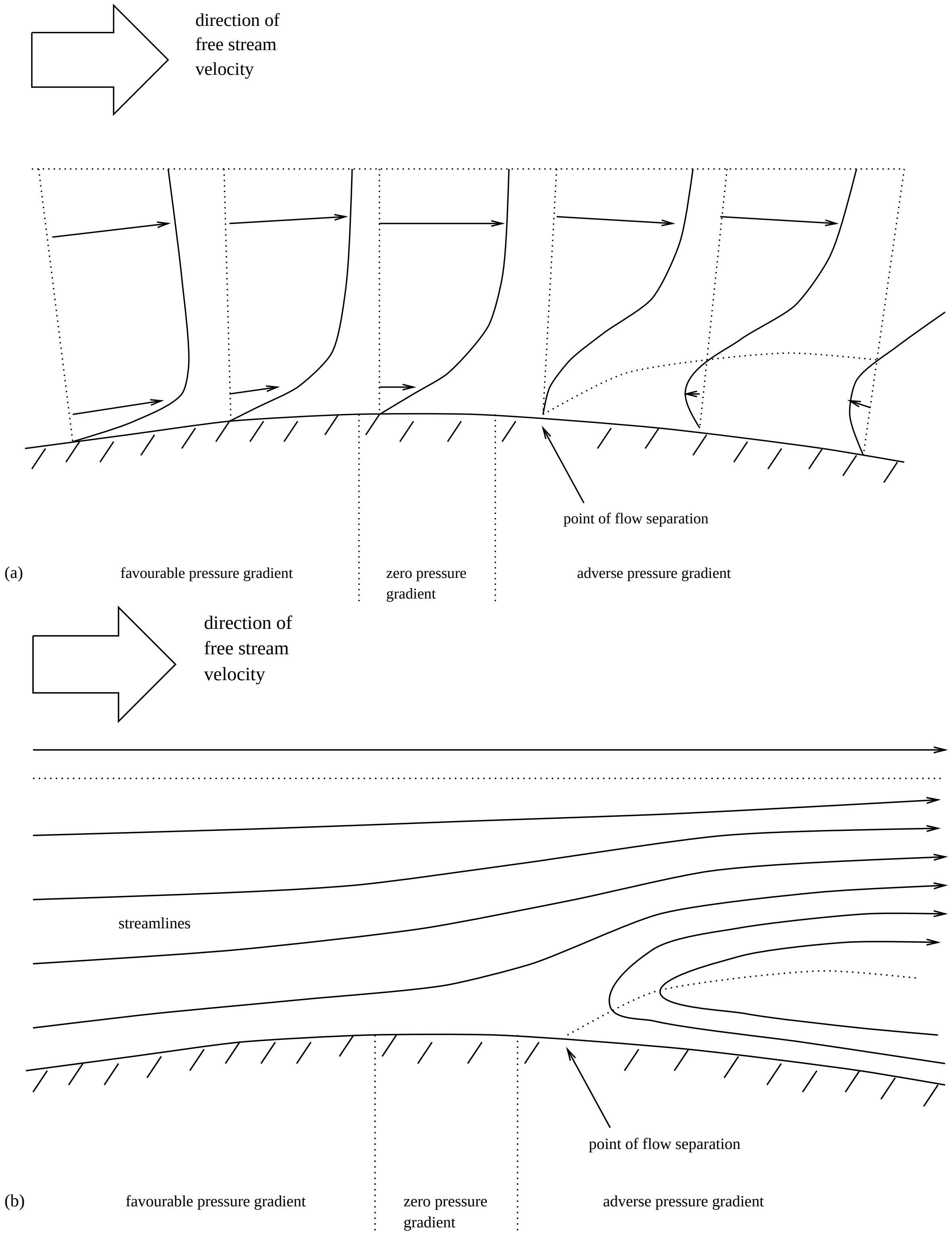

Figure 3.4: Schematic of a changing boundary layer under the influence of a variable pressure gradient

For $\beta > 0$ there will be a favourable pressure gradient ($\mathrm{d}p/\mathrm{d}x < 0$) and for $\beta < 0$ an adverse pressure gradient ($\mathrm{d}p/\mathrm{d}x > 0$). If $\beta > 0$ then the flow close to the surface is up a positive gradient slope and will be accelerating to overcome this. Hence the pressure gradient will be favourable. If $\beta < 0$ then the flow close to the surface is down a negative gradient slope and will be decelerating to maintain continuity. Hence the pressure gradient will be adverse. If $\beta = 0$ then the flow is over a flat plate and will have no acceleration or deceleration. Hence the pressure gradient will be zero. (Note that the sign of the pressure gradient may also be determined on substituting $U_\infty(x)$ into (3.20).)

The shear stress on the surface ($z = 0$) will be $\mu \partial u/\partial z$ where μ is the dynamic viscosity of the fluid. For a large enough adverse pressure gradient (as the pressure gradient opposes the motion) there will be a point where the shear stress on the surface is zero. This point is known as the point of flow separation. Increasing the adverse pressure gradient still further may lead to a small region of reversed flow close to the boundary surface. This may lead to a separated shear layer where streamlines close to the boundary surface are forced up over the region of reversed flow. Convection of vorticity from the boundary surface is increased after boundary-layer separation (compared to an attached boundary layer).

Figure 3.4 is a sketch of a flow over a slightly curved surface. The curvature of the surface allows the flow to experience a changing pressure gradient. The upper sketch (a) shows the velocity profiles in the boundary layer. The point of flow separation is marked and there is a small region of reversed flow downstream of this point. The lower sketch (b) is for the same boundary layer and shows the resultant streamline pattern.

The changing velocity profiles sketched in figure 3.4(a) may all be represented by Falkner–Skan boundary-layer profiles. For $\beta > 0$ the solution of (3.25), (3.26) is unique and increasing β leads to stronger favourable pressure gradients. Setting $\beta = 0$ gives the flow over a flat plate with zero pressure gradient. This is approximately the third (from the left) profile in figure 3.4(a). For $\beta < 0$ the solution of (3.25), (3.26) is not unique. For $-0.1988 < \beta < 0$ there exists two solutions of the Falkner–Skan problem.

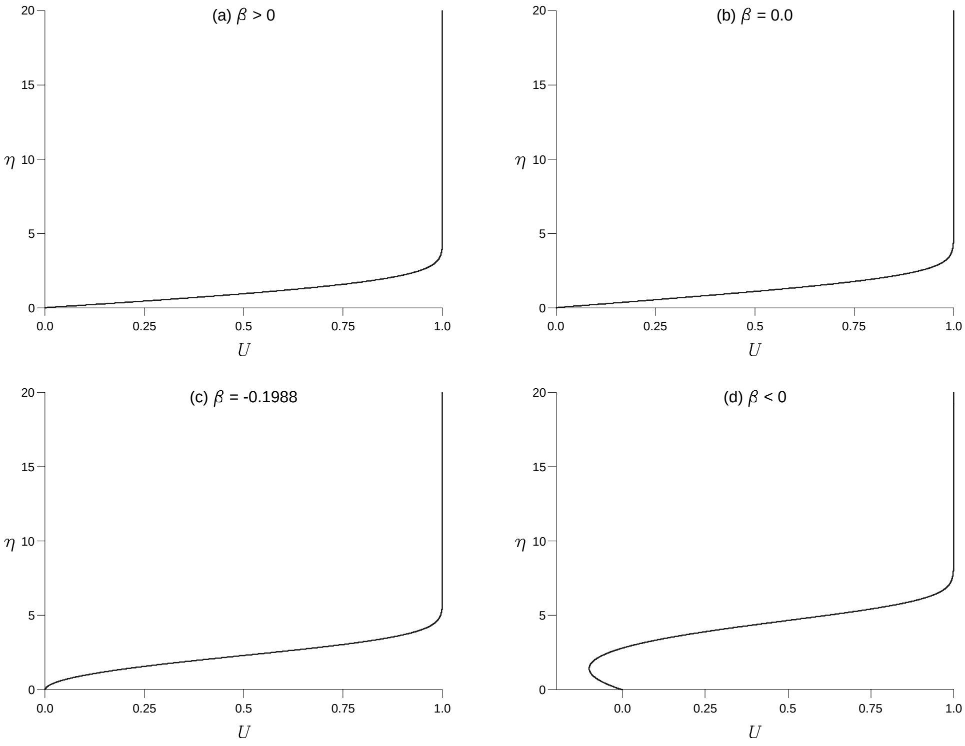

Figure 3.5: Falkner–Skan profiles for different values of β.

The choice of $f''(0)$ is not unique and there are two families of solutions. One family of solutions has a small region of reversed flow close to the boundary surface. The other family is a continuous extension of the Falkner–Skan boundary layer as the parameter β changes sign. For $\beta = -0.1988$ the solution is unique as a solution of (3.25), (3.26) only exists when $f''(0) = 0$. Hence the shear stress at the boundary surface is zero and the Falkner–Skan profile is on the verge of separation (fourth profile from the left in figure 3.4(a)). For $\beta < -0.1988$ there is no continuous extension of the solution to the Falkner–Skan problem.

Figure 3.5 shows a selection of Falkner–Skan boundary-layer profiles calculated for different values of β.

3.2.2 Modelling the laminar boundary layer over an aerofoil

In Chapter 2 mean boundary-layer profiles were presented for cases 1, 5 and 6. As discussed, the flow was found to separate upstream of the trailing edge and the profiles exhibit small regions of reversed flow close to the aerofoil surface. The boundary layer over the aerofoil was gradually changing because of the aerofoil curvature. Falkner–Skan boundary-layer profiles appear suitable to use to model the flow over an aerofoil because they exhibit similar characteristics on varying the parameter β.

There are several measurable quantities which are commonly used to describe boundary-layer flows. The boundary-layer thickness δ is usually measured up to a point where $u/U_\infty \approx 0.99$. However a more commonly used experimental measure of a boundary layer is the displacement thickness $\delta^\star$. This measures the loss of mass flux in the boundary layer as a result of the fluid's viscosity. The loss of mass flux in a boundary layer will be

$$\rho \int_0^h (U_\infty - u)\ \mathrm{d}z\ , \tag{3.30}$$

where the upper limit h is taken far outside of the boundary layer. Let the loss of mass flux in the absence of a boundary layer be $\rho U_\infty \delta^\star$, whence

$$\delta^\star = \int_0^h \left(1 - \frac{u}{U_\infty}\right)\ \mathrm{d}z\ , \tag{3.31}$$

after comparison with (3.30). The flow of a viscous fluid around a solid body may be thought of in terms of an inviscid fluid flowing around a new body defined as the original body plus the displacement thickness $\delta^\star$. The displacement thickness may be thought of as the amount the free stream is deflected by the boundary layer.

Similarly, the momentum thickness θ, defined by

$$\theta = \int_0^h \frac{u}{U_\infty}\left(1 - \frac{u}{U_\infty}\right)\ \mathrm{d}z\ , \tag{3.32}$$

is a measure of the loss of momentum flux due to a boundary layer.

The displacement and momentum thicknesses for the Falkner–Skan boundary layer are found to be,

$$\delta^\star(x) \quad = \quad (\nu x/U_\infty)^{1/2}\,(2/(m+1))^{1/2} \int_0^\infty (1 - f')\ \mathrm{d}\eta\ , \tag{3.33}$$

$$\theta(x) \;=\; (\nu x/U_\infty)^{1/2}\,(2/(m+1))^{1/2}\int_0^\infty f'\,(1-f')\;\mathrm{d}\eta\,. \tag{3.34}$$

To model the flow over the aerofoil, we represent the flow at specified locations, called stations, by different Falkner–Skan profiles. Both $\delta^\star$ and θ may be measured experimentally using the LDA. A valid approach may be to match either $\delta^\star$ or θ with a Falkner–Skan profile at each station. However $\delta^\star$ and θ both depend on x, the distance from the leading edge of the rigid plate in the Falkner–Skan formulation. This distance x has *no* physical relationship with the location of the station on the aerofoil.

Instead of using either the displacement or momentum thickness, consider their ratio, the shape factor H,

$$H = \delta^\star/\theta\,. \tag{3.35}$$

The shape factor H may be seen (from (3.33) and (3.34)) to be independent of x. For each Falkner–Skan boundary-layer profile there exists a *unique* shape factor which may be calculated.

To model the flow over the aerofoil, boundary-layer measurements were taken at (typically) twelve stations across the chord. At each station the shape factor was measured and the flow at that station was modelled by a Falkner–Skan boundary layer with the same shape factor.

Figure 3.6 shows the locations of the stations for cases 1 and 4. The first station was placed near to the maximum thickness point on both aerofoils. The stations were not distributed evenly across the aerofoils. The flow developed more rapidly near the trailing edge and to model this the stations there were placed closer together. Also note that the location of each station varied slightly for the different cases.

As a further comparison between the measured profiles and the Falkner–Skan profiles the pressure gradients were also compared. For the flow over the aerofoil the prediction code discussed in §2.3.4 was used to predict the pressure gradient. The code was only able to predict the pressure gradient when the flow was attached. The pressure gradient in the Falkner–Skan boundary layer was calculated using (3.20) where the density of air $\rho \approx 1.225\,\mathrm{kg\,m^{-3}}$. A comparison between the experimental and predicted data against the Falkner–Skan profiles is presented in appendix A. The

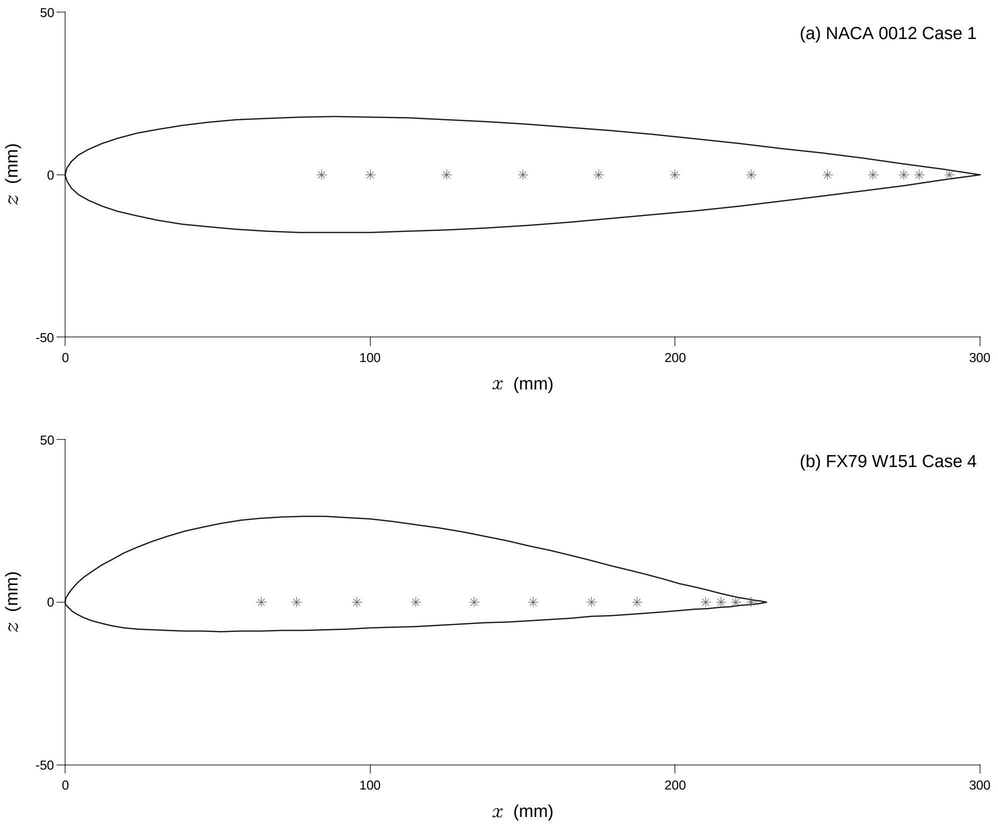

Figure 3.6: Location of stations on the aerofoil where experimental results were obtained: (a) NACA 0012 case 1 and (b) FX79 W151 case 4.

shape factor H appears to be a reasonable quantity with which to match the profiles, and importantly it was measurable everywhere on the aerofoil. Figure 3.7 shows the Falkner–Skan profiles used to model the boundary layer for case 1, at stations 1, 7, 8 and 12. These profiles show the development of the flow over the aerofoil and that the flow separation has been incorporated into the model, (i.e. figure 3.7(d)).

At each station the characteristic length scale is assumed to be $\delta^\star$. In the stability calculations presented in this chapter, the Orr–Sommerfeld equation (3.13) is solved by fixing $\omega = \alpha c$ and R and then finding the wavenumber α. We introduce the Reynolds number $R_{\delta^\star} = U_\infty \delta^\star/\nu$ based on the displacement thickness, and, the non-dimensional frequency $\omega = 2\pi f \delta^\star/U_\infty$, which are used when solving the Orr–Sommerfeld equation in this stability analysis.

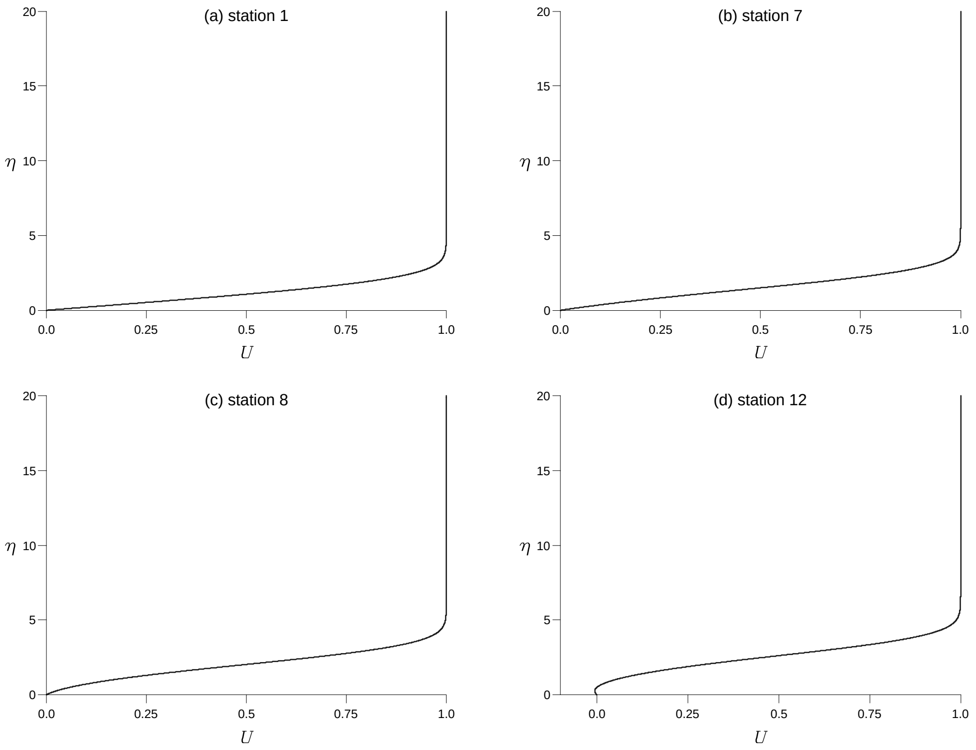

Figure 3.7: Falkner–Skan boundary-layer profiles at stations 1, 7, 8 and 12 for case 1.

3.3 Linear stability of laminar boundary-layer flow over an aerofoil

The development of a disturbance in a laminar boundary layer described by both temporal and spatial modes was addressed by Bouthier [6]. Using the perturbation technique, the method of multiple scales, he introduced a slow time and length scale

$$T = \epsilon t \ \text{ and } \ X = \epsilon x \,, \tag{3.36}$$

as suitable scalings for a boundary-layer flow. The stream function $\psi(x, z, t) = F(X, z, T; \epsilon)$ was expressed as an expansion in terms of the small parameter ϵ,

$$F = F_0 + \epsilon F_1 + \epsilon^2 F_2 + \dots \ . \tag{3.37}$$

Bouthier then demonstrated that the leading term F_0 in (3.37) may be written as

$$F_0 = A(X,T)\Phi_0(X,z,T)e^{i\theta(X,T)/\epsilon}\ , \tag{3.38}$$

where $\theta(X,T)$ is referred to as the phase function. Φ_0 satisfied the Orr–Sommerfeld equation

$$\left(D^2-\alpha^2\right)^2\Phi_0 = iR\left\{(\alpha U-\omega)(D^2-\alpha^2)-\alpha U''\right\}\Phi_0\ , \tag{3.39}$$

where

$$\omega \ = \ -\partial\theta/\partial T\ , \tag{3.40}$$

$$\alpha \ = \ \partial\theta/\partial X\ . \tag{3.41}$$

Using (3.40) and (3.41) together with the chain rule

$$\delta\theta = \frac{\partial\theta}{\partial X}\delta X + \frac{\partial\theta}{\partial T}\delta T\ , \tag{3.42}$$

we find

$$F_0 = A(X,T)\Phi_0(X,z,T)e^{i\left\{\int\alpha\mathrm{d}x-\int\omega\mathrm{d}t\right\}}\ . \tag{3.43}$$

Bouthier was also able to show that Φ_0 may be expressed in terms of a similarity variable $\eta = z/g(X)$, and hence the stream function ψ for a boundary-layer flow is shown to be

$$\psi = A(X,T)\Phi_0(\eta)e^{i\left\{\int\alpha\mathrm{d}x-\int\omega\mathrm{d}t\right\}} + O(\epsilon) \quad \text{as} \ \ \epsilon\to 0\ . \tag{3.44}$$

Note that for constant wavenumber α and frequency ω the exponent in (3.44) is simply $i(\alpha x-\omega t)$, as in (3.14).

Gaster & Grant [20] modelled the development of a wave packet with fixed frequency in a laminar boundary layer by taking a stream function of the form,

$$\psi(x,z) = A(x)\phi(x,z)e^{i\left\{\int\alpha(x)\mathrm{d}x-\omega t\right\}}\ , \tag{3.45}$$

where the factor $A(x)$ was approximately constant for a large enough Reynolds number.

Gaster [19] had also previously shown the relationship between temporal and spatial modes. The ratio of the amplitude between x and x_0 for a temporal mode wave packet is

$$\exp\left\{\int_{x_0}^{x}\alpha c_i/c_g\mathrm{d}x\right\}\ , \tag{3.46}$$

where c_g is the group velocity of the wave packet. Thus amplification occurs when αc_i and c_g have the same sign. Gaster has shown that the amplification (3.46) is the same as

$$\exp\left\{-\int_{x_0}^{x} \alpha_i(x)\mathrm{d}x\right\} \,, \tag{3.47}$$

for weakly amplified spatial modes.

From (3.44), (3.45) and (3.47) the amplification of a wave with fixed frequency and a *slowly* varying complex wavenumber $\alpha(x)$ from x_0 to a station x downstream of x_0 is,

$$\frac{A(x)}{A(x_0)} = \exp\left\{-\int_{x}^{x} \alpha_i(x)\mathrm{d}x\right\} \,. \tag{3.48}$$

(3.48) is the solution of

$$\frac{\mathrm{d}A}{\mathrm{d}x} = -\alpha_i(x)A \,, \tag{3.49}$$

which is a suitable model of the linear growth of normal modes with amplitude $A(x)$.

3.3.1 Initial hypothesis and method

In Chapter 2 the frequency spectra taken at various locations in the boundary layer on the pressure surface of the aerofoil reveal a dominant disturbance of discrete frequency with amplitude increasing with distance downstream. The disturbance (for each case) remains at a fixed frequency, the frequency of the acoustic tone. It appears that disturbances grow mostly in the neighbourhood of a region of reversed flow close to the trailing edge of the aerofoil. These disturbances appear suitable to be modelled by spatial modes of fixed frequency with *slowly* changing wavelengths to account for the development of the boundary layer.

However from linear stability analysis a broad range of frequencies would be unstable at any station downstream of the 'critical point' on the aerofoil. The term 'critical point' is used loosely here to define the point on the aerofoil when the boundary layer first becomes unstable. Downstream of the critical point, all disturbances with unstable frequencies may be amplified. The frequency spectra in Chapter 2 clearly show that for each case only *one* discrete frequency mode was amplified significantly above the background level.

Initial hypothesis

'The frequency of the dominant disturbance detected in the boundary layer on the pressure surface of the aerofoil may be predicted by the frequency of the linear mode with maximum amplification over the aerofoil.'

The amplification of disturbances of fixed frequency is given by (3.48) where x_0 is taken to be close to the 'critical point' on the aerofoil and x at the trailing edge.

The hypothesis is an attempt to combine the theoretical approach of the linear stability analysis with the experimental observations. The linear stability analysis assumed that the flow extends over an infinite domain, i.e. $-\infty < x < \infty$. As discussed in §3.1.1, the solution of the linearized equations of fluid motion may be obtained after performing Fourier and Laplace transforms in space (say x) and time t respectively. The complete solution is then expressed in terms of Fourier and Laplace inversions. From Fourier inversion the solution is expressed as the integral over *all* wavenumbers α, (i.e. $\int_{-\infty}^{\infty} .. \mathrm{d}\alpha$). If $R > R_c$ then the flow will be unstable over a range of wavenumbers α and there will be a continuum of unstable normal modes.

An alternative description of the development of a flow may be thought of in terms of bifurcation theory. In §6.1.5 the bifurcations of Jeffery–Hamel flow are discussed, including Serrin's theorem and the principle of the exchange of instabilities.

The development of the flow may be thought of by considering the changes which occur by increasing the Reynolds number R. The assumption of an infinite domain made in the linear stability analysis is physically unrealistic. In the wind-tunnel experiments the domain is prescribed by the dimensions of the tunnel. The domain of an aircraft in flight may reasonably be taken to be that of the atmosphere. From Serrin's theorem the flow will be stable for a small enough Reynolds number. On increasing R the flow will remain stable until $R = R_c$ when a bifurcation will occur. For a boundary-layer flow the principle of exchange of stabilities will not be valid and the flow will bifurcate from a stable, steady flow to an oscillatory flow. This is known as a Hopf bifurcation. (The principle of exchange of stabilities for a boundary-layer flow appears in general not to hold because $\omega \neq 0$ as $R \to R_c$.) Increasing R will lead to further bifurcations of the flow. Fourier analysis of the flow would then reveal a set of discrete frequencies. At high enough Reynolds numbers the nonlinear interaction of the unstable waves will lead eventually to a turbulent flow.

This model of the development of the flow appears to describe the experimental observations more closely than the linear stability analysis because for $R > R_c$ the flow is characterized by a discrete set of unstable frequencies. The initial hypothesis presented attempts to reconcile these two descriptions of the flow evolution by predicting that the flow will bifurcate to a frequency close to that predicted from linear stability theory.

Method

§3.2.2 describes how Falkner–Skan boundary-layer profiles are used to model the flow over the aerofoil. Figure 3.6 shows the location of stations 1 to 12 where the profiles were matched for cases 1 and 4.

The linear stability analysis described assumes a parallel basic flow. As mentioned, the theory is commonly utilized to investigate the development of quasi-parallel flows. A boundary layer is an example of a quasi-parallel flow, that is a flow where the basic velocity profile $U(x, z) \approx U(z)$. The analysis also assumed that the basic flow was bounded in the z-direction. In §3.4.2 an 'artificial' boundary is imposed in the free stream outside of the boundary layer, where the boundary conditions are determined using the asymptotic solution of the Orr–Sommerfeld equation as $z \to \infty$.

The main assumption is that the flow remains *stable* until at least station 1 on the aerofoil. Clearly the flow around the leading edge may not be assumed to be quasi-parallel. There will be a stagnation point at the 'nose' of the aerofoil and instabilities may develop there. However there exist strong favourable pressure gradients around the nose of the aerofoil which accelerate the flow and are assumed to dampen any instabilities associated with the stagnation point. With this assumption the flow is assumed to be stable at the start of the region of quasi-parallel flow. The aerofoil is only inclined at small angles of incidence and it is assumed that the mean-flow will remain quasi-parallel until the trailing edge of the aerofoil.

As discussed, we chose 12 stations where the flow is matched to a Falkner–Skan profile. At each station the Orr–Sommerfeld equation is solved with the velocity profile U given by the respective Falkner–Skan boundary layer. A frequency f is chosen and at each station along the aerofoil the values of ω and $R_{\delta^\star}$ are calculated, (see §3.2.2 for the definitions of ω and $R_{\delta^\star}$). The complex wavenumber α may then be determined at each station for the values of $(R_{\delta^\star}, \omega)$. On calculating α at all the stations, a polynomial may be used to obtain an approximate function $\alpha_i(x)$. In practice a least-squares polynomial was used to fit a function through the twelve values of α_i which had been calculated. The error between the least-squares polynomial and the twelve (x, α_i) points was usually minimized by a polynomial with degree less than eleven, typically of degree between five and seven. On constructing a polynomial function $\alpha_i(x)$, the amplification was calculated by using (3.48) with x_0 = station 1 and x = station 12. The amplification of the spatial modes was calculated over a range of frequencies to determine the amplification over the aerofoil as a function of frequency.

3.4 The method of compound matrices

The Orr–Sommerfeld equation (3.13) is a fourth-order, linear, differential eigenvalue problem. The problem is formulated for the flow of a viscous fluid between two parallel, impermeable walls. At each wall there are two boundary conditions specifying no slip and no penetration. For a bounded flow the problem may be solved numerically by using the method of orthonormalization (cf. §6.3). In a channel the eigenfunction $\phi(z)$ is unknown and the method of orthonormalization takes into account all possible forms of the eigenfunction. The method is designed for *stiff* two-point boundary-value problems of which the Orr–Sommerfeld equation is ideally suited. However as discussed in §3.3.1, the Orr–Sommerfeld equation is also commonly used to model the stability of quasi-parallel flows and flows with unbounded domains. The method of orthonormalization is not suitable for unbounded flows. To solve the Orr–Sommerfeld equation for boundary-layer flow (quasi-parallel, semi-infinite flow) the method of compound matrices was used.

3.4.1 Characteristic values of the Orr–Sommerfeld equation

For a linear differential operator with algebraic coefficients the local solutions will be nearly exponential. The slow variation of the coefficients allow the solutions to be expressed locally as $\sim e^{\lambda z}$ where $\Re(\lambda)$ is referred to as the characteristic value of the equation. In a stiff problem the ratio of the characteristic values will be large. Standard shooting methods commonly fail because the base solutions become dominated by one of the characteristic values and they lose their linear independence. (For bounded flows the method of orthonormalization is a shooting method designed to ensure the base solutions remain linearly independent across the domain of the flow.) The method of compound matrices is a shooting method designed for stiff differential equations which may be implemented for problems with bounded or unbounded domains.

If in the Orr–Sommerfeld equation the velocity profile $U(z)$ and also $U''(z)$ are assumed to be locally constant then solutions of the form $\phi \sim e^{\lambda z}$ satisfy

$$\left\{\lambda^2 - \alpha^2 - i\alpha R(U - c)\right\}\left\{\lambda^2 - \alpha^2\right\} + i\alpha R U'' = 0\,. \tag{3.50}$$

This is a quadratic in λ^2 and for large R the characteristic values will be

$$\alpha,\quad -\alpha,\quad (\alpha R)^{1/2} \quad \text{and} \quad -(\alpha R)^{1/2}\,, \tag{3.51}$$

which clearly differ in size when $R \gg 1$.

3.4.2 Boundary-layer flow

The basic velocity profile for the flow in the free stream outside of the boundary layer (say where $z \gg 1$) is

$$U(z) = 1, \quad U''(z) = 0\,. \tag{3.52}$$

Hence for $z \gg 1$ the Orr–Sommerfeld equation is reduced to a differential equation with constant coefficients

$$(D^2 - \alpha^2)^2\phi = i\alpha R(1 - c)(D^2 - \alpha^2)\phi\,, \tag{3.53}$$

with solution

$$\phi(z) \sim C_1 e^{\alpha z} + C_2 e^{-\alpha z} + C_3 e^{\beta z} + C_4 e^{-\beta z}\,, \tag{3.54}$$

where $\beta^2 = [\alpha^2 + i\alpha R(1-c)]$ and C_i are constants. To ensure that the solution ϕ is bounded $\forall z$, impose the boundary conditions

$$\begin{aligned} \phi'' + (\alpha+\beta)\phi' + \alpha\beta\phi &= 0\,, & (3.55)\\ \phi''' + (\alpha+\beta)\phi'' + \alpha\beta\phi' &= 0\,, & (3.56) \end{aligned}$$

at $z = z_2$. Then the solution ϕ takes the form,

$$\phi(z) \sim C_2 e^{-\alpha z} + C_4 e^{-\beta z} \tag{3.57}$$

for $z > z_2$. The boundary conditions (3.55), (3.56) are satisfied when $C_1 = C_3 = 0$ ensuring that the solution ϕ is bounded as $z \to \infty$. The problem is reduced to integrating over a finite domain by imposing an artificial boundary at $z = z_2$ where the eigenfunction ϕ calculated on $[z_1, z_2]$ is matched to the asymptotic solution of the Orr–Sommerfeld equation (3.57) valid as $z \to \infty$.

For boundary-layer flows assume the Cartesian axes are situated such that the boundary is at $z = z_1 = 0$. The boundary conditions, (in addition to (3.55), (3.56)) at z_1 will be

$$\phi(0) = \phi'(0) = 0\,. \tag{3.58}$$

The method of compound matrices assumes (3.57) is the form of the eigenfunction $\phi(z)$ at $z = z_2$. The method of orthonormalization admits *all* possible forms of $\phi(z)$ in the bounded channel. In this sense the method of compound matrices is more restrictive than the method of orthonormalization but it is well suited for boundary-layer flows.

3.4.3 Calculation of the eigenvalue c

The method of compound matrices followed is described by Ng & Reid [36], and is also summarized in Drazin & Reid [13] pp. 311–317.

Consider the fourth-order differential equation

$$\phi^{iv} - a_1\phi''' - a_2\phi'' - a_3\phi' - a_4\phi = 0\,, \tag{3.59}$$

where in the specific case of the Orr–Sommerfeld equation

$$\begin{aligned} a_1 &= 0\,, & (3.60)\\ a_2 &= 2\alpha^2 + i\alpha R(U-c)\,, & (3.61)\\ a_3 &= 0\,, & (3.62)\\ a_4 &= -\left\{\alpha^4 + i\alpha R[\alpha^2(U-c) + U'']\right\}\,. & (3.63)\end{aligned}$$

Let $\boldsymbol{\phi} = [\phi, \phi', \phi'', \phi''']^{\mathrm{T}}$ and then express (3.59) as a system of four first-order equations

$$\boldsymbol{\phi}' = \mathbf{A}(z)\boldsymbol{\phi}\,, \tag{3.64}$$

where

$$\mathbf{A}(z) = \begin{bmatrix} 0 & 1 & 0 & 0 \\ 0 & 0 & 1 & 0 \\ 0 & 0 & 0 & 1 \\ a_4 & a_3 & a_2 & a_1 \end{bmatrix}\,. \tag{3.65}$$

Let $\boldsymbol{\phi_1}$ and $\boldsymbol{\phi_2}$ be two linearly independent solutions of (3.64) which satisfy the boundary conditions at $z = z_1$ and z_2. Then without loss of generality assume

$$\begin{aligned} \boldsymbol{\phi_1}(z_1) &= [0,0,1,0]^{\mathrm{T}}\,, & (3.66)\\ \boldsymbol{\phi_1}(z_2) &= [1,-\alpha,\alpha^2,-\alpha^3]^{\mathrm{T}}e^{-\alpha z}\,, & (3.67)\\ \boldsymbol{\phi_2}(z_1) &= [0,0,0,1]^{\mathrm{T}}\,, & (3.68)\\ \boldsymbol{\phi_2}(z_2) &= [1,-\beta,\beta^2,-\beta^3]^{\mathrm{T}}e^{-\beta z}\,. & (3.69)\end{aligned}$$

Now construct the vector $\mathbf{y} = [y_1, y_2, y_3, y_4, y_5, y_6]^{\mathrm{T}}$ where

$$\begin{aligned} y_1 &= \phi_1\phi_2' - \phi_1'\phi_2\,, & (3.70)\\ y_2 &= \phi_1\phi_2'' - \phi_1''\phi_2\,, & (3.71)\\ y_3 &= \phi_1\phi_2''' - \phi_1'''\phi_2\,, & (3.72)\\ y_4 &= \phi_1'\phi_2'' - \phi_1''\phi_2'\,, & (3.73)\\ y_5 &= \phi_1'\phi_2''' - \phi_1'''\phi_2'\,, & (3.74)\\ y_6 &= \phi_1''\phi_2''' - \phi_1'''\phi_2''\,. & (3.75)\end{aligned}$$

Then from direct calculation $\mathbf{y}$ satisfies

$$\mathbf{y}' = \mathbf{B}(z)\mathbf{y} \, , \tag{3.76}$$

where

$$\mathbf{B}(z) = \begin{bmatrix} 0 & 1 & 0 & 0 & 0 & 0 \\ 0 & 0 & 1 & 1 & 0 & 0 \\ a_3 & a_2 & a_1 & 0 & 1 & 0 \\ 0 & 0 & 0 & 0 & 1 & 0 \\ -a_4 & 0 & 0 & a_2 & a_1 & 1 \\ 0 & -a_4 & 0 & -a_3 & 0 & a_1 \end{bmatrix} . \tag{3.77}$$

The form of the eigenfunction at $z = z_2$ is known and hence the problem is solved most efficiently using backward integration. (The numerical method is designed to alleviate the problems of parasitic growth in the solution caused by the the cumulation of errors over the integration. The outer boundary conditions were chosen to destroy the exponentially growing solutions. Backward integration steps in the opposite direction to the inadmissible solutions and therefore should reduce the growth of errors.)

Using (3.67) and (3.69) the following expression may be formed,

$$\mathbf{y}(z_2) = [1, -(\alpha+\beta), (\alpha^2+\alpha\beta+\beta^2), \alpha\beta, -\alpha\beta(\alpha+\beta), \alpha^2\beta^2]^{\mathrm{T}} \, , \tag{3.78}$$

where $\mathbf{y}(z_2)$ has been suitably normalized. The boundary conditions (3.58) at $z = z_1 = 0$ may be expressed as,

$$\begin{pmatrix} 1 & 0 & 0 & 0 \\ 0 & 1 & 0 & 0 \end{pmatrix} \boldsymbol{\phi}(0) = \mathbf{0} \, . \tag{3.79}$$

Substituting $\boldsymbol{\phi} = \boldsymbol{\phi_1}$ and $\boldsymbol{\phi_2}$ into (3.79) gives the eigenvalue relation

$$y_1(0) = 0 \, . \tag{3.80}$$

An iterative procedure such as Newton's method may then be used to vary the eigenvalue c until $y_1(0)$ is as close to zero as some prescribed tolerance level.

In practice (3.76) was integrated using a fourth-order Runge–Kutta integration scheme from $z_2 = 10$ to $z_1 = 0$ with 1000 integration steps. The starting values of

$\mathbf{y}(z_2)$ were given by (3.78). The eigenvalue c was taken when $y_1(0) < 10^{-12}$. By using Newton's method this tolerance was usually reached after several iterations. Increasing z_2 and the number of integration steps was found to be unnecessary in the majority of cases (although calculations were run at $z_2 = 20$ and with 2000 steps to ensure the consistency of the results).

Convergence of the method relied heavily on the accuracy of the initial value (or guess) taken for the eigenvalue c. For fixed α and R there exists a discrete spectrum of eigenvalues. (For unbounded flows the spectrum is usually made up of a discrete and continuous set of eigenvalues.) For flows such as plane Poiseuille flow and boundary layers there is at most one unstable eigenvalue for each point in the (R, α)-plane. For unbounded flows the continuous spectrum of eigenvalues will be stable, and hence only consideration of the discrete spectrum of eigenvalues is required. For each point in the (R, α)-plane the aim is to find the most unstable eigenvalue, that is the eigenvalue c with maximum value of c_i.

As a starting point, calculations were performed using the Blasius boundary layer. The results were compared with published results (Mack [30]) and were found to be in good agreement. Marginal stability curves for the Blasius and Falkner–Skan boundary layers were calculated by using quadratic extrapolation. Initially three points were found close together in the (R, α)-plane where $c_i = 0$. Then quadratic extrapolation was used to provide a suitable estimate for a neighbouring eigenvalue c on the marginal stability curve. The path of the marginal stability curve was then traced out by searching for eigenvalues where $c_i = 0$.

3.4.4 Calculation of the eigenfunction $\boldsymbol{\phi}$

After calculating the eigenvalue c the corresponding eigenfunction $\phi(z)$ may be calculated. There exist constants A and B such that

$$\boldsymbol{\phi} = A\boldsymbol{\phi_1} + B\boldsymbol{\phi_2}\,, \tag{3.81}$$

because $\boldsymbol{\phi_1}$ and $\boldsymbol{\phi_2}$ are linearly independent. The constants A and B may be eliminated from the four equations in (3.81) in four alternative ways giving

$$y_1\phi'' - y_2\phi' + y_4\phi = 0\,, \tag{3.82}$$

$$y_1\phi''' - y_3\phi' + y_5\phi = 0\,, \tag{3.83}$$

$$y_2\phi''' - y_3\phi'' + y_6\phi = 0\,, \tag{3.84}$$

$$y_4\phi''' - y_5\phi'' + y_6\phi' = 0\,. \tag{3.85}$$

The coefficients y_i are known from calculation of the eigenvalue. The eigenfunction may be calculated from integration of one of (3.82), (3.83), (3.84) and (3.85). To reduce numerical error the direction of integration should be in the opposite sense to the direction used when calculating the coefficients y_i (see Davey [10]). In addition to the boundary conditions (3.58), the normalizing condition $\phi''(0) = 1$ was imposed at $z = 0$.

3.5 Results

Results are presented for the six cases already introduced in Chapter 2. Table 3.1 is reproduced from §2.4.1 outlining the six cases.

Case	Aerofoil	Angle	U_∞	Tone
1	NACA 0012	$-4°$	$30\,\mathrm{ms}^{-1}$	1048 Hz
2	NACA 0012	$-4°$	$38\,\mathrm{ms}^{-1}$	1280 Hz
3	NACA 0012	$-4°$	$44\,\mathrm{ms}^{-1}$	1420 Hz
4	FX79 W151	$-3°$	$30\,\mathrm{ms}^{-1}$	1192 Hz
5	NACA 0012	$-3°$	$8\,\mathrm{ms}^{-1}$	no tone
6	NACA 0012	$0°$	$17\,\mathrm{ms}^{-1}$	no tone

Table 3.1: Details of cases of tonal noise investigated.

In Chapter 2 experimental results, and the conclusions drawn from these, were presented for each of the cases listed in table 3.1. Results were also presented in §2.4.4 for a high free-stream velocity case for the NACA 0012 aerofoil with no discrete tones. The discrete tones were eliminated after the onset of turbulent flow *before* the trailing edge of the aerofoil. No theoretical results are presented in this chapter for high free-stream velocities because the quasi-parallel flow approximation is clearly invalid. The linear stability analysis described in this chapter is only applicable to laminar flow.

3.5.1 Tonal cases: 1, 2, 3 and 4

Figure 3.8 plots the marginal stability curves at stations 1 to 12 for case 1. The marginal curve for each station is labelled. The asterisks denote the location in the $(R_{\delta^\star}, \omega)$-plane of a T–S wave, at the frequency of the tone, at the twelve stations along the aerofoil. The Reynolds number $R_{\delta^\star}$ at each station is indicated on the $R_{\delta^\star}$-axis.

Figure 3.9 plots the growth rate $-\alpha_i$ against frequency f at stations 3 to 12 for case 1. The growth rate and frequency are both plotted as dimensional quantities. The growth rate curve for each station is labelled. The solid vertical line is the frequency of the tone. The two vertical dashed lines are the frequencies with maximum growth rate at stations 7 and 8. The relevance of these lines is discussed in §3.6.1.

Figure 3.10 plots the amplification (3.48) from station 1 (x_0) to station 12 (x) for T–S waves with fixed frequency for case 1. The amplification and frequency are both plotted as dimensional quantities. The solid vertical line is the frequency of the tone. Figure 3.11 is a similar plot showing the amplification between stations 1 and 7 (solid line) and between stations 1 and 8 (dashed line).

Figure 3.12 is a plot of $\alpha_i(x)$ for a T–S wave with frequency 1048 Hz, the frequency of the tone. The vertical axis (α_i) and horizontal axis (x) are both dimensional. The values of α_i at each station are denoted by a plus symbol. The solid curve is the least-squares polynomial fitted through these points to obtain an approximate polynomial $\alpha_i(x)$.

Figure 3.13 is a plot of the amplification $A(x)/A(x_0)$ of a T–S wave with frequency 1048 Hz. The vertical axis ($\ln\,(A(x)/A(x_0))$) is the natural logarithm of the amplification of the T–S wave from station 1, and the horizontal axis (x) is the distance (in m) from the leading edge of the aerofoil. By the trailing edge the T–S wave has been amplified to approximately $e^{11.3} \approx 80,000$ times the amplitude at station 1.

Figures 3.14 — 3.17 plot the development of $|\phi'(z)|$ over the NACA 0012 aerofoil for a T–S wave with frequency 1048 Hz. From (3.7) and (3.8)

$$u' = \phi'(z)e^{i\alpha(x-ct)}\,, \qquad (3.86)$$

$$w' = -i\alpha\phi(z)e^{i\alpha(x-ct)}\,, \qquad (3.87)$$

and hence

$$|u'| = |\phi'(z)|e^{-\alpha_i x}\,, \qquad (3.88)$$

$$|w'| = \alpha|\phi(z)|e^{-\alpha_i x}\,. \qquad (3.89)$$

The graphs of $|\phi'(z)|$ show the amplitude of the streamwise perturbation u' in the z direction. These curves are analogous to the rms boundary-layer profiles presented in Chapter 2.

Figures 3.18 — 3.21 plot the development of the Reynolds stress over the NACA

0012 aerofoil for a T–S wave with frequency 1048 Hz. The physical significance of the Reynolds stress is discussed in §3.6.1. For now it is defined to be

$$\tau = \tfrac{1}{2}\alpha(\phi_r\phi_i' - \phi_i\phi_r')e^{2\alpha c_i t}\,, \tag{3.90}$$

where the quantity

$$S(z) = (\phi_r\phi_i' - \phi_i\phi_r')\,, \tag{3.91}$$

is normalized and plotted in the Reynolds stress figures. The horizontal solid line in each diagram indicates the location of the critical layer. The critical layer is centred about the point z_c where

$$U(z_c) = c\,. \tag{3.92}$$

Note that for spatial modes the point z_c is taken to be where

$$U(z_c) = \frac{\omega\alpha_r}{\alpha_r^2 + \alpha_i^2}\,. \tag{3.93}$$

Figure 3.22 plots the marginal stability curves at stations 1 to 12 for case 2. Note that for case 2 the displacement thickness measured at station 12 was less than that at station 11. (This indicates the boundary layer is probably close to transition.) As a result $R_{\delta^\star}$ is less at station 12 than station 11. Figure 3.23 plots the growth rate $-\alpha_i$ against frequency f at stations 3 to 12 for case 2. Once again the solid vertical line is the frequency of the tone and the two vertical dashed lines are the frequencies with maximum growth rate at stations 7 and 8. Figure 3.24 plots the amplification (3.48) from station 1 (x_0) to station 10 (x) for T–S waves with fixed frequency for case 2. Figure 3.25 is a similar plot showing the amplification between stations 1 and 7. (The amplification between stations 1 and 8 is not shown on this plot because of the different scales. The amplification factor for case 2 from station 1 to 8 is $\approx 40,000$.)

Figure 3.26 plots the marginal stability curves at stations 1 to 12 for case 3. Figure 3.27 plots the growth rate $-\alpha_i$ against frequency f at stations 3 to 12 for case 3. Once again the solid vertical line is the frequency of the tone and the two vertical dashed lines are the frequencies with maximum growth rate at stations 9 and 10. Figure 3.28 plots the amplification (3.48) from station 1 (x_0) to station 12 (x) for T–S waves with fixed frequency for case 3. Figure 3.29 is a similar plot showing the amplification between stations 1 and 9 (solid line) and between stations 1 and 10 (dashed line).

Figure 3.30 plots the marginal stability curves at stations 1 to 12 for case 4. Figure 3.31 plots the growth rate $-\alpha_i$ against frequency f at stations 1 to 12 for case 4. Once again the solid vertical line is the frequency of the tone and the two vertical dashed lines are the frequencies with maximum growth rate at stations 8 and 9. Figure 3.32 plots the amplification (3.48) from station 1 (x_0) to station 12 (x) for T–S waves with fixed frequency for case 4. Figure 3.33 is a similar plot showing the amplification between stations 1 and 8 (solid line) and between stations 1 and 9 (dashed line).

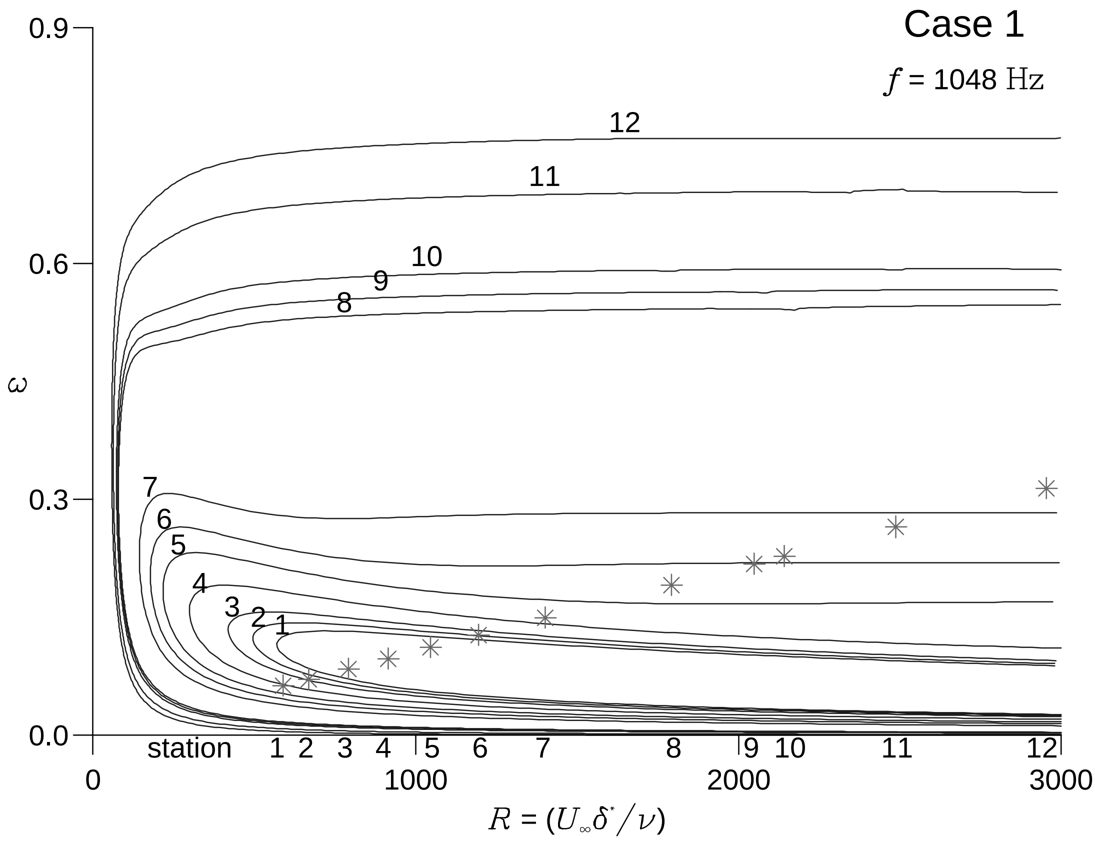

Figure 3.8: Marginal stability curves for case 1.

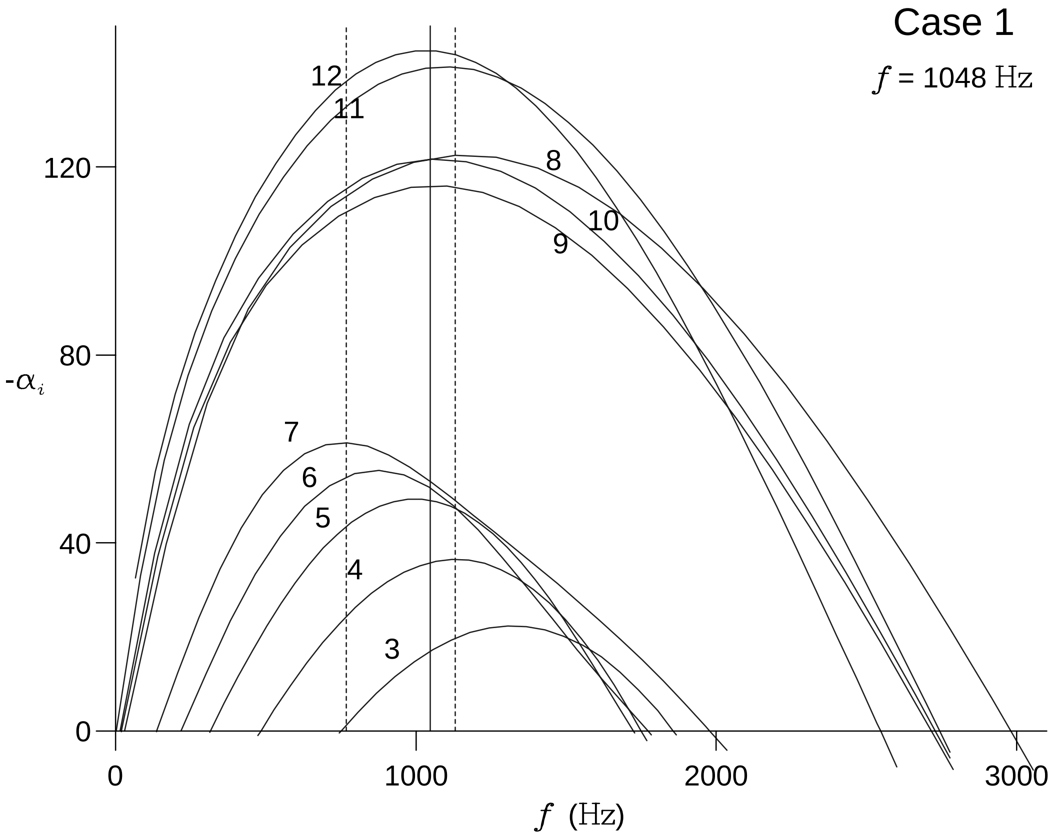

Figure 3.9: Growth rate curves for case 1.

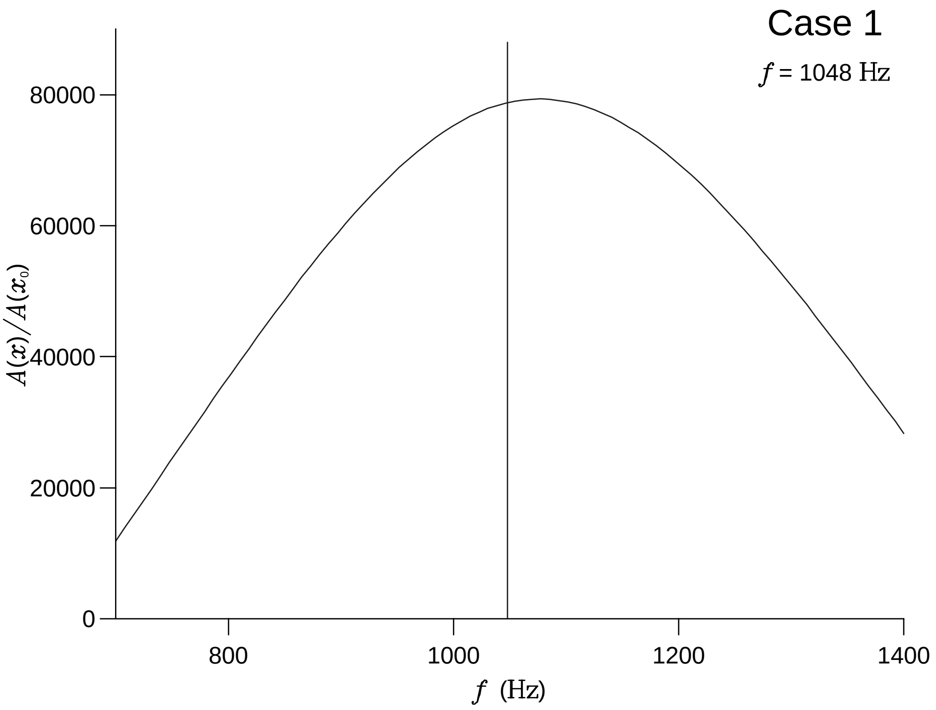

Figure 3.10: Amplification of T–S waves with fixed frequency from stations 1 to 12 for case 1.

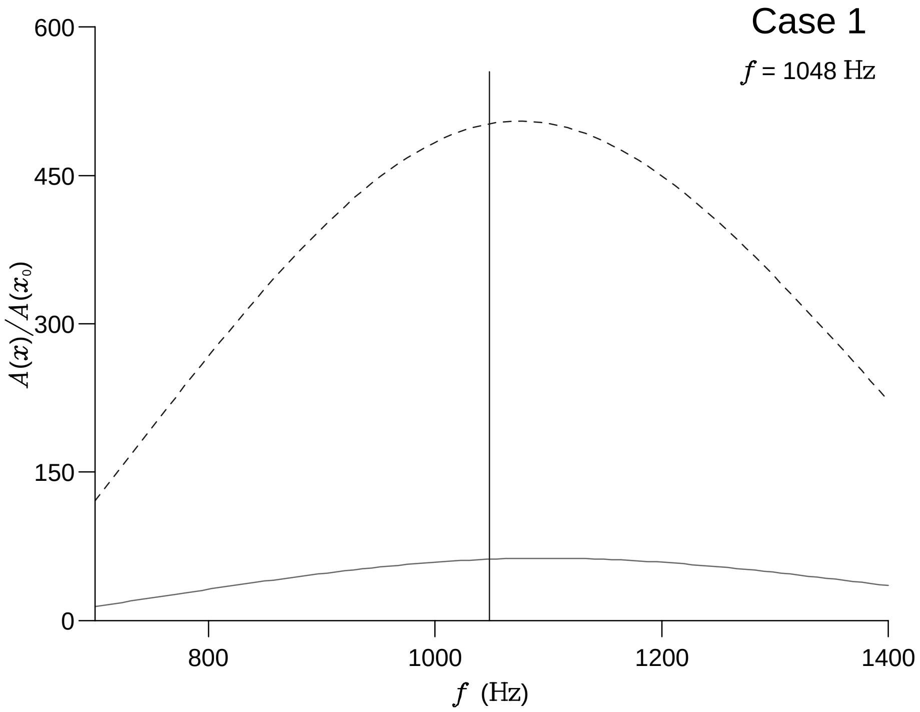

Figure 3.11: Amplification of T–S waves with fixed frequency: —— from stations 1 to 7, - - - from stations 1 to 8, for case 1.

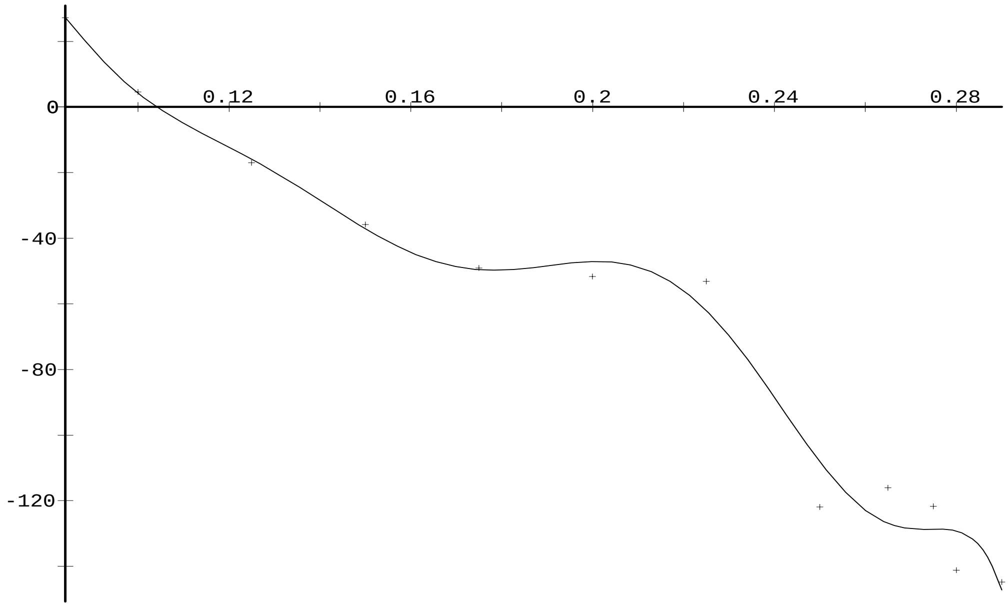

Figure 3.12: Case 1, least-squares polynomial $\alpha_i(x)$ for a T–S wave with $f = 1048\,\mathrm{Hz}$: horizontal axis — x, distance from leading edge (m), vertical axis — $\alpha_i(x)$ (m^{-1}).

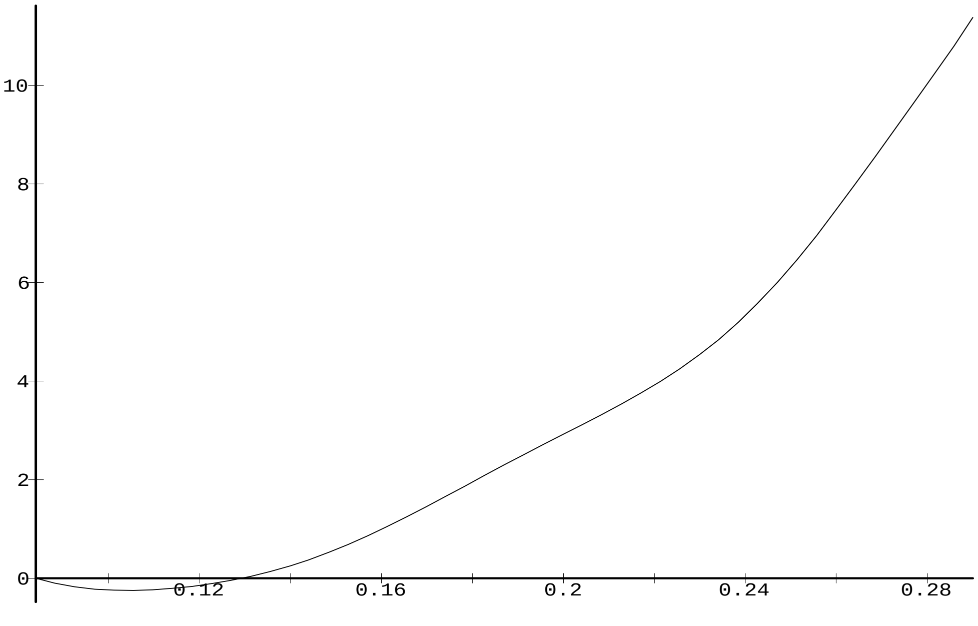

Figure 3.13: Case 1, amplification $A(x)/A(x_0)$ for a T–S wave with $f = 1048\,\mathrm{Hz}$: horizontal axis — x, distance from leading edge (m), vertical axis — ln $(A(x)/A(x_0))$.

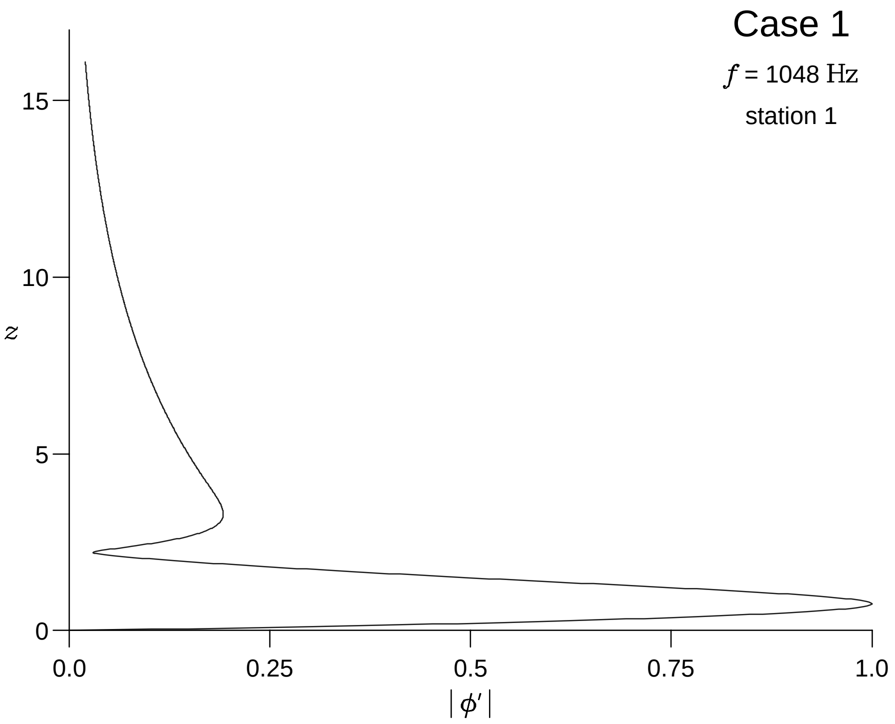

Figure 3.14: Streamwise amplitude of a T–S wave with $f = 1048\,\mathrm{Hz}$ at station 1.

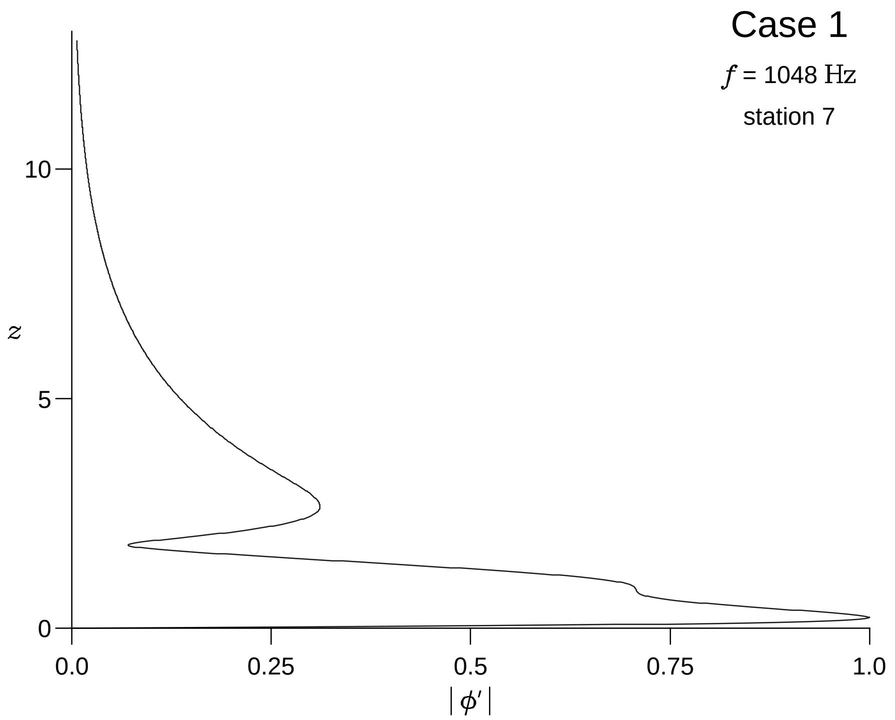

Figure 3.15: Streamwise amplitude of a T–S wave with $f = 1048\,\mathrm{Hz}$ at station 7.

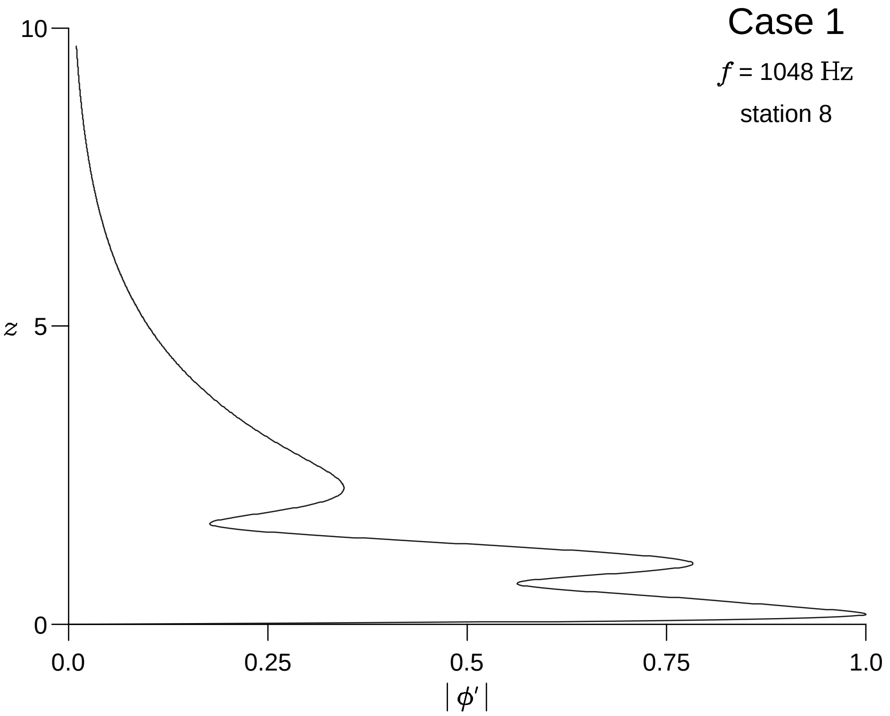

Figure 3.16: Streamwise amplitude of a T–S wave with $f = 1048\,\mathrm{Hz}$ at station 8.

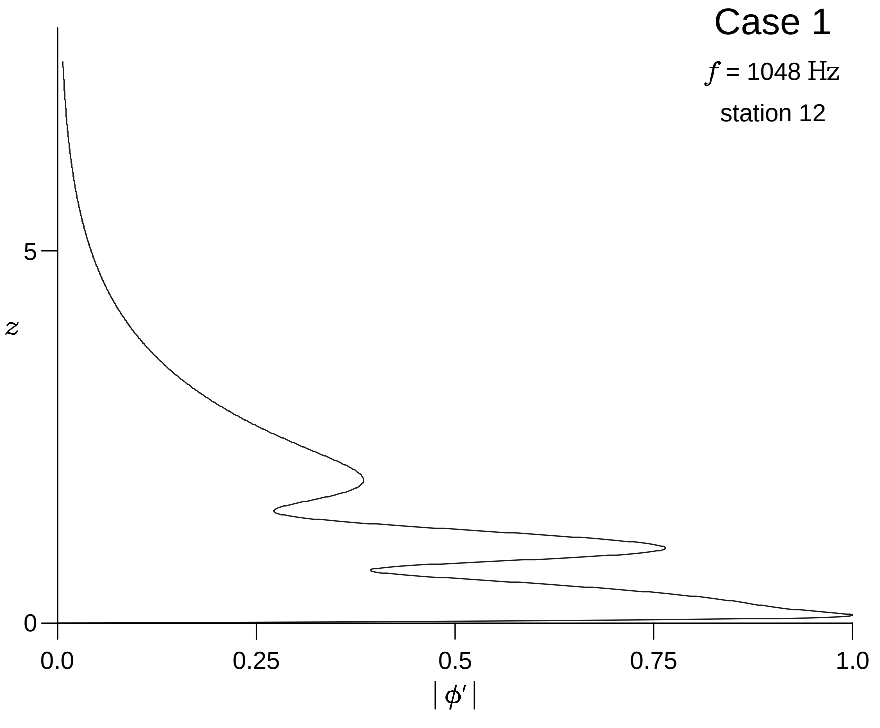

Figure 3.17: Streamwise amplitude of a T–S wave with $f = 1048\,\mathrm{Hz}$ at station 12.

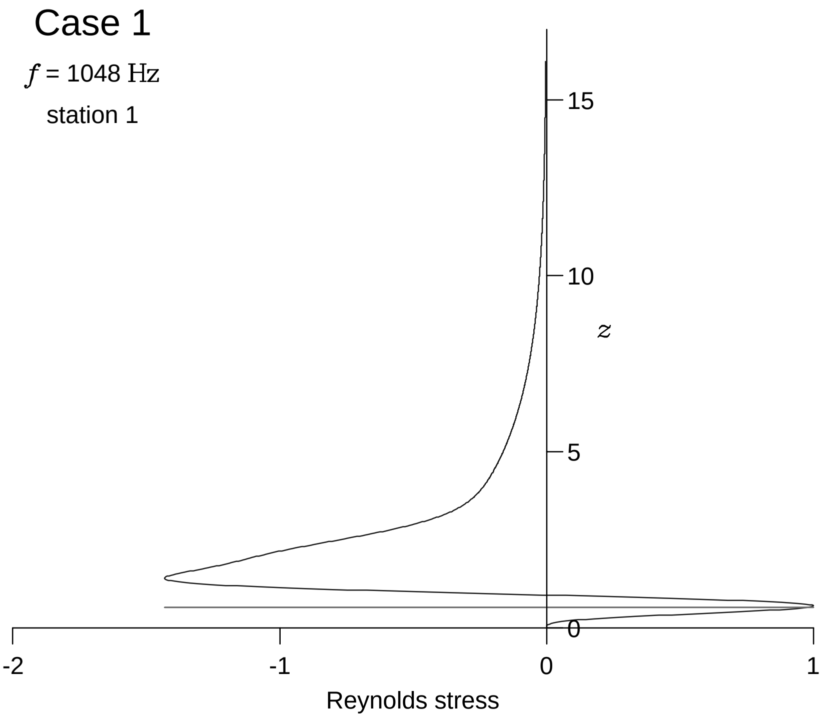

Figure 3.18: Reynolds stress for a T–S wave with $f = 1048\,\text{Hz}$ at station 1.

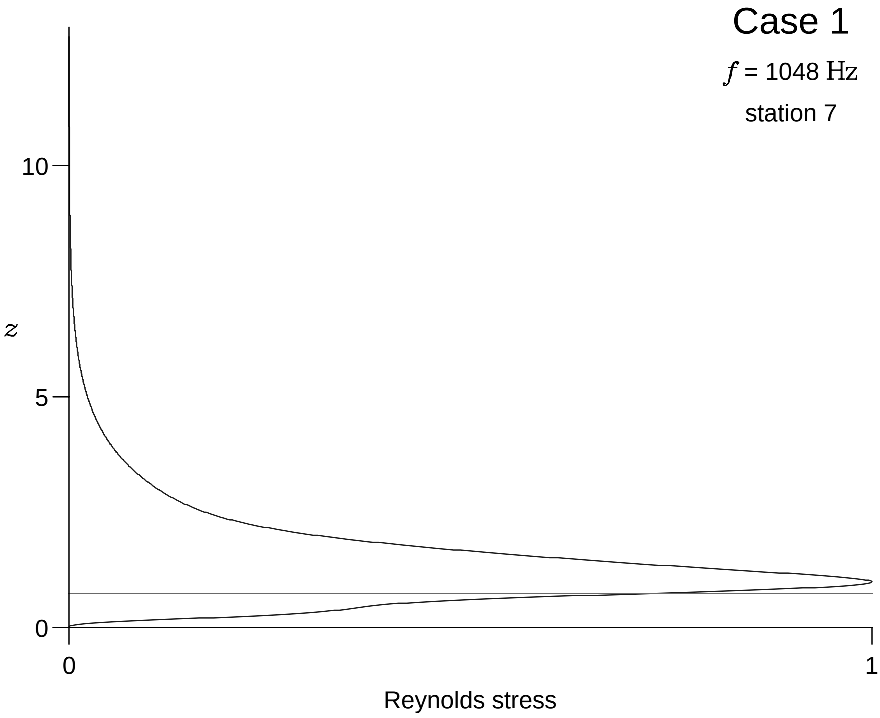

Figure 3.19: Reynolds stress for a T–S wave with $f = 1048\text{Hz}$ at station 7.

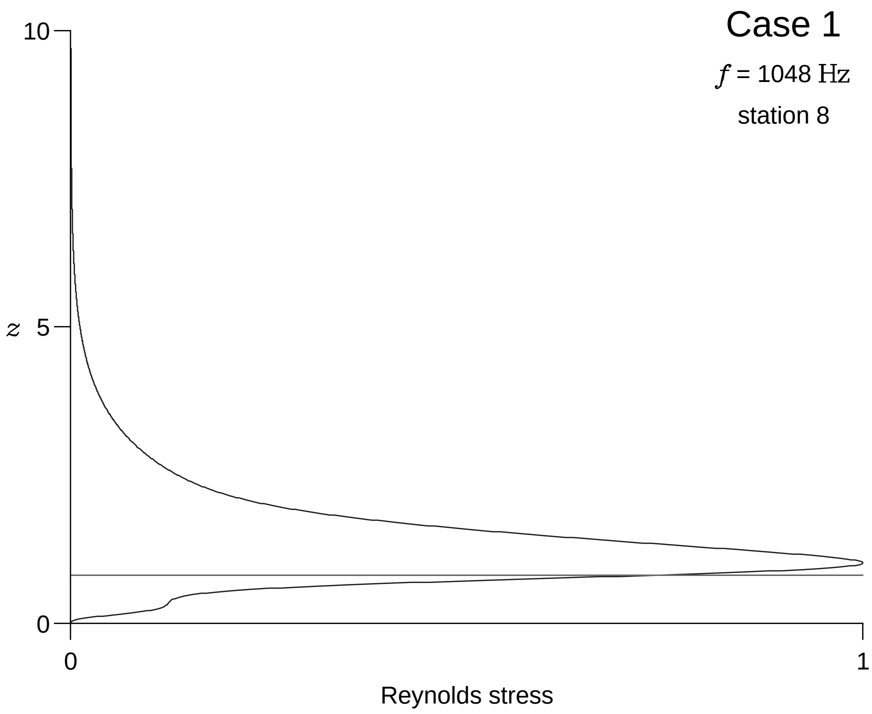

Figure 3.20: Reynolds stress for a T–S wave with $f = 1048\,\text{Hz}$ at station 8.

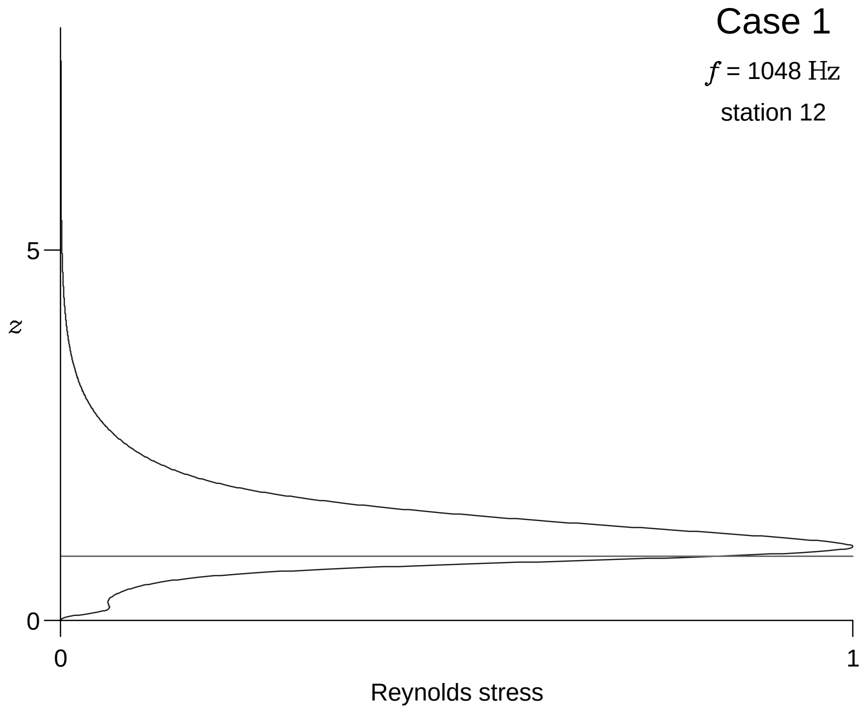

Figure 3.21: Reynolds stress for a T–S wave with $f = 1048\,\text{Hz}$ at station 12.

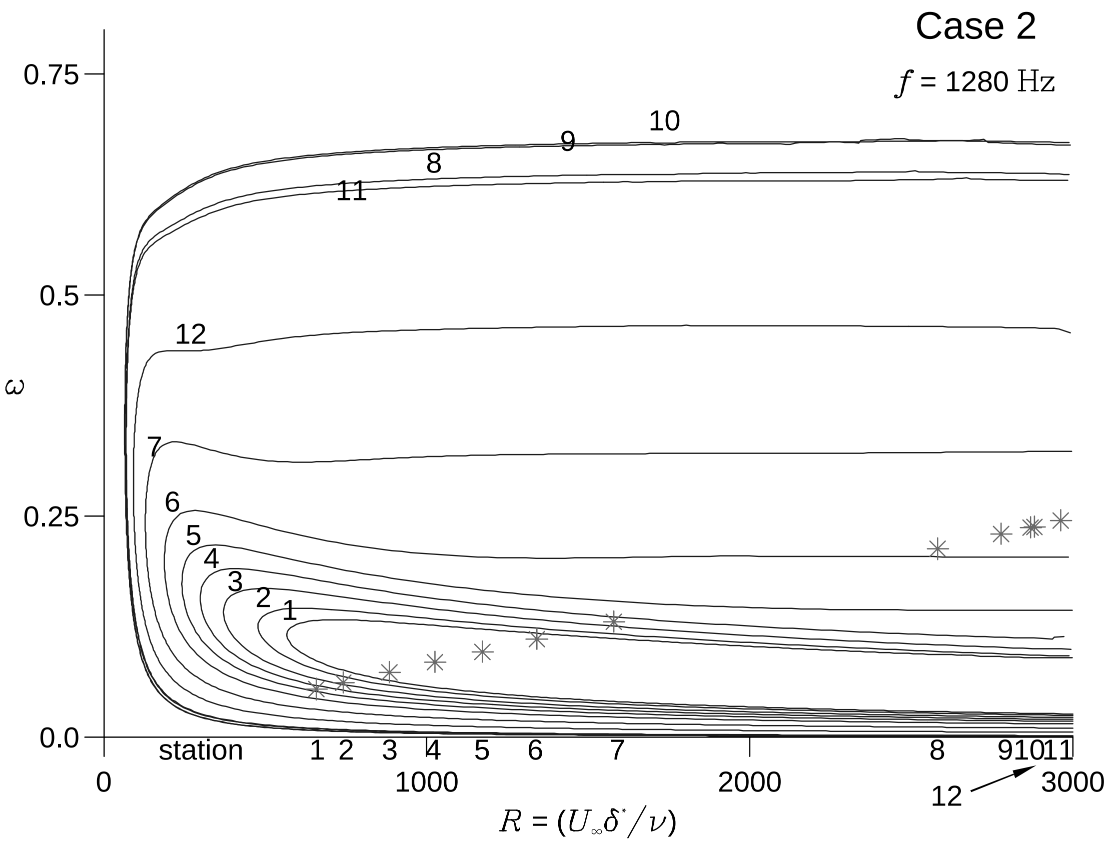

Figure 3.22: Marginal stability curves for case 2.

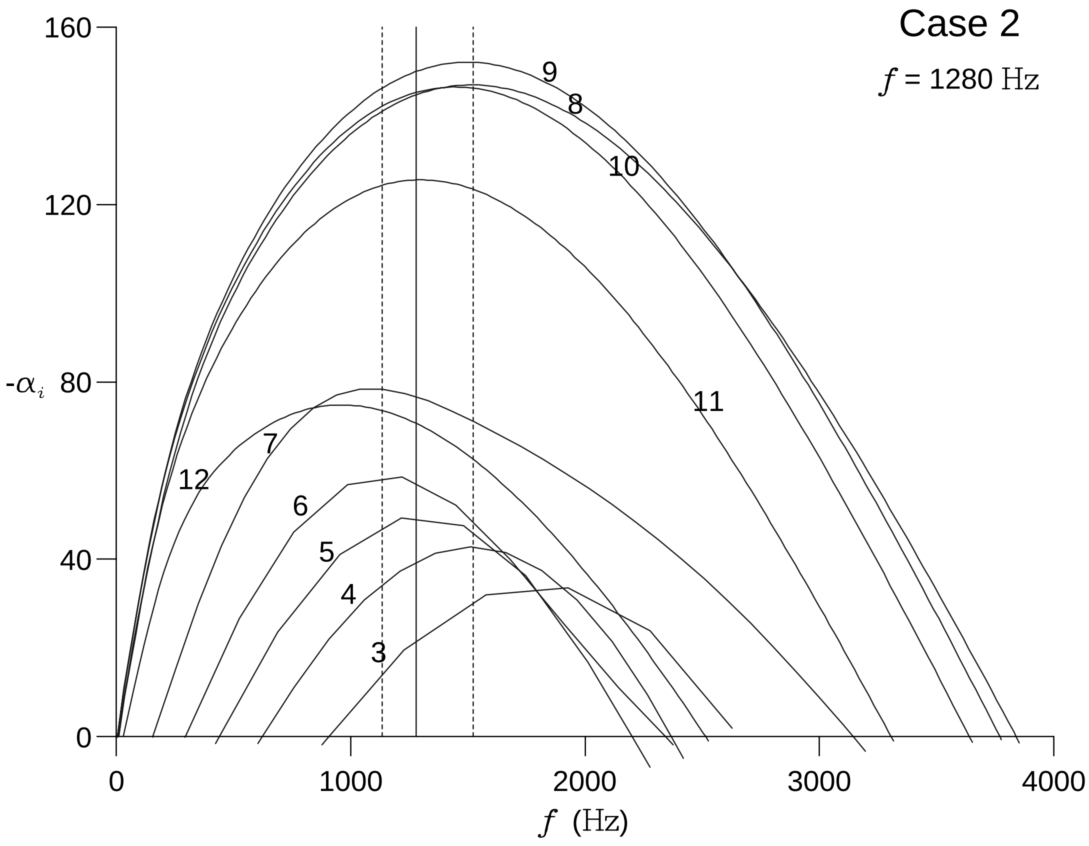

Figure 3.23: Growth rate curves for case 2.

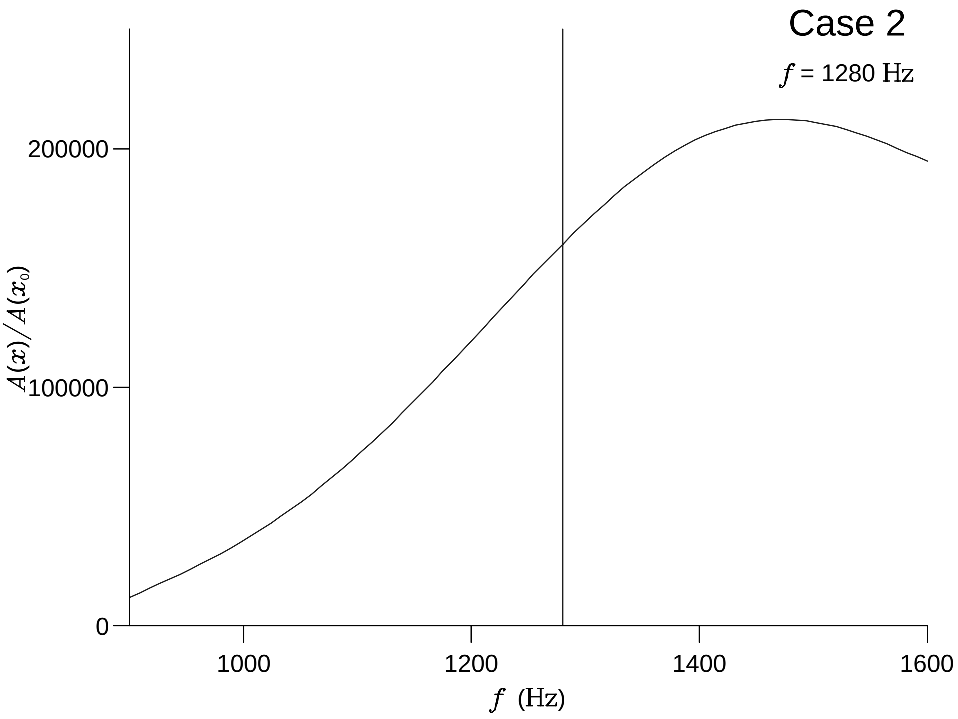

Figure 3.24: Amplification of T–S waves with fixed frequency from stations 1 to 10 for case 2.

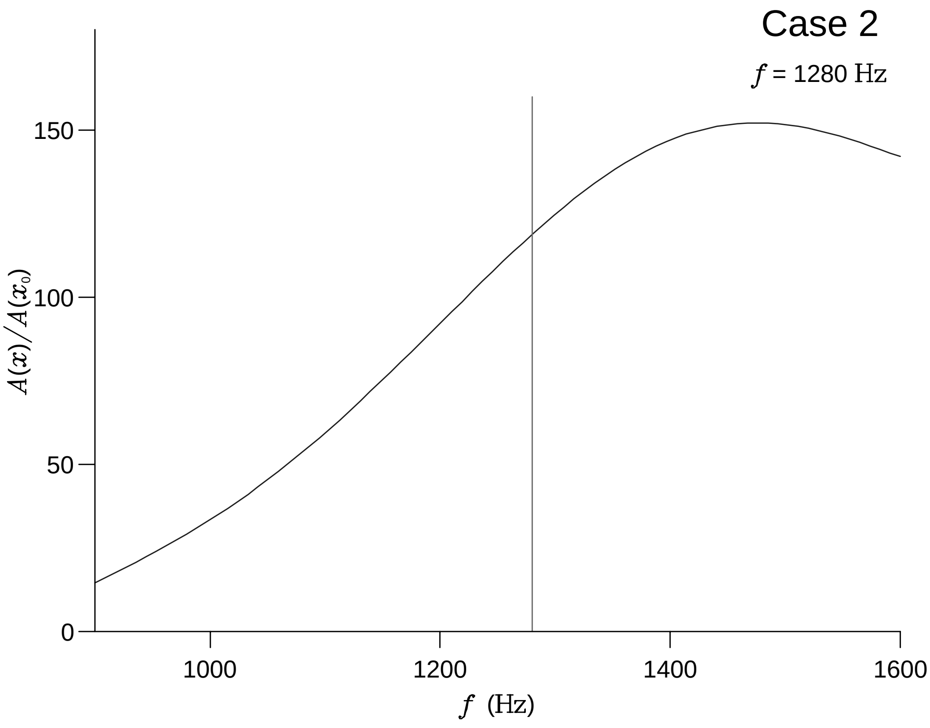

Figure 3.25: Amplification of T–S waves with fixed frequency from stations 1 to 7 for case 2.

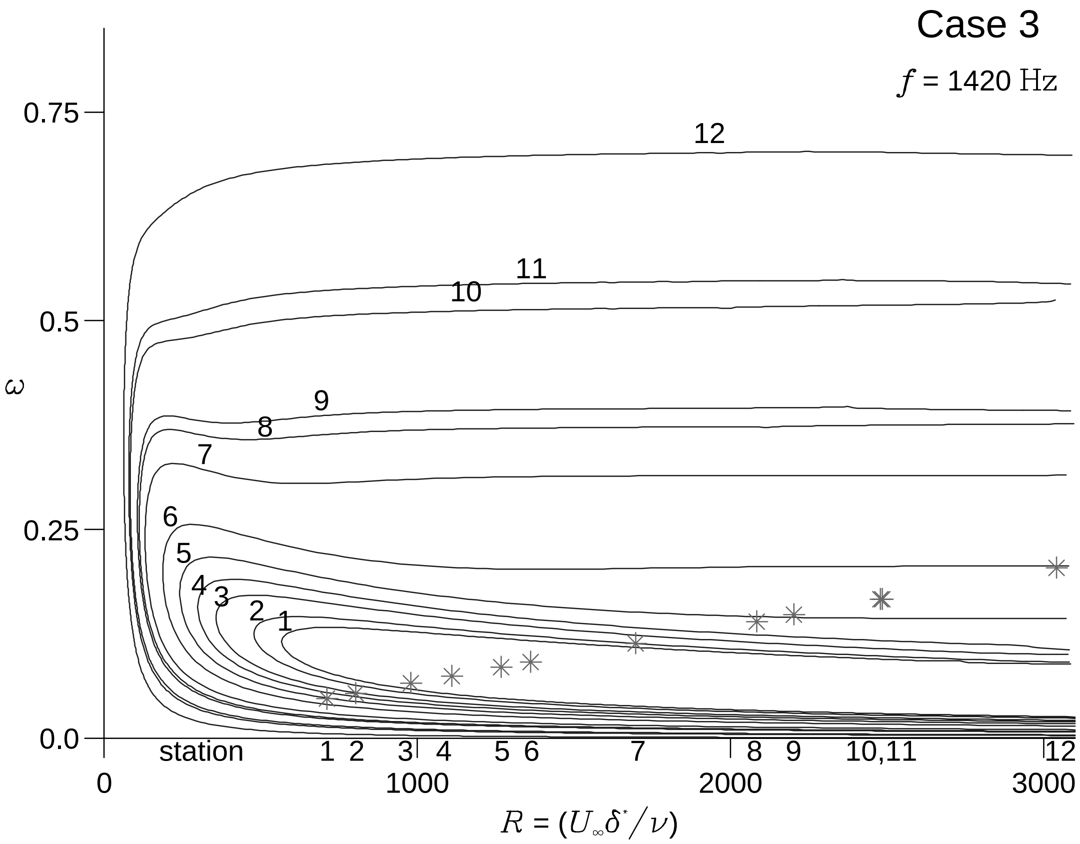

Figure 3.26: Marginal stability curves for case 3.

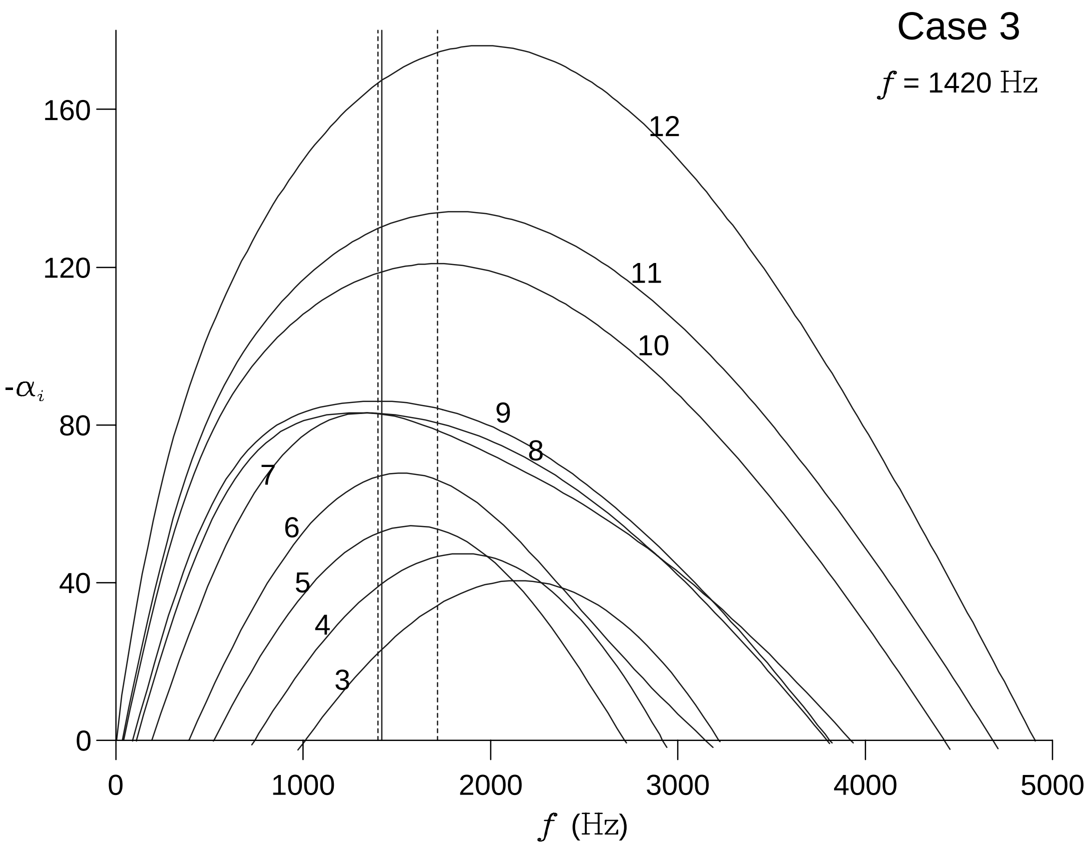

Figure 3.27: Growth rate curves for case 3.

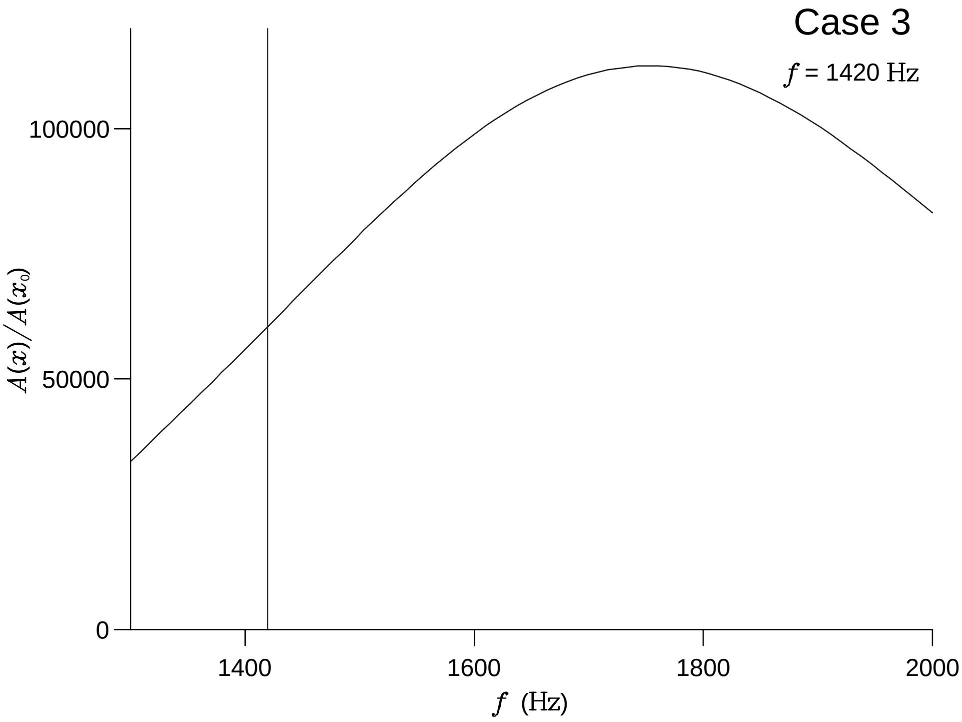

Figure 3.28: Amplification of T–S waves with fixed frequency from stations 1 to 12 for case 3.

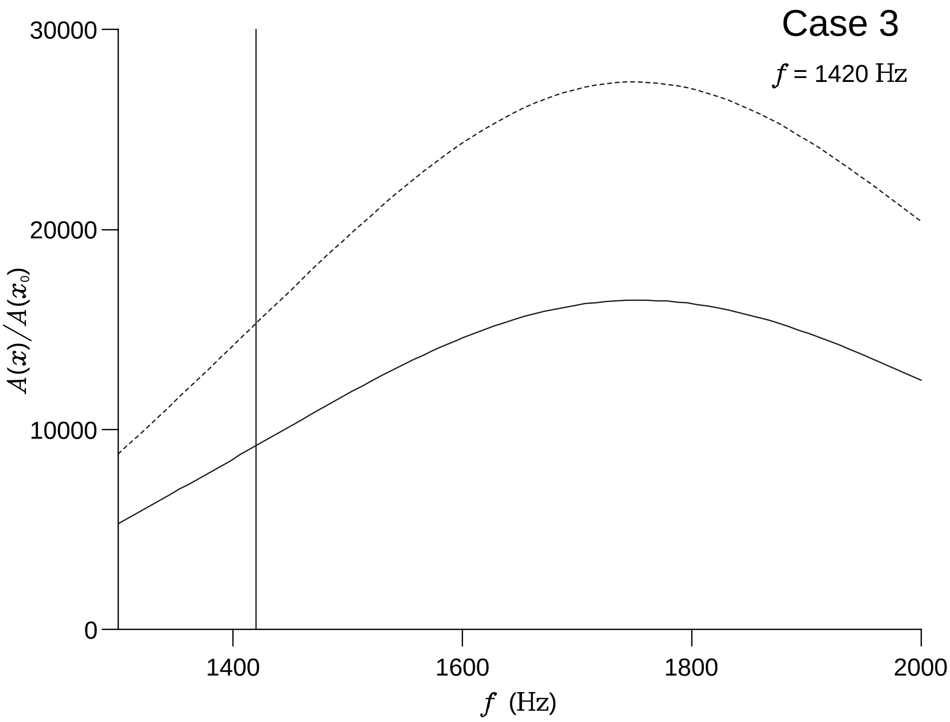

Figure 3.29: Amplification of T–S waves with fixed frequency: —— from stations 1 to 9, - - - from stations 1 to 10, for case 3.

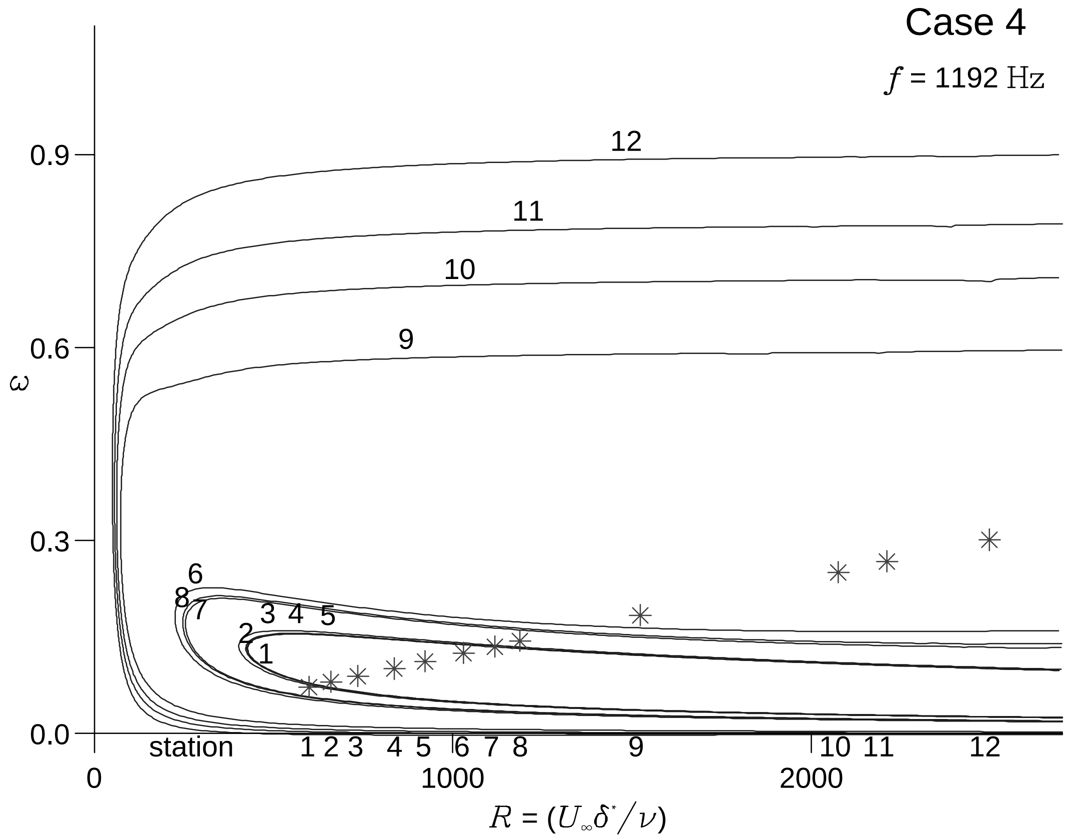

Figure 3.30: Marginal stability curves for case 4.

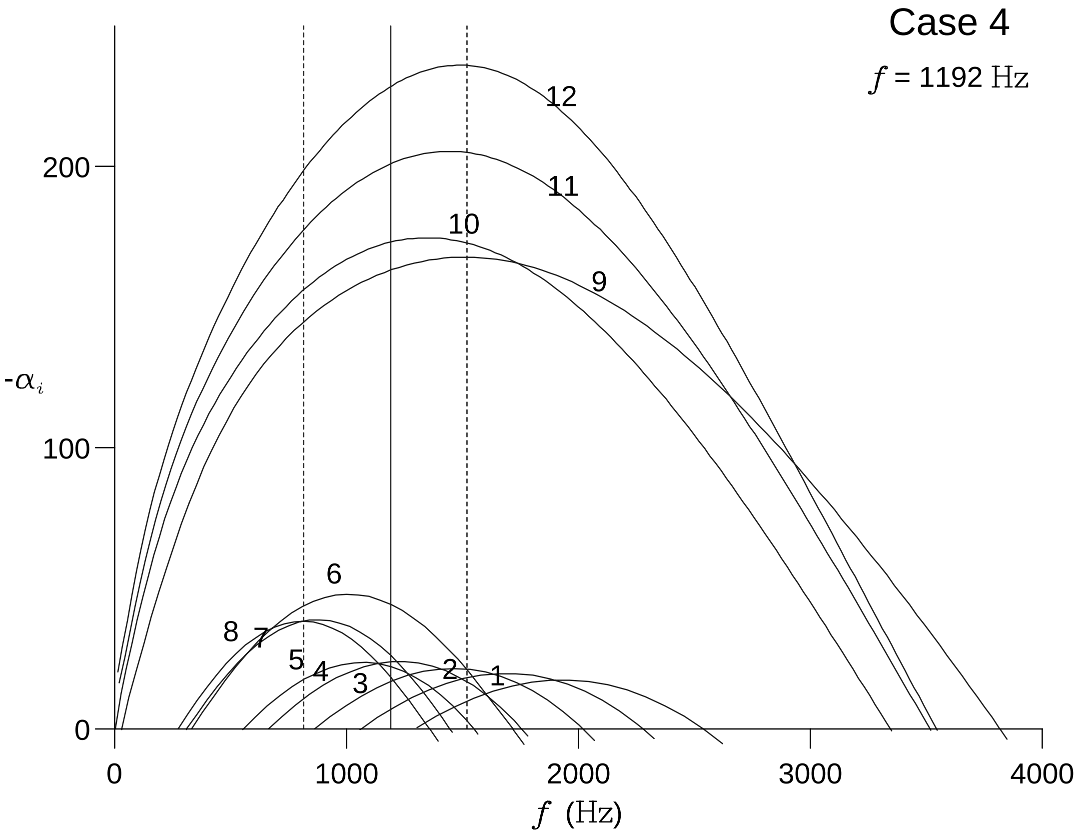

Figure 3.31: Growth rate curves for case 4.

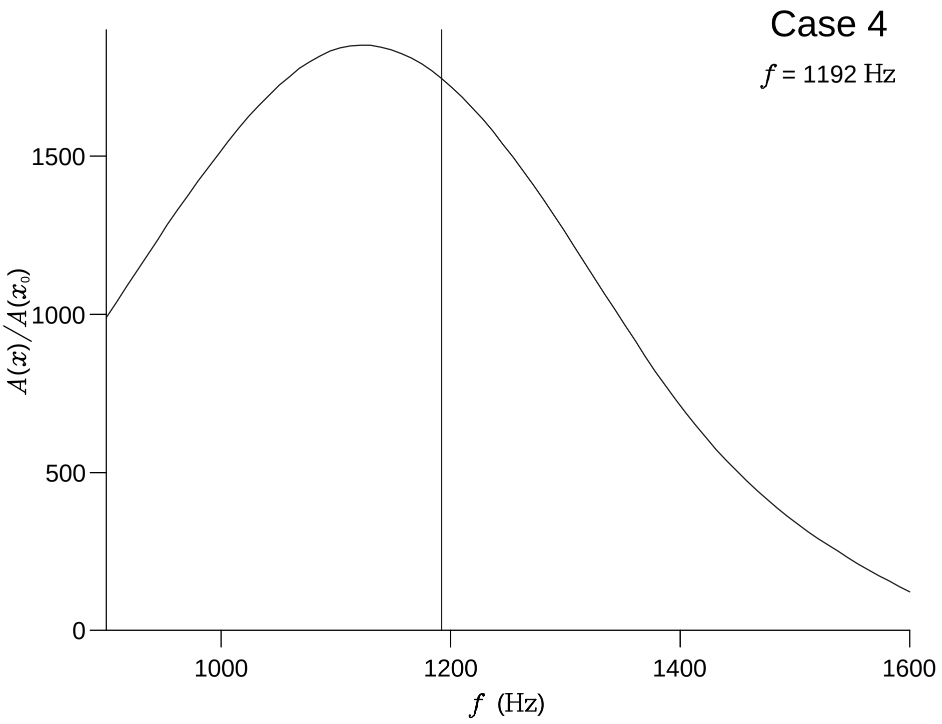

Figure 3.32: Amplification of T–S waves with fixed frequency from stations 1 to 12 for case 4.

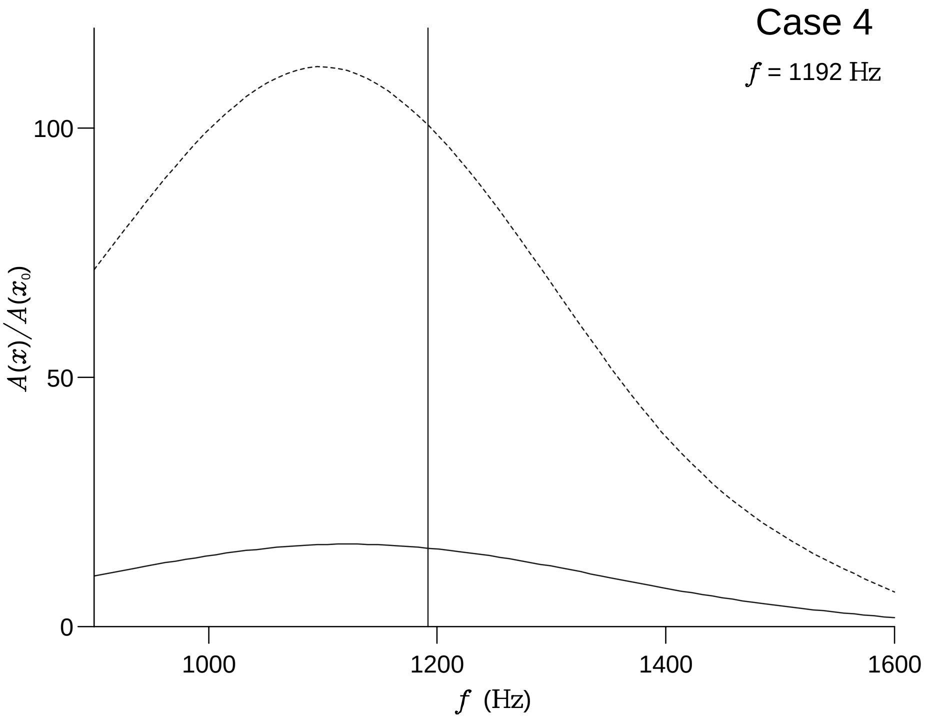

Figure 3.33: Amplification of T–S waves with fixed frequency: —— from stations 1 to 8, - - - stations 1 to 9, for case 4.

3.5.2 No-tone case 5

Figure 3.34 plots the marginal stability curves at stations 1 to 12 for case 5. Figure 3.35 plots the growth rate $-\alpha_i$ against frequency f at stations 3 to 12 for case 5. Figure 3.42 plots the amplification (3.48) from station 3 (x_0) to station 12 (x) for T–S waves with fixed frequency for case 5. The growth was only calculated from station 3 because at stations 1 and 2 the flow was stable to all modes. Figures 3.36 — 3.39 plot the development of $|\phi'(z)|$ over the NACA 0012 aerofoil for a T–S wave with frequency 150 Hz, the approximate frequency of maximum growth from figure 3.42.

3.5.3 No-tone case 6

Figure 3.40 plots the marginal stability curves at stations 1 to 12 for case 6. Although no tones were detected for case 6, the asterisks denote the location in the $(R_{\delta^\star}, \omega)$-plane of a T–S wave, with frequency 542 Hz, at the twelve stations along the aerofoil. This is the frequency observed in the frequency spectrum for case 6, see figure 2.17(a). Figure 3.41 plots the growth rate $-\alpha_i$ against frequency f at stations 1 to 12 for case 6. The solid vertical line is the frequency 542 Hz. Figure 3.43 plots the amplification (3.48) from station 1 (x_0) to station 12 (x) for T–S waves with fixed frequency for case 6.

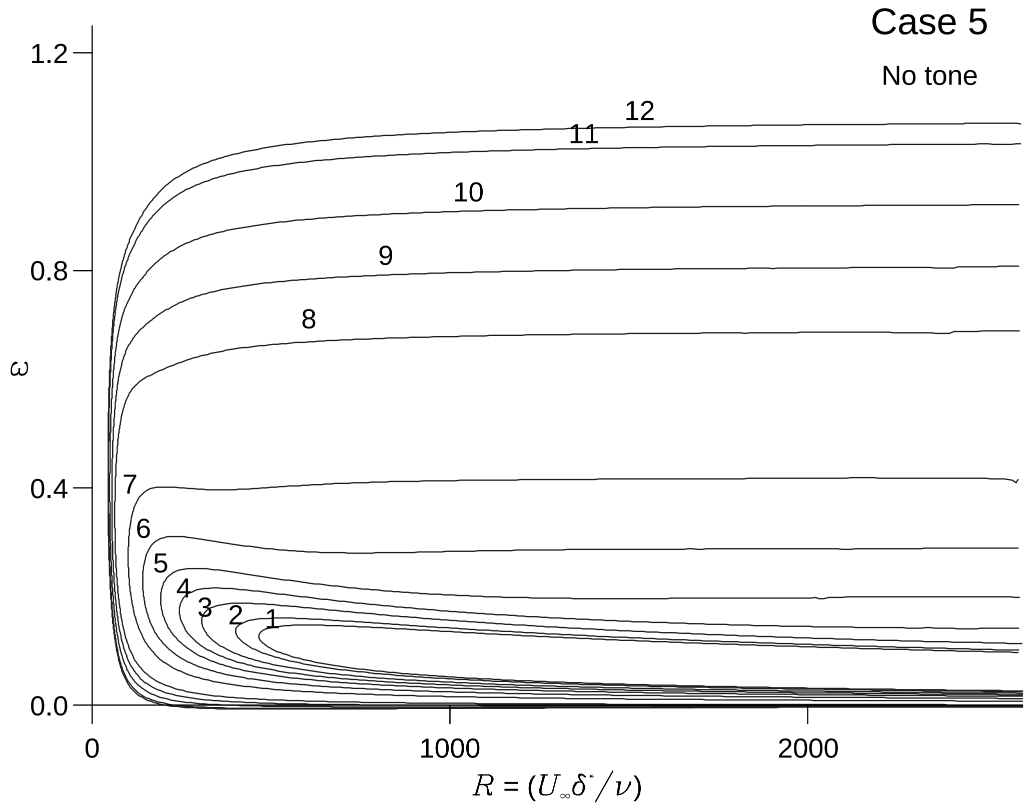

Figure 3.34: Marginal stability curves for case 5.

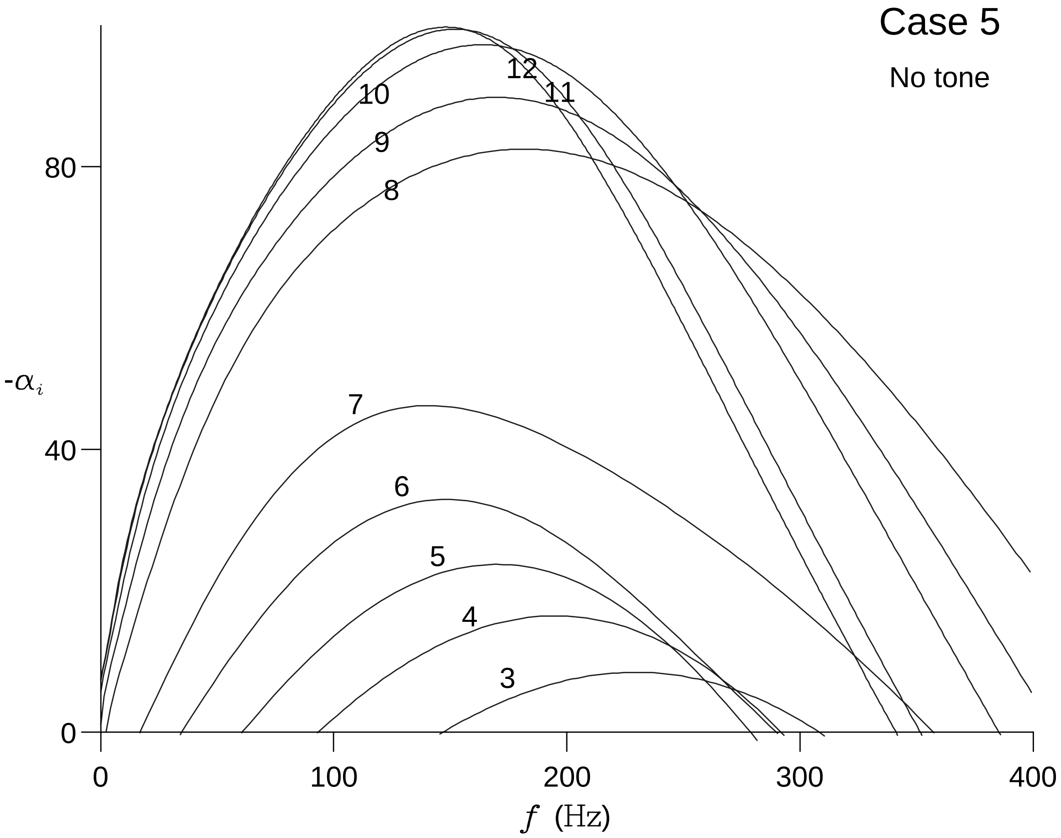

Figure 3.35: Growth rate curves for case 5.

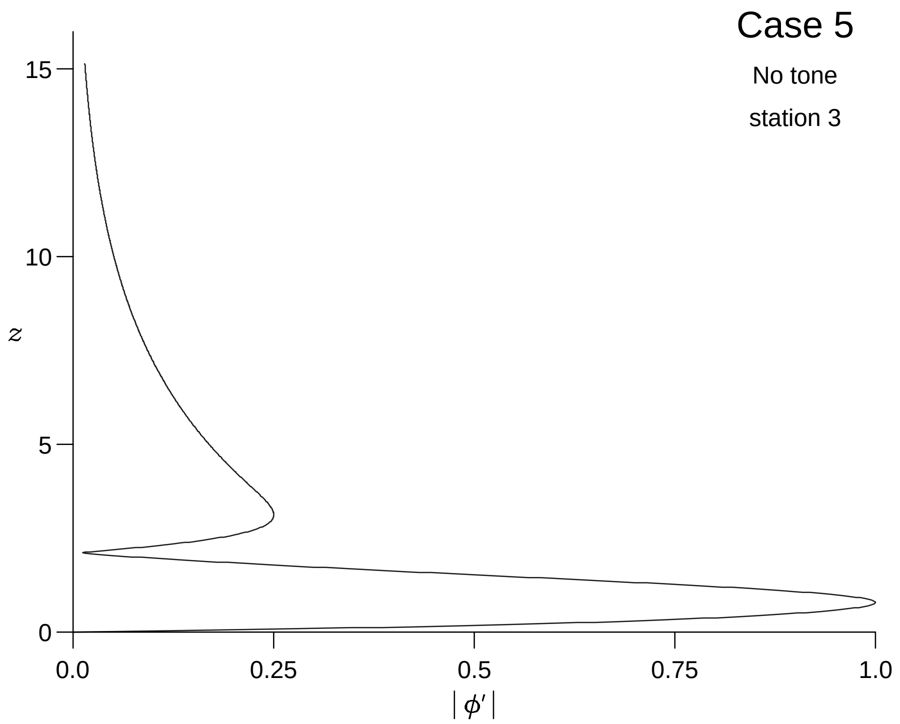

Figure 3.36: Streamwise amplitude of a T–S wave with $f = 150\,\text{Hz}$ at station 3.

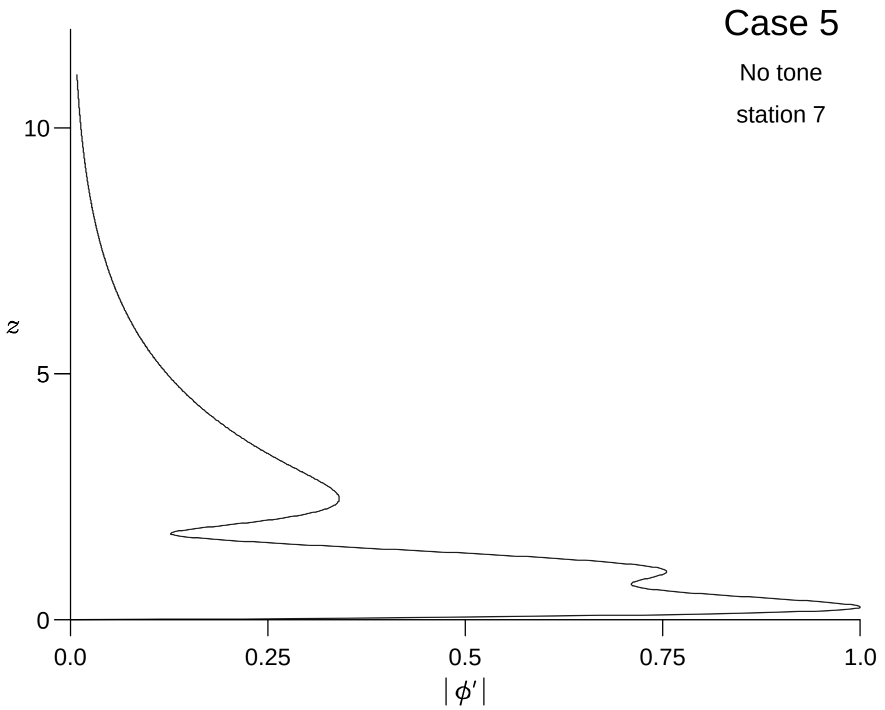

Figure 3.37: Streamwise amplitude of a T–S wave with $f = 150\,\text{Hz}$ at station 7.

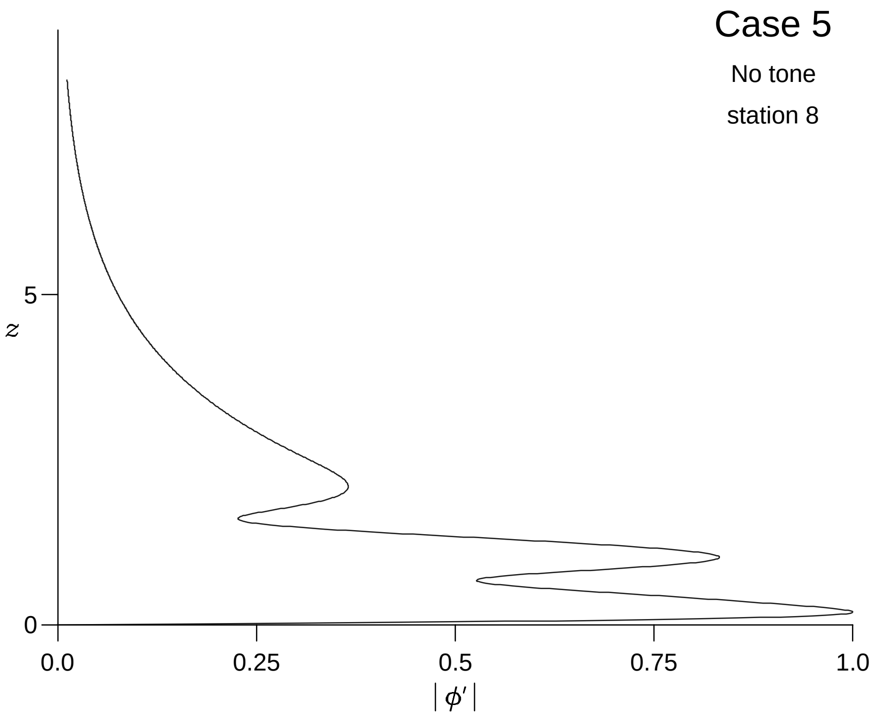

Figure 3.38: Streamwise amplitude of a T–S wave with $f = 150\,\text{Hz}$ at station 8.

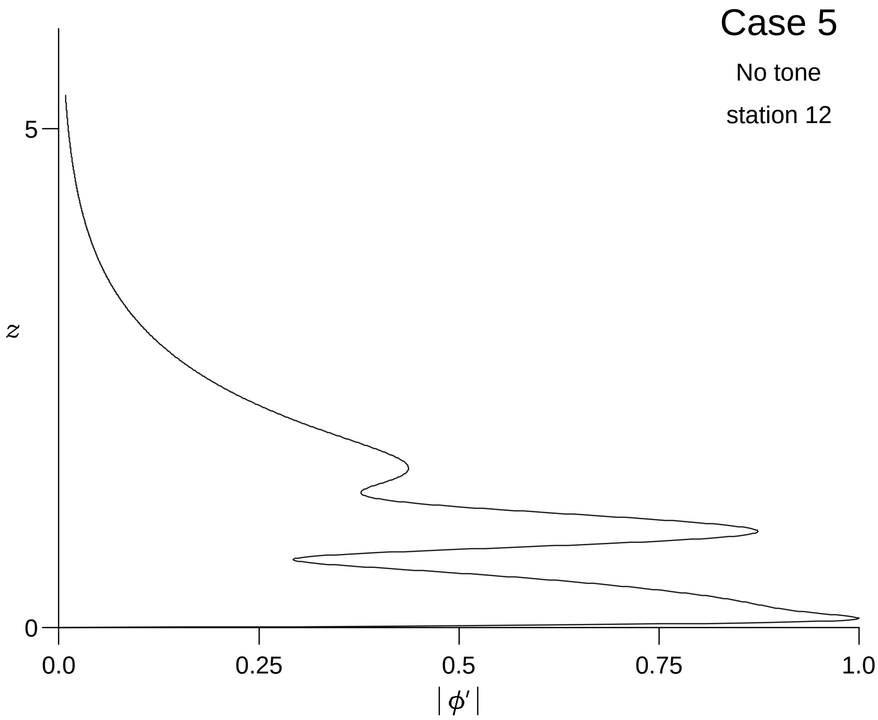

Figure 3.39: Streamwise amplitude of a T–S wave with $f = 150\,\text{Hz}$ at station 12.

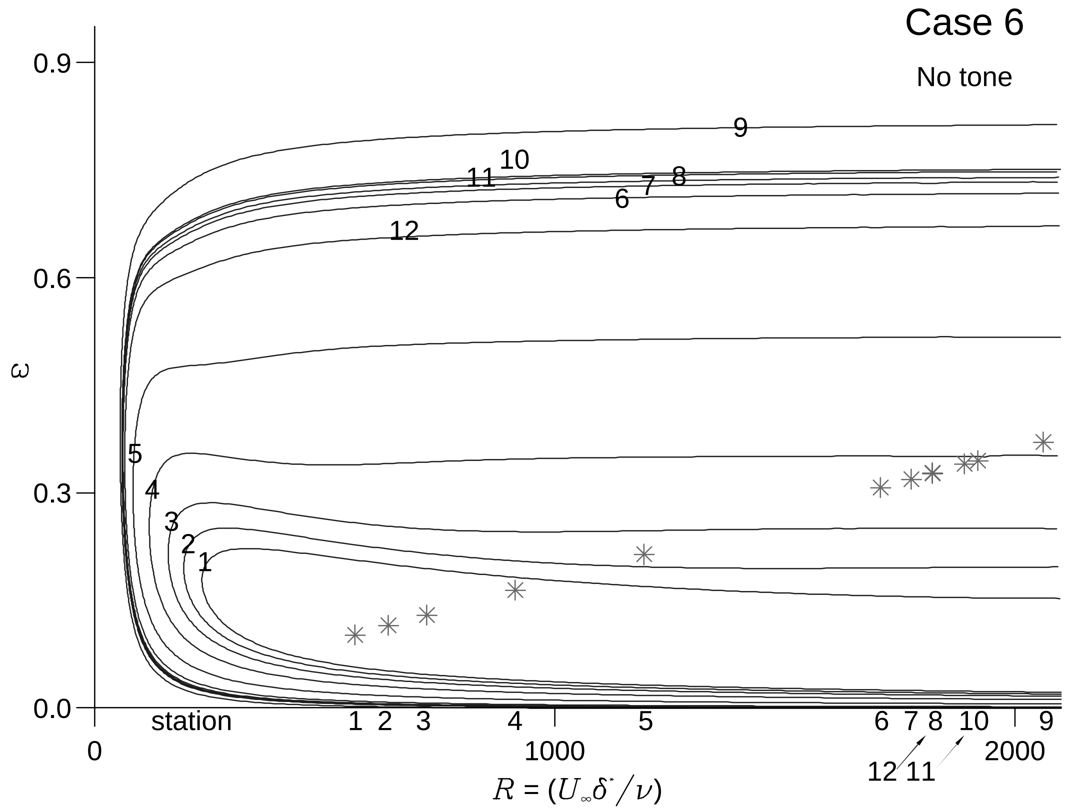

Figure 3.40: Marginal stability curves for case 6.

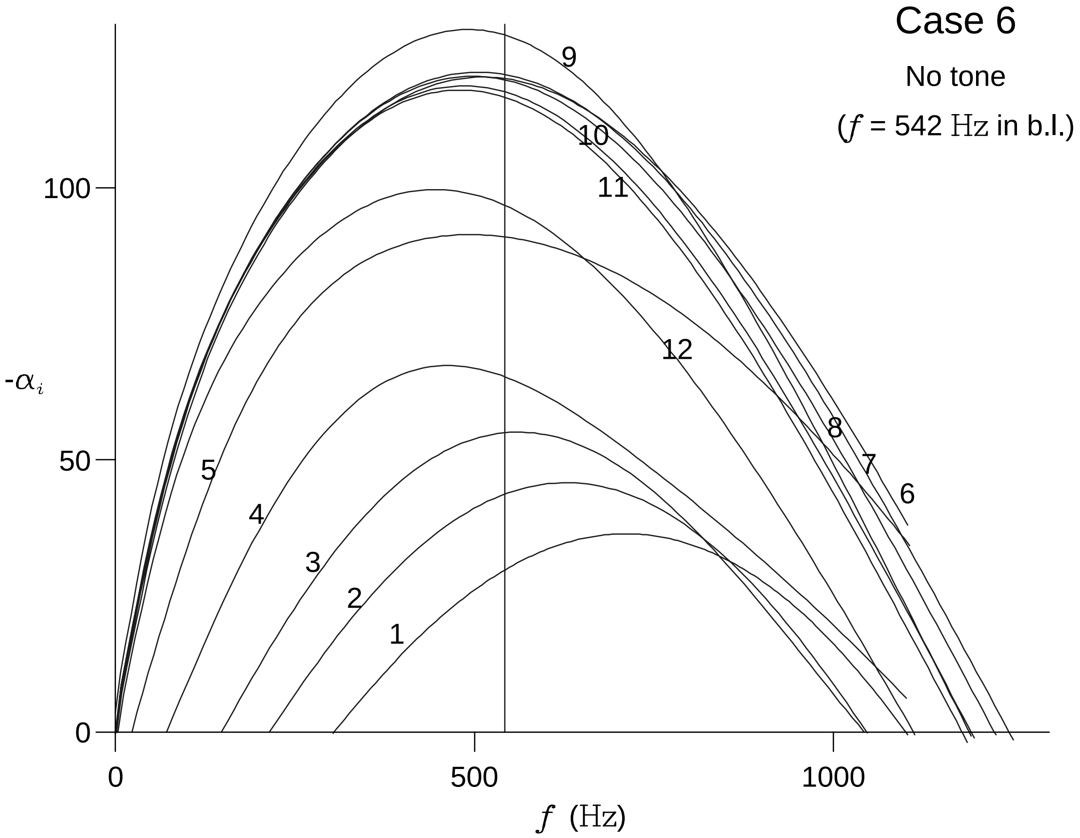

Figure 3.41: Growth rate curves for case 6.

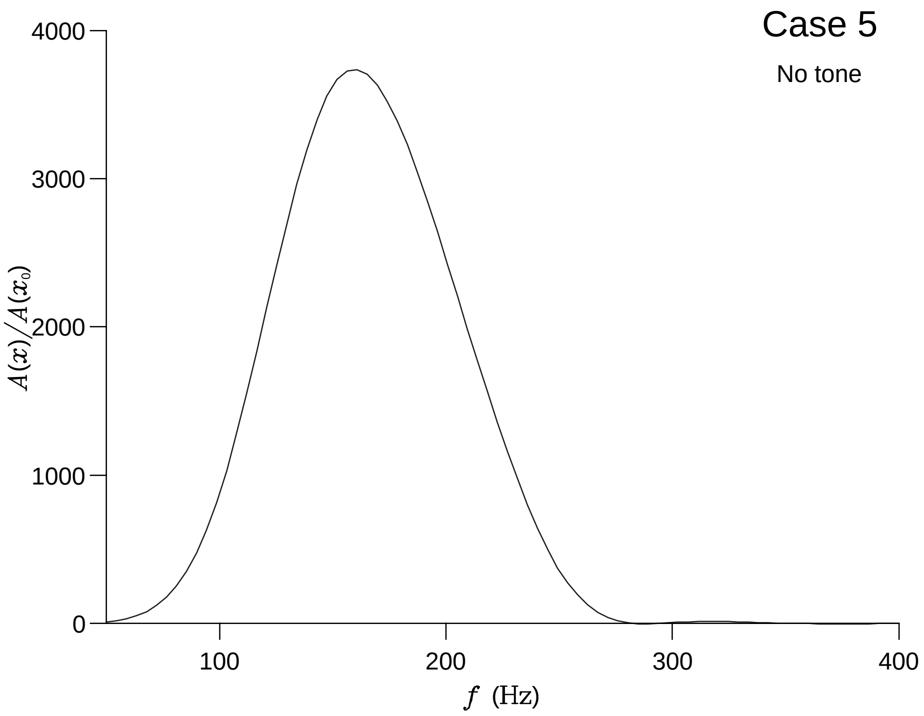

Figure 3.42: Amplification of T–S waves with fixed frequency from stations 3 to 12 for case 5.

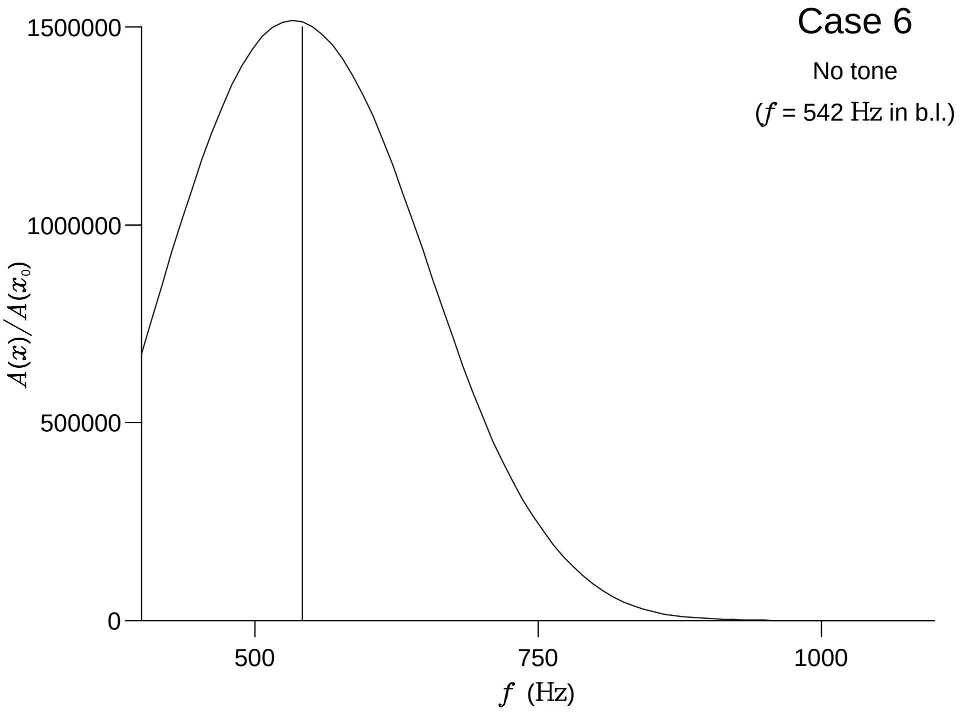

Figure 3.43: Amplification of T–S waves with fixed frequency from stations 1 to 12 for case 6.

3.5.4 Quasi-parallel approximation

The method followed assumed the flow over the majority of the aerofoil was approximately parallel. The inherent assumption of the Orr–Sommerfeld analysis was that the basic flow (at a specific station) extended unchanged over $-\infty < x < \infty$. The relevant length scale was assumed to be the wavelength of a T–S wave. The quasi-parallel approximation assumes that over one wavelength the basic flow is unchanged. The T–S waves calculated had slowly varying wavelengths over the aerofoil. With increasing wavelength the quasi-parallel approximation may become invalid at some stations on the aerofoil.

Results are presented for cases 1, 2 and 3 for T–S waves at the frequency of the tonal noise, 1048 Hz, 1280 Hz and 1420 Hz respectively. At each station the displacement thickness $\delta^\star$ was taken to be a measure of the boundary layer. The 'change' in the boundary layer with distance downstream was taken to be represented by the 'change' in $\delta^\star$.

At each station the wavelength λ of the least stable mode, at the frequency of the tone, was calculated. Then a least-squares polynomial was fitted through the λ and $\delta^\star$ points at each station to obtain polynomial expressions $\lambda(x)$ and $\delta^\star(x)$. The curves $\lambda(x)$ and $\delta^\star(x)$ are shown for cases 1, 2 and 3 in figures 3.44, 3.45, 3.47, 3.48, 3.50 and 3.51 respectively. For all three cases the wavelength λ varied between approximately 10 and 12 mm with distance downstream. Similarly the displacement thickness $\delta^\star$ varied between approximately 0.3 mm and 1.2 mm. In all three cases the wavelength and displacement thickness were found to increase slowly with distance downstream.

By using the polynomial expressions $\lambda(x)$ and $\delta^\star(x)$, the 'change' in the boundary layer over one wavelength was expressed as

$$\frac{\delta^\star(x+\lambda(x))-\delta^\star(x)}{\delta^\star(x)} \times 100\,, \tag{3.94}$$

where (3.94) measures the percentage growth of the displacement thickness over one wavelength at a point x.

For case 1 the growth of $\delta^\star$ was $\approx 10\%$ over one wavelength until 40 mm from the trailing edge when the growth increased to over 20%. A change of 10% represents an increase of $\approx 0.05\,\mathrm{mm}$ in $\delta^\star$ over one wavelength for this case. For cases 2 and 3, $\delta^\star(x)$ started to decrease close to the trailing edge. This suggests the onset of transition. It is clear that the validity of approximating a transitional flow by a laminar flow with the same shape factor is highly questionable. However, once again the growth is $O(10\%)$ until approximately $40\,\mathrm{mm}$ from the trailing edge.

In each case the quasi-parallel approximation appears to be reasonable until about $40\,\mathrm{mm}$ upstream of the trailing edge of the aerofoil. This approximately coincides with the flow separation on the aerofoil. After flow separation the profiles 'change' more rapidly.

The validity of the calculations close to the trailing edge of the aerofoil are indeed questionable. However, the quasi-parallel approximation is assumed to be reasonable over the majority of the aerofoil. In §3.6.1 the tonal frequency is shown to be 'selected' just before flow separation. The frequency may be predicted by considering the amplification up to approximately station 7 in most cases. The quasi-parallel approximation certainly appears valid until *after* the tonal frequency has been 'selected'.

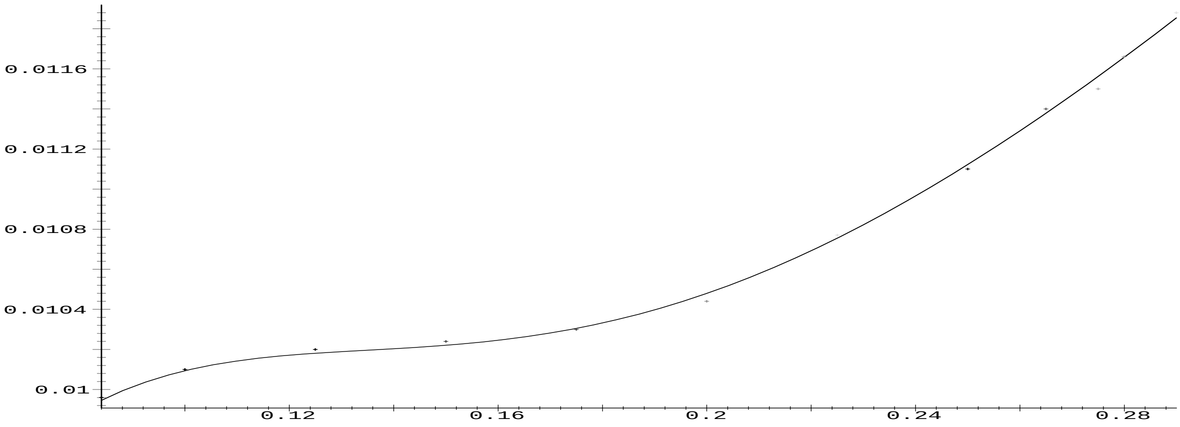

Figure 3.44: Wavelength $\lambda(x)$ of a T–S wave with $f = 1048\,\text{Hz}$ for case 1: horizontal axis — x, distance from leading edge (m), vertical axis — $\lambda(x)$ (m).

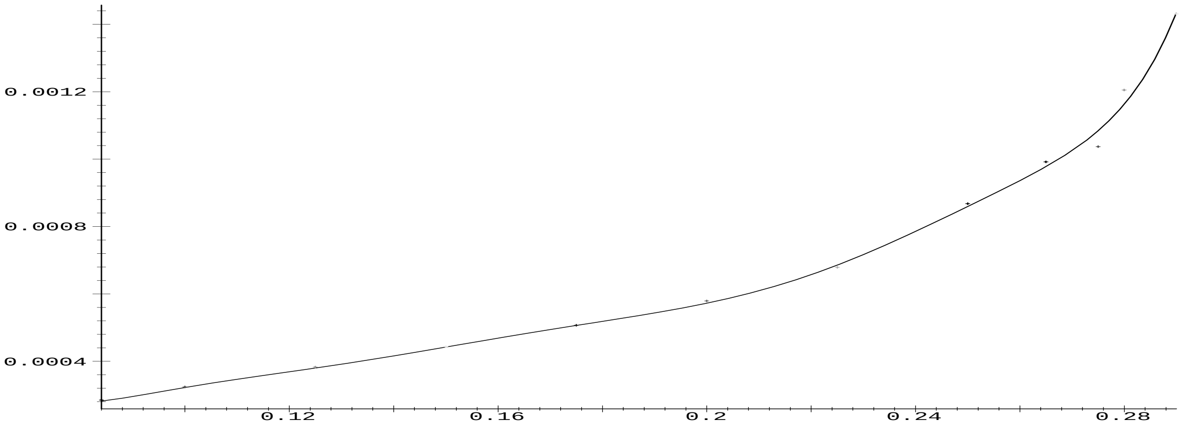

Figure 3.45: Displacement thickness $\delta^\star(x)$ of the boundary layer for case 1: horizontal axis — x, distance from leading edge (m), vertical axis — $\delta^\star$ (m).

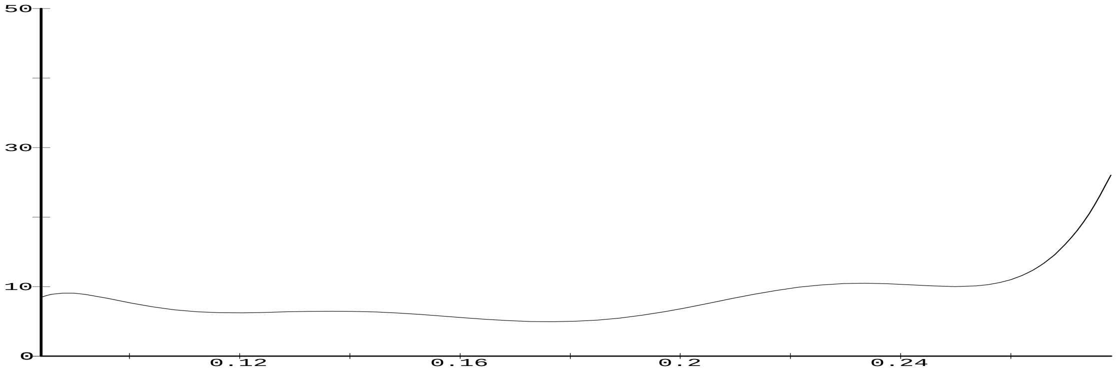

Figure 3.46: Growth of boundary layer over one T–S wavelength with $f = 1048\,\text{Hz}$ for case 1: horizontal axis — distance from leading edge (m), vertical axis — percentage growth.

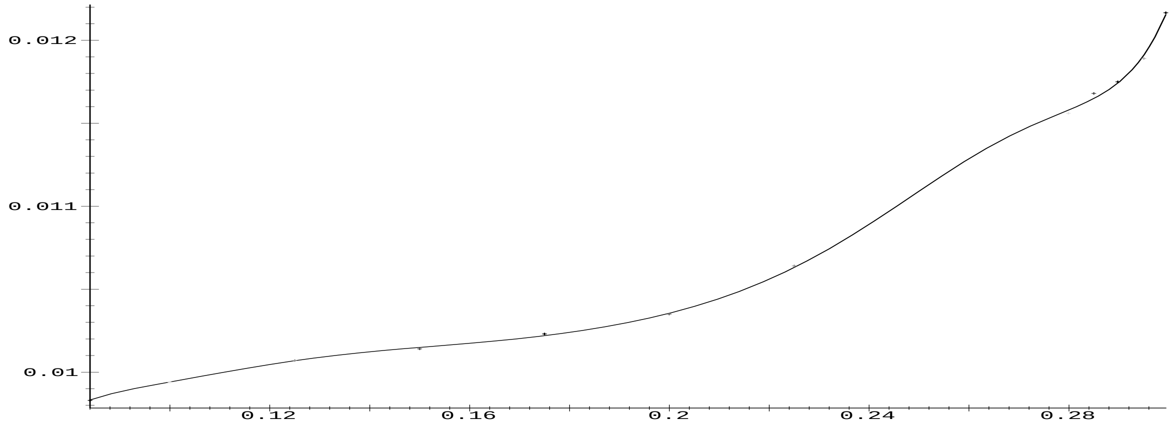

Figure 3.47: Wavelength $\lambda(x)$ of a T–S wave with $f = 1280\,\text{Hz}$ for case 2: horizontal axis — x, distance from leading edge (m), vertical axis — $\lambda(x)$ (m).

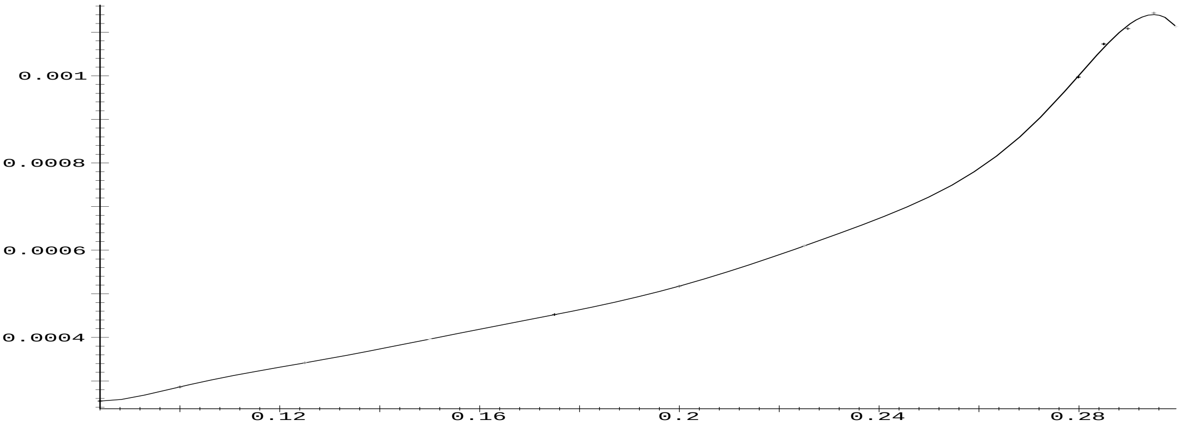

Figure 3.48: Displacement thickness $\delta^\star(x)$ of the boundary layer for case 2: horizontal axis — x, distance from leading edge (m), vertical axis — $\delta^\star$ (m).

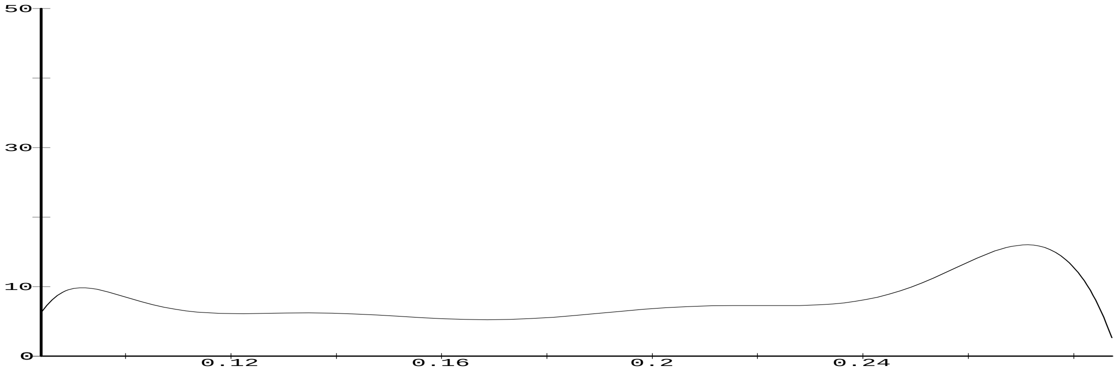

Figure 3.49: Growth of boundary layer over one T–S wavelength with $f = 1280\,\text{Hz}$ for case 2: horizontal axis — distance from leading edge (m), vertical axis — percentage growth.

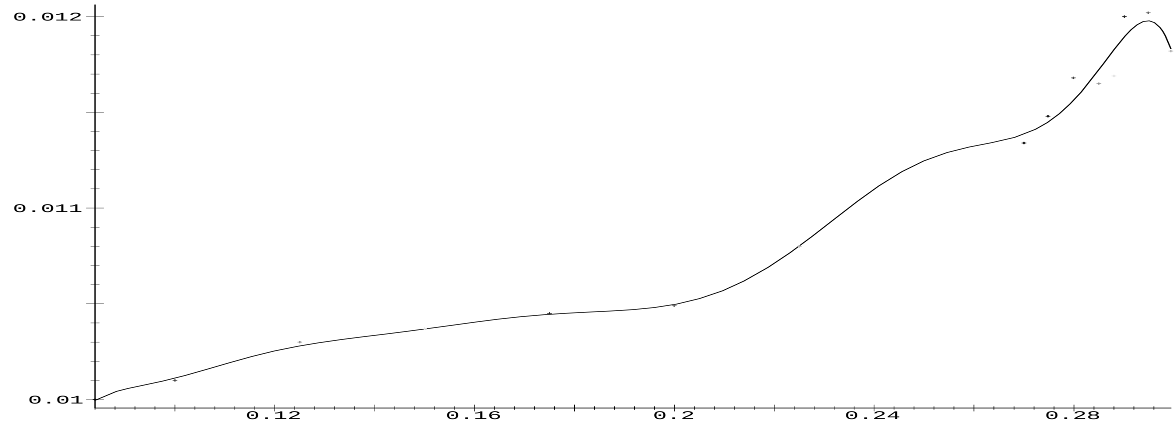

Figure 3.50: Wavelength $\lambda(x)$ of a T–S wave with $f = 1420\,\text{Hz}$ for case 3: horizontal axis — x, distance from leading edge (m), vertical axis — $\lambda(x)$ (m).

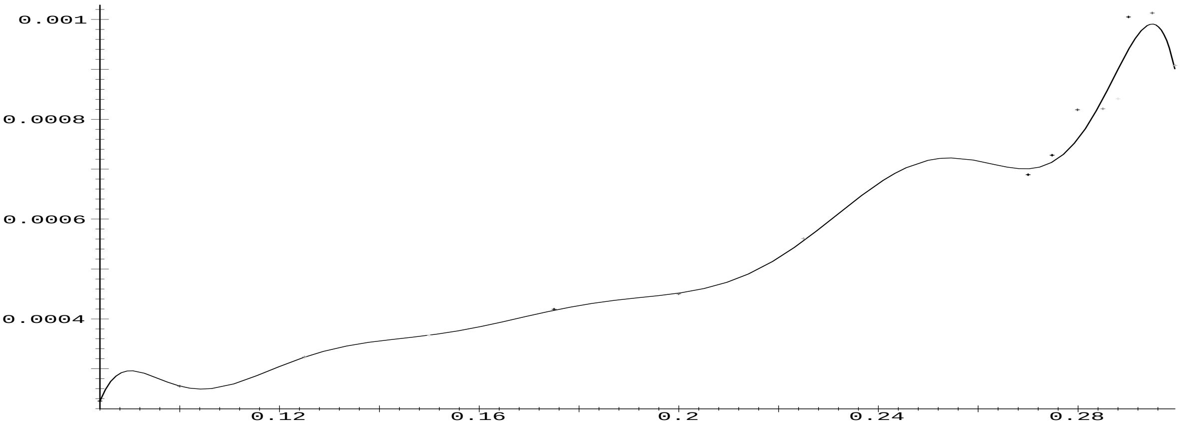

Figure 3.51: Displacement thickness $\delta^\star(x)$ of the boundary layer for case 3: horizontal axis — x, distance from leading edge (m), vertical axis — $\delta^\star$ (m).

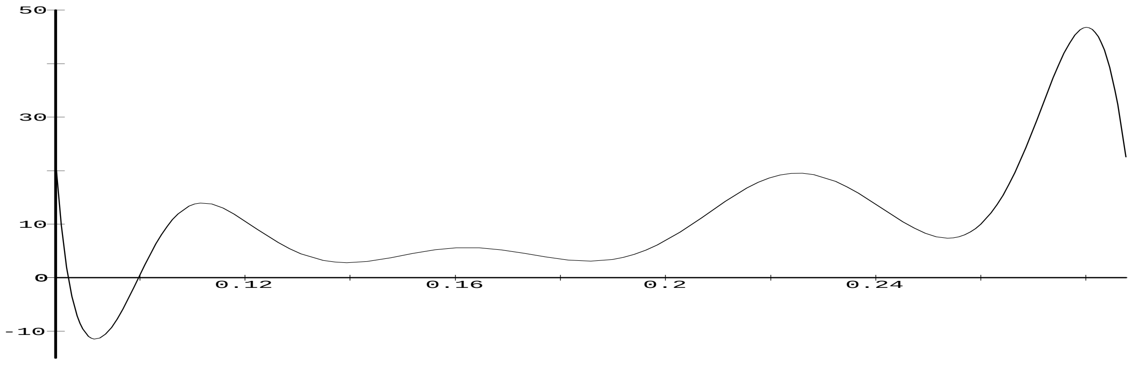

Figure 3.52: Growth of boundary layer over one T–S wavelength with $f = 1420\,\text{Hz}$ for case 3: horizontal axis — distance from leading edge (m), vertical axis — percentage growth.

3.6 Discussion

3.6.1 Tonal cases: 1, 2, 3 and 4

A comprehensive set of results is presented in §3.5.1 for tonal case 1. For tonal cases 2, 3 and 4 only marginal curve, growth rate and amplification plots are presented. The discussion will concentrate on the results for case 1. Then it will be seen that the comments and conclusions reached are (in the main) applicable to the other cases as well.

Figure 3.8 of the marginal curves at the stations along the aerofoil reveals the changing stability characteristics of the velocity profiles with streamwise distance downstream from the aerofoil leading edge. There are several points to note. Firstly from station 3 onwards the frequency of the tone, 1048 Hz, translates to an *unstable* boundary-layer frequency. From station 3 onwards the asterisks lie inside their respective marginal stability curves. The experimental results showed the existence of the tone was dependent on a large T–S wave at the same frequency. T–S waves with frequency 1048 Hz will be amplified from station 3 until the trailing edge of the aerofoil. For case 1, 1048 Hz is a *stable* frequency until station 3. The assumption that instabilities associated with the leading edge do not interfere with the development of instabilities between station 1 and the trailing edge appears reasonable. Before station 3 any perturbations with frequency 1048 Hz will be stable, in fact they will decay exponentially until the 'critical point' between stations 2 and 3.

The structure of the marginal curves appears to change with distance downstream. From stations 1 to 4 there is a narrow band of unstable frequencies between the lower and upper branches of the marginal curves. The upper and lower branches appear to converge as $R_{\delta^\star} \to \infty$. From stations 5 to 7 there is still a narrow band of unstable frequencies between the lower and upper branches of the marginal curves, but the branches do not appear to converge as $R_{\delta^\star} \to \infty$. Finally, from stations 8 to 12 there is a broad band of unstable frequencies between the lower and upper branches of the marginal curves with each curve having a 'flattened' nose. The critical Reynolds number (i.e. $R_{\delta^\star c}$) decreases on approaching the trailing edge of the aerofoil. The lower branches of the marginal curves for the stations close to the trailing edge tend to $\omega = 0$ as $R_{\delta^\star} \to \infty$. That is for $R_{\delta^\star} > R_{\delta^\star c}$, perturbations will be unstable for $0 < \omega < \omega_{\text{upper branch}}$. Again the branches do not appear to converge as $R_{\delta^\star} \to \infty$. A final observation is that on several of the curves (notably at stations 7, 8, 9 and 10) there is a 'kink' in the marginal curve. The 'kink' is located on the upper branch, close to the 'nose' of the marginal curve, in each case. The relevance of this observation is discussed soon.

In §3.1.1, Rayleigh's inflexion-point theorem stated that a *necessary* condition for instability of an inviscid, bounded flow was the existence of an inflexion point in the velocity profile away from the boundary walls. Rayleigh was able to extend this theorem to unbounded, shear flows where he showed that an inflexion point in the profile is a *necessary* and *sufficient* condition for instability.

Using this extension of Rayleigh's theorem, Falkner–Skan boundary-layer profiles with an inflexion point sufficiently away from the boundary will be unstable as $R_{\delta^\star} \to \infty$. Hence the lower and upper branches of the marginal stability curve do not converge as $R_{\delta^\star} \to \infty$. Thus for case 1, downstream from station 5 the profiles remain unstable as $R_{\delta^\star} \to \infty$ through the inviscid dynamics of an inflexion-point profile.

The inflexion point must be located 'sufficiently away from the boundary' so that the profile may locally be approximated by an inviscid shear layer. The effect of viscosity through the no slip condition is only significant in a thin layer of fluid (viscous wall layer) near the boundary. If the inflexion point is outside this layer then the stability of the flow as $R_{\delta^\star} \to \infty$ may be modelled by the stability of an inflexional shear layer. If the inflexion point is located in or sufficiently close to the viscous wall layer then the stability may not be governed by the inflexion point. Viscosity may have a stabilizing effect at high enough Reynolds numbers causing the branches of the marginal curves to converge, (stations 1 to 4 for case 1). The mechanisms of instability are discussed soon.

Figure 3.9 only plots the growth rate curves from stations 3 to 12. The growth rate curves are seen to divide naturally into two characteristic forms corresponding to the marginal curves from stations 3 to 7 and 8 to 12. From stations 3 to 7 there is a narrow band of unstable frequencies which have low growth rates. The maximum growth rate at each station increases slowly while the corresponding frequency of the maximum growth rate *decreases.* The frequency with maximum growth rate at station 7 is less than 1048 Hz (the frequency of the tone). Then from stations 8 to 12 there is a broad band of unstable frequencies with a sudden increase in the growth rates, (approximately three-fold). The distance between stations 7 and 8 is only 24 mm. The frequencies of the modes with maximum growth rate also increase. The frequency of the mode with maximum growth rate at station 8 is now greater than 1048 Hz. In fact all the frequencies of modes with maximum growth rate now appear to be close to the frequency of the tone. The three-fold increase in $-\alpha_i$ leads to a significant increase in the amplification of T–S waves, (as their growth downstream is $\propto e^{-\alpha_i x}$).

Figure 3.10 shows remarkable agreement between the hypothesis presented in §3.3.1 and the experimental results. The amplification between stations 1 and 12 of modes with fixed frequency revealed that a mode with frequency 1050 Hz was amplified nearly $80,000$ times on reaching station 12, (almost at the trailing edge). The prediction error is minimal in this case. In figure 3.11 the amplification between stations 1 and 7, and, 1 and 8 is shown. The frequency of the mode with maximum amplification at station 7 appears slightly higher than 1050 Hz. However, by station 8 the frequency of the mode with maximum amplification is clearly centred around 1050 Hz. The amplification factor at this station is only approximately 500.

Three observations are noted from figures 3.10 and 3.11. Firstly, the frequency of the tonal noise has been predicted by finding the T–S wave with maximum amplification over the aerofoil. This makes the subtle assumption that the infinitesimal perturbations at different frequencies over the aerofoil all have similar initial amplitudes. Secondly, the large amplification of the mode takes place between stations 8 and 12. Thirdly, the quasi-parallel flow approximation was seen in §3.5.4 to be much worse near the trailing edge of the aerofoil, where the displacement thickness changed significantly over one T–S wavelength. The validity of the results at the later stations is thus questionable. However, the frequency of the mode with maximum amplification is already determined at station 8, where the quasi-parallel flow approximation is still valid. From stations 8 to 12 this frequency remains the most amplified frequency, allowing an accurate prediction even though the flow is not quasi-parallel at the trailing edge of the aerofoil.

Figure 3.12 is an example of a least-squares polynomial $\alpha_i(x)$ calculated for a T–S wave with frequency 1048 Hz, for case 1. For each case many of these polynomials were calculated in order to find the amplification of modes with fixed frequency over the aerofoil. The value of α_i at each station is indicated by a plus sign. The least-squares polynomial was chosen to have a degree less than eleven because, although a polynomial with degree eleven would pass through each α_i point, the polynomial was found to oscillate dramatically (the curve was seen to cut the x-axis several times). The x-axis ($\alpha_i = 0$) separates the stable and unstable regions, and in reality $\alpha_i(x)$ would not be expected to oscillate between stable and unstable behaviour.

Figure 3.13 shows the amplification of the mode in figure 3.12 with distance from the leading edge of the aerofoil. The linear growth is exponential and by the trailing edge the amplification factor (as already seen in figure 3.10) is greater than $80,000$. In figure 3.13 the amplification rate appears to change at a point approximately 60 mm upstream of the trailing edge of the aerofoil. The gradient of the curve in figure 3.13 is observed to steepen downstream of this point. As a result the majority of the linear growth of the mode occurs downstream of this point, which lies between stations 7 and 8 (for this case). The mode with frequency 1048 Hz has already been shown to be the most amplified on reaching this point. Figure 3.13 demonstrates that there is an observable change in the amplification rate about a point between stations 7 and 8, which leads to a large increase in the total amplification.

Figures 3.14 — 3.17 plot the amplitude of the streamwise velocity perturbations at a frequency of 1048 Hz at four stations on the aerofoil. These plots are analogous to the rms velocity profiles presented in Chapter 2 because they give a measure of the amplitude of the disturbances in the z direction. The rms velocity profiles presented in Chapter 2 are dimensional and therefore a direct comparison is not permitted with the eigenfunctions obtained by using linear theory because the normalization of the eigenfunctions is arbitrary. However, the characteristics of the eigenfunction profiles may be compared with the rms profiles, e.g. for case 1 compare the eigenfunction plots with figure 2.8. (Note that the location of the rms velocity profiles is not the same as the stations used for the calculations in case 1.)

Approaching the trailing edge of the aerofoil the rms velocity profiles change from a distinctive two-peaked profile to a three-peaked profile. The peak with the largest magnitude is close to the aerofoil surface. The three-peaked rms profiles were measured close to the trailing edge of the aerofoil, through the region of reversed flow. The characteristic two- and three-peaked shape is repeated in the eigenfunction curves. In figure 3.15 the eigenfunction profile is on the verge of changing from a two- to three-peaked profile. From station 8 the eigenfunctions all exhibit three-peaked profiles. Before station 7 the profiles each have two peaks.

The two-peaked eigenfunctions are associated with the low growth rates from stations 1 to 7, and the three-peaked eigenfunctions with the high growth rates from stations 8 to 12, in case 1. In the wind-tunnel experiments, large amplification of the T–S waves occurred after the flow separation, i.e. where there was a small region of reversed flow. The large amplification is incorporated into the model and in this case occurs downstream of station 7 on the aerofoil. The governing mechanisms of instability are now discussed.

Mechanisms of instability

The effect of viscosity in dissipating the energy of a disturbance is described by the energy equation. The energy equation is derived by expressing the velocity $\mathbf{u}$ and pressure p as the sum of a mean and perturbation component

$$\mathbf{u} = \overline{\mathbf{u}} + \mathbf{u}' \quad \text{and} \quad p = \overline{p} + p' \, , \tag{3.95}$$

where the perturbations $\mathbf{u}', p'$ have zero mean,

$$\overline{\mathbf{u}'} = \overline{p'} = 0 \, . \tag{3.96}$$

The energy equation is then derived by substituting (3.95) into the Navier–Stokes equations (3.11) and subtracting from this the mean Navier–Stokes equations, giving

$$\frac{\partial I_1}{\partial t} = I_2 - R^{-1} I_3 \,, \tag{3.97}$$

where

$$\begin{aligned} I_1 &= \int_V \tfrac{1}{2}\overline{u_i' u_i'}\, \mathrm{d}V \,, && (3.98) \\ I_2 &= -\int_V \frac{\partial \overline{u_i}}{\partial x_j}\overline{u_i' u_j'}\, \mathrm{d}V \,, && (3.99) \\ I_3 &= \int_V \overline{\left(\frac{\partial u_i'}{\partial x_j}\right)^2}\, \mathrm{d}V \,, && (3.100) \end{aligned}$$

and V is the domain of flow.

I_1 is the mean disturbance kinetic energy in V. I_3/R is the viscous dissipation which is seen to always reduce the disturbance kinetic energy. I_2 is the product of the Reynolds stresses $\tau = -\overline{u_i' u_j'}$ and the mean-velocity gradient in V. A necessary condition for a disturbance is

$$I_2 > I_3/R \,. \tag{3.101}$$

The Reynolds stress τ is the mean of the product of the velocity perturbations. Averaging in the streamwise direction we find

$$\overline{u_i' u_j'} = \frac{\alpha}{2\pi}\int_0^{2\pi/\alpha} u_i' u_j' \, \mathrm{d}x \,, \tag{3.102}$$

which reduces to (3.90) when the velocity perturbations are expressed in normal mode form (3.86), (3.87). The magnitude of the Reynolds stress depends upon the phase of the velocity perturbations. In the fluid, the magnitude of the Reynolds stress (3.90) will increase if ϕ and ϕ' are out of phase. The Reynolds stress is maximized when ϕ and ϕ' are $\pi/2$ out of phase.

Prandtl initially showed that viscous forces produced a phase shift of the components of disturbance velocity. At large enough values of αR viscous effects are significant in two regions: near the rigid boundary and in the critical layer centred about z_c (3.92) where the background velocity is equal to the phase velocity of the disturbance.

In §3.2 it was shown that viscous effects are essentially negligible throughout the fluid flow over a surface, except in a thin layer near the surface, known as the boundary layer. The structure of the boundary layer is considered for large αR to determine the lower and upper branches of the marginal stability curve. The boundary layer approximation to the Orr–Sommerfeld equation (3.13) up to $O(\delta)$, where $\delta \ll 1$, from the boundary surface becomes

$$-c\phi'' = \frac{1}{i\alpha R}\phi^{iv} \, , \tag{3.103}$$

where $\delta \sim (\alpha R)^{-1/2}$. Equation (3.103) may be solved analytically to obtain an expression for the eigenfunction ϕ up to δ above the boundary surface. This region is known as the viscous wall layer.

The Orr–Sommerfeld equation (3.13) up to $O(\delta)$, where again $\delta \ll 1$, from the point $z = z_c$ is approximately

$$i\alpha R U_c'(z - z_c)\phi'' = \phi^{iv} \, , \tag{3.104}$$

where $U(z_c) = U_c$ and $\delta \sim (\alpha R U_c')^{-1/3}$. Equation (3.104) reduces to an Airy equation from which an expression may be found for the eigenfunction ϕ valid through a layer of thickness 2δ centred about the point z_c. This region is known as the critical layer.

For large αR the boundary layer may be described as having a triple-deck or quintuple-deck structure. For a triple-deck, the two regions where viscous effects are significant coincide. The critical layer lies inside the viscous wall layer close to the boundary surface. In a quintuple-deck the critical layer is entirely separate from the viscous wall layer and the effects of viscosity are significant in two regions in the boundary layer. In 1979, Smith [40] recognized that at large R, the lower branch of the marginal stability curve for the Blasius boundary layer had a triple-deck structure. Then in 1981, Bodonyi & Smith [5] derived a quintuple-deck structure at large R on the upper branch of the marginal stability curve for the Blasius boundary layer. Previously the theory concerning the triple-deck boundary-layer structure was developed by Stewartson & Williams [41], Neiland [35] and Messiter [32] around 1969, although not in connection with the Orr–Sommerfeld equation. Figure 3.53 is a schematic of a triple- and quintuple-deck boundary-layer structure.

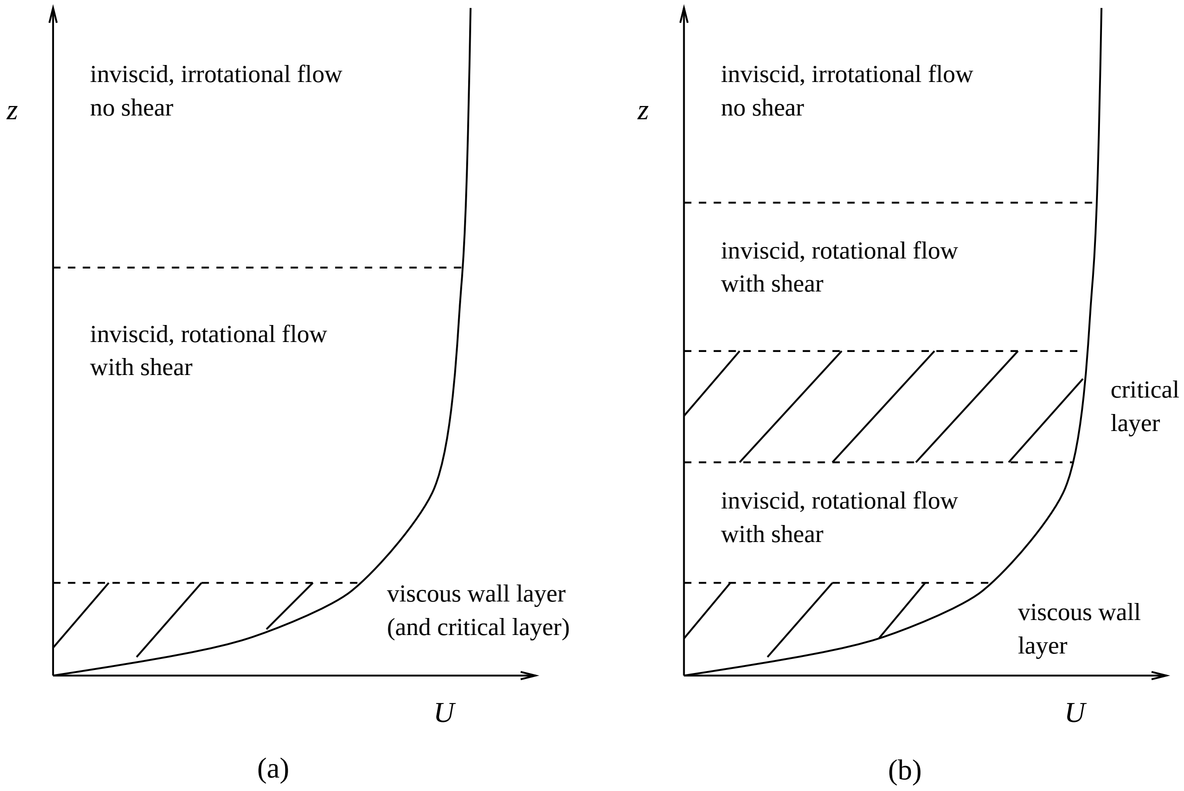

Figure 3.53: (a) triple-deck, (b) quintuple-deck boundary layer schematics.

Contributions to the perturbation kinetic energy through I_2 in the energy equation (3.97) are through the product of positive Reynolds stresses in the viscous wall and critical layers with the mean-velocity gradient. Outside these regions the contribution to I_2 is negligible because the Reynolds stresses are much lower and also the mean-velocity gradient tends to zero outside of the boundary layer.

Viscous forces appear to modify the phases of the velocity perturbations which lead to the positive Reynolds stresses enabling transfer of energy from the mean-flow to the disturbance. In Healey [22], calculations of the eigenfunctions for a quintuple-deck structure revealed a phase jump across z_c. The dominant viscous effect for this structure was shown to be the critical layer. For a triple-deck structure, no phase shift was seen across the point z_c (which lies inside the viscous wall layer), and the leading effects of viscosity are now located in the viscous wall layer.

Boundary-layer disturbances growing because of the transfer of energy by the viscous mechanisms described above are known as Tollmien–Schlichting waves (which in this thesis have been referred to as T–S waves).

As $R \to \infty$ the stability of a flow is governed by inviscid dynamics described by the Rayleigh equation (3.9). As already mentioned the stability characteristics of a flow of an inviscid fluid depend largely on the location of any inflexion points. From the Rayleigh equation it is seen that the point z_c and the inflexion point will coincide for $R = \infty$.

The mechanism of instability of an inviscid, inflexional velocity profile is perhaps not as well understood as the viscous instability mechanism (described above).

Lin [27], presents an argument using vorticity dynamics to account for the destabilizing effect of an inflexion point. For a two-dimensional, laminar, parallel flow $\mathbf{u} = (u(z), 0)$ the magnitude of the vorticity ζ_0 will be u_z. The inflexion point $u_{zz} = 0$ will thus give a maximum or minimum of vorticity. The vorticity equation reduces to

$$\frac{\mathrm{D}\zeta_0}{\mathrm{D}t} = 0 \,, \tag{3.105}$$

which implies that each fluid element maintains its vorticity during two-dimensional motion. The fluid flow may then be considered as a collection of layers all with the same vorticity. The behaviour is then considered if a fluid element is displaced having either as excess or deficit of vorticity with its surroundings. Lin calculated that a fluid element with an excess of vorticity will be accelerated in the positive z direction with acceleration

$$\frac{1}{\Gamma}\int\!\!\int (w'(x,z))^2 D\zeta_0(z)\,\mathrm{d}x\mathrm{d}z \,, \tag{3.106}$$

where w' is the velocity perturbation in the z direction, $D\zeta_0$ is the vorticity gradient of the mean-flow and Γ is the total strength of the vorticity of the perturbation. The vorticity ζ may be expressed as $\zeta_0 + \zeta'$ where ζ' is the perturbation vorticity. Then $\Gamma = \int\int \zeta' \,\mathrm{d}x\mathrm{d}z$ where the integral is over the area of the vorticity perturbation. If ζ_0 and ζ' have the the same sign then there will be an excess of vorticity and $\Gamma > 0$. If ζ_0 and ζ' have opposite signs then there will be a deficit of vorticity and $\Gamma < 0$. If the mean-vorticity profile is monotonically increasing or decreasing (i.e. $D\zeta_0 > 0$ or $D\zeta_0 < 0$ everywhere) then an element of fluid with an excess or deficit of vorticity with its surroundings will undergo an acceleration. Let a fluid element E_1 from layer L_1

be interchanged with fluid element E_2 from layer L_2, where without loss of generality the vorticity in layer L_2 is greater than in L_1. Figure 3.54 shows that for a monotonic vorticity profile the fluid elements E_1 and E_2 are returned to their respective layers. With $D\zeta_0$ only one sign then the direction of the acceleration depends only on the sign of Γ. Fluid element E_1 has a deficit of vorticity when located in layer L_2 and hence $\Gamma < 0$. Similarly, E_2 has an excess of vorticity in L_1 and hence $\Gamma > 0$. The direction of motion of the two fluid elements will return each element to their respective layers. This action clearly has a stabilizing effect on the fluid.

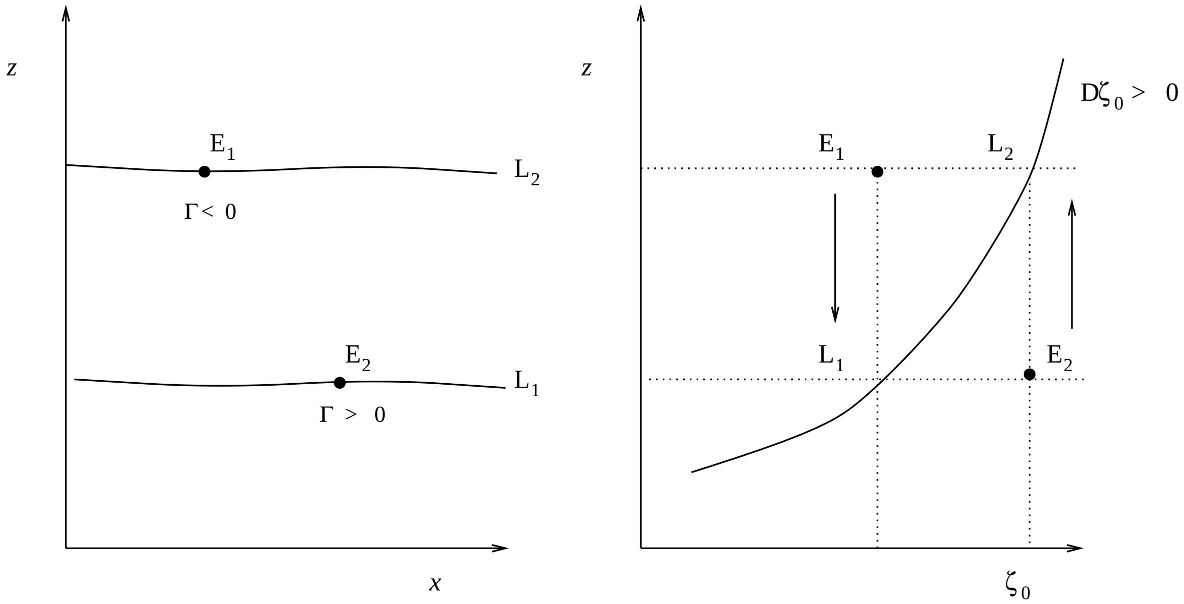

Figure 3.54: Schematic of the stabilizing effect of a shear flow with a monotonic vorticity profile

If there is an extremum of vorticity (i.e. an inflexion point in the velocity profile) then interchanging two fluid elements from either side of the extremum may not lead to an excess or deficit of vorticity with its surroundings. Hence the fluid elements will not undergo the restoring action described previously for a monotonic vorticity profile. The interchange of fluid elements may lead to a disturbance which persists. In figure 3.55 an interchange of fluid elements about the vorticity extremum leads to both fluid elements undergoing an acceleration in the same direction. This action may have a destabilizing effect on the fluid.

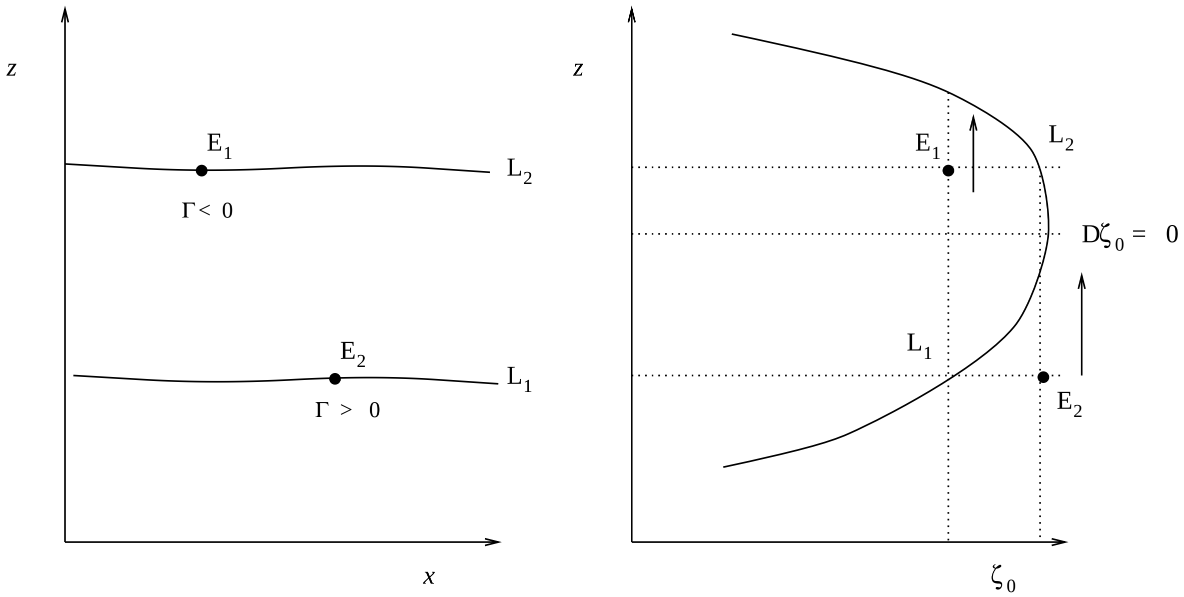

Figure 3.55: Schematic of the destabilizing effect of a shear flow with an inflexion point.

Boundary-layer disturbances whose growth is dominated by the inviscid dynamics of an inflexional velocity profile will be referred to as *inflexional waves* (note that inflexional waves may also be referred to as inviscid waves in the literature). For inflexional boundary-layer profiles, T–S and inflexional waves may coexist. The dominant instability mechanism may change with changes in the velocity profile.

Healey [22] investigated the dominant instability mechanisms for boundary-layer flows under the influence of a small adverse pressure gradient. His initial assumption was that inflexional modes were the dominant mechanism in transition from a laminar to a turbulent boundary layer. However his surprising conclusion was that for the adverse pressure gradients under consideration the transition was likely to be driven by viscous instabilities, i.e. T–S waves.

There exists a 'kink' on the upper branch of the marginal stability curve for the Blasius boundary layer at $R_{\delta^\star} \approx 10^5$. Healey demonstrated that for $R_{\delta^\star} < 10^5$ the critical layer lies inside the viscous wall layer on the upper branch of the marginal curve. For $R_{\delta^\star} > 10^5$ the critical layer is separate from the viscous wall layer. For large $R_{\delta^\star}$ on the lower branch, and up to the 'kink' on the upper branch of the marginal curve, the boundary layer has a triple-deck form. After the ‘kink’ on the upper branch of the marginal curve the boundary layer has a quintuple-deck form.

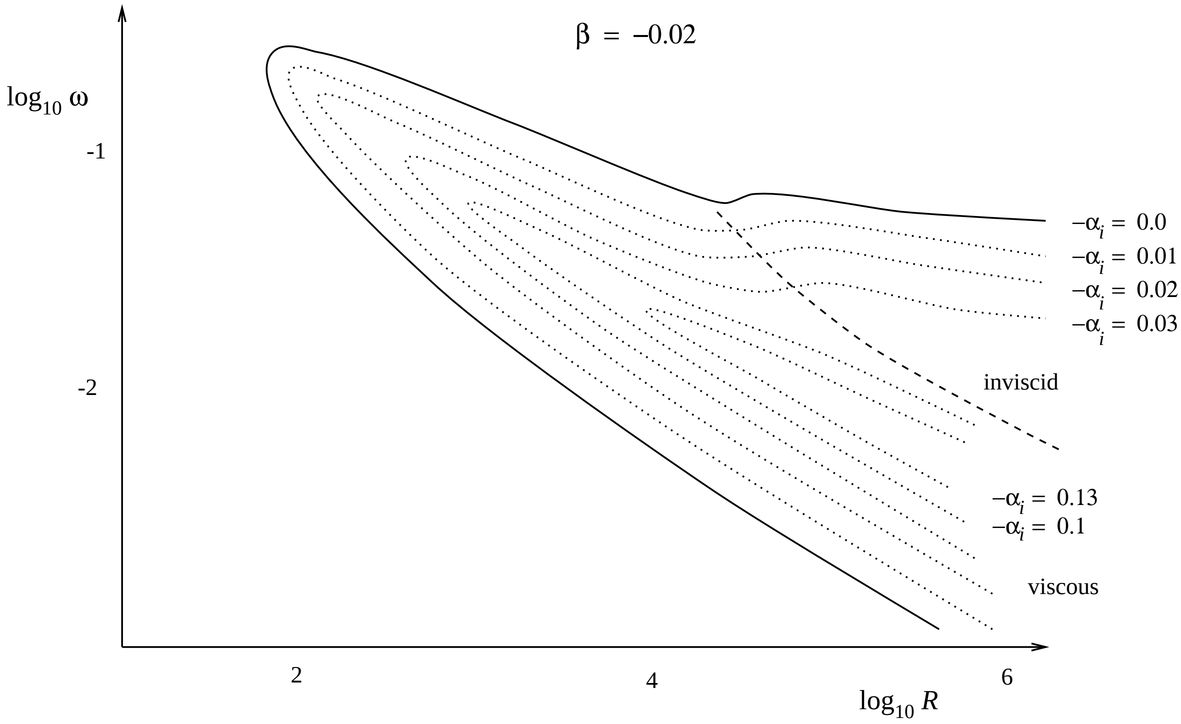

Figure 3.56: Growth rate contours $-\alpha_i$ for Falkner–Skan boundary layer with $\beta = -0.02$, (adapted from Healey [22]).

Figure 3.56 is a sketch of the constant growth rate contours for a Falkner–Skan profile with a small adverse pressure gradient ($\beta \approx -0.02$). With stronger adverse pressure gradients the ‘kink’ on the upper branch of the marginal curve moves to lower $R_{\delta^\star}$. After the ‘kink’ in the marginal curve, the contours just below the curve are nearly horizontal. They correspond to inviscid/inflexional waves because they are independent of $R_{\delta^\star}$. The solutions of the Orr–Sommerfeld and Rayleigh equations would give approximately the same result. The growth rates at the same Reynolds number near the lower branch are higher. The thick dashed line sketched on figure 3.56 approximately separates the unstable region into viscous and inviscid regions where these mechanisms dominate.

Figure 3.57 is a sketch of the marginal stability curves for various values of β. For $\beta \geq 0$ there is no inflexion point on the boundary-layer profile. The constant growth rate contours inside their respective marginal curves do not appear horizontal after the 'kink' in the marginal curve, and hence for $\beta \geq 0$ the dominant instability mechanism will always remain viscous. For decreasing β the 'kink' moves to lower Reynolds numbers. For $\beta < 0$ the upper branch appears nearly horizontal after the 'kink' and an increasingly large region of the unstable region between the upper and lower branches of the marginal curve will be dominated by inviscid/inflexional instabilities.

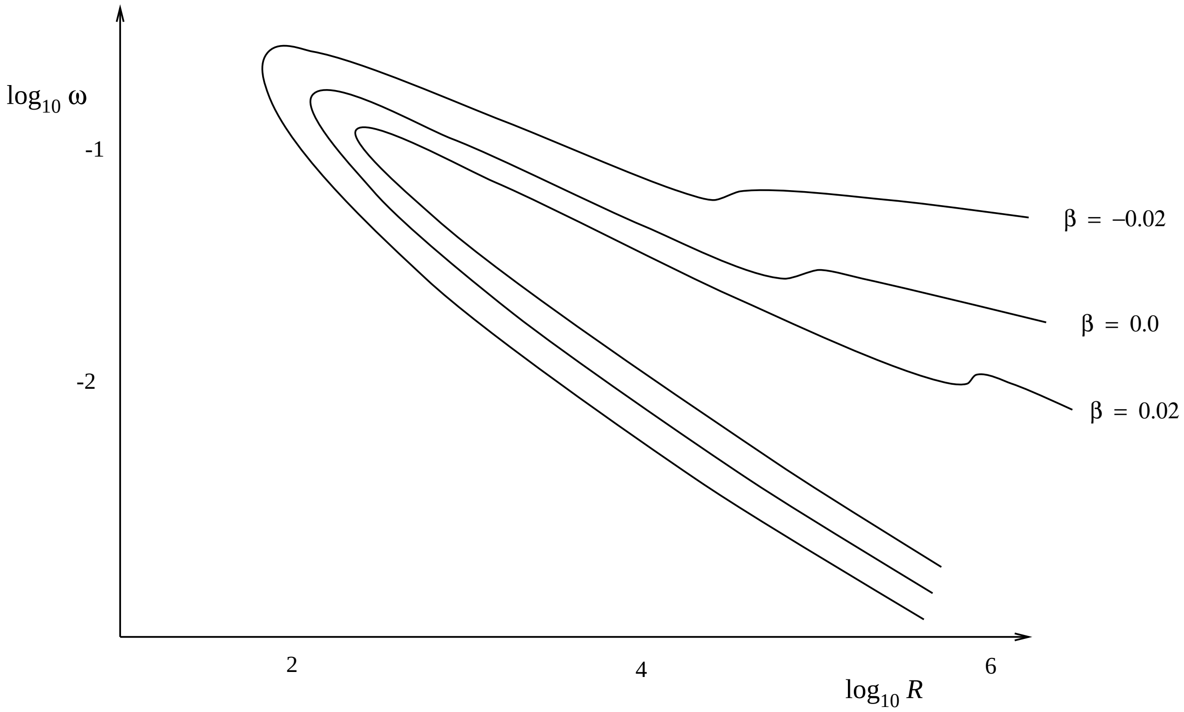

Figure 3.57: Marginal stability curves for varying β, (adapted from Healey [22]).

Healey modelled a set of experiments for the flow over a flat plate inclined at a small angle of negative incidence. In these experiments the value of $R_{\delta^\star}$ was measured at the point of transition. He modelled the flow using Falkner–Skan profiles and the strongest adverse pressure gradient was for a profile with $\beta = -0.12$. For $\beta = -0.12$ transition was observed where $R_{\delta^\star} \approx 1400$. For these low values of $R_{\delta^\star}$ and β (compared with the values considered in this work), Healey found that the amplification of the viscous instabilities was much greater than the amplification of the inviscid instabilities. The low-frequency viscous instabilities (close to the lower branch) were amplified more than the high-frequency inviscid instabilities close to the upper branch. Healey concluded that in the experiments he modelled it was the viscous instabilities which drove the transition. Healey noted that inviscid waves would be expected to dominate further downstream, but in the experiments he considered transition had already occurred.

Healey's results may be used to describe the results in §3.5. For case 1 the flow was still laminar at the trailing edge of the aerofoil. In this case, at station 12 $R_{\delta^\star} = 2862$ and $\beta = -0.195$. At station 7 $R_{\delta^\star} = 1358$ and $\beta = -0.1358$. The values of $R_{\delta^\star}$ and β at station 7 correspond approximately with the values of $R_{\delta^\star}$ and β when transition occurred in the experiments described by Healey. He concluded that up to $R_{\delta^\star} \approx 1400$ viscous instability was the dominant instability mechanism.

In case 1 there appears to be a change in the dominant instability mechanism between approximately stations 7 and 8. Until station 7 the growth rates are low and the frequency of the mode with maximum growth rate is decreasing at successive stations (see figure 3.9). Comparing with the results presented in Healey then until station 7 the dominant instability mechanism will be viscous, that is the boundary-layer instability waves are taken to be T–S waves until approximately station 7.

The marginal curves in figure 3.8 (notably stations 7 to 10), reveal the remnants of the 'kink' on their upper branches. At station 7 the 'kink' is at approximately $R_{\delta^\star} = 1000$. By station 8 the 'kink' is almost at the 'nose' of the marginal curve, $R_{\delta^\star} \approx 200$. From station 8 onwards the dominant instability mechanism will be inviscid for all $(R_{\delta^\star}, \omega)$ apart from a thin region between the 'kink' and the 'nose' of the marginal curve, and for frequencies very close to the lower branch. Up to station 7 the asterisks lie relatively close to the lower branches of their respective marginal curves. They appear to lie in the viscous dominated domains of their marginal curves (see figure 3.56). From station 8 onwards the asterisks clearly lie well above the lower branches of their marginal curves in domains dominated by inviscid instabilities.

The large growth rates from stations 8 to 12 in figure 3.9 reflect the change in instability mechanism to inviscid/inflexional waves (hereafter referred to as just inflexional waves). The boundary-layer instability wave propagating over the aerofoil with frequency 1048 Hz will experience changing dominant instability mechanisms. Initially the perturbation energy will be generated by the Reynolds stresses in the viscous wall layer. Further downstream, as the boundary-layer profile gradually changes then the critical layer will separate from the viscous wall layer. This also implies that the inflexion point will move from the viscous wall layer (as the critical point and inflexion point coincide at $R_{\delta^\star} = \infty$), and the growth of the perturbation will be governed by the inviscid dynamics of the inflexion point.

The inflexional instabilities have maximum growth rates at higher frequencies than the viscous instabilities. From figure 3.11 it appears that the tonal frequency 1048 Hz is already the dominant frequency. The frequency of the mode with maximum growth rate at station 7 and 8 (shown by the dashed vertical lines in figure 3.9) bound the tonal frequency. These dashed lines show the frequency of the modes with maximum growth rate near the end of the viscous region and at the beginning of the inviscid region. It appears that the frequency of the mode with maximum amplification is 'selected' between stations 7 and 8. The frequency of the mode with maximum amplification at station 8 is then observed to have the maximum amplification until the trailing edge.

Relating this description to the wind-tunnel experiments by Dr. Nash, as the flow separates and there is a small region of reversed flow, the inflexion point in the profile moves further away from the aerofoil surface. As discussed, when the inflexion point is sufficiently removed from the surface it will dominate the instability. To remove the inflexion point sufficiently from the surface of the aerofoil, flow separation is required. Somewhere near the point of flow separation the dominant instability mechanism will change. The frequency of the mode which undergoes the large amplification is also 'selected' near this point. The mode which has the maximum amplification in the linear regime extends into the nonlinear regime. As a result linear theory is able to predict the tonal frequency.

When there is only a small adverse pressure gradient (upstream of the point of flow separation), the inflexion point is located very close to the aerofoil surface and the instabilities may be taken to be T–S waves. Their amplification is relatively small and the frequency spectrum measured in the boundary layer will not reveal any discrete peaks, (see figure 2.11(a)). Previous papers which have used stability characteristics of the (Blasius) boundary layer over a flat plate will not have taken into account the amplification due to the inflexion point because the flat plate boundary layer has an inflexion point located only at $z = 0$.

Figures 3.18 — 3.21 plot the Reynolds stress (3.91) at stations 1, 7, 8 and 12 respectively. At station 1 the Reynolds stress changes sign just above the point z_c. The sign of the Reynolds stress indicates whether energy is transferred to or from the perturbation. A T–S wave with frequency 1048 Hz at station 1 is stable. The larger, negative portion of the Reynolds stress indicates that over the majority of the boundary-layer energy is actually transferred from the perturbation to the mean-flow. Hence the perturbation is stable at station 1. At stations 7, 8 and 12 the Reynolds stress is positive everywhere. Energy will be transferred from the mean-flow to the perturbation at each of these stations. The maximum amplitude of the Reynolds stress is located near the critical layer at each of these stations. Recall that contributions to the Reynolds stress are from the viscous wall and critical layers. When the critical layer is separate from the viscous wall layer the dominant contribution is from the critical layer. At station 12 there is a very small peak close to $z = 0$ and then the larger peak close to z_c. By station 12 the critical layer has been shown to be separated from the viscous wall layer. It is proposed that the small peak close to $z = 0$ in figure 3.21 is due to the viscous wall layer and the larger peak further away from the boundary is due to the critical layer. The contribution to the Reynolds stress by the critical layer is greater than the viscous wall layer. However, from stations 8 to 12 the dominant instability mechanism has already been shown to be through the inflexion point.

The marginal curve, growth rate and amplification plots for cases 2, 3 and 4 reveal the same characteristics as for case 1. For case 2 (only) the amplification of boundary-layer instability waves was not calculated beyond station 10. In case 2 measurements were actually obtained up to 99% chord. However, after 97% chord the measured shape factor H reduced. A decreasing shape factor may indicate transition to turbulence (because H for a turbulent boundary layer is less than H for a laminar boundary layer). For case 3 experimental results were not obtained so close to the trailing edge. The location of station 10 in case 2 is at the same location as station 12 in case 3

(See appendix A for further details). For case 2 the viscous growth is taken to be up to station 7, and case 3 up to station 9. In both cases the frequency of the modes with maximum growth rate before and after the change in the dominant instability mechanism 'bound' the tonal frequency. In case 2 the frequency of the mode with the greatest linear amplification is $\approx 1450\,\mathrm{Hz}$ and case 3 $\approx 1750\,\mathrm{Hz}$. The prediction error for case 2 is approximately 13% and for case 3, 23%. In both cases the shape of the amplification curve has been determined by the change in the instability mechanism. Figure 3.25 and figure 3.29 for cases 2 and 3 respectively show that by stations 7 and 9 the frequency of the mode with the greatest amplification is effectively determined. These predictions are clearly not as close as for case 1. However, considering that only linear theory has been used (and the approximations that have been made) they are still reasonable.

The prediction error in these cases increases with the free-stream velocity U_∞. There are several possible reasons for the increase in the error. The accuracy of the experimental measurements may decrease slightly with increasing U_∞. The amplification of the instabilities will increase with increasing U_∞ (as $R_{\delta^\star}$ increases). Hence the instabilities will not remain linear so far downstream. Where the amplitude of the instabilities becomes greater then they will interact with the mean-flow. In the weakly nonlinear stability analysis in Chapter 4 the mean-flow distortion by finite amplitude disturbances is taken into account. It is reasonable to expect that the errors inherent in modelling the boundary-layer flow with Falkner–Skan profiles increase with U_∞.

Case 4 is the only case conducted using the FX79 W151 aerofoil. $U_\infty = 30\,\mathrm{ms}^{-1}$, the same as for case 1 with the NACA 0012 aerofoil. The marginal curve and growth rate plots (figures 3.30 and 3.31) for case 4 reveal the change in instability mechanism more dramatically than for the NACA 0012 aerofoil. From stations 1 to 8 the dominant instability mechanism is clearly viscous. The marginal curves do not show the 'kink' on their upper branches, and the lower and upper branches for these stations converge as $R_{\delta^\star} \to \infty$. The corresponding growth rates at stations 1 to 8 are low. Then from stations 9 to 12 the dominant instability mechanism is clearly inviscid. The 'kink' on the upper branches of the marginal curves is very close to the 'nose' of the curves and the corresponding growth rates are very high. The frequency of the mode with the greatest linear amplification is $\approx 1150\,\mathrm{Hz}$, that is a prediction error of 4%. This mode has also been 'selected' to undergo large amplification by station 9 (see figures 3.32 and 3.33).

The frequency prediction method is clearly not confined to one type of aerofoil. In fact the method only assumes a quasi-parallel flow which is found on many aerofoils. The frequency prediction for case 4 is very reasonable. Although results were only taken at $U_\infty = 30\,\mathrm{ms}^{-1}$, it is anticipated that the prediction error would increase with increasing U_∞ for the same reasons discussed when using the NACA 0012 aerofoil. The more dramatic changes in the marginal stability and growth rate curves are attributed to the different shape of the aerofoil.

Finally for case 4 note that the amplification factor in figure 3.32 is only approximately 2000 compared with up to $200,000$ on the NACA 0012 aerofoil. However the growth rates appear to be of similar magnitude. The difference in the amplification appears to be due to the different length and shape of the aerofoils. For the NACA 0012 aerofoil the amplification was calculated by integrating over a length of 210 mm. For the FX79 W151 aerofoil the integration was conducted over only 160 mm. The majority of the growth has been shown to occur over the region of reversed flow near the trailing edge of the aerofoil. For case 1 on the NACA 0012 this was approximately 40 mm, compared with only 15 mm on the FX79 W151 aerofoil. The difference in the amplification factors obtained may be severe when comparing different aerofoils because the growth is exponential.

The description of the development of the boundary-layer instabilities remains the same for both aerofoils. The growth appears to be depend on the flow separation and the subsequent region of reversed flow, to enable the instability to be dominated by the inflexion point.

3.6.2 No-tone case 5

The experimental results for case 5 in §2.4.3 show a relatively large region of reversed flow *but* no large amplification of the boundary-layer instabilities. Without this amplification there were no discrete tones generated.

The marginal curves plotted in figure 3.34 appear similar to the ones for the tonal cases. The corresponding growth rate curves (figure 3.35) at each station show an increase in the growth rate between stations 7 and 8, where previously this was attributed to the change in the dominant instability mechanism. There are two observable differences between figure 3.35 and the previous growth rate figures for the tonal cases. The maximum growth rates for the tonal cases with the NACA 0012 aerofoil for cases 1, 2 and 3 were ≈ 140, ≈ 150, and ≈ 180 respectively. The maximum amplification factor for each case was of order $100,000$. For case 5 the maximum growth rates were ≈ 100 resulting in an amplification factor of $O(1000)$ (see figure 3.42).

At station 12, the growth rate curves for the tonal cases reveal a broad band of unstable frequencies. The unstable frequency band ranges from 0 to 5000 Hz for the tonal cases 1, 2 and 3. For case 5 at station 12 the unstable frequency band lies between 0 and 400 Hz. This is reflected in the amplification curve (figure 3.42) whence only a narrow band of frequencies are amplified between stations 3 and 12, namely 50 to 300 Hz.

These results initially appear to contradict the description of the amplification of the boundary-layer instabilities. Previously the presence of a small region of reversed flow was required to amplify the instabilities. In the region of reversed flow the instability was mainly governed by the inflexion point in the profile which was located outside of the viscous wall layer. For case 5 there was a large region of reversed flow, (see §2.4.3 figure 2.14), and the eigenfunction curves presented, (figures 3.36 — 3.39) reveal that by station 7 the eigenfunction has a characteristic three-peaked profile associated with instability *after* the point of separation. Case 5 is the case with the largest region of reversed flow *but* the experimental results clearly reveal no large amplification of the boundary-layer instabilities. The amplification of modes with fixed frequency is relatively weak compared with the tonal cases, and is only over a narrow band of frequencies. It is assumed that the amplification is not sufficient to initiate the resonance generating tonal noise. Presumably the amplification of the instability must generate a mode with a large enough amplitude sufficient to generate acoustic waves at the trailing edge of the aerofoil (see §5.1).

The growth rate $-\alpha_i$ was only integrated from stations 3 to 12 because at stations 1 and 2 the flow was stable for all frequencies. Although the flow separation occurred slightly upstream of the point in the tonal cases, the flow remained stable further downstream. This does not account for the reduction in the amplification because even in the tonal cases only a small band of frequencies were unstable at stations 1 and 2, and, the amplification was very low at the initial stations anyway because the mechanism was predominantly viscous.

The weaker amplification is attributed to the reduced growth rates calculated over the aerofoil. The lower growth rates and narrow band of amplified frequencies may be predicted by considering the typical length and velocity scales in case 5. The typical velocity scale U_∞ is less than in the tonal cases. The large region of reversed flow results in a typical length scale $\delta^\star$ greater than in the tonal cases. The dimensional frequency f is obtained after multiplying the non-dimensional frequency ω by $U_\infty/(2\pi\delta^\star)$. The quantity $U_\infty/\delta^\star$ is less than in the tonal cases and hence the band of unstable frequencies at each station will be narrower.

At the trailing edge $R_{\delta^\star} \approx 2500$ in case 5 compared with $R_{\delta^\star} \approx 3000$ in the tonal cases. The growth rates $-\alpha_i$ are less than in the tonal cases because the Reynolds numbers over the aerofoil are less. The growth rates over the unstable range of the marginal curves reduce as $R_{\delta^\star} \to R_{\delta^\star c}$.

Further, the dimensions of the growth rate $[-\alpha_i] = [L]^{-1}$ where the length scale L is $\delta^\star$. For the no tone case 5, $1/\delta^\star$ is less than for the tonal cases and the dimensional growth rates will be lower.

As described in §2.4.3, the flow at this low U_∞ will be relatively stable and small perturbations will not be amplified sufficiently to generate tonal noise. With increasing U_∞ the amplification will increase until reaching some critical level where the amplification is sufficient to initiate tonal noise.

3.6.3 No-tone case 6

In §2.4.5, no tones were heard from the NACA 0012 aerofoil when placed at 0° incidence to the free stream. The experimental results indicated the presence of a large boundary-layer instability at 542 Hz upstream of the trailing edge in case 6. However, boundary-layer transition occurred upstream of the trailing edge of the aerofoil in this case, and the discrete frequency mode was destroyed before it reached the trailing edge. The calculations for case 6 were performed up to station 12, situated 35 mm upstream of the trailing edge. By station 12 the shape factor H of the boundary layer had started to decrease (indicating the onset of transition).

Figures 3.40 and 3.41 of the marginal and growth rate curves are similar to the same curves for the tonal cases for the NACA 0012 aerofoil. Note that the maximum growth rates are ≈ 130, of similar magnitude to the growth rates in the tonal cases, i.e. greater than for the other no-tone case 5. The amplification of modes with a fixed frequency is shown in figure 3.43 to be centred near the frequency 542 Hz. The maximum amplification factor is $1,500,000$.

As discussed in §2.4.5, inclining the aerofoil at small angles of incidence to the free stream moves the point of separation downstream towards the trailing edge. If the flow separates sufficiently closely to the trailing edge then the flow remains 'quasi-laminar' until the trailing edge. (Note 'quasi-laminar' is taken to mean that discrete peaks in the frequency spectrum would remain detectable.)

In case 6, the process of amplification of the instabilities takes place further upstream. This has been successfully modelled and the frequency prediction error was low, as would be expected by considering $U_\infty = 17\,\mathrm{ms}^{-1}$. The development of the boundary layer is assumed to be the same as for the tonal cases. The process has been modelled using linear theory (although for this case with a linear amplification factor $1,500,000$ it is assumed that the linear regime does not extend to station 12), and the discrete frequency peak detected in figure 2.17(a) has been predicted. It is predicted that if the natural transition was prevented then a tone of 542 Hz would be heard from the aerofoil for this case.

Chapter 4

Weakly nonlinear stability theory

The theory concerning the spatial growth of two-dimensional finite-amplitude wave disturbances for parallel and nearly parallel flow of a viscous incompressible fluid has been developed by Itoh [24], [25]. He describes the theory for parallel flow, (such as plane Poiseuille flow) and for a nearly parallel flow — the Blasius boundary layer. The analysis for both cases is similar apart from two additional considerations are required for the nearly parallel flow; namely the variation of the boundary-layer thickness with distance downstream and the inclusion of a small normal component of velocity.

The weakly nonlinear stability analysis for the Falkner–Skan boundary layer presented in this chapter follows the procedure described by Itoh. By choosing a suitable form for the basic stream function the equations for the fundamental and harmonic disturbance are found to be identical to those derived by Itoh [25] for the Blasius boundary layer. Recall from §3.2.1 the derivation of the Falkner–Skan boundary-layer equation, with parameter $\beta = 2m/(m+1)$. The Blasius boundary layer is a special case of the Falkner–Skan boundary layer with $\beta = 0$. In this chapter, the algebra is simplified by using the Falkner–Skan parameter m instead of β.

Only the equation for the mean-flow distortion depends explicitly on the Falkner–Skan parameter m. The modified equations for the basic velocity profile and the mean-flow distortion reduce to those presented in Itoh [25] as $m \to 0$.

4.1 Mathematical formulation for the Falkner–Skan boundary layer

Consider a flat plate with Cartesian coordinates x parallel and y normal to the plate with the origin situated at the leading edge. Similarly, the basic velocity profile $\mathbf{u}$ has components (u, v) in the (x, y) directions.

Introduce the stream function of the flow ψ such that $\mathbf{u} = (\psi_y, -\psi_x)$ and then ψ will satisfy the vorticity equation,

$$\left\{\Delta - \frac{1}{\nu}\left(\frac{\partial}{\partial t} + \frac{\partial\psi}{\partial y}\frac{\partial}{\partial x} - \frac{\partial\psi}{\partial x}\frac{\partial}{\partial y}\right)\right\}\Delta\psi = 0\,, \tag{4.1}$$

where $\Delta = \partial^2/\partial x^2 + \partial^2/\partial y^2$. The quantities are nondimensionalized as follows,

$$x^* = \frac{x}{L}\,, y^* = \frac{y}{\delta^\star}\,, \psi^* = \frac{\psi}{\delta^\star U_\infty}\,, t^* = \frac{U_\infty t}{\delta^\star} \text{ and } R = \frac{U_\infty \delta^\star}{\nu} \tag{4.2}$$

where L is the distance downstream from the leading edge, $\delta^\star$ the boundary-layer displacement thickness, U_∞ the free-stream velocity and R the Reynolds number. For a boundary-layer flow, $\delta^\star$ is proportional to $\sqrt{\nu L/U_\infty}$. Define $\delta^\star = r\sqrt{\nu L/U_\infty}$, where r is a constant. Also define ϵ to be the ratio of the boundary-layer displacement thickness to the distance downstream, which will be assumed to be small such that

$$\epsilon = \frac{\delta^\star}{L} = \frac{r^2}{R} \ll 1\,. \tag{4.3}$$

Writing (4.1) in terms of the nondimensional variables (4.2) and dropping the asterisks gives the nondimensional vorticity equation,

$$\left\{\left(\frac{\partial^2}{\partial y^2} + \epsilon^2\frac{\partial^2}{\partial x^2}\right) - r^2\left(\frac{1}{\epsilon}\frac{\partial}{\partial t} + \frac{\partial\psi}{\partial y}\frac{\partial}{\partial x} - \frac{\partial\psi}{\partial x}\frac{\partial}{\partial y}\right)\right\}\left\{\frac{\partial^2}{\partial y^2} + \epsilon^2\frac{\partial^2}{\partial x^2}\right\}\psi = 0\,. \tag{4.4}$$

Expand the stream function as a Fourier series,

$$\psi(x, y, t) = \Psi_0(x, y) + \sum_{k=-\infty}^{\infty}\psi_k(x, y)\exp\left(-ik\beta t\right)\,, \tag{4.5}$$

where $\beta \in \mathbb{R}$ and Ψ_0 is the stream function of the steady, basic velocity profile. Taking the complex conjugate of (4.5) and noting that ψ is real implies that $\psi_{-k} = \widetilde{\psi}_k$.

Now seek a solution of the form

$$\begin{aligned}
\psi_0(x,y) &= |A_1|^2\psi_0^*(x,y)\,, \\
\psi_1(x,y) &= A_1\psi_1^*(x,y)\,, \\
\psi_2(x,y) &= A_1^2\psi_2^*(x,y)\,, \\
&\vdots \\
\psi_k(x,y) &= A_1^k\psi_k^*(x,y)\,,
\end{aligned} \tag{4.6}$$

where $A_1 \in \mathbb{C}$ and the ψ_k^*'s are all normalized functions. Our normalization is defined in §4.1.6. Now substitute (4.6) into (4.5) and assume that A_1 is small so that components higher than second degree in A_1 are negligible. The stream function ψ is written as,

$$\psi(x,y,t) = \Psi_0(x,y)+\psi_0(x,y)+\psi_1(x,y)e^{-i\beta t}+\widetilde{\psi}_1(x,y)e^{i\beta t}+\psi_2(x,y)e^{-2i\beta t}+\widetilde{\psi}_2(x,y)e^{2i\beta t}, \tag{4.7}$$

where ψ_0 represents the mean-flow distortion, ψ_1 is the fundamental disturbance and ψ_2 the (first) harmonic disturbance. The mean-flow distortion is due to the interaction between the disturbances and the basic velocity profile. In linear theory the amplitude of the disturbances is assumed to remain small so that there is no distortion of the basic velocity. Here weakly nonlinear disturbances are assumed to be large enough to slightly influence the basic velocity profile. The modified mean-flow may be thought of as $\Psi_0 + \psi_0$.

Substituting (4.7) into (4.4) results in the following set of equations

$$L_0[\psi_0] = M[\psi_1,\widetilde{\psi}_1]\,, \tag{4.8}$$

$$L_1[\psi_1] = M[\psi_1,\psi_0] + M[\widetilde{\psi}_1,\psi_2]\,, \tag{4.9}$$

$$L_2[\psi_2] = \tfrac{1}{2}M[\psi_1,\psi_1]\,, \tag{4.10}$$

where the operators L_k and M are defined by

$$\begin{aligned}
L_k[\psi] &= \Bigg[\left(\frac{\partial^2}{\partial y^2}+\epsilon^2\frac{\partial^2}{\partial x^2}\right)^2 - r^2\Bigg\{\left(-\frac{1}{\epsilon}ik\beta + \frac{\partial\Psi_0}{\partial y}\frac{\partial}{\partial x} - \frac{\partial\Psi_0}{\partial x}\frac{\partial}{\partial y}\right)\left(\frac{\partial^2}{\partial y^2}+\epsilon^2\frac{\partial^2}{\partial x^2}\right) \\
&+ \left(\frac{\partial^2}{\partial y^2}+\epsilon^2\frac{\partial^2}{\partial x^2}\right)\frac{\partial\Psi_0}{\partial x}\frac{\partial}{\partial y} - \left(\frac{\partial^2}{\partial y^2}+\epsilon^2\frac{\partial^2}{\partial x^2}\right)\frac{\partial\Psi_0}{\partial y}\frac{\partial}{\partial x}\Bigg\}\Bigg]\psi\,,
\end{aligned} \tag{4.11}$$

$$
\begin{aligned}
M[\psi,\phi] = \; r^2 & \left[\left(\frac{\partial\psi}{\partial y}\frac{\partial}{\partial x} - \frac{\partial\psi}{\partial x}\frac{\partial}{\partial y}\right)\left(\frac{\partial^2}{\partial y^2} + \epsilon^2\frac{\partial^2}{\partial x^2}\right)\phi \right. \\
+ & \left.\left(\frac{\partial\phi}{\partial y}\frac{\partial}{\partial x} - \frac{\partial\phi}{\partial x}\frac{\partial}{\partial y}\right)\left(\frac{\partial^2}{\partial y^2} + \epsilon^2\frac{\partial^2}{\partial x^2}\right)\psi\right] .
\end{aligned}
\tag{4.12}
$$

4.1.1 Basic flow

The basic flow stream function Ψ_0 satisfies,

$$
\left\{\left(\frac{\partial^2}{\partial y^2} + \epsilon^2\frac{\partial^2}{\partial x^2}\right) - r^2\left(\frac{\partial\Psi_0}{\partial y}\frac{\partial}{\partial x} - \frac{\partial\Psi_0}{\partial x}\frac{\partial}{\partial y}\right)\right\}\left(\frac{\partial^2}{\partial y^2} + \epsilon^2\frac{\partial^2}{\partial x^2}\right)\Psi_0 = 0 . \tag{4.13}
$$

As is well known in the classical theory of boundary layers, a similarity solution for (4.13) may be obtained using the transformation of variables,

$$
\eta = yx^{-(1-m)/2} \; , \; \Psi_0 = x^{(m+1)/2}F_0(\eta) , \tag{4.14}
$$

which after neglecting terms of $O(\epsilon^2)$ reduces (4.13) to an ordinary differential equation in terms of the similarity variable η,

$$
F_0''' + \tfrac{1}{2}r^2(m+1)F_0F_0'' + mr^2(1 - F_0'^2) = 0 , \tag{4.15}
$$

with the boundary conditions,

$$
F_0 = F_0' = 0 \;\text{ on }\; \eta = 0 \;\text{ and }\; F_0' \to 1 \;\text{ as }\; \eta \to \infty . \tag{4.16}
$$

The problem defined by (4.15) and (4.16) is an alternative version of the Falkner–Skan problem (3.25), (3.26) formulated in §3.2.1 for the boundary-layer flow over a flat plate inclined at an angle $\beta\pi/2$ to the horizontal (where $\beta = 2m/(m+1)$).

The constant r is calculated by using (3.33),

$$
r = \left(\frac{2}{m+1}\right)^2 \int_0^\infty (1 - f')\,\mathrm{d}\eta . \tag{4.17}
$$

Hence before solving (4.15), (4.16), the Falkner–Skan problem (3.25), (3.26) in terms of f is solved in order to calculate r. The extra numerical work required calculating f and F_0 ensures that the equations for the fundamental and harmonic disturbance are independent of m.

We approximate the weak nonparallelism of the flow as follows. The reference length scale in the x direction L is not suitable when considering boundary-layer disturbances which typically have wavelengths $O(\delta^\star)$. Therefore introduce a new variable ξ such that x (dimensional) varies by $\delta^\star$ as ξ varies from 0 to 1. Hence, if we let $x = L + \delta^\star \xi$ then

$$x^* = 1 + \epsilon\xi \, , \tag{4.18}$$

and once again drop the asterisk.

Now substituting (4.18) into Ψ_0 (4.14) and then expanding F_0 as a Taylor series about y gives,

$$\Psi_0(\xi, y) = F_0(y) + \tfrac{1}{2}\epsilon\xi \Big\{ (m+1)F_0(y) - (1-m)yF_0'(y) \Big\} + O(\epsilon^2) \, . \tag{4.19}$$

4.1.2 Outline of solution procedure

Assume the fundamental disturbance takes the same *form* as from the linear theory,

$$\psi_1(\xi, y) = A_1\phi_1(y)e^{i\alpha_1\xi} \, , \tag{4.20}$$

where ϕ_1 is a normalized function and $\alpha_1 = \alpha_{1r} + i\alpha_{1i}$ *close* to the wavenumber of the least stable linear mode.

Substitute a leading-order approximation to ψ_1 (4.20) into the right-hand sides of (4.8) and (4.10) to find ψ_0 and ψ_2. These are then substituted into the right-hand side of (4.9) which is then solved to find the next approximation to ψ_1.

It is natural to use the least stable linear instability mode as the first approximation to ψ_1 because the fundamental mode is assumed to be of a similar form. The least stable linear instability mode is calculated by solving the Orr–Sommerfeld equation.

4.1.3 The Orr–Sommerfeld equation

The derivation of the familiar Orr–Sommerfeld equation is discussed in §3.1.2. Linear disturbances satisfy

$$L_1[\psi_1] = 0 \, . \tag{4.21}$$

Writing the least stable linear instability mode as $A_1\phi_1^{(0)}(y)e^{i\alpha_1^{(0)}\xi}$ reduces (4.21) to the Orr–Sommerfeld equation,

$$\left(\frac{\mathrm{d}^2}{\mathrm{d}y^2}-\alpha_1^{(0)2}\right)^2\phi_1^{(0)}=iR\left\{\left(\alpha_1^{(0)}F_0'-\beta\right)\left(\frac{\mathrm{d}^2}{\mathrm{d}y^2}-\alpha_1^{(0)2}\right)-\alpha_1^{(0)}F_0'''\right\}\phi_1^{(0)}\,. \tag{4.22}$$

The boundary conditions ensure there is zero velocity on the surface and that the disturbances decay exponentially as $y\to\infty$

$$\phi_1^{(0)}(0)=\phi_1^{(0)\prime}(0)=0\,, \tag{4.23}$$

$$\left.\begin{array}{ccccccc}\phi_1^{(0)\prime\prime} & + & (\alpha_1^{(0)}+\zeta_1^{(0)})\phi_1^{(0)\prime} & + & \alpha_1^{(0)}\zeta_1^{(0)}\phi_1^{(0)} & = & 0\\ \phi_1^{(0)\prime\prime\prime} & + & (\alpha_1^{(0)}+\zeta_1^{(0)})\phi_1^{(0)\prime\prime} & + & \alpha_1^{(0)}\zeta_1^{(0)}\phi_1^{(0)\prime} & = & 0\end{array}\right\}\ \text{as}\ y\to\infty \tag{4.24}$$

where $\zeta_1^{(0)}=\sqrt{\alpha_1^{(0)2}+iR(\alpha_1^{(0)}-\beta)}\,.$

4.1.4 Mean-flow distortion

Substituting (4.20) into (4.8) gives,

$$L_0[\psi_0]=|A_1|^2p_0(y)e^{-\tau_0\xi}\,, \tag{4.25}$$

where p_0 and τ_0 are,

$$p_0(y)=iR\left[\left(\alpha_1\frac{\mathrm{d}\widetilde{\phi}_1}{\mathrm{d}y}+\widetilde{\alpha}_1\widetilde{\phi}_1\frac{\mathrm{d}}{\mathrm{d}y}\right)\left(\frac{\mathrm{d}^2}{\mathrm{d}y^2}-\alpha_1^2\right)\phi_1-\left(\widetilde{\alpha}_1\frac{\mathrm{d}\phi_1}{\mathrm{d}y}+\alpha_1\phi_1\frac{\mathrm{d}}{\mathrm{d}y}\right)\left(\frac{\mathrm{d}^2}{\mathrm{d}y^2}-\widetilde{\alpha}_1^2\right)\widetilde{\phi}_1\right], \tag{4.26}$$

$$\tau_0=\alpha_1-\widetilde{\alpha}_1=2\alpha_{1i}\,. \tag{4.27}$$

Now solve (4.25) by firstly solving the associated homogeneous equation. The similarity between the basic flow and the mean-flow distortion lead to seeking a solution of the form

$$\begin{aligned}\psi_0(\xi,y) &= |A_1|^2(1+\epsilon\xi)^{(m+1)/2}\phi_0\left(y(1+\epsilon\xi)^{-(1-m)/2}\right)e^{-\kappa\xi}\,, && (4.28)\\ &= |A_1|^2\Big[\phi_0(y)+\tfrac{1}{2}\epsilon\xi\left\{(m+1)\phi_0(y)-(1-m)y\phi_0'(y)\right\}\\ &\quad +\ O(\epsilon^2)\Big]e^{-\kappa\xi} && (4.29)\end{aligned}$$

as $\epsilon \to 0$, where ϕ_0 is a normalized function. Substituting (4.29) and (4.19) into the left-hand side of (4.25) will give an ordinary differential equation for ϕ_0,

$$\begin{aligned}&\left[\frac{\mathrm{d}^4}{\mathrm{d}y^4} + \tfrac{1}{2}r^2(m+1)F_0(y)\frac{\mathrm{d}^3}{\mathrm{d}y^3} + \left\{R\kappa - \tfrac{1}{2}r^2(3m-1)\right\}F_0'(y)\frac{\mathrm{d}^2}{\mathrm{d}y^2}\right.\\ &\left.-\tfrac{1}{2}r^2(3m-1)F_0''(y)\frac{\mathrm{d}}{\mathrm{d}y} + \left\{\tfrac{1}{2}r^2(m+1) - R\kappa\right\}F_0'''(y)\right]\phi_0(y) = 0\,.\end{aligned} \tag{4.30}$$

Consider the asymptotic solution of (4.30) as $y \to \infty$. The Falkner–Skan boundary layer permits a small constant component of velocity v in the far-field and as $y \to \infty$,

$$F_0(y) \sim y + a,\;\; F_0'(y) \to 1,\;\; F_0''(y) \to 0 \;\text{ and }\; F_0'''(y) \to 0\,, \tag{4.31}$$

where a is a constant. Using (4.31), (4.30) reduces to

$$\left[\frac{\mathrm{d}^4}{\mathrm{d}y^4} + \tfrac{1}{2}r^2(m+1)(y+a)\frac{\mathrm{d}^3}{\mathrm{d}y^3} + \left\{R\kappa - \tfrac{1}{2}r^2(3m-1)\right\}\frac{\mathrm{d}^2}{\mathrm{d}y^2}\right]\phi_0(y) = 0 \tag{4.32}$$

in the far-field.

The asymptotic solution for ϕ_0 is found to be,

$$\begin{aligned}\phi_0(y) \sim A + B(y+a) + C(y+a)^{-3}e^{-r^2(m+1)(y+a)^2/4} +&\\ D(y+a)^{\left\{r^2(5m+1)-2R\kappa\right\}/r^2(m+1)} \quad \text{as} \;\; y \to \infty\,.&\end{aligned} \tag{4.33}$$

For the velocity in the far-field to vanish except for a small constant component v we take boundary conditions that ensure

$$B = D = 0\,. \tag{4.34}$$

The boundary conditions for ϕ_0 are

$$\phi_0(0) = \phi_0'(0) = 0\,, \tag{4.35}$$

$$\left.\begin{array}{rcccl}(y+a)\phi_0'' & - & (4mr^2 - 2R\tau_0)\phi_0'/r^2(m+1) & = & 0\\ \phi_0''' & + & \tfrac{1}{2}r^2(m+1)(y+a)\phi_0'' & = & 0\end{array}\right\} \text{ as } \; y \to \infty\,. \tag{4.36}$$

Let κ_0 be the least eigenvalue of (4.32), (4.35) and (4.36) and assume that all other modes decay fast enough such that only one mode of the complementary function need be considered.

Now search for a particular solution of the form

$$\psi_0(\xi,y) = |A_1|^2\frac{\gamma}{\tau_0-\kappa_0}\Big[g_0(y)+\tfrac{1}{2}\epsilon\xi\left\{(m+1)g_0(y)-(1-m)yg_0'(y)\right\}+O(\epsilon^2)\Big]e^{-\tau_0\xi}\ , \tag{4.37}$$

where g_0 is a normalized function, γ a real constant and the singularity when $\kappa_0=\tau_0$ ensures the particular solution is valid for all τ_0.

Following the method for solving the homogeneous equation, the ordinary differential equation for g_0 will be

$$\left[\frac{\mathrm{d}^4}{\mathrm{d}y^4}+\tfrac{1}{2}r^2(m+1)F_0(y)\frac{\mathrm{d}^3}{\mathrm{d}y^3}+\left\{R\tau_0-\tfrac{1}{2}r^2(3m-1)\right\}F_0'(y)\frac{\mathrm{d}^2}{\mathrm{d}y^2}\right.$$
$$\left.-\tfrac{1}{2}r^2(3m-1)F_0''(y)\frac{\mathrm{d}}{\mathrm{d}y}+\left\{\tfrac{1}{2}r^2(m+1)-R\tau_0\right\}F_0'''(y)\right]\frac{\gamma}{\tau_0-\kappa_0}g_0(y)=p_0(y)\ . \tag{4.38}$$

Writing

$$G_0(y)=\frac{\gamma}{\tau_0-\kappa_0}g_0(y)\ , \tag{4.39}$$

and noting that $p_0\to 0$ as $y\to\infty$, gives boundary conditions of the same form as in the homogeneous case, namely

$$G_0(0)=G_0'(0)=0\ , \tag{4.40}$$

$$\left.\begin{array}{rcrcl}(y+a)G_0'' & - & (4mr^2-2R\tau_0)G_0'/r^2(m+1) & = & 0\\ G_0''' & + & \tfrac{1}{2}r^2(m+1)(y+a)G_0'' & = & 0\end{array}\right\}\ \text{as}\ y\to\infty\ . \tag{4.41}$$

The constant γ is chosen to normalize g_0. In the weakly nonlinear regime the growth rate $(-\alpha_{1i})$ of disturbances is small and because $\tau_0=2\alpha_{1i}$ then τ_0 is also small and may be assumed to be $O(\epsilon)$. In practice, the eigenvalues κ_n are all found to be positive and and hence the solution of the homogeneous equation may be ignored. This assumption is still valid even if $\kappa_0=O(\tau_0)$ because the singularity when $\kappa_0=\tau_0$ ensures that the particular solution (4.37) dominates the solution.

4.1.5 Harmonic disturbance

Represent the particular solution of (4.10) as,

$$\psi_2(\xi,y)=A_1^2g_2(y)e^{i\tau_2\xi}\ , \tag{4.42}$$

where again g_2 is a normalized function. The imaginary parts of the eigenvalues of the homogeneous equation $L_2[\psi_2] = 0$ are found to be greater than $\Im(\tau_2)$ and hence the solution of the homogeneous equation and any singularities of the particular solution may be ignored. Then equation (4.10) to leading order becomes,

$$\left[\left(\frac{\mathrm{d}^2}{\mathrm{d}y^2} - \tau_2^2\right)^2 - iR\left\{\left(-2\beta + \tau_2\frac{\mathrm{d}F_0}{\mathrm{d}y}\right)\left(\frac{\mathrm{d}^2}{\mathrm{d}y^2} - \tau_2^2\right) - \tau_2\frac{\mathrm{d}^3F_0}{\mathrm{d}y^3}\right\}\right] g_2(y) = p_2(y)\,, \tag{4.43}$$

where

$$\begin{aligned} p_2(y) &= i\alpha_1 R\left(\frac{\mathrm{d}\phi_1}{\mathrm{d}y} - \phi_1\frac{\mathrm{d}}{\mathrm{d}y}\right)\left(\frac{\mathrm{d}^2}{\mathrm{d}y^2} - \alpha_1^2\right)\phi_1\,, & (4.44)\\ \tau_2 &= 2\alpha_1\,. & (4.45) \end{aligned}$$

The harmonic disturbance g_2 satisfies an inhomogeneous Orr–Sommerfeld equation (4.43). The boundary conditions will be the same as for the homogeneous Orr–Sommerfeld equation,

$$g_2(0) = g_2'(0) = 0\,, \tag{4.46}$$

$$\left.\begin{aligned} g_2'' + (\tau_2+\zeta_2)\,g_2' + \tau_2\zeta_2 g_2 &= 0\\ g_2''' + (\tau_2+\zeta_2)\,g_2'' + \tau_2\zeta_2 g_2' &= 0 \end{aligned}\right\} \text{ as } y \to \infty\,, \tag{4.47}$$

where $\zeta_2 = \sqrt{\tau_2^2 + iR(\tau_2 - 2\beta)}$. The two boundary conditions (4.47) applied as $y \to \infty$ take the same form as (4.24), the boundary conditions as $y \to \infty$ for the homogeneous Orr–Sommerfeld equation. In both cases the boundary conditions ensure that the solution does not grow exponentially as $y \to \infty$. For inhomogeneous Orr–Sommerfeld equations (such as (4.43)) the exponentially growing contributions to the general solution are from the complementary function, that is from the solution of the associated homogeneous equation. Hence the boundary conditions required to destroy the exponentially growing terms are the same as for the homogeneous equation.

4.1.6 Fundamental disturbance

On having already assumed the form of the fundamental disturbance (4.20), then using (4.37) and (4.42), (4.9) becomes

$$\left[\left(\frac{\partial^2}{\partial y^2}+\frac{\partial^2}{\partial \xi^2}\right)^2 - R\left\{\left(-i\beta+\frac{\mathrm{d}F_0}{\mathrm{d}y}\frac{\partial}{\partial \xi}\right)\left(\frac{\partial^2}{\partial y^2}+\frac{\partial^2}{\partial \xi^2}\right)-\frac{\mathrm{d}^3F_0}{\mathrm{d}y^3}\frac{\partial}{\partial \xi}\right\}\right]\psi_1 =$$

$$A_1|A_1|^2\left[\frac{\gamma}{\tau_0-\kappa_0}q_0(y)+q_2(y)\right]e^{i\tau_1\xi}\ , \quad (4.48)$$

where

$$\begin{aligned} q_0(y) \;&=\; R\left\{\left(i\alpha_1\frac{\mathrm{d}g_0}{\mathrm{d}y}+\tau_0 g_0\frac{\mathrm{d}}{\mathrm{d}y}\right)\left(\frac{\mathrm{d}^2}{\mathrm{d}y^2}-\alpha_1^2\right)\phi_1-\left(\tau_0\frac{\mathrm{d}\phi_1}{\mathrm{d}y}+i\alpha_1\phi_1\frac{\mathrm{d}}{\mathrm{d}y}\right)\right.\\ &\left.\left(\frac{\mathrm{d}^2}{\mathrm{d}y^2}+\tau_0^2\right)g_0\right\}\ , \qquad (4.49)\\ q_2(y) \;&=\; iR\left\{\left(\tau_2\frac{\mathrm{d}\widetilde{\phi}_1}{\mathrm{d}y}+\widetilde{\alpha}_1\widetilde{\phi}_1\frac{\mathrm{d}}{\mathrm{d}y}\right)\left(\frac{\mathrm{d}^2}{\mathrm{d}y^2}-\tau_2^2\right)g_2-\left(\widetilde{\alpha}_1\frac{\mathrm{d}g_2}{\mathrm{d}y}+\tau_2 g_2\frac{\mathrm{d}}{\mathrm{d}y}\right)\right.\\ &\left.\left(\frac{\mathrm{d}^2}{\mathrm{d}y^2}-\widetilde{\alpha}_1^2\right)\widetilde{\phi}_1\right\}\ , \qquad (4.50)\\ \tau_1 \;&=\; 2\alpha_1-\widetilde{\alpha}_1=\alpha_1+2i\alpha_{1i}\ . \qquad (4.51) \end{aligned}$$

Once again the solution of (4.48) will be the solution of the homogeneous equation plus a particular solution. The homogeneous equation is simply the Orr–Sommerfeld equation (cf. §4.1.3). As for the mean-flow distortion, order the imaginary parts of the eigenvalues, say $\alpha_{1i}^{(0)}<\alpha_{1i}^{(1)}<\ldots<\alpha_{1i}^{(n)}$, and assume that for $n\geq 1$ the growth of these modes will be significantly less than for the mode with $n=0$. Hence approximate the solution of the homogeneous equation by $\phi_1^{(0)}(y)\exp\left(i\alpha_1^{(0)}\xi\right)$ and as for the mean-flow distortion then consider the case when $\tau_1=\alpha_1^{(0)}$.

Consider the particular solution expanded in terms of the eigenfunctions of the homogeneous equation and then the coefficient of $\phi_1^{(0)}\exp\left(i\tau_1\xi\right)$ will be of the form $C/(\tau_1-\alpha_1^{(0)})$ where C is a constant. Take out this term explicitly from the particular solution and then add another solution of the homogeneous equation such that the full solution is then valid even when $\tau_1=\alpha_1^{(0)}$. The full solution may be written as

$$\psi_1(\xi,y)=A_1\left[\left\{e^{i\alpha_1^{(0)}\xi}+|A_1|^2\left(\frac{\gamma}{\tau_0-\kappa_0}\lambda_0+\lambda_2\right)\frac{e^{i\tau_1\xi}-e^{i\alpha_1^{(0)}\xi}}{\tau_1-\alpha_1^{(0)}}\right\}\phi_1^{(0)}(y)+\right.$$

$$\left.|A_1|^2\left\{\frac{\gamma}{\tau_0-\kappa_0}f_0(y)+f_2(y)\right\}e^{i\tau_1\xi}\right]\ . \quad (4.52)$$

Define the amplitude at the origin to be

$$A_1 = \frac{\partial^2 \psi_1}{\partial y^2} \Big|_{(\xi,y)=(0,0)} \ . \tag{4.53}$$

The second derivative is used as this is the first non-zero y derivative of ψ_1 at the origin (due to the origin being located on the boundary). For (4.52) to satisfy the definition of A_1 (4.53) the normalizing conditions are defined to be,

$$\phi_1^{(0)\prime\prime}(0) = 1 \ \text{ and } \ f_0''(0) = f_2''(0) = 0\,. \tag{4.54}$$

The constants λ_0 and λ_2 in (4.52) are determined such that f_0 and f_2 satisfy the normalizing conditions (4.54).

The constants λ_0, λ_2 and the functions f_0, f_2 will be evaluated by substituting (4.52) into (4.48) which, after writing

$$\mathcal{L} = \left[\left(\frac{\partial^2}{\partial y^2} - \tau_1^2 \right)^2 - R \left\{ \left(-i\beta + i\tau_1 \frac{\mathrm{d}F_0}{\mathrm{d}y} \right) \left(\frac{\partial^2}{\partial y^2} - \tau_1^2 \right) - i\tau_1 \frac{\mathrm{d}^3 F_0}{\mathrm{d}y^3} \right\} \right] \tag{4.55}$$

will result in the following equations for f_0 and f_2:

$$\begin{aligned} \mathcal{L}[f_0] &= q_0(y) - \frac{\lambda_0}{\tau_1 - \alpha_1^{(0)}} \mathcal{L}[\phi_1^{(0)}(y)]\,, & (4.56)\\ \mathcal{L}[f_2] &= q_2(y) - \frac{\lambda_2}{\tau_1 - \alpha_1^{(0)}} \mathcal{L}[\phi_1^{(0)}(y)]\,. & (4.57) \end{aligned}$$

Then writing

$$\begin{aligned} f_0(y) &= f_0^{(0)}(y) + \lambda_0 f_0^{(1)}(y)\,, & (4.58)\\ f_2(y) &= f_2^{(0)}(y) + \lambda_2 f_2^{(1)}(y)\,, & (4.59) \end{aligned}$$

such that for $i = 0, 2$

$$\begin{aligned} \mathcal{L}[f_i^{(0)}(y)] &= q_i(y)\,, & (4.60)\\ \mathcal{L}[f_i^{(1)}(y)] &= -\frac{1}{\tau_1 - \alpha_1^{(0)}} \mathcal{L}[\phi_1^{(0)}(y)]\,, & (4.61) \end{aligned}$$

we deduce

$$\begin{aligned} \lambda_0 &= -f_0^{(0)\prime\prime}(0)/f_0^{(1)\prime\prime}(0)\,, & (4.62)\\ \lambda_2 &= -f_2^{(0)\prime\prime}(0)/f_2^{(1)\prime\prime}(0)\,. & (4.63) \end{aligned}$$

The boundary conditions for f_0 and f_2 will be,

$$f_0(0) = f_0'(0) = 0\,, \tag{4.64}$$

$$f_2(0) = f_2'(0) = 0\,, \tag{4.65}$$

$$\left.\begin{array}{ccccccc} f_0'' & + & (\tau_1+\zeta_1)f_0' & + & \tau_1\zeta_1 f_0 & = & 0 \\ f_0''' & + & (\tau_1+\zeta_1)f_0'' & + & \tau_1\zeta_1 f_0' & = & 0 \end{array}\right\} \text{ as } y \to \infty\,, \tag{4.66}$$

$$\left.\begin{array}{ccccccc} f_2'' & + & (\tau_1+\zeta_1)f_2' & + & \tau_1\zeta_1 f_2 & = & 0 \\ f_2''' & + & (\tau_1+\zeta_1)f_2'' & + & \tau_1\zeta_1 f_2' & = & 0 \end{array}\right\} \text{ as } y \to \infty\,, \tag{4.67}$$

where $\zeta_1 = \sqrt{\tau_1^2 + iR(\tau_1 - \beta)}\,.$

4.1.7 Next approximation to ψ_1

Having taken $A_1\phi_1^{(0)}(y)\exp\left(i\alpha_1^{(0)}\xi\right)$ as the first approximation to ψ_1 and then solved (4.8), (4.9) and (4.10), the next approximation to ψ_1 may be found by comparing (4.52) with (4.20). Modified values for ϕ_1 and α_1 may then be recalculated as

$$\phi_1(y) = \frac{1}{A_1}\lim_{\xi\to 0}\psi_1(\xi, y) = \phi_1^{(0)}(y) + |A_1(0)|^2\left(\frac{\gamma}{2\alpha_{1i} - \kappa_0}f_0(y) + f_2(y)\right)\,, \tag{4.68}$$

$$\alpha_1 = \frac{1}{iA_1}\lim_{\substack{\xi\to 0\\ y\to 0}}\frac{\partial^3\psi_1(\xi, y)}{\partial\xi\partial y^2} = \alpha_1^{(0)} + |A_1(0)|^2\left(\frac{\gamma}{2\alpha_{1i} - \kappa_0}\lambda_0 + \lambda_2\right)\,. \tag{4.69}$$

The modified values of ϕ_1 and α_1 depend upon the magnitude of the disturbance at the origin. As $|A_1(0)| \to 0$ then $\phi_1 \to \phi_1^{(0)}$ and $\alpha_1 \to \alpha_1^{(0)}$, the expressions obtained from linear stability theory for infinitesimally small disturbances.

The damping rate is given by,

$$\alpha_{1i} = \alpha_{1i}^{(0)} + |A_1(0)|^2\left(\frac{\gamma}{2\alpha_{1i} - \kappa_0}\lambda_{0i} + \lambda_{2i}\right)\,. \tag{4.70}$$

Equation (4.70) is a quadratic in terms of α_{1i} and describes the relationship between the damping rate and the magnitude of the disturbance at the origin. The solution of (4.70) may be written as,

$$\alpha_{1i} = \tfrac{1}{4}(\kappa_0 + 2\alpha_{1i}^{(0)} + 2\lambda_{2i}|A_1(0)|^2)$$
$$\pm\tfrac{1}{4}\sqrt{(\kappa_0 + 2\alpha_{1i}^{(0)} + 2\lambda_{2i}|A_1(0)|^2)^2 - 8(\kappa_0\alpha_{1i}^{(0)} + \kappa_0|A_1(0)|^2\lambda_{2i} - \gamma|A_1(0)|^2\lambda_{0i})}\,, \tag{4.71}$$

where the negative root in (4.71) is chosen to ensure that $\alpha_{1i} \to \alpha_{1i}^{(0)}$ as $|A_1(0)| \to 0$.

If the disturbance equilibrates then $\alpha_{1i} = 0$ and the equilibration amplitude will be given by

$$|A_{1e}|^2 = \frac{-\alpha_{1i}^{(0)}}{\lambda_i} \, , \text{ where } \lambda_i = -\frac{\gamma}{\kappa_0}\lambda_{0i} + \lambda_{2i} \, , \tag{4.72}$$

and so we require that $-\alpha_{1i}^{(0)}/\lambda_i > 0$ for equilibration.

Having defined the amplitude of the fundamental disturbance at the origin by (4.53) then define the magnitude of the mean-flow distortion $A_0(\xi)$ and the fundamental disturbance $A_1(\xi)$ by

$$A_0(\xi) = \frac{\partial^2 \psi_0}{\partial y^2}|_{y=0} \, , \tag{4.73}$$

$$A_1(\xi) = \frac{\partial^2 \psi_1}{\partial y^2}|_{y=0} \, . \tag{4.74}$$

Then using (4.29) and (4.20) together with (4.73), (4.74) and the normalizing conditions leads to the following expressions for the growth of the mean-flow distortion and fundamental disturbance close to the origin:

$$A_0(\xi) = |A_1(0)|^2 \frac{\gamma}{2\alpha_{1i} - \kappa_0} e^{-2\alpha_{1i}\xi} \, , \tag{4.75}$$

$$|A_1(\xi)|^2 = |A_1(0)|^2 e^{-2\alpha_{1i}\xi} \, . \tag{4.76}$$

The wavenumber α_1 (4.69) close to the origin is dependent on the magnitude of the fundamental disturbance $|A_1(0)|$ at the origin. When considering the propagation of disturbances further than a *small* distance from the origin, a simple transformation of variable allows the origin to be relocated at various downstream locations. The wavenumber α_1 may be assumed to be dependent on $|A_1(\xi)|$ when considering a disturbance propagating downstream.

The amplitude A_1 will satisfy

$$\frac{\mathrm{d}A_1}{\mathrm{d}\xi} = i\alpha_1 A_1 \, , \tag{4.77}$$

because the fundamental disturbance (4.20) takes the same form as from the linear theory. On substituting (4.69) into (4.77), we find

$$\frac{\mathrm{d}A_1}{\mathrm{d}\xi} = i\alpha_1^{(0)} A_1 + i\left(\frac{\gamma}{\tau_0 - \kappa_0}\lambda_0 + \lambda_2\right)|A_1|^2 A_1 \, , \tag{4.78}$$

which describes the weakly nonlinear development of (small) finite-amplitude disturbances.

4.1.8 Weakly nonlinear stability of laminar boundary-layer flow over an aerofoil

In Chapter 3 the amplification of boundary-layer disturbances with a fixed frequency was calculated by using (3.48), having firstly obtained a polynomial expression for $\alpha_i(x)$. The amplification of fixed frequency weakly nonlinear disturbances may also be calculated by using (3.48) because the disturbances take the same form as in the linear theory. At each station a weakly nonlinear correction to $\alpha_{1i}^{(0)}$ may be made following (4.70). The modified values of α_{1i} may then be used (following the procedure described in §3.3) to calculate the amplification of boundary-layer disturbances with fixed frequency.

The correction to $\alpha_{1i}^{(0)}$ involves the constants γ, κ, λ_{0i}, λ_{2i} and the amplitude $|A_1(0)|$. The constants may be calculated at each station over the aerofoil. The origin is then relocated at each station with the amplitude $|A_1(0)|$ determined as follows.

The initial amplitude $|A_1(0)|$ at station 1 may be chosen fairly arbitrarily. The only assumption made thus far about A_1 is that it is small enough to truncate the Fourier series expansion (4.5) by neglecting terms higher than second degree in A_1. Having chosen a suitable value for $|A_1(0)|$ at station 1 then α_{1i} at station 1 may be calculated. Then the growth of the amplitude $|A_1|$ between stations 1 and 2 may be approximated using (4.76). This will provide the value of $|A_1(0)|$ used for the weakly nonlinear correction at station 2. This process may be repeated to provide the value of $|A_1(0)|$ at each station over the aerofoil.

The choice of $|A_1(0)|$ at station 1 is valid if the final value of $|A_1(0)|$ used for station 12 is still small enough to ensure the Fourier series may be truncated. In practice the most significant weakly nonlinear correction is obtained when $|A_1(0)|$ at station 12 is $O(10^{-1})$.

In §3.5.4 the validity of the quasi-parallel approximation was discussed. In addition to the approximations already discussed, the calculation of $|A_1(0)|$ at each station also involves a similar approximation. Previously the velocity profile was assumed to be little changed over one wavelength. The use of (4.76) to calculate a suitable value for $|A_1(0)|$ at the next station rests on the assumption that the velocity profile is unchanged between the two stations. This method describes a practical approach to calculate realistic values of $|A_1(0)|$ to be used at each station. Between each station there is a continuous development of the velocity profile. When calculating the growth of $|A_1|$ between each station the velocity profile is assumed to be unchanged. The assumption that the velocity profile changes only at each station and not continuously is only used to enable a practical method to calculate suitable values of $|A_1(0)|$. Clearly this may be improved by taking more stations closer together.

4.2 The method of compound matrices (for inhomogeneous problems)

The method of compound matrices used for solving stiff, homogeneous, ordinary differential equations is discussed in §3.4. The method may be extended (see Davey [10]) to solve inhomogeneous problems such as the fourth-order ordinary differential equation,

$$L[\phi] = \phi^{iv} - a_1\phi''' - a_2\phi'' - a_3\phi' - a_4\phi = r \, , \tag{4.79}$$

where r is a given function of the independent variable.

The solution ϕ may be written as the sum of the complementary function plus a particular integral. Following the method described in §3.4, let ϕ_1 and ϕ_2 be two linearly independent solutions of the homogeneous equation $L[\phi_i] = 0$ and let ψ be any solution of the inhomogeneous equation $L[\psi] = r$.

Consider the solution matrix

$$\Psi = \begin{pmatrix} \psi & \phi_1 & \phi_2 \\ \psi' & \phi_1' & \phi_2' \\ \psi'' & \phi_1'' & \phi_2'' \\ \psi''' & \phi_1''' & \phi_2''' \end{pmatrix} \tag{4.80}$$

from which four (3×3) matrix determinants may be extracted (referred to as the 'minors' of the (4.80)).

The vector $\mathbf{z} = [z_1, z_2, z_3, z_4]^{\mathrm{T}}$ may be constructed from the four minors of (4.80) such that

$$\begin{aligned}
z_1 &= \psi(\phi_1'\phi_2'' - \phi_1''\phi_2') - \phi_1(\psi'\phi_2'' - \psi''\phi_2') + \phi_2(\psi'\phi_1'' - \psi''\phi_1') \,, && (4.81)\\
z_2 &= \psi(\phi_1'\phi_2''' - \phi_1'''\phi_2') - \phi_1(\psi'\phi_2''' - \psi'''\phi_2') + \phi_2(\psi'\phi_1''' - \psi'''\phi_1') \,, && (4.82)\\
z_3 &= \psi(\phi_1''\phi_2''' - \phi_1'''\phi_2'') - \phi_1(\psi''\phi_2''' - \psi'''\phi_2'') + \phi_2(\psi''\phi_1''' - \psi'''\phi_1'') \,, && (4.83)\\
z_4 &= \psi'(\phi_1''\phi_2''' - \phi_1'''\phi_2'') - \phi_1'(\psi''\phi_2''' - \psi'''\phi_2'') + \phi_2'(\psi''\phi_1''' - \psi'''\phi_1'') \,. && (4.84)
\end{aligned}$$

Recall from §3.4.3 the construction of the vector $\mathbf{y}$ and the resulting system of six, first order equations (3.76) from $\mathbf{y}'$. On differentiating $\mathbf{z}$ and using (4.79) the following system of four, first order equations may be derived

$$\begin{aligned}
z_1' &= z_2 \,, && (4.85)\\
z_2' &= a_2 z_1 + a_1 z_2 + z_3 + r y_1 \,, && (4.86)\\
z_3' &= -a_3 z_1 + a_1 z_3 + z_4 + r y_2 \,, && (4.87)\\
z_4' &= a_4 z_1 + a_1 z_4 + r y_4 \,. && (4.88)
\end{aligned}$$

When solving inhomogeneous problems of the form of (4.79), the vectors $\mathbf{y}$ and $\mathbf{z}$ must be calculated simultaneously by using the two coupled systems of six and four first order equations for $\mathbf{y}'$ and $\mathbf{z}'$ respectively.

Assume that there exist constants C_1 and C_2 such that the solution ϕ may be written as

$$\phi = C_1\phi_1 + C_2\phi_2 + \psi \,, \qquad (4.89)$$

and similarly for ϕ', ϕ'' and ϕ'''. The constants C_1 and C_2 may be eliminated in four alternative ways resulting in the set of equations for ϕ :

$$\begin{aligned}
y_1\phi'' - y_2\phi' + y_4\phi &= z_1 \,, && (4.90)\\
y_1\phi''' - y_3\phi' + y_5\phi &= z_2 \,, && (4.91)\\
y_2\phi''' - y_3\phi'' + y_6\phi &= z_3 \,, && (4.92)\\
y_4\phi''' - y_5\phi'' + y_6\phi' &= z_4 \,. && (4.93)
\end{aligned}$$

Any one of these four equations may be integrated to evaluate ϕ.

To ensure numerical stability the direction of integration of (say) (4.90) must be in the opposite sense to the direction followed when evaluating the coefficients y_1—y_6 and z_1—z_4. Following the method used when solving the Orr–Sommerfeld equation (§3.4.3) the coefficients y_1—y_6 and z_1—z_4 were calculated on integration from ∞ to 0. The asymptotic form of ϕ_1 and ϕ_2 may easily be calculated far away from the boundary layer. Then the coefficients y_1—y_6 may be set according to their asymptotic form (such as (3.78)).

The asymptotic form of ψ for the three equations of interest here, namely (4.8), (4.9) and (4.10), may not be derived so easily far away from the boundary layer. However on inspection it is seen that $|\psi|$ for all three equations will be exponentially small as $y \to \infty$. The initial vector (such as (3.78)) which $\mathbf{y}$ is set to at the start of the integration is normalized to ensure the components of $\mathbf{y}$ are $O(1)$. Multiplying the components of $\mathbf{z}$ with the same normalizing factor ensures the components of $\mathbf{z}$ will be approximately $O(|\psi|)$ at the start of the integration. However $|\psi|$ will be exponentially small as $y \to \infty$ and in practice

$$\mathbf{z} = [0, 0, 0, 0]^{\mathrm{T}}, \tag{4.94}$$

is used at the start of the integration.

4.3 Results

4.3.1 Comparison with results from Itoh

The analysis presented by Itoh [25] developed for the Blasius boundary layer leads to an expression for the equilibration amplitude $|A_{1e}|$ which may occur if $\alpha_{1i}^{(0)} > 0$ and $\lambda_i < 0$, or if $\alpha_{1i}^{(0)} < 0$ and $\lambda_i > 0$, (see (4.72)). Brief numerical results are presented in Itoh [25]. Results are presented below which compare calculated values of $|A_{1e}|$ and λ_i with those obtained by Itoh.

Table 4.1 shows reasonable agreement between the calculated values of $|A_{1e}|$ using

R	β	$\alpha_1^{(0)}$	$\lvert A_{1e}\rvert$	$\lvert A_{1e}\rvert$ (Itoh)
1000	0.0688	$0.2046 - 0.0042i$	0.109	0.12
1000	0.086	$0.2463 - 0.0071i$	0.136	0.19
2000	0.0344	$0.1258 - 0.00075i$	0.067	0.06
2500	0.0344	$0.1286 - 0.0035i$	0.087	0.11
3000	0.0344	$0.1311 - 0.0055i$	0.080	0.14

Table 4.1: Comparison of equilibration amplitude $|A_{1e}|$.

R	β	$\alpha_1^{(0)}$	λ_i	λ_i (Itoh)
596.3	0.0907	$0.2433 + 0i$	0.169	> 0
540.0	0.1053	$0.2725 + 0i$	0.079	> 0
520.1	0.1173	$0.2971 + 0i$	0.045	> 0
519.1	0.1198	$0.3024 + 0i$	0.198	> 0
521.3	0.1248	$0.3131 + 0i$	-0.844	< 0
524.6	0.1271	$0.3182 + 0i$	-0.019	< 0
545.6	0.1332	$0.3326 + 0i$	-0.094	< 0

Table 4.2: Comparison of λ_i with R close to R_c.

the method of compound matrices and those given by Itoh. (The values listed in tables 4.1 and 4.2 attributed to Itoh were obtained from figures 1 and 2 in Itoh [25] and so may not be precisely what Itoh calculated.)

Itoh [25] plots the curve $\lambda_i = 0$ together with the marginal stability curve $\alpha_{1i}^{(0)} = 0$ for the Blasius boundary layer. The curves intersect at approximately $R = 520$, i.e. at the critical Reynolds number R_c. Table 4.2 shows a series of calculated values of λ_i moving along the marginal stability curve for the Blasius boundary layer (for R close to R_c). Clearly, λ_i changes sign where $R \approx 520$. The regions where $\lambda_i > 0$ and $\lambda_i < 0$ are also consistent with Itoh.

Comparisons with the numerical results from Itoh [25] are made in order to determine the accuracy of the results, (presented shortly in §4.3.2), obtained for the

Falkner–Skan boundary layer. The agreement with Itoh in table 4.1 is not as close as expected. Comparing numerical results without specific knowledge of the numerical schemes used, particularly if substantial increases in computational power have occurred since Itoh worked, may be difficult. Care has been taken to ensure the accuracy of the current results, and these results clearly show at worst reasonable agreement with Itoh.

Itoh [25] applied the outer boundary conditions for the mean-flow distortion, harmonic and fundamental disturbance at $y = 1$. This is surprising because $y = 1$ would not appear to be sufficiently far away from the boundary layer to be a suitable point to impose the outer boundary conditions. In the results presented in §4.3.2 the outer boundary conditions were imposed at $y = 8$. I hope that this has improved the accuracy of the numerical results obtained.

4.3.2 Tonal cases: 1, 2, 3 and 4

Results are presented for tonal cases 1, 2, 3 and 4, (see table 3.1 for details). For each case the amplification of disturbances with a fixed frequency is calculated by using a weakly nonlinear correction to $\alpha_1^{(0)}$ at each station over the aerofoil. The choice of $|A_1(0)|$ at station 1 for each case was fairly arbitrary. A range of values for $|A_1(0)|$ at station 1 was used in order to find the largest value of $|A_1(0)|$ such that at station 12 $|A_1|$ remained $O(10^{-1})$. From (4.69) it is seen that the weakly nonlinear correction to $\alpha_1^{(0)}$ is proportional to $|A_1(0)|^2$. Therefore the most significant corrections occur as $|A_1|$ approaches $O(10^{-1})$. Once $|A_1|$ is $O(10^{-1})$ then no further calculations are permitted because $|A_1|$ must remain small enough to allow the higher order terms in the Fourier series expansion of ψ to be ignored.

All the results presented are such that $|A_1|$ is $O(10^{-1})$ at station 12. The weakly nonlinear amplification is denoted by the solid curve for each case. For comparison the linear amplification is also shown with a dashed curve. Further, for case 1 streamwise mean-flow distortion and harmonic disturbance profiles are presented, at the frequency of the observed tone. Only results from the first, last and two intermediate stations are shown. Recall from §3.5.1 that the two intermediate stations (7 and 8) are approximately situated across the region where there is a change in the nature of the dominant stability mechanism.

Finally, a comparison between the linear eigenfunctions $|\phi_1^{(0)}|$, $|\phi_1^{(0)\prime}|$ and the fundamental disturbance functions $|\phi_1|$, $|\phi_1'|$ is shown for case 1, also at the frequency of the observed tone. The comparison is shown at the same four stations where mean-flow distortion and harmonic disturbance profiles were also presented. The linear eigenfunctions are denoted by the dashed curves and the fundamental disturbances by solid curves.

In all the figures containing mean-flow distortion, harmonic and fundamental disturbance profiles, the horizontal dotted line indicates the location of the critical layer.

Similar results for cases 2, 3 and 4 are not presented here. The features described in §4.4 relating to the figures of the various disturbance profiles are repeated in cases 2, 3 and 4.

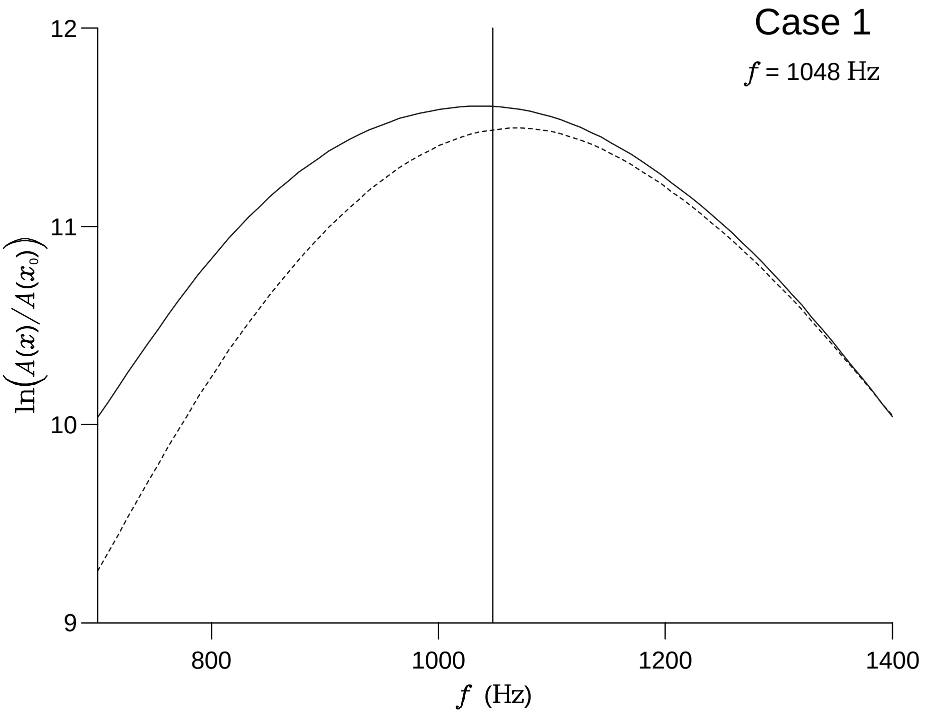

Figure 4.1: Amplification of boundary-layer instability waves of fixed frequency: —— weakly nonlinear, - - - linear, for case 1.

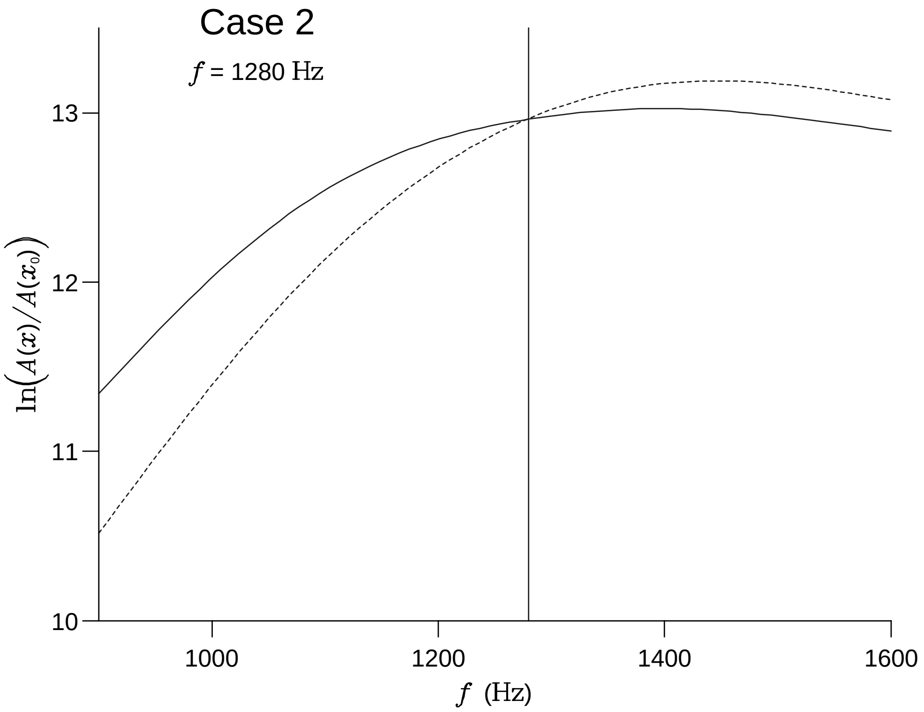

Figure 4.2: Amplification of boundary-layer instability waves of fixed frequency: —— weakly nonlinear, - - - linear, for case 2.

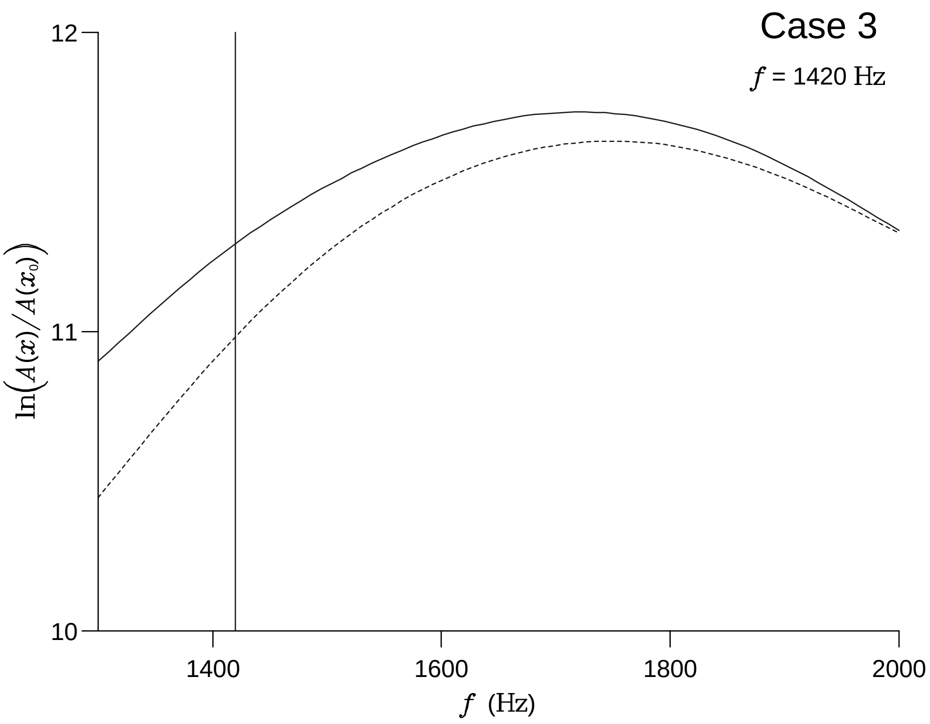

Figure 4.3: Amplification of boundary-layer instability waves of fixed frequency: —— weakly nonlinear, - - - linear, for case 3.

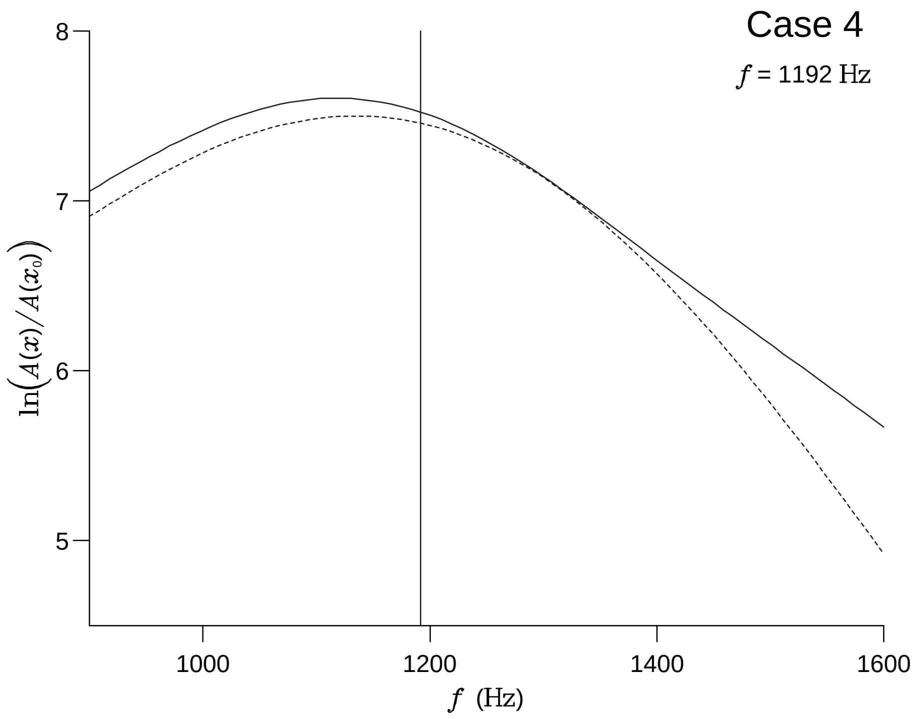

Figure 4.4: Amplification of boundary-layer instability waves of fixed frequency: —— weakly nonlinear, - - - linear, for case 4.

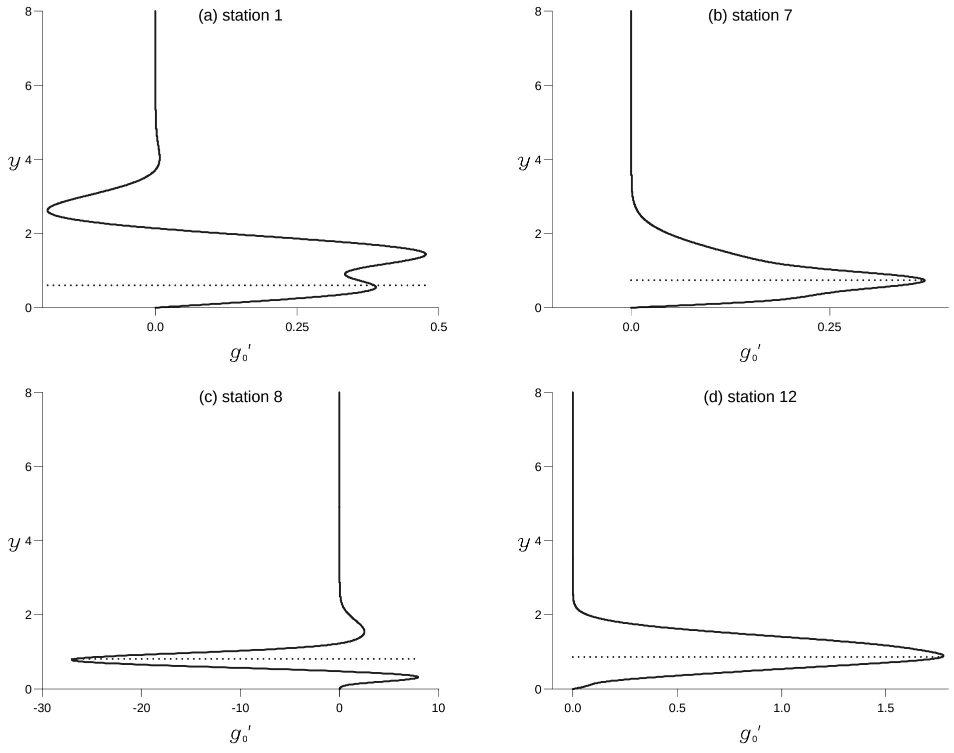

Figure 4.5: Streamwise mean-flow distortion profiles for case 1.

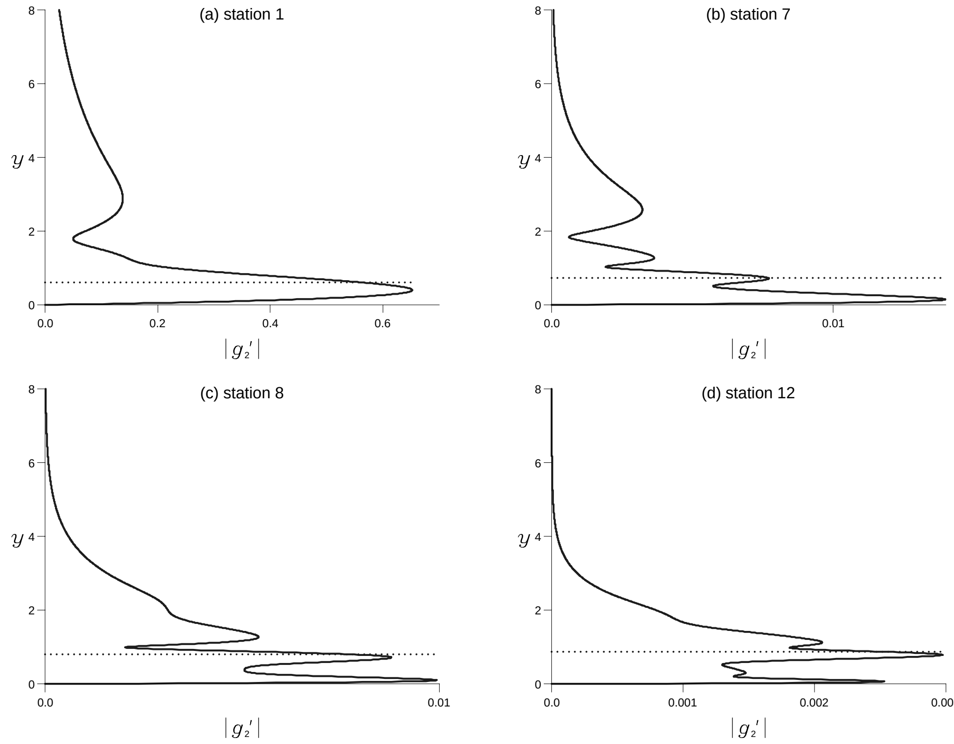

Figure 4.6: Streamwise harmonic disturbance profiles for case 1.

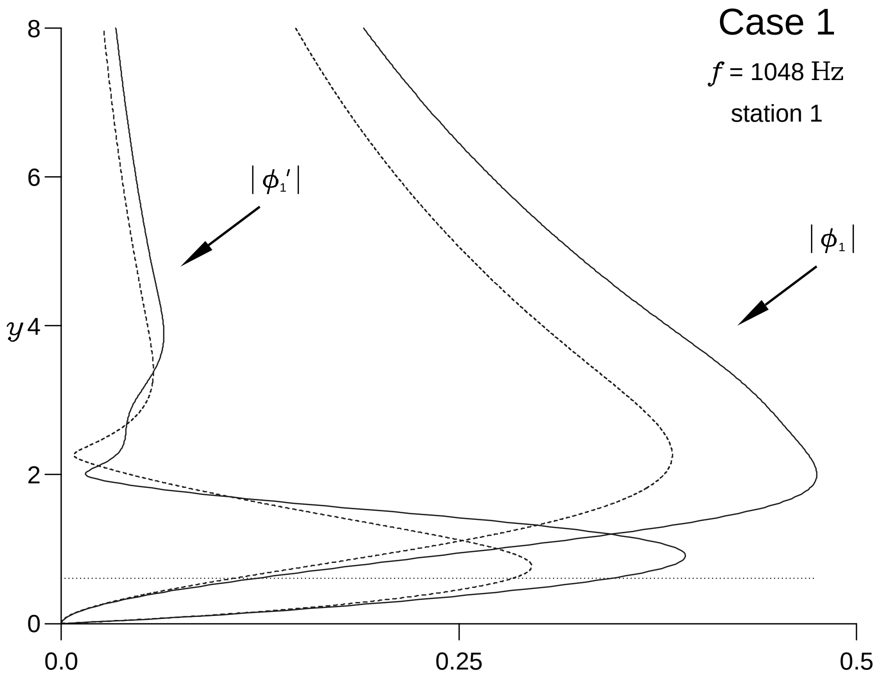

Figure 4.7: Streamwise and transverse fundamental disturbance profiles for case 1: —— weakly nonlinear, - - - linear.

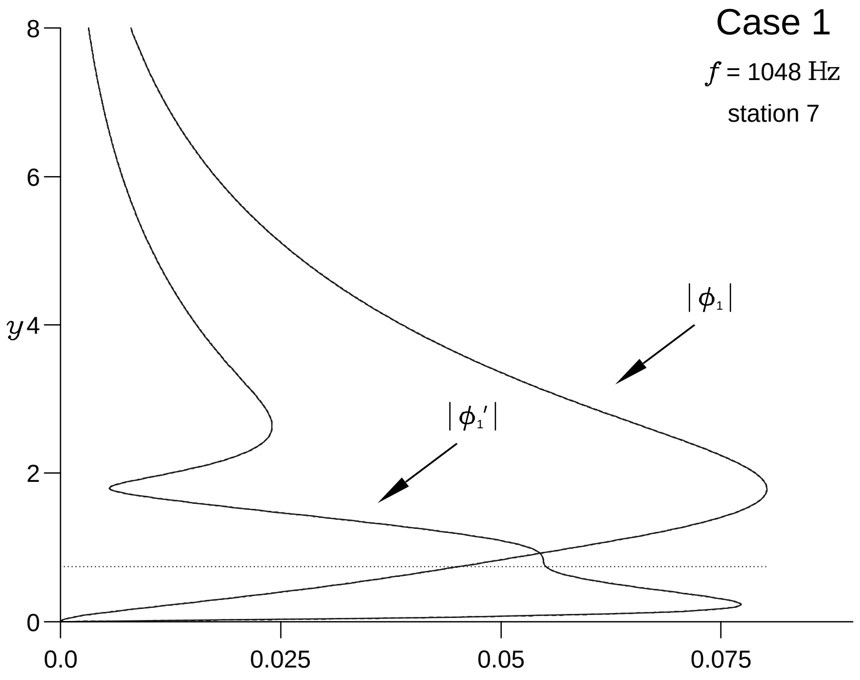

Figure 4.8: Streamwise and transverse fundamental disturbance profiles for case 1: —— weakly nonlinear, - - - linear.

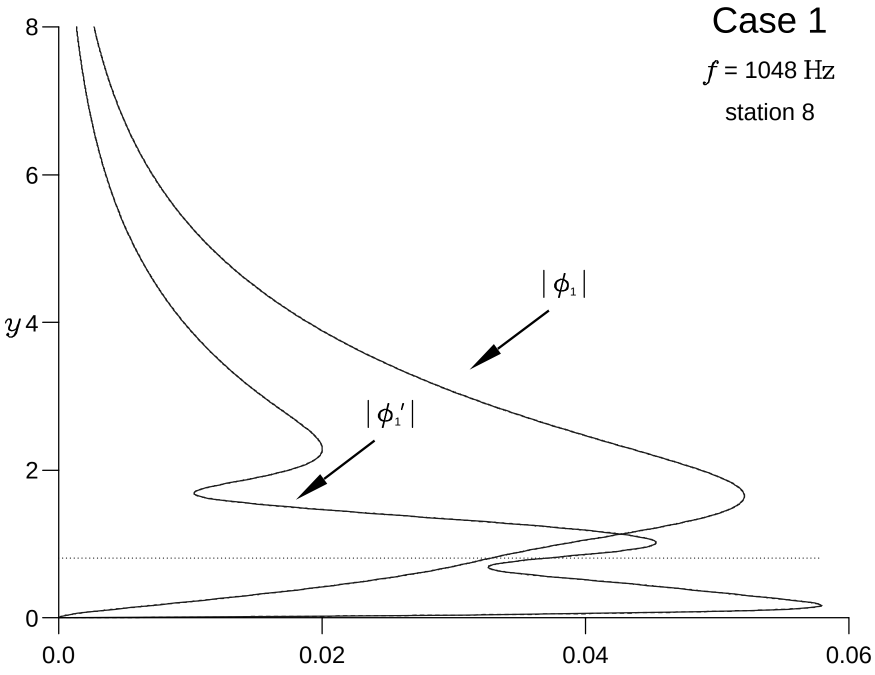

Figure 4.9: Streamwise and transverse fundamental disturbance profiles for case 1: —— weakly nonlinear, - - - linear.

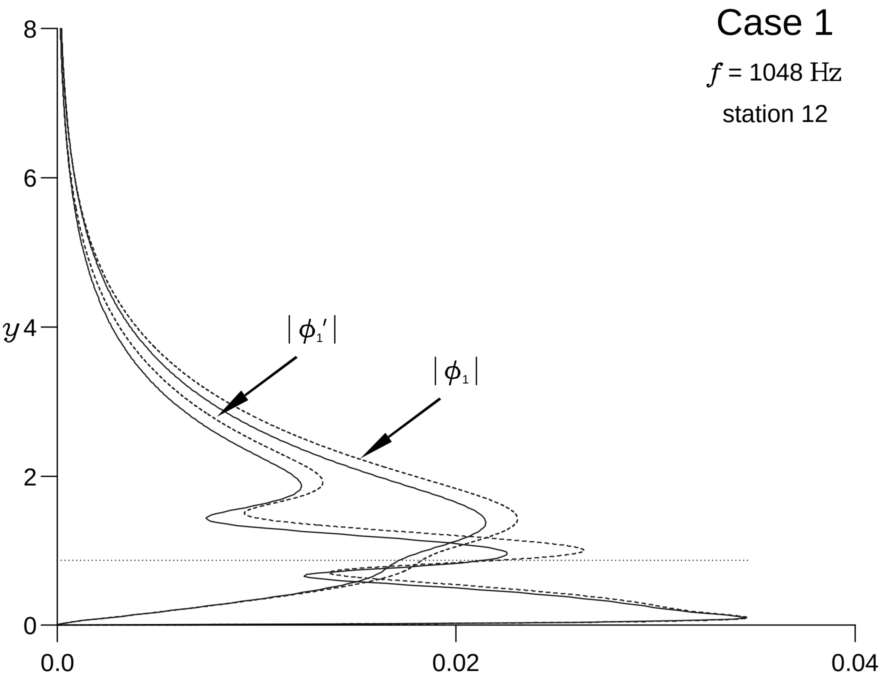

Figure 4.10: Streamwise and transverse fundamental disturbance profiles for case 1: —— weakly nonlinear, - - - linear.

4.4 Discussion

The amplification from stations 1 to 12 of disturbances with a fixed frequency for cases 1, 2, 3 and 4 is shown in figures 4.1, 4.2, 4.3 and 4.4 respectively. In each figure the weakly nonlinear amplification is shown with a solid line and the linear amplification with a dashed line. Once again the solid vertical line denotes the frequency of the observed tone.

Recall from §3.5.1 that the linear results predicted the frequency of the tone remarkably well for cases 1 and 4. For cases 2 and 3 the frequency prediction was within 25%. As discussed, the prediction error increased with increasing Reynolds number of the flow (that is $R = U_\infty c/\nu$). At higher Reynolds numbers the total amplification of the infinitesimal disturbances increased, and a linear description of these disturbances would become increasingly unrealistic. It was hoped that the inclusion of weak nonlinearity in the model would reduce the prediction error at higher Reynolds numbers.

For each case the frequency of the mode with maximum amplification obtained by using weakly nonlinear theory is slightly less than the frequency obtained using linear theory. For cases 1 and 4 the decrease is small, which was expected because linear theory had already been shown to accurately predict the tonal frequencies for these cases with lower Reynolds numbers. The inclusion of a weakly nonlinear correction at each station has not significantly altered the frequency prediction. This provides further evidence of the suitability of only using a linear prediction model for low Reynolds number flows.

For case 2 the frequency of the mode with maximum amplification predicted by using weakly nonlinear theory is 1370 Hz, a prediction error of 7% compared with 13% when only using linear theory. For case 3 the predicted frequency is now 1700 Hz, with prediction error 20% compared with 23% when only using linear theory.

Clearly the weakly nonlinear stability analysis has slightly decreased the frequency of the mode with maximum amplification in each case, compared with only using linear stability analysis. In fact cases 1, 2 and 4 all have prediction errors less than 10% when using the weakly nonlinear stability analysis. The inclusion of the extra terms in the Fourier expansion of the stream function ψ (4.7) (compared with a linear analysis) has decreased the predicted frequencies from those previously obtained. This reduction, particularly with higher Reynolds number flows, was desirable as the linear predictions were becoming increasingly too large.

The prediction error for case 3 is still relatively large (compared with cases 1, 2 and 4). The Reynolds number of the flow for case 3 is greater than for the other cases. Presumably, inclusion of further terms in the Fourier expansion of ψ would result in an improved prediction frequency. However, a full nonlinear analysis has not been attempted for case 3.

Having discussed the comparison between the weakly nonlinear and linear amplification results, the weakly nonlinear correction at individual stations on the aerofoil is considered. A significant weakly nonlinear correction may only be seen at several stations on the aerofoil. Intuitively, the weakly nonlinear correction would be expected to be most significant near the trailing edge of the aerofoil where the amplitude of the disturbances is greater than further upstream. Table 4.3 provides details of the weakly nonlinear correction to the wavenumber α_1 at each station, for case 1.

The results in table 4.3 reveal that the weakly nonlinear correction is significant near the trailing edge of the aerofoil *and* somewhat suprisingly when the flow is linearly stable. In this example the disturbance is linearly stable at stations 1 and 2. With the weakly nonlinear correction the disturbance at station 1 is less stable. From stations 2 to 8 there is no significant weakly nonlinear correction to $\alpha_1^{(0)}$. Any weakly nonlinear correction is only significant after the sixth decimal place.

This may be compared with the description presented in §3.5.1 whence the development of an instability downstream over the aerofoil was considered in two parts. Initially the disturbance was governed by the viscous Tollmien–Schlichting mechanism of instability. For case 1, a change in the dominant instability mechanism was shown to occur approximately between stations 7 and 8. Downstream of station 8 the disturbance was governed largely by inviscid dynamics. The majority of the amplification occurred downstream of station 8, (i.e. the growth rates associated with inviscid instabilities are typically an order of magnitude greater than corresponding viscous

station	$\alpha_1^{(0)}$	α_1
1	$0.179847 + 0.007752i$	$0.161526 + 0.002481i$
2	$0.202054 + 0.001497i$	$0.202054 + 0.001497i$
3	$0.236226 - 0.006513i$	$0.236226 - 0.006513i$
4	$0.271745 - 0.015877i$	$0.271745 - 0.015877i$
5	$0.309209 - 0.024876i$	$0.309209 - 0.024876i$
6	$0.348262 - 0.029921i$	$0.348262 - 0.029921i$
7	$0.395947 - 0.036062i$	$0.395947 - 0.036062i$
8	$0.489847 - 0.105807i$	$0.489848 - 0.105807i$
9	$0.545300 - 0.115110i$	$0.545336 - 0.115126i$
10	$0.567196 - 0.126202i$	$0.567430 - 0.126440i$
11	$0.649518 - 0.170151i$	$0.654790 - 0.169816i$
12	$0.756804 - 0.207224i$	$0.800370 - 0.214388i$

Table 4.3: Weakly nonlinear corrections to α_1 at stations 1 to 12 for case 1.

instability growth rates).

Comparison of $\alpha_1^{(0)}$ and α_1 in table 4.3 demonstrates that between stations 3 and 8 the disturbances remain approximately linear. The relatively small amplification of T–S waves (compared with inflexional waves) results in negligible weakly nonlinear corrections.

Downstream of station 8 the amplification increases rapidly through the inviscid dynamics of the inflexion point. By station 12 the weakly nonlinear correction to $\alpha_1^{(0)}$ is significant from the second decimal place. The difference between the growth rates $\alpha_{1i}^{(0)}$ and α_{1i} at station 12 is approximately 3.5%. The weakly nonlinear correction may appear small but recall that the growth of the disturbances is $\exp(-\alpha_{1i}x)$.

For case 1, streamwise mean-flow distortion and harmonic disturbance profiles are presented at stations 1, 7, 8 and 12 in figures 4.5 and 4.6 respectively. Figures 4.7, 4.8, 4.9 and 4.10 compare streamwise and transverse linear Orr–Sommerfeld eigenfunction profiles with the modified fundamental disturbance profiles given by (4.68), also at stations 1, 7, 8 and 12.

The features observed in figures 4.7 — 4.10 are consistent with those described from the data in table 4.3. The Orr–Sommerfeld eigenfunctions are normalized at each station such that $\phi_1^{(0)\prime\prime} = 1$. Hence the amplitude of these eigenfunctions may not be compared between stations (because the normalizing factor will vary). Only the characteristics of the shape of each profile may be considered. However, at each station the amplitude of the Orr–Sommerfeld eigenfunction may be compared with that of the corresponding fundamental and harmonic disturbance profiles.

The Orr–Sommerfeld eigenfunction profile coincides with the fundamental disturbance profile at stations 7 and 8. As discussed, between stations 3 and 8 the contribution from the weakly nonlinear corrections was expected to be minimal. The profiles at stations 1 and 12 reveal slight modifications. The disturbance at station 1 is stable and the streamwise profiles have the characteristic two-peaked shape described in §3.5.1. The disturbance at station 12 is highly unstable and the streamwise profiles have the characteristic three-peaked shape also described in §3.5.1. Figure 4.7 shows that the linear theory has under-estimated the magnitude of the fundamental disturbance profiles through the boundary layer. On the other hand, figure 4.10 shows that the linear theory has slightly over-estimated the magnitude of the fundamental disturbance profiles through the boundary layer.

These observations together with the results presented in table 4.3 confirm that weakly nonlinear corrections are significant near the trailing edge of the aerofoil (as expected), and when the flow is linearly stable. Changes in the total amplification calculated for disturbances with fixed frequency occur through modifications to the flow when it is stable as well as the modifications to the highly unstable flow. However, the destabilizing effect of the weakly nonlinear correction at station 1 will only modify the total amplification slightly. The change in $\alpha_1^{(0)}$ at station 1 will not significantly alter the amplification compared with the changes in $\alpha_1^{(0)}$ from stations 9 to 12. These modifications slightly reduce the frequency of the mode with maximum amplification calculated using linear theory. However, over most of the surface of the aerofoil the assumption that the disturbances remain linear appears to be valid.

In figures 4.7 — 4.10 the location of the critical layer only changes slightly between the stations. In §3.5.1 the contribution to the instability via Reynolds stresses centred about the critical layer was discussed.

Comparison of the streamwise harmonic disturbances (figure 4.6) with their corresponding fundamental disturbance profiles provides further evidence of the linearity of the disturbances. The structure of the harmonic disturbance profile is seen to become more complicated with distance downstream over the aerofoil. Up to four peaks may be present on moving through the boundary layer. On approaching station 12 the harmonic disturbance decays more rapidly with distance normal to the boundary. The disturbance becomes more concentrated inside the boundary layer. The disturbance has decayed almost to zero by $y = 4$. In contrast, the fundamental disturbance decays to zero at approximately $y = 8$. The decay of the fundamental mode outside of the boundary layer may be shown to be proportional to $\exp(-\alpha_{1r} y)$, (see §3.4.2 for details). Similarly, the decay of the harmonic mode outside of the boundary layer will be proportional to $\exp(-\tau_{2r} y) = \exp(-2\alpha_{1r} y)$. The decay of higher harmonics will be even more rapid.

At each station the magnitude of $|A_1||\phi_1'|$ may be compared with that of $|A_1|^2|g_2'|$ at various locations in the boundary layer. The ratio $|A_1||\phi_1'|/|A_1|^2|g_2'|$ is an estimate of the size of the fundamental compared with the harmonic disturbance. The ratio of the magnitude of the fundamental to the harmonic disturbance at stations 7 and 8 is $O(10^3)$. At station 12 the ratio has rapidly decreased. The ratio varies between 19.0 and 23.3 when calculated at each of the three peaks in $|\phi_1'|$ in figure 4.10, ($y =$ 0.1, 0.96 and 1.86). Harmonic disturbances occur through the nonlinear interaction of the fundamental mode with the mean-flow. The ratio of $O(10^3)$ at stations 7 and 8 for the magnitude of the fundamental to the harmonic disturbance compared with ≈ 20 at station 12 supports the assertion that weak nonlinearity is only significant near the trailing edge of the aerofoil.

A rough comparison may be made between this result and figure 2.10. In figure 2.10 frequency spectra are shown in the boundary layer 5 mm upstream of the trailing edge. (Station 12 is actually 9 mm upstream of the trailing edge.) The difference between the fundamental and harmonic disturbance is found to be 32.9 dB in 2.10(c). Using (2.3), the ratio of the amplitude of the fundamental to the harmonic disturbance will be $10^{(32.9/20)} \approx 44$. Both results confirm that a weakly nonlinear description of the flow appears to be a realistic model of the instabilities.

Finally, the streamwise mean-flow distortion profiles (figure 4.5) show that when the flow is unstable the significant distortion to the mean-flow will occur across the critical layer. Recall that the mean-flow distortion g_0 was normalized such $g_0''(0) = 1$. Hence (as before) the scales on the g_0' axis in each figure are not comparable. At station 1 the mean-flow distortion extends further away from the boundary than for the unstable stations. However, the actual mean-flow distortion $|A_1|^2 g_0'$ will be infinitesimal compared with the latter stations because at station 1, $|A_1|^2 \sim O(10^{-9})$ (for this case).

When the flow is unstable the mean-flow distortion is confined to inside the boundary layer. As previously stated, the mean-flow distortion appears to be across the critical layer. In the critical layer the phase velocity of the instability is equal to the mean-flow velocity. The Tollmien–Schlichting mechanism of instability is via the extraction of energy from the mean-flow through Reynolds stresses (which occur in the critical layer). Hence, the mean-flow distortion is significant about the location where the transfer of energy occurs. At station 12 the instability is no longer governed by the viscous Tollmien–Schlichting mechanism. The mean-flow distortion is still centred about the critical layer. It appears that at station 12 the same viscous mechanism determines the mean-flow distortion. Whether this would remain so is unclear. If the flow were to continue to develop and the inflexional instabilities continued to amplify then the interaction between the instabilities and the mean-flow would increase. With increasing Reynolds number the thickness of the critical layer decreases and it is questionable that the mean-flow distortion will remain centred about the critical layer. However at present the behaviour of the mean-flow distortion with larger Reynolds numbers is unknown.

Chapter 5

Conclusions

The aero-acoustic feedback models proposed by Tam [42], Wright [44], Longhouse [28], Fink [18] and Arbey & Bataille [3] (see Chapter 1), may all be simplified by breaking down each model into the following three components.

1. Formation of T–S waves in the pressure surface boundary layer.
2. Generation of sound through the diffraction of the T–S waves at the aerofoil trailing edge.
3. Feedback.

Tonal noise will only occur when all three components are present. To suppress the tonal noise, at least one of the components must be removed from the system.

The development of boundary-layer instability waves has been extensively investigated in Chapters 3 and 4.

The generation of sound by diffraction at a sharp edge has been investigated by numerous authors. (The work of Ffowcs-Williams and Hall, concerning the sound field radiated by a distribution of turbulent eddies close to the edge of a half-plane, was briefly mentioned in §1.2.)

The generation of sound by a T–S wave passing over a sharp edge was studied by Aizin [1]. He solved the problem by using the Wiener–Hopf technique. His analysis appears to be suitable for use in this problem. The following section briefly describes how Aizin employed the Wiener–Hopf technique to calculate the sound field resulting from the diffraction of a T–S wave at a sharp edge.

The feedback process described in all the aforementioned papers involves a coupling between acoustic waves propagating in the free stream and the boundary-layer instability waves. The acoustic waves travel upstream from the trailing edge of the aerofoil, thus completing the feedback loop. Boundary-layer instability waves are usually triggered by either imperfections in the boundary surface or from external sources in the free stream, commonly free-stream turbulence or sound waves.

In §5.2, the suitability of the aero-acoustic feedback model will be discussed. An alternative model will be proposed based on the observations and results presented in Chapters 2, 3 and 4.

Finally, suggestions for future work will be discussed.

5.1 Sound generation by a Tollmien–Schlichting wave at the end of a plate in a flow

The Wiener–Hopf technique is a method often used to solve linear partial differential equations analytically on semi-infinite intervals. The technique uses complex Fourier transforms and knowledge of their analytical properties to be able to reduce the p.d.e.'s to suitable algebraic equations. The final solution is found by taking inverse Fourier transforms. For a concise summary and examples of the Wiener–Hopf procedure see 'Modern Methods in Analytical Acoustics' [15].

Aizin [1] considers the diffraction of a T–S wave at the end of a flat plate in a uniform flow. The uniform flow is taken to be the Blasius boundary layer. Aizin only considers the problem with a T–S wave on one side of the plate. An aerofoil is a slender body, and on assuming it is long enough, (i.e. chord length $c \gg$ T–S wavelength λ_{TS}), to a first approximation the problem may be considered by replacing the aerofoil by a flat plate. The Blasius boundary layer may be replaced by a Falkner–Skan boundary layer with non-zero pressure gradient to further improve the model.

One would expect the fluctuating stresses exerted on the trailing edge of the aerofoil to be closely related to the diffracted sound field.

5.1.1 Set-up

A rigid semi-infinite plate is fixed on $y = 0$ for $x \leq 0$. On either side of the plate there exists a steady velocity profile $U_0(y)$, namely the Blasius boundary layer. A T–S wave propagates on the upper side of the plate ($y > 0$) towards the edge $(x, y) = (0, 0)$.

For low Mach number flows the problem may be solved in two stages.

Firstly, solve the problem of a T–S wave incident on the edge of the plate in the near-field, assuming incompressibility. (For low Mach number flows compressible effects in the near-field may be assumed to be negligible because the compressible stability equations reduce to the incompressible stability equations as $M = U_0/a_0 \rightarrow 0$.)

Secondly, compare the solution with that of a sound wave in the far-field. The flow is assumed to be compressible in the far-field because incompressible hydrodynamic perturbations decay exponentially whereas sound decays algebraically. The far-field will be dominated by sound.

As discussed in §3.5.1, for large enough Reynolds number R, the critical layer will be separate from the viscous layer. For $x > 0$ and large enough R, replace the viscous layer by a surface of discontinuity over which matching conditions are set. Figure 5.1 shows the set-up of the problem. Note that U_0' is discontinuous over the surface of discontinuity on $y = 0, x > 0$.

Express the velocity $\mathbf{u} = \mathbf{u_0} + \mathbf{u_1}$ as the sum of the basic flow $\mathbf{u_0} = (U_0(y), 0, 0)$ and a small perturbation $\mathbf{u_1}$. Similarly, the pressure p is the sum of the (constant) background pressure p_0 plus a small perturbation $p_1(x, y)\exp[i(\beta z - \omega t)]$. The velocity perturbation $\mathbf{u_1}$ may also be expressed in normal mode form,

$$\mathbf{u_1} = \left.\begin{array}{rr} [\mathbf{u_{TS}}(y)\exp(i\alpha_1 x) + \mathbf{u}_-(x, y)]\exp[i(\beta z - \omega t)] & x < 0 \\ \mathbf{u}_+(x, y)\exp[i(\beta z - \omega t)] & x > 0 \end{array}\right\}, \tag{5.1}$$

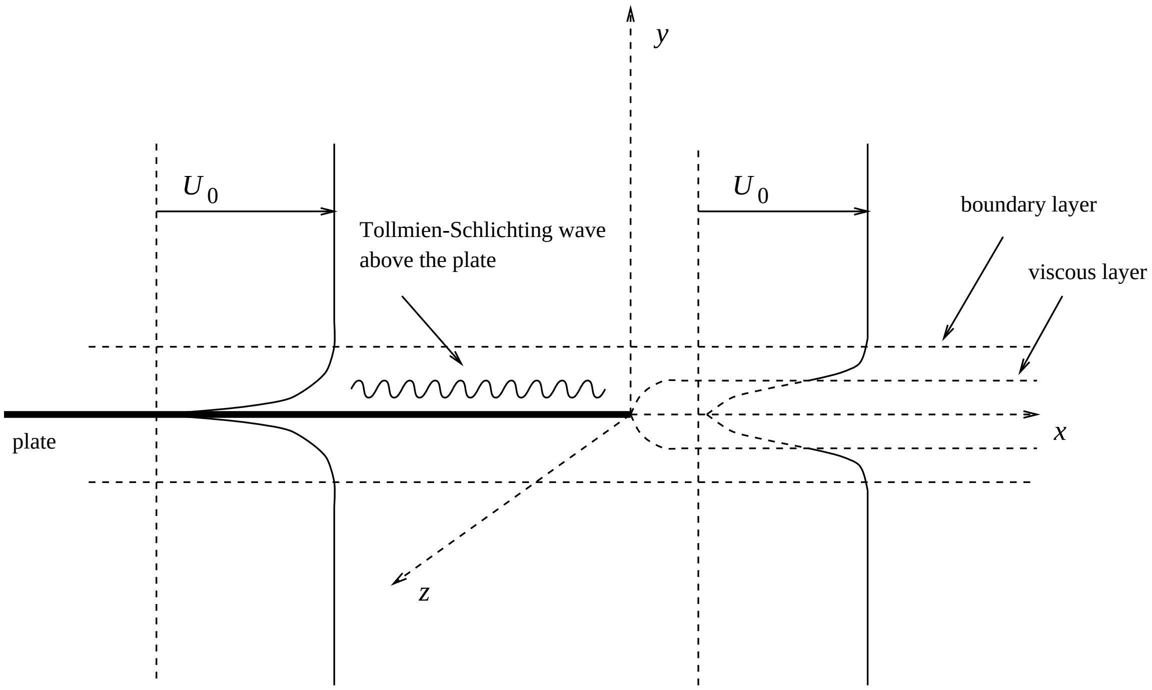

Figure 5.1: Set-up

where $\mathbf{u}_-$ is a linear combination of waves travelling to the left of $x = 0$ and $\mathbf{u}_+$ a linear combination travelling to the right of $x = 0$. The z-component β of the T–S wave vector is assumed to be small.

Substituting $\mathbf{u}$ and p into the Navier–Stokes equations and linearizing gives,

$$\begin{aligned}\frac{\partial \mathbf{u_1}}{\partial t} + U_0 \frac{\partial \mathbf{u_1}}{\partial x} + U_0'(\mathbf{u_1}.\mathbf{j})\mathbf{i} &= -\nabla p_1 + \frac{1}{R}\nabla^2 \mathbf{u_1}\,, \qquad (5.2)\\ \nabla.\mathbf{u_1} &= 0\,, \qquad (5.3)\end{aligned}$$

with boundary conditions,

$$\begin{aligned}\mathbf{u_1} &= \mathbf{0} \qquad y = 0,\ x < 0\,, \qquad (5.4)\\ \mathbf{u_1} &\to \mathbf{0} \qquad y \to \pm\infty\,, \qquad (5.5)\end{aligned}$$

and matching conditions,

$$[\mathbf{u_1}] = \left[\frac{\partial \mathbf{u_1}}{\partial y}\right] = [p_1] = 0 \quad y = 0,\ x > 0\,, \qquad (5.6)$$

where

$$[f] = f(x, 0^+) - f(x, 0^-)\,. \qquad (5.7)$$

The linearized Navier–Stokes equations (5.2), and the boundary and matching conditions (5.4), (5.5), (5.6) are all symmetric about $y = 0$. Hence $\mathbf{u_1}$ may be represented as the sum of a symmetric and antisymmetric part. Write the antisymmetric part as

$$\mathbf{u_1} = \left[\tfrac{1}{2}\mathbf{u_{TS}}(y)\exp(i\alpha_1 x) + (u, v, w)\right]\exp[i(\beta z - \omega t)]\,. \tag{5.8}$$

Substitute $\mathbf{u_1}$ into (5.2), (5.3) and take full Fourier transforms in x of each equation. After combining the equations to eliminate the pressure terms, the resulting equation may be simplified to that of the familiar Orr–Sommerfeld equation,

$$L^2[V] = i\alpha R[(U_0 - c)L - U_0'']V\,, \tag{5.9}$$

where

$$V = \frac{1}{\sqrt{2\pi}}\int_{-\infty}^{\infty} v e^{-i\alpha x}\mathrm{d}x\,, \tag{5.10}$$

$$L = \frac{\mathrm{d}^2}{\mathrm{d}y^2} - \gamma^2\,, \tag{5.11}$$

$\gamma^2 = \alpha^2 + \beta^2$ and $c = \omega/\alpha$.

Define V_+ and V_- as the half-Fourier transforms such that

$$V_+ = \frac{1}{\sqrt{2\pi}}\int_{0}^{\infty} v e^{-i\alpha x}\mathrm{d}x\,, \tag{5.12}$$

$$V_- = \frac{1}{\sqrt{2\pi}}\int_{-\infty}^{0} v e^{-i\alpha x}\mathrm{d}x\,, \tag{5.13}$$

and then the following conditions may be derived:

$$V_- = 0 \quad \text{on} \quad y = 0\,, \tag{5.14}$$

$$V_-' = 0 \quad \text{on} \quad y = 0\,, \tag{5.15}$$

$$V_+' = 0 \quad \text{on} \quad y = 0\,, \tag{5.16}$$

$$V \to 0 \quad \text{as} \quad y \to \pm\infty\,, \tag{5.17}$$

$$V_+''' + i\alpha R U_0' V_+ + \frac{i v_{TS}'''}{2\sqrt{2\pi}(\alpha_1 - \alpha)} = 0 \quad \text{on} \quad y = 0\,. \tag{5.18}$$

Conditions (5.14), (5.15), (5.16) and (5.17) may be easily derived using the boundary and matching conditions together with the continuity equation. Condition (5.18) is derived by substituting (5.8) into (5.2), (5.3) and then taking positive half-Fourier transforms of the equations. Once again the equations are combined to eliminate the pressure terms. The resulting expression is integrated from $y = -\epsilon$ to ϵ. The problem is then reduced to an equation (5.18) balancing the discontinuity of U_0' at $y = 0$ with the highest derivatives in V_+ and v_{TS}, as $\epsilon \to 0$.

The problem formulated by (5.9) and (5.14) — (5.18) is now solved using the Wiener–Hopf technique.

5.1.2 The Wiener–Hopf technique

The Wiener–Hopf technique is commonly used to solve diffraction problems at the edge of a semi-infinite flat plate.

Firstly, write the solution V of (5.9) as

$$V = c_1\phi_1 + c_2\phi_2 \,, \tag{5.19}$$

where ϕ_1 and ϕ_2 are asymptotic solutions which for large y are decaying inviscid and viscous solutions respectively. Hence

$$V = c_1 e^{-\gamma y} + c_2 e^{-\sqrt{\gamma^2 + iR(\alpha-\omega)}\,y} \ \text{ as } \ y \to \infty \tag{5.20}$$

for fixed (R, γ), and V will have four branch points when

$$\alpha = i\beta, -i\beta, \, \omega \ \text{ and } \ \omega + i\gamma^2/R \,. \tag{5.21}$$

If (5.18) was replaced by the condition $V_+ = 0$ on $y = 0$ then (5.9) and (5.14) — (5.18) would be the usual *free* Orr–Sommerfeld eigenvalue problem. However (5.18) is a forcing condition required as a result of the geometry of the problem (i.e. the singularity of U_0' at $y = 0$). Hence V will be singular for the discrete spectrum $\{\alpha\}$ of the forced Orr–Sommerfeld eigenvalue problem (including $\alpha = \alpha_1$).

Figure 5.2 is a sketch of the α-plane with the location of the isolated singularities and the branch cuts of V (5.19). The domains of analyticity for V_+ ($\oplus$) and V_- ($\ominus$) are shown respectively below and above the contours c_+ and c_-.

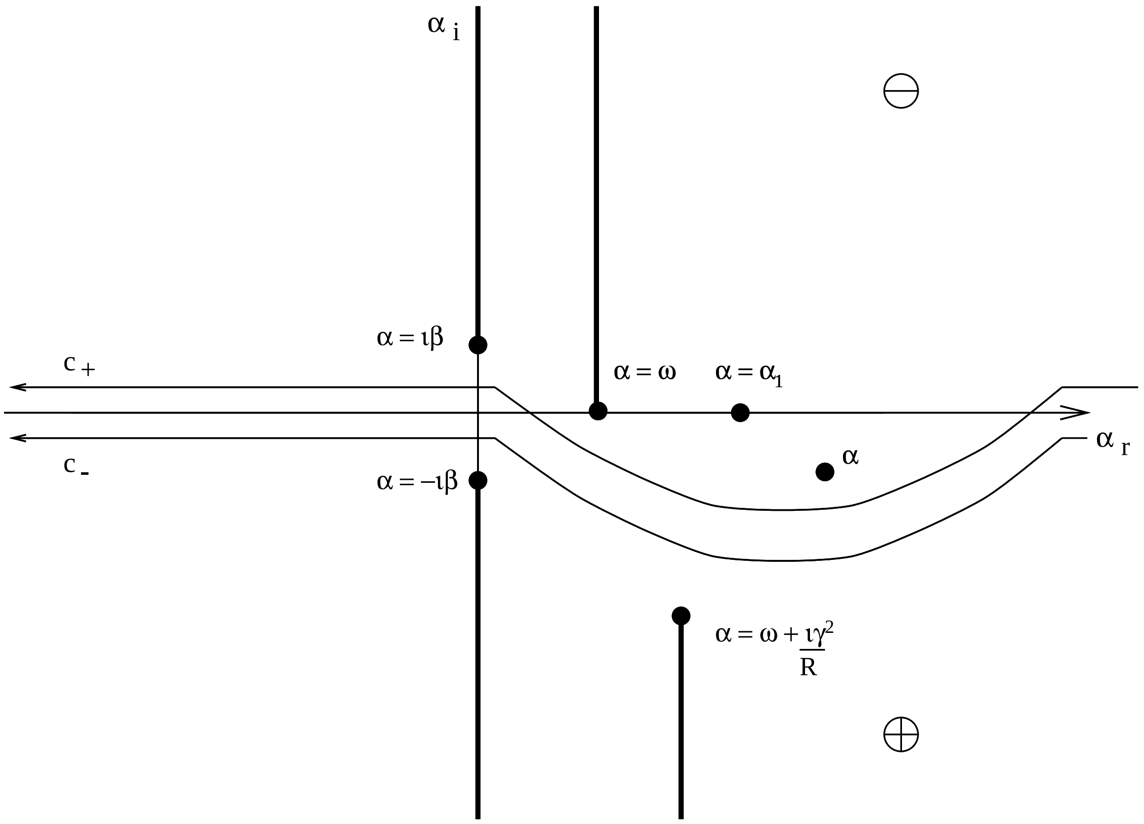

Figure 5.2: α-plane

Using the Navier–Stokes equations (5.2) and the continuity equation (5.3) it is straightforward to show that

$$v_{TS}'''(0) = (\alpha_1^2 + \beta^2) R p_{TS}(0) \, , \tag{5.22}$$

where $p_{TS}(0)$ is the pressure due to the T–S wave on $y = 0$. Using (5.19) and (5.22), (5.18) may be rewritten as

$$V_-''' - \frac{a}{\alpha_1 - \alpha} = V_+ F \, , \tag{5.23}$$

where

$$a = \frac{i(\alpha_1^2 + \beta^2) R p_{TS}(0)}{2\sqrt{2\pi}} \, , \tag{5.24}$$

$$F = \left[i\alpha R U_0' + \frac{\phi_1'''\phi_2' - \phi_2'''\phi_1'}{\phi_1\phi_2' - \phi_1'\phi_2} \right]_{y=0} . \tag{5.25}$$

By considering the Orr–Sommerfeld equation (5.9) in the limit as $\alpha_r \to \pm\infty$, (5.25) gives

$$\lim_{\alpha_r \to \pm\infty} \left(\frac{F}{2\gamma^3} \right) = 1 \, . \tag{5.26}$$

Use (5.26) and the basic product factorization for the Wiener–Hopf technique to write

$$F = 2\gamma^3 \frac{K_+}{K_-} \, , \tag{5.27}$$

where

$$K_+ \quad = \quad \exp\left\{ \frac{1}{2\pi i} \int_{c_+} \frac{\ln(F/2\gamma^3)}{t-\alpha} \mathrm{d}t \right\} \, , \tag{5.28}$$

$$K_- \quad = \quad \exp\left\{ \frac{1}{2\pi i} \int_{c_-} \frac{\ln(F/2\gamma^3)}{t-\alpha} \mathrm{d}t \right\} \, . \tag{5.29}$$

Further factorize

$$2\gamma^3 = 2\gamma_-^3 \gamma_+^3 \, , \tag{5.30}$$

where $\gamma_- = \sqrt{\alpha + i\beta}$ is analytic above c_- and $\gamma_+ = \sqrt{\alpha - i\beta}$ is analytic below c_+ . Finally add $aK_-(\alpha_1)/(\alpha_1 - \alpha)\gamma_-^3(\alpha_1)$ to each side of (5.23) to ensure that the left hand side (LHS) remains analytic at $\alpha = \alpha_1$.

The Wiener–Hopf equation is now

$$\frac{V_-''' K_-}{\gamma_-^3} - \frac{a}{(\alpha_1 - \alpha)} \left\{ \frac{K_-}{\gamma_-^3} - \frac{K_-(\alpha_1)}{\gamma_-^3(\alpha_1)} \right\} = 2\gamma_+^3 V_+ K_+ + \frac{aK_-(\alpha_1)}{(\alpha_1 - \alpha)\gamma_-^3(\alpha_1)} \, , \tag{5.31}$$

whence the LHS of (5.31) will be analytic in the ⊖ region and the RHS analytic in the ⊕ region. By analytic continuation (5.31) defines a function, say $J(\alpha)$, which is analytic in the whole α-plane.

Close to the edge of the plate the stream function of the flow will satisfy the biharmonic equation $\nabla^4 \psi = 0$ (i.e. there is Stokes flow). Solution of the biharmonic equation in polar coordinates will be

$$\psi \sim r^{3/2} \left(\cos\tfrac{3}{2}\theta + 3\cos\tfrac{1}{2}\theta \right) \quad , \quad r \ll 1 \, . \tag{5.32}$$

The behaviour of V_+ and V_-''' as $|\alpha| \to \infty$ may be derived by using (5.32) and the Abelian theorem. After some work it may be shown that

$$V_+(y=0) \quad \sim \quad \alpha^{-3/2} \;\; \text{as} \;\; |\alpha| \to \infty \;\; , \;\; \alpha_i < 0 \, , \tag{5.33}$$

$$V_-'''(y=0) \quad \sim \quad \alpha^{3/2} \;\; \text{as} \;\; |\alpha| \to \infty \;\; , \;\; \alpha_i > 0 \, . \tag{5.34}$$

Further it may be shown that,

$$K_-, K_+ \quad \rightarrow \quad 1 \qquad \text{as } |\alpha| \rightarrow \infty \,, \tag{5.35}$$

$$\gamma_-, \gamma_+ \quad \sim \quad \alpha^{1/2} \text{ as } |\alpha| \rightarrow \infty \,. \tag{5.36}$$

Then use (5.33) — (5.36) to show that the RHS of (5.31) is bounded as $|\alpha| \rightarrow \infty$ for $\alpha_i < 0$, and that the LHS of (5.31) is bounded as $|\alpha| \rightarrow \infty$ for $\alpha_i > 0$. Hence, J is analytic and bounded in the whole α-plane and by Liouville's theorem will be equal to a constant, say C.

5.1.3 The scattered hydrodynamic potential in the near-field

Define the velocity potential ϕ such that,

$$u = \frac{\partial \phi}{\partial x} \text{ and } v = \frac{\partial \phi}{\partial y} \,, \tag{5.37}$$

and define Φ to be the full Fourier transform in x of ϕ. Using (5.10) it may be shown that,

$$\frac{\mathrm{d}\Phi}{\mathrm{d}y} = V \,. \tag{5.38}$$

Then equation (5.20) shows that $V \approx c_1 \exp(-\gamma y)$ for $y \gg 1$. Therefore,

$$\Phi \approx -\frac{c_1}{\gamma} e^{-\gamma y} \quad , \quad y \gg 1 \,, \tag{5.39}$$

and only the constant c_1 remains to be calculated.

Rearranging the LHS of the Wiener–Hopf equation (5.31) (which is equal to a constant) and using contour integration gives

$$V_-''' = \frac{a}{(\alpha_1 - \alpha)} - b \,, \tag{5.40}$$

where

$$b = \frac{a\gamma_-}{\gamma_-(\alpha_1)} \exp\left\{ \frac{(\alpha_1 - \alpha)}{2\pi i} I(\alpha) \right\} \left\{ \frac{1}{\alpha_1 - \alpha} - \mathrm{C} \right\} \,, \tag{5.41}$$

with

$$I(\alpha) = \int_{c_-} \frac{\ln(F/\gamma)}{(t - \alpha_1)(t - \alpha)} \mathrm{d}t \,. \tag{5.42}$$

On using (5.18) and (5.40), it is straightforward to show that

$$V''' + i\alpha R U_0' V = -b \ \text{ on } \ y = 0\,. \tag{5.43}$$

Then the constants c_1 and c_2 may be obtained from the following system:

$$\begin{aligned} c_1\phi_1' + c_2\phi_2' &= 0\,, \quad \text{on } y = 0\,, & (5.44)\\ c_1(\phi_1''' + i\alpha R U_0'\phi_1) + c_2(\phi_2''' + i\alpha R U_0'\phi_2) &= -b\,, \ \text{ on } \ y = 0\,. & (5.45)\end{aligned}$$

Note that (5.44) is derived from (5.15), (5.16) and (5.19), (5.45) from (5.43) and (5.19).

The potential ϕ is determined by taking the inverse Fourier transform of Φ. The behaviour of ϕ will be governed by the behaviour of Φ as $\gamma \to 0$ (see (5.39)). Having evaluated the constant c_1 then we find

$$\Phi \approx \frac{\mathrm{D}}{\gamma_-}\exp\left\{\frac{(\alpha_1 + i\beta)}{2\pi i} I(-i\beta) - \gamma y\right\}\ ,\quad y \gg 1\,, \gamma \to 0\,, \tag{5.46}$$

for a constant D such that

$$\mathrm{D} = a\left(\mathrm{C} - 1/(\alpha_1 + i\beta)\right)/2\omega R\beta\gamma_-(\alpha_1)\,. \tag{5.47}$$

Recall that β was assumed to be small. For D to remain finite as $\beta \to 0$ take $\mathrm{C} = 1/\alpha_1$.

Finally the integral $I(-i\beta)$ is calculated (only as an approximation as $R \to \infty$), and the potential ϕ for $r \gg 1$ will be

$$\phi = \frac{1}{\sqrt{2\pi}}\int_{-\infty}^{\infty}\Phi e^{i\alpha x}\mathrm{d}\alpha \approx \frac{p_{TS}(0)\exp(-i\pi/8)}{\omega\sqrt{2\pi\alpha_1}}\ \frac{\sin(\theta/2)}{\sqrt{r}}\ . \tag{5.48}$$

Figure 5.3 is a plot of the contours $\sin(\theta/2)/\sqrt{r} = \text{const.}$ with the Cartesian axes (x, y) shown for reference. For $r \gg 1$ the hydrodynamic potential ϕ will be constant on these contours. The contours show that the scattered hydrodynamic field has a cardioid shape with the cusp centred at the edge of the plate.

5.1.4 The scattered sound potential in the far-field

Following (5.48) the acoustic potential ϕ for $r \gg 1$ is assumed to take the form,

$$\phi = g(r)\sin(\theta/2)\exp[i(\beta z - \omega t)]\,. \tag{5.49}$$

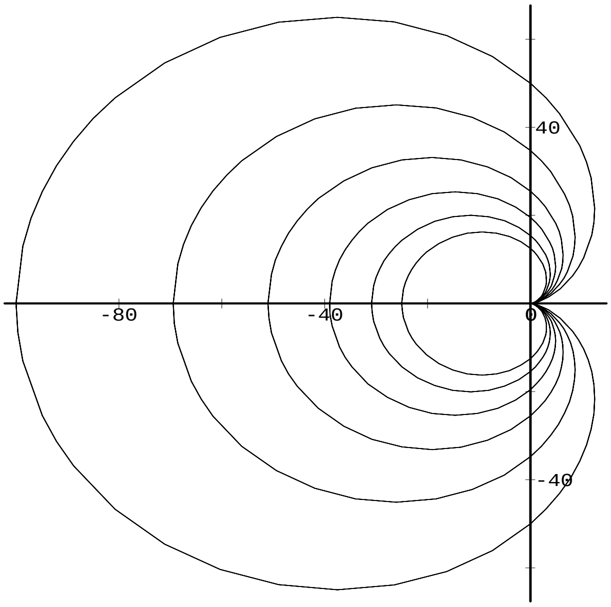

Figure 5.3: Sketch of the contour lines $\sin(\theta/2)/\sqrt{r} = \text{const.}$.

The acoustic potential (5.49) will satisfy the linearized wave equation,

$$\frac{\partial^2 \phi}{\partial t^2} = a_0^2 \nabla^2 \phi \,, \tag{5.50}$$

when

$$g(r) \propto \frac{\exp(ikr)}{\sqrt{r}} \,, \tag{5.51}$$

where $k^2 = \omega^2/a_0^2 - \beta^2$.

The form of the acoustic potential ϕ for $r \gg 1$ is found by comparing (5.49) and (5.51) with (5.48),

$$\phi = \frac{p_{TS}(0)}{\omega\sqrt{2\pi\alpha_1}} \frac{\sin(\theta/2)}{\sqrt{r}} \exp[i(kr + \beta z - \omega t - \pi/8)] \,. \tag{5.52}$$

The sound pressure field p' may easily be derived from (5.52) after noting that $p' \propto -\partial\phi/\partial t$ (from consideration of the conservation of momentum).

Finally, Aizin comments that a similar calculation for the symmetric part of $\mathbf{u_1}$ reveals that the contribution from the symmetric solution may be neglected.

5.2 Analysis of the feedback model

The formation of instability waves in the pressure surface boundary layer has been thoroughly discussed in Chapters 2, 3 and 4. Comparison between the experimental and theoretical results has shown reasonable agreement and led to a further understanding of the nature of the flow over the two aerofoils investigated.

The development of the boundary-layer instability waves may be summarized as follows. The flow is stable at station 1, that is approximately 80 mm downstream of the leading edge. Any instabilities associated with the stagnation point close to the aerofoil leading edge are damped as the flow accelerates around the 'nose' of the aerofoil. The development of any instabilities downstream of station 1 is assumed to be independent of any leading edge effects.

Downstream of station 1 the flow is unstable to a range of frequencies. The growth of the boundary-layer instability waves is governed by the viscous mechanism proposed by Tollmien and Schlichting and the waves are referred to as T–S waves. The growth of these T–S waves is small relative to the growth which is observed close to the trailing edge. The T–S waves appear suitable to be modelled using linear theory.

Experimental results reveal the existence of a small region of separated flow close to the aerofoil trailing edge (typically 20 to 30 mm upstream of the trailing edge). The flow separation is caused by the adverse pressure gradient near the trailing edge. Boundary-layer flows with an adverse pressure gradient have an inflexion point away from the boundary. The stability characteristics of an inviscid flow depend largely on the location of any inflexion points.

There is a change in the dominant instability mechanism as the T–S wave approaches the trailing edge of the aerofoil. It is proposed that the inflexion point becomes sufficiently removed from the viscous wall layer such that close to the trailing edge the boundary-layer instability waves are now governed by the inviscid dynamics of the inflexion point. The waves are there referred to as inflexional waves. It has been demonstrated that the growth rates associated with the inflexional waves are greater than those associated with the T–S waves. The majority of the growth of the boundary-layer instability waves occurs approximately downstream of the point of flow separation (typically 20 to 30 mm upstream of the trailing edge).

The strong amplification of the inflexional waves appears to be a necessary condition for the generation of tonal noise. It may not be a sufficient condition in the sense that the flow at the trailing edge is required to remain quasi-laminar for the generation of tonal noise. The amplification of the boundary-layer instability waves may rapidly lead to flow transition. The region of separated flow must be located sufficiently close to the trailing edge to ensure that the flow remains quasi-laminar at the trailing edge. (Note, a quasi-laminar boundary layer is assumed to be a boundary layer *close* to transition which retains any discrete frequency structure in its frequency spectrum.)

There is remarkably close agreement between the linear and weakly nonlinear results. The experimental results indicate the presence of weak nonlinearity close to the trailing edge of the aerofoil. It is proposed that the inflexional instability may be modelled initially by using weakly nonlinear theory. This appears to be valid until very close to the trailing edge of the aerofoil. As a result the agreement between the experimental and theoretical results is good.

For higher Reynolds number flows (such as case 2) the weakly nonlinear approximation appears to be unsuitable at station 12 (approximately 5 mm upstream of the trailing edge for case 2). However, the selection of one, discrete frequency, boundary-layer instability wave and its subsequent large amplification appears to be determined close to the point of flow separation. The frequency 'selected' for amplification will remain the most amplified frequency up to the trailing edge of the aerofoil. In other words, from an initial set of unstable discrete frequencies, one frequency will eventually dominate over all the others. Weakly nonlinear theory (or even linear theory) may predict the frequency of the mode with maximum amplification because the frequency is 'selected' in a region where the theory is valid. The frequency of the mode with maximum amplification appears to be 'selected' in the region where the nature of the dominant instability mechanism is changing.

The large amplification of the inflexional waves leads to the formation of a vortex street in the aerofoil wake. Recall from (3.7), (3.8) that the x-velocity perturbation will be

$$u' = \Re\left\{\psi'_z\right\} = |\phi'(z)|e^{-\alpha_i x}\cos[\alpha_r x - \alpha c t + \arg\phi'(z)] \, , \tag{5.53}$$

where the phase is $\arg\phi'(z)$. This phase describes what is known as the 'tilt' of the boundary-layer instability waves. With increasing nonlinearity and 'tilt' the inflexional waves tend to roll up into vortices which are shed from the trailing edge of the aerofoil into the wake.

Normally the frequency of the disturbances in the wake is *not* related to the frequency of the boundary-layer disturbances because the wake and the boundary layer are effectively decoupled. The development of infinitesimal disturbances in the boundary layer is described by the viscous Orr–Sommerfeld problem (3.13) whereas for the wake the inviscid Rayleigh problem (3.9) is used.

However, at each resonant frequency the wake instabilities are controlled by the pressure surface boundary layer. It is reasonable to assume that the frequencies in the suction surface boundary layer are in a broad band. The frequency of the vortex street is determined by the amplification of a 'selected' boundary-layer instability wave with fixed frequency. Tonal noise is heard when the whole system is 'ringing' at one frequency.

In principle this is in agreement with Paterson et al. [16], who attributed the tonal noise to vortex shedding. However, it is concluded that the tonal noise mechanism is *not* the same as the constant Strouhal number problem for bluff bodies, see §1.3 (1.5). Paterson et al. assume that the frequency may be predicted by knowing the free-stream velocity U_∞ and the boundary-layer thickness at the trailing edge, on assuming a constant Strouhal number.

The Strouhal number was not a constant in this investigation. The frequency of the boundary-layer instability waves and the vortex wake appears to be determined by the stability characteristics of the boundary-layer profile at stations located over approximately two thirds of the aerofoil, not just the profile at the trailing edge of the aerofoil.

As the vortices are shed into the wake it has been observed experimentally that the separation bubble will slightly expand and contract. The diffraction of the inflexional waves at the trailing edge of the aerofoil (cf. Aizin [1]) results in an oscillating hydrodynamic field close to the sharp edge. The feedback will be discussed soon.

The Orr–Sommerfeld theory uses a local approximation on a given flow. The approximation assumes that the local flow extends unchanged on an infinite domain, $x \in (-\infty, \infty)$. A Fourier transform with respect to x may then be taken and the solution sought on taking an inverse Fourier transform. (As noted in §3.1.1, for a two-dimensional problem a Laplace transform in time will also be taken.) This approach was used by Aizin [1] and is described in §5.1.1. The inverse Fourier transform assumes an infinite continuum in the wavenumber (or frequency). In §5.1.3 the solution (5.48) is found on integrating the wavenumber α from $-\infty \to \infty$.

In the Orr–Sommerfeld problem, for $R > R_c$ there is a continuous band of unstable wavenumbers (or frequencies) and the wavenumber (or frequency) spectrum exhibits a broad band of amplified wavenumbers (or frequencies).

In a bounded system, say $x \in [-L, L]$, the perturbation stream function may be represented by a Fourier series, (e.g. §4.1, (4.5)). Then the stream function is constructed with a discrete set of wavenumbers (or frequencies).

The flow over the aerofoil is bounded by the constraints of the wind-tunnel and the aerofoil chord length. All flows are bounded, even if the bounds are sometimes very large, such as the height of the atmosphere. The Orr–Sommerfeld problem is only an approximation because the wavenumber (or frequency) spectrum for all flows is discrete.

An alternative approach to the problem would be to discard the above local approximation and apply bifurcation theory to the flow as a whole. For a small enough R there will exist a unique, stable steady flow around the aerofoil, (cf. Serrin's theorem §6.1.5). With increasing R, the steady flow will remain stable until $R = R_c$. Then a Hopf bifurcation will occur and the flow will bifurcate from a steady, stable flow to a periodic, stable flow. This is known as a super-critical bifurcation. At any fixed station on the aerofoil the observed flow remains unchanged with increasing time. (However the flow will develop with increasing distance downstream over the aerofoil.) With further increases of R there may be more bifurcations resulting in quasi-periodic flow and eventually chaos.

From the linear (and weakly nonlinear results) it is proposed that the Orr–Sommerfeld theory may be used to obtain an approximation of f, the frequency observed in the flow after the Hopf bifurcation. It is proposed that the flow will bifurcate to a frequency *close* to the frequency of the mode with maximum linear amplification over the aerofoil. (This may not coincide exactly with the frequency of the mode with maximum linear amplification because only a discrete set of frequencies is permitted.)

In §5.1.4, the sound generation by a T–S wave scattered at the edge of a sharp flat plate is calculated. There are several characteristics of the solution (5.52) which appear suitable to be used in the description of tonal noise.

Firstly, the frequency of the sound is equal to the frequency of the T–S wave. The experimental results confirm the presence of one discrete fundamental frequency in the boundary layer, wake, and free stream, namely the frequency of the tone.

The analytic expressions (5.48) and (5.52) are only valid for $r \gg 1$. The method assumes the scattered field is incompressible close to the sharp edge. In the far-field the incompressible hydrodynamic field is matched to a solution of the wave equation. In other words, Aizin assumes that compressibility is only significant in the far-field. A reasonable assumption may be to assume that sound propagates in the free stream, but to assume that the boundary layer remains incompressible. Sound waves in the free stream may excite small-amplitude instabilities in the boundary layer under certain flow conditions, as will be discussed soon.

The flow close to the sharp edge is assumed to be an incompressible hydrodynamic field comprised of the boundary-layer and the scattered field. The minimum radial distance from the trailing edge to a point in the scattered field when the flow is assumed to be compressible, and hence admit a sound wave, is an open question.

Figure 2.25 confirms the presence of an oscillating hydrodynamic field, at the frequency of the tone, centred about the trailing edge of the aerofoil. Nash [33] confirmed that the oscillations were hydrodynamic and, as noted in §2.6, the oscillations may not be attributed entirely to decaying boundary-layer instabilities. The existence of the oscillating hydrodynamic field *outside* of the boundary layer in figure 2.25 leads one to doubt the hypothesis proposed by several previous authors attributing tonal noise to an aero-acoustic feedback loop.

The transformation of free-stream oscillations into small-amplitude disturbances in the boundary layer is known as boundary-layer receptivity. Typically the boundary layer is receptive to turbulence or sound waves in the free stream. (Another common source of small-amplitude disturbances is irregularities in the boundary surface.) Boundary-layer receptivity only influences the generation of the small disturbances, not their subsequent propagation. Kerschen ([26], (1989)) separates boundary-layer receptivity into two categories: natural and forced receptivity.

Natural receptivity occurs when the external disturbances in the free stream have wavelengths which are much greater than the wavelengths of boundary-layer instability waves. The most common example of this is sound. A wavelength conversion process is required because the free-stream disturbance will not contain much energy at the wavelengths of the boundary-layer instabilities.

Forced receptivity occurs when the external disturbances in the free stream have wavelengths of the same order of magnitude as those in the boundary layer. There will then be a direct coupling, i.e. a direct transfer of energy. An example of this would be a localized unsteady pressure field outside of the boundary layer.

Forced receptivity occurs more easily than natural receptivity. Natural receptivity essentially occurs in two regions: at the leading edge and where the boundary layer changes rapidly. Rapid adjustments in the boundary layer may be due to a sudden change in the curvature or through irregularities on the surface. Natural receptivity does not occur in a parallel flow region where the Orr–Sommerfeld problem is valid. Hence natural receptivity is usually associated with non parallel mean-flows.

Dovgal et al. [14] comment that velocity profiles within a separation bubble are more receptive than flows similar to the Blasius boundary layer. Dovgal and Kozlov [11] investigated experimentally the flow of a laminar boundary layer with adverse pressure gradients, subject to an acoustic field. They found that the acoustic field excited T–S waves at the frequency of the sound. However, the amplitude of the T–S waves was only significant at the start of the region of adverse pressure gradient, i.e. close to the separation point. The amplification of the T–S waves downstream of this point was greater than the amplitude of the excited disturbance. Hence, the development of the disturbances was not influenced by the sound downstream of the separation point. Boundary-layer receptivity may be significant close to the point of flow separation. (Note that Dovgal and Kozlov used a loudspeaker to generate an acoustic field.)

For case 1, $\lambda_{ac} \approx 320\,\mathrm{mm}$ compared with $\lambda_{TS} \approx 11\,\mathrm{mm}$. The aero-acoustic feedback loop proposed by Wright [44], Longhouse [28], Fink [18] and Arbey & Bataille [3] assumed a coupling between sound waves propagating upstream from the trailing edge and T–S waves propagating downstream in the boundary layer. It was proposed that the coupling began where the flow became unstable, i.e. where $R \approx R_c$. A resonant tone was heard if the acoustic and hydrodynamic waves were in phase. A ‘jump’ in the tonal frequency occurred when there was a 2π phase change around the loop. There are several reasons to question the suitability of the aero-acoustic feedback loop proposed by the aforementioned authors.

Firstly, the amplification of the boundary-layer instability waves is dominated by the region of separated flow. This region is relatively small compared with the aerofoil chord. The ‘critical point’ on the aerofoil would appear to be close to the point of flow separation, not where the flow becomes unstable (R_c). The growth of T–S waves between R_c and the separation point is relatively small. The frequency spectra do not reveal any discrete amplitude peaks between R_c and the separation point. There may be several discrete frequency T–S waves propagating downstream but their amplitude will be relatively small. Any coupling between sound and hydrodynamic waves at R_c would have negligible effect on the amplification close to the separation point.

Further, boundary-layer receptivity will be very weak where $R \approx R_c$. Upstream of the separation point the quasi-parallel flow approximation is very good. Natural receptivity only occurs in regions of non-parallel flow. Natural receptivity would occur close to the leading edge and possibly close to the separation point. Receptivity at the leading edge has already been briefly discussed. The accelerating flow will dampen any instabilities excited there.

The existence of 'jumps' in the tonal frequency in figure 2.5 is debatable. There may be a 'jump' at approximately $U_\infty = 47\,\mathrm{ms}^{-1}$ but a 'ladder' structure is not present. It is proposed that the 'critical point' is the point of flow separation. The distance between the 'critical point' and the trailing edge is small, approximately 20 mm say. However, $\lambda_{ac} \approx 320\,\mathrm{mm}$ and the simple feedback mechanisms described in §1.3, such as (1.9) appear to be unsuitable because $\lambda_{ac} \gg L$ (where L is the 'length' of the feedback loop).

From the results in this thesis an alternative hypothesis is proposed.

'A resonance between the boundary-layer instability waves, vortex wake and oscillating mean-flow generates tonal noise.'

The process may be considered to be entirely hydrodynamic. In the far-field the result of the resonance is a sound wave. The process is controlled by the pressure surface boundary layer. The boundary layer remains quasi-laminar until the trailing edge to ensure the diffraction of the inflexional waves. The diffraction of the inflexional waves creates external hydrodynamic oscillations in the free stream. These oscillations are strongest close to the trailing edge. Forced boundary-layer receptivity close to the separation point between the inflexional waves and the mean-flow appears a more suitable feedback model, as opposed to previous models which assume natural receptivity occurs where $R \approx R_c$.

Natural receptivity may occur close to the separation point. As previously discussed, it is an open question as to where the scattered field may be assumed to remain incompressible. Forced receptivity appears to be more significant because it has been shown experimentally that there are external hydrodynamic oscillations outside of the boundary layer. Natural receptivity may occur close to the separation point but the large variation in the relevant length scales suggests that forced receptivity will be more dominant.

The 'ringing' of the inflexional waves, the vortex wake and the mean-flow, at one discrete frequency, is detected by a microphone situated in the far-field as radiating sound waves. The frequency is controlled by the development of instabilities in the pressure surface boundary layer. A frequency prediction may be obtained by calculating the growth of spatial modes with fixed frequency in the boundary layer.

5.3 Proposals for future work

Only two aerofoil profiles were used during the wind-tunnel experiments. The tonal noise mechanism was the same on each aerofoil, being controlled by a region of separated flow close to the trailing edge. An investigation of more aerofoil profiles would be required to predict the likelihood of tonal noise. Presumably the flow over many aerofoil profiles will not separate close to the trailing edge and tonal noise may not occur. However, as mentioned in §1.1, laminar flow is a desirable state to reduce drag, and tonal noise is directly related to the existence of laminar flow.

Previous authors have observed multiple tones for certain flow conditions. It has been suggested that more than one feedback loop may be present over the aerofoil span. In this thesis the aim was to understand the simplest two-dimensional mechanism. An aerofoil is three-dimensional and the existence of different frequencies in the boundary layer in the spanwise direction could also be investigated.

Further analytic work may be possible concerning the diffraction of the inflexional waves at the trailing edge of the aerofoil. Aizin [1] considers the diffraction at the edge of a flat plate with a Blasius boundary-layer profile. A thin wedge may be used instead of a flat plate and a Falkner–Skan velocity profile may be incorporated into the model. Presumably the Falkner–Skan profile which matches the boundary layer at the trailing edge would be suitable for this model.

The receptivity of the boundary layer may also be investigated further. Kerschen [26] reports that asymptotic methods have been successfully used to show that a wavelength conversion may take place in regions of a boundary layer where the mean-flow changes rapidly on a short streamwise length scale. It is proposed that forced receptivity is more likely close to the separation point because of the existence of the hydrodynamic field in the free stream. Forced receptivity may occur more easily because no wavelength conversion process is required. The nature of the receptivity of the separation bubble requires further work.

Finally, in §1.1 the study of tonal noise was motivated by the existence of noise heard from rotating blades, in particular wind-turbines. In this thesis a fixed aerofoil in a uniform free stream is considered. Rotational effects have not been considered thus far. The effect of rotation and the interaction of the blades (particularly the leading edge) with the wake from a neighbouring blade may also be investigated.

Chapter 6

On the stability of Jeffery–Hamel flows

This final chapter briefly discusses some linear stability analysis work conducted on Jeffery–Hamel flows. This chapter is a joint piece of work with Prof. P.G. Drazin. The work in this chapter may be viewed separately from the previous six chapters studying the discrete frequency tones generated by aerofoils. However, the theory and experience gained from particularly Chapter 3 has been used extensively in the preparation of this chapter.

6.1 Introduction

6.1.1 The Jeffery–Hamel problem

A class of exact solutions of the Navier–Stokes equations were originally presented by Jeffery in 1915 and independently by Hamel in 1916 for the steady radial flow of a viscous, incompressible fluid between two fixed, plane, intersecting walls driven by a line source (or sink) at their intersection.

On taking polar coordinates (r, θ) consider two rigid, impermeable walls given by $\theta = \pm\alpha$ whose intersection is at $r = 0$. Now let the flow between $\theta = \pm\alpha$ be driven by a line source (or sink) of strength Q positioned at $r = 0$.

In polar coordinates the velocity components are given by

$$u_r = \frac{\partial \psi}{r \partial \theta} \quad \text{and} \quad u_\theta = -\frac{\partial \psi}{\partial r} \,, \tag{6.1}$$

where ψ is the stream function. Figure 6.1 is a sketch of the basic set-up for Jeffery–Hamel flow.

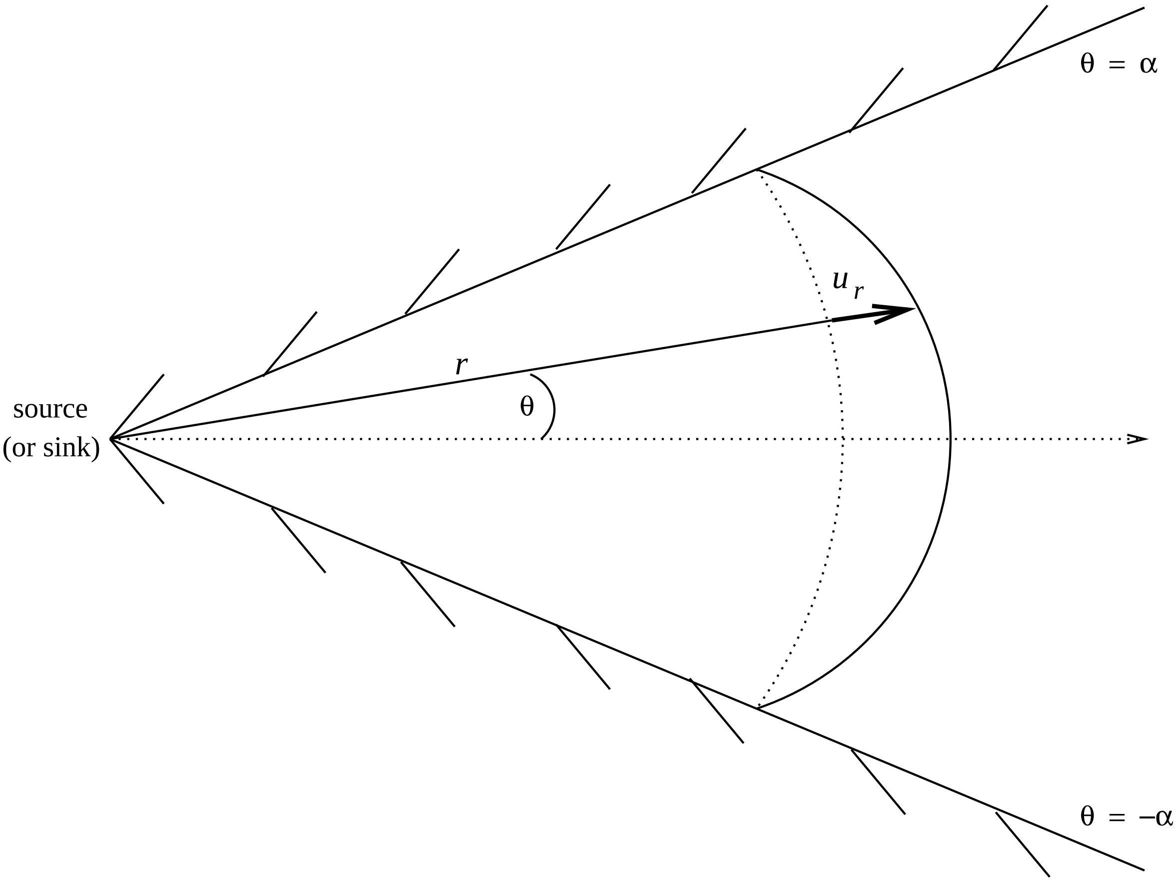

Figure 6.1: Basic set-up

The vorticity (defined as the curl of the velocity) $\zeta = -\nabla^2 \psi$ where in polar coordinates the Laplacian is $\nabla^2 = \partial^2/\partial r^2 + \partial/r\partial r + \partial^2/r^2\partial\theta^2$.

Taking the curl of the Navier–Stokes equations gives the vorticity equation governing the two-dimensional motion of the flow

$$\nu \nabla^2 \zeta = \frac{\partial \zeta}{\partial t} + \frac{1}{r} \frac{\partial(\zeta, \psi)}{\partial(r, \theta)} \,, \tag{6.2}$$

with boundary conditions for no slip or penetration at the walls

$$\psi = \pm\tfrac{1}{2}Q, \quad \partial\psi/\partial\theta = 0 \quad \text{at} \quad \theta = \pm\alpha\,. \tag{6.3}$$

Now search for a steady, purely radial flow, i.e.

$$u_\theta \equiv 0, \quad \Rightarrow \quad \psi \equiv \psi(\theta)\,. \tag{6.4}$$

Writing $\psi = \frac{1}{2}Q\Psi(\theta)$ and defining the Reynolds number as $R = Q/2\nu$ reduces (6.2) to

$$\frac{\mathrm{d}^4\Psi}{\mathrm{d}\theta^4} + 4\frac{\mathrm{d}^2\Psi}{\mathrm{d}\theta^2} + 2R\frac{\mathrm{d}\Psi}{\mathrm{d}\theta}\frac{\mathrm{d}^2\Psi}{\mathrm{d}\theta^2} = 0\,, \tag{6.5}$$

with boundary conditions (6.3) now

$$\Psi = \pm 1, \quad \frac{\mathrm{d}\Psi}{\mathrm{d}\theta} = 0 \quad \text{at} \quad \theta = \pm\alpha\,. \tag{6.6}$$

The Jeffery–Hamel problem is defined by (6.5) and (6.6) resulting in a basic flow in the region $-\alpha \le \theta \le \alpha$ given by $u_r = \frac{1}{2}Q\mathrm{d}\Psi/r\mathrm{d}\theta$.

Commonly the Jeffery–Hamel flow in a wedge is mapped to a channel with walls at $y = \pm 1$ by the simple transformation $y = \theta/\alpha$. Let $\Psi(\theta) \equiv G(y)$ and then the Jeffery–Hamel problem is written as

$$G_{yyyy} + 4\alpha^2 G_{yy} + 2R\alpha G_y G_{yy} = 0\,, \tag{6.7}$$

$$G = \pm 1, \quad G_y = 0 \quad \text{at} \quad y = \pm 1\,. \tag{6.8}$$

Note that as $\alpha \to 0$ then a solution of (6.7) will be plane Poiseuille flow with velocity profile given by $G_y = \frac{3}{2}(1 - y^2)$.

6.1.2 Classification of Jeffery–Hamel flows

For each pair of values of (α, R) there exists an infinity of solutions to the Jeffery–Hamel problem. The majority of these solutions will be of no practical importance as they will be highly unstable and in practice will never be observable.

The qualitatively different solutions have been classified by Fraenkel (1962) and the most common flows are referred to as I or $\mathrm{II}_1, \mathrm{II}_2, \mathrm{III}_1, \mathrm{IV}_1$ and V_1. These may be seen sketched schematically in figure 6.2.

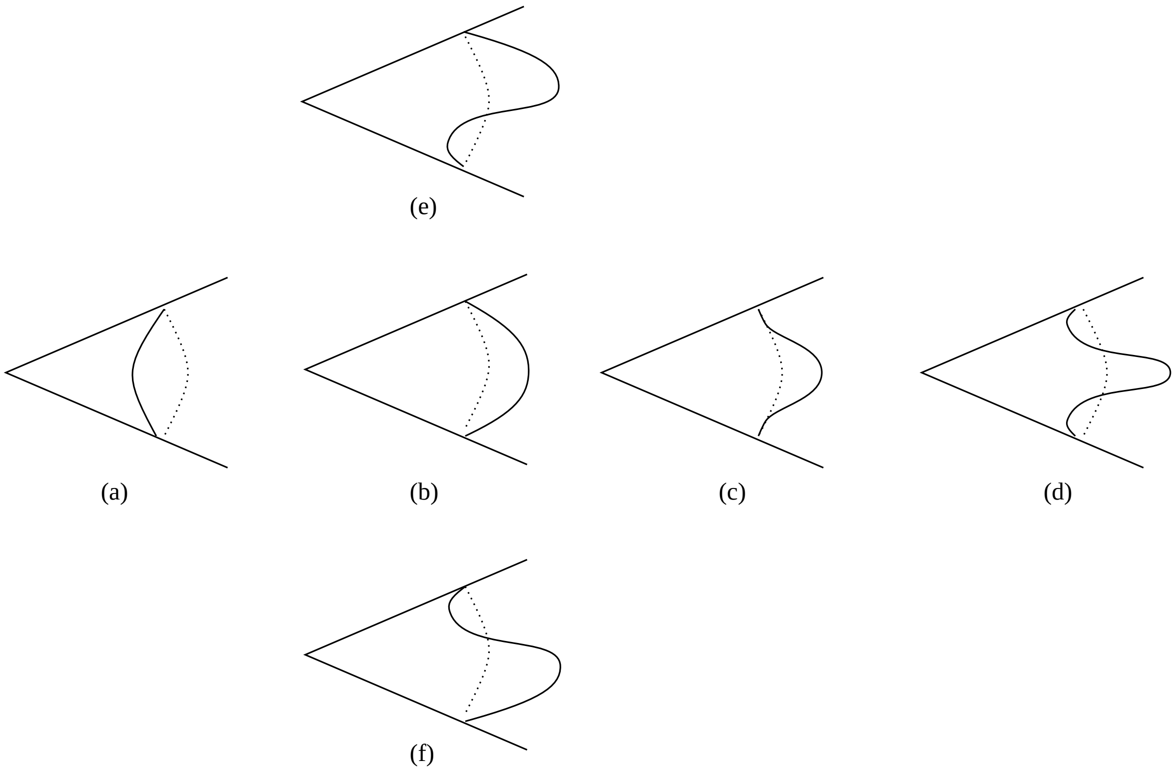

Figure 6.2: Sketches of velocity profiles of the primary Jeffery–Hamel flows; (a) III_1, (b) I or II_1, (c) marginal stability, (d) II_2, (e) V_1 and (f) IV_1.

Briefly, one may see that I or II_1 is a uniform outward flow and III_1 a uniform inward flow, both with symmetry about $\theta = 0$. The sign of R determines the type of source at $r = 0$. (For $R > 0$ the flux Q will be positive and at $r = 0$ there will be a line source. Similarly there will be a line sink at $r = 0$ when $R < 0$.) II_2 is also symmetric about $\theta = 0$ but now has small reversed flow components at each wall (small in the sense that the net flow is still outwards). IV_1 and V_1 are the mirror image of each other in the line $\theta = 0$. They are asymmetric flows with each having one small region of reversed flow (again small in the sense that there is net outflow).

The different types of Jeffery–Hamel flow exist in different regions of the (α, R)-plane. The boundary between regions I or II_1 and II_2 is given by the equation $R = R_2(\alpha)$ or $\alpha = \alpha_2(R)$. As $\alpha \to 0$ then $R_2(\alpha) \sim 4.712/\alpha$. Similarly, the boundary of region II_2 is denoted by $R = R_3(\alpha)$ or $\alpha = \alpha_3(R)$ and as $\alpha \to 0$ then $R_3(\alpha) \sim 5.461/\alpha$.

Figure 6.3 shows the curves $R = R_2(\alpha)$ and $R = R_3(\alpha)$ with some of the different

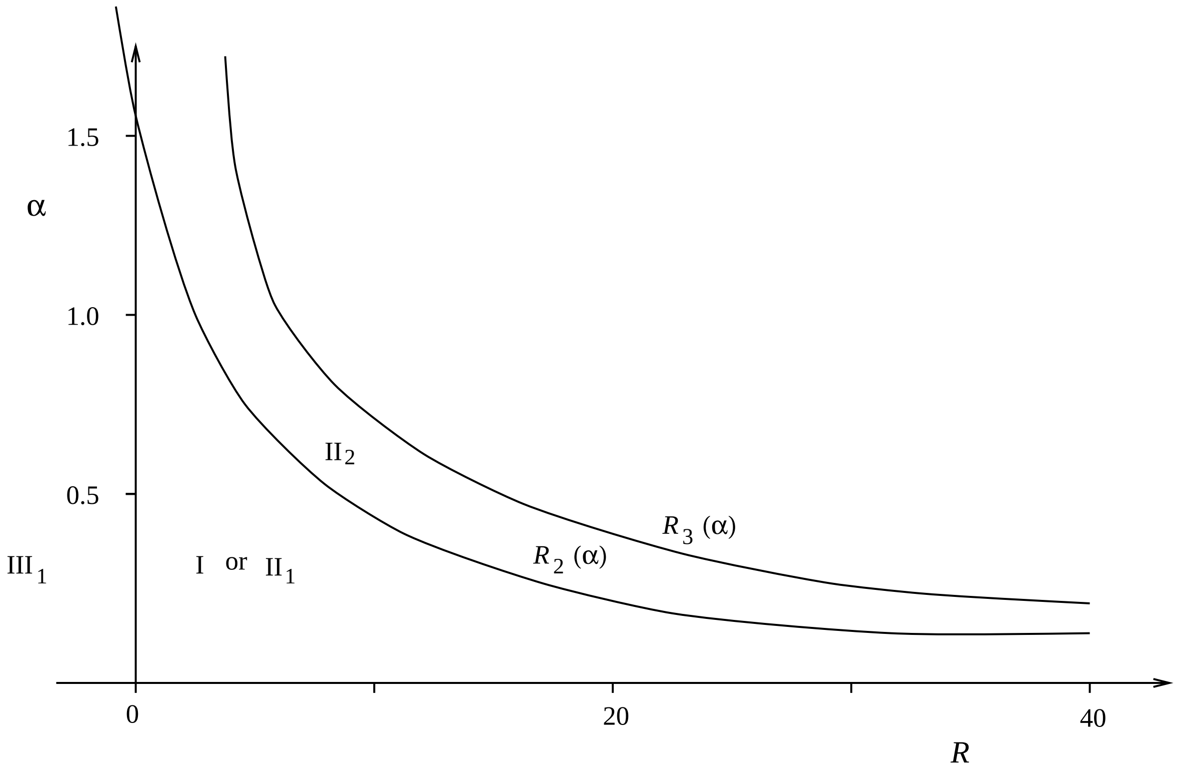

Figure 6.3: (α, R)-plane for Jeffery–Hamel flows.

Jeffery–Hamel flow regions. The solution of (6.7), (6.8) has no continuous extension for $R > R_3(\alpha)$ (cf. §6.1.5, figure 6.5).

6.1.3 Stability of Jeffery–Hamel flows

To examine the linear stability of Jeffery–Hamel flows write the stream function ψ as

$$\psi = \tfrac{1}{2}Q(G + \psi')\,, \tag{6.9}$$

where ψ' is a small perturbation of the steady stream function G and may be a function of r, θ, t, α and R.

Putting (6.9) into the vorticity equation (6.2) and boundary conditions (6.3) and then linearizing the resultant expression gives the governing equation for the stability of Jeffery–Hamel flow to small perturbations,

$$\left(\nabla^2\psi'\right)_t + \frac{RG_y}{\alpha r}\left(\nabla^2\psi'\right)_r - \frac{RG_{yyy}}{\alpha^3 r^3}\psi'_r - \frac{2RG_{yy}}{\alpha^2 r^4}\psi'_\theta = \nabla^4\psi'\,, \tag{6.10}$$

with boundary conditions

$$\psi' = \psi'_\theta = 0 \quad \text{on} \quad \theta = \pm\alpha \, . \tag{6.11}$$

Note on the method of normal modes

As discussed in more detail in §3.1.1 the usual way of proceeding would be to try to separate the variables (in this case r and t) and then express any disturbance as a superposition of normal modes. This may be justified by taking Fourier and Laplace transforms.

When considering problems in a wedge (say, $0 \leq r < \infty, \ \ -\alpha \leq \theta \leq \alpha$) the Mellin transform is commonly used. The Mellin transform is defined as

$$M[\phi(r)] = \int_0^\infty \phi(r) r^{\lambda-1} \mathrm{d}r \, , \tag{6.12}$$

and after integrating by parts it may be shown that

$$M\left[r\frac{\partial}{\partial r}\left(r\frac{\partial \phi}{\partial r}\right)\right] = \lambda^2 M[\phi(r)] \, , \tag{6.13}$$

provided that $r^\lambda \phi$ and $r^{\lambda+1}\partial\phi/\partial r$ vanish as $r \to 0, \infty$. Recall that in polar coordinates the Laplacian may alternatively be written as $\nabla^2 = (\partial/r\partial r)(r\partial/\partial r) + \partial^2/r^2\partial\theta^2$, which after multiplying by r^2 is comparable with (6.13), and hence the Mellin transform may commonly be used to solve partial differential equations in a wedge shaped domain. The Mellin transform may then be used to justify searching for modes proportional to r^λ in the same sense as when Fourier transforms were used in §3.1.1 to justify seeking for normal modes proportional to $e^{i\alpha x}$.

However, the variables r and t in (6.10) are *not* separable as may be easily seen by attempting to find modes of the form,

$$\psi'(r,\theta,t) = \Re\left\{ r^\lambda e^{st}\phi(\theta)\right\} \, . \tag{6.14}$$

All the terms in (6.10) are found to be proportional to $r^{\lambda-4}e^{st}$ *except* $\left(\nabla^2\psi'\right)_t$ which is proportional to $r^{\lambda-2}e^{st}$. Hence, you are unable to eliminate both r and t together.

The linear stability problem for normal modes of the form

$$\psi'(r,\theta,t) = \Re\left\{ e^{st}\phi(r,\theta)\right\} \, , \tag{6.15}$$

is only reducible to a partial differential equation for independent variables r, θ and this problem remains difficult with little progress made on finding the eigenvalues s.

6.1.4 The Dean problem

In 1934 Dean found that (6.10) would reduce to a linear, ordinary differential equation for steady, spatial modes of the form

$$\psi'(r,\theta) = \Re\left\{r^{\lambda}\phi(y)\right\} \ , \tag{6.16}$$

where as before $y = \theta/\alpha$. (By setting $s = 0$ in (6.14) the $(\nabla^2\psi')_t$ term in (6.10) is zero and the method of normal modes is valid.) These modes grow or decay in space like $\exp\left\{\Re(\lambda)\ln r\right\}$ and oscillate sinusoidally like $\exp\left\{i\Im(\lambda)\ln r\right\}$.

Then the stability problem (6.10), (6.11) reduces to

$$\phi^{iv}+\alpha^2[\lambda^2+(\lambda-2)^2]\phi''+\alpha^4\lambda^2(\lambda-2)^2\phi = \alpha R[(\lambda-2)G_y(\phi''+\alpha^2\lambda^2\phi)-2G_{yy}\phi'-\lambda G_{yyy}\phi], \tag{6.17}$$

$$\phi = \phi' = 0 \quad \text{at} \quad y = \pm 1 \ , \tag{6.18}$$

where a prime denotes differentiation with respect to y. The eigenvalue problem posed by (6.17), (6.18) is referred to as the 'Dean problem' and its solutions as 'Dean modes'.

Dean found two exact solutions to (6.17), (6.18),

$$\lambda = 0 \ , \quad \phi = G_y \ ; \quad \lambda = 2 \ , \quad \phi = G_y \ , \tag{6.19}$$

which hold if $G_{yy} = 0$ at $y = \pm 1$. From figure 6.2, this may be seen qualitatively to be the marginal stability profile (c), which will be shown in the next section to occur on the boundary $R_2(\alpha)$. Drazin ([12], p. 51) also found two further exact solutions on the boundary $R = R_2(\alpha)$, both with $\lambda = -1$.

Banks et al. ([4], p. 569) plot the real part of the eigenvalues λ when $R = 0$ and find two countably infinite families of eigenvalues. They suggest a criterion for *spatial* stability that $\Re(\lambda) \geq 2$ for one family and $\Re(\lambda) \leq 0$ for the other family of eigenvalues. (For spatial stability the direction of the group velocity for each of the families of eigenvalues will be in the opposite direction to that of their algebraic growth.)

6.1.5 Bifurcations of Jeffery–Hamel flows

The bifurcations of two-dimensional channel flows (including Jeffery–Hamel flow) were re-examined by Sobey & Drazin in 1986. They described the classification (due to Fraenkel) of Jeffery–Hamel flows in terms of bifurcation theory, as well as looking at various other channel flows. The work of Sobey & Drazin described in this section may also be found in the lecture notes by Drazin ([12], (1995)), and, the weakly nonlinear stability theory in Drazin & Reid [13] §49.1.

Serrin's theorem (cf. [13], §53.1) describes how a viscous fluid in a bounded region will be stable provided the Reynolds number R is below some (small) lower bound. For flow in an unbounded domain such as channels and pipes there will be a similar criteria if all perturbations are assumed to be spatially periodic in directions which extend to infinity.

Use Serrin's theorem and consider increasing R slowly from zero in the Jeffery–Hamel problem. Initially there will be a unique, steady flow in the channel. As R increases slowly the flow will go through a series of bifurcations eventually becoming strongly nonlinear and then turbulence will follow.

Assuming normal modes of the form (6.15), then the eigenvalue $s = i\omega$ where ω is the frequency of the perturbation. If $\omega = 0$ at the margin of stability then the principle of exchange of stabilities is said to be valid and the flow will bifurcate to another steady flow. A pitchfork bifurcation will occur. If $\omega \neq 0$ then the exchange of instabilities will not be valid and the flow will bifurcate to an oscillatory flow. A Hopf bifurcation will occur. A bifurcation may be either sub- or supercritical. The type of bifurcation present may be found by considering weakly nonlinear stability theory.

Note on weakly nonlinear stability theory

Weakly nonlinear hydrodynamic stability theory has already been discussed in detail in Chapter 4.

In the 1940's, Landau considered flow near the margin of stability when $(R - R_c)$

is small. For $(R-R_c)$ small enough, assume that the most unstable mode is growing slowly while all the other modes are still decaying. After a sufficient time (or distance) nonlinear effects will become significant and harmonics will be generated and the disturbance will distort the mean-flow.

Landau described the amplitude $|A|$ of the fundamental mode of the disturbance by the equation

$$\frac{\mathrm{d}}{\mathrm{d}t}|A|^2 = 2\sigma|A|^2 - l|A|^4 \,, \tag{6.20}$$

where σ and l are real constants, with l now known as the Landau constant. If $l = 0$ then the solution of (6.20) will be $|A| \propto e^{\sigma t}$, which describes linear growth.

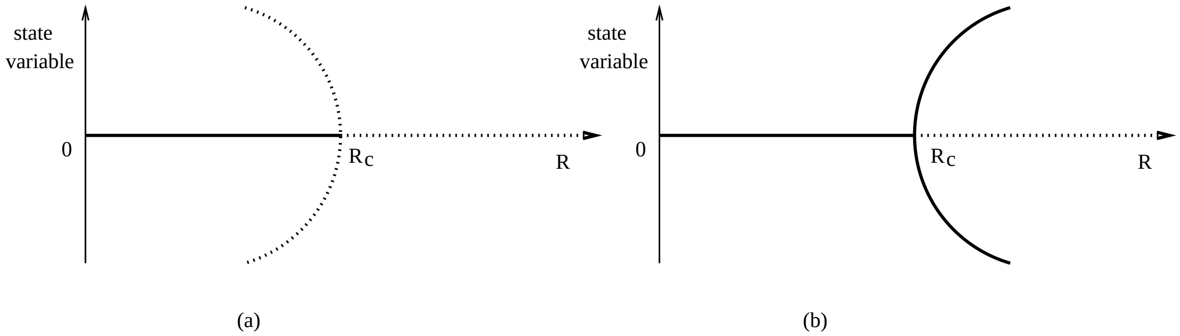

Figure 6.4: (a) subcritical pitchfork bifurcation, (b) supercritical pitchfork bifurcation. Note that the solid curves represent stable and the dotted curves unstable solutions.

If $R > R_c$ then (assuming R is only slightly greater than R_c), $\sigma > 0$. If also $l > 0$ then as $t \to \infty$ the amplitude $|A|$ of (6.20) will equilibrate and,

$$|A| \to A_e = \sqrt{\frac{2\sigma}{l}} \quad \text{as} \quad t \to \infty \,. \tag{6.21}$$

This is an example of supercritical stability where the flow is linearly unstable but inclusion of nonlinear terms reveals that the flow will settle down to a new laminar flow.

Similarly for this example if $R < R_c$ then $\sigma < 0$. Now if $l < 0$ then the size of the initial perturbation will determine the magnitude of A as $t \to \infty$. If the initial perturbation (say A_0) is greater than A_e (6.21) then,

$$|A| \to \infty \quad \text{as} \quad t \to -\frac{1}{2s}\ln\left\{\frac{A_0^2}{A_0^2 - 2\sigma/l}\right\} \,, \tag{6.22}$$

and the solution breaks down after a finite time even though $R < R_c$. This is an example of subcritical instability where instability may occur even though the flow is linearly stable.

Figure 6.4 shows two pitchfork bifurcation diagrams where the horizontal axis may be the Reynolds number and the vertical axis represents some state variable. (For Jeffery–Hamel flow α instead of R may be used and the state variable is commonly the central streamline velocity.) The solid lines represent stable and the dotted lines unstable solutions.

Calculation of the Landau constant will give the type of bifurcation present and as seen from this simple example if $\Re(l) > 0$ then it will be supercritical and if $\Re(l) < 0$ subcritical. In reality if σ or l is complex then the bifurcation will be a Hopf bifurcation (as now there will be a sinusoidal part to $e^{\sigma t}$).

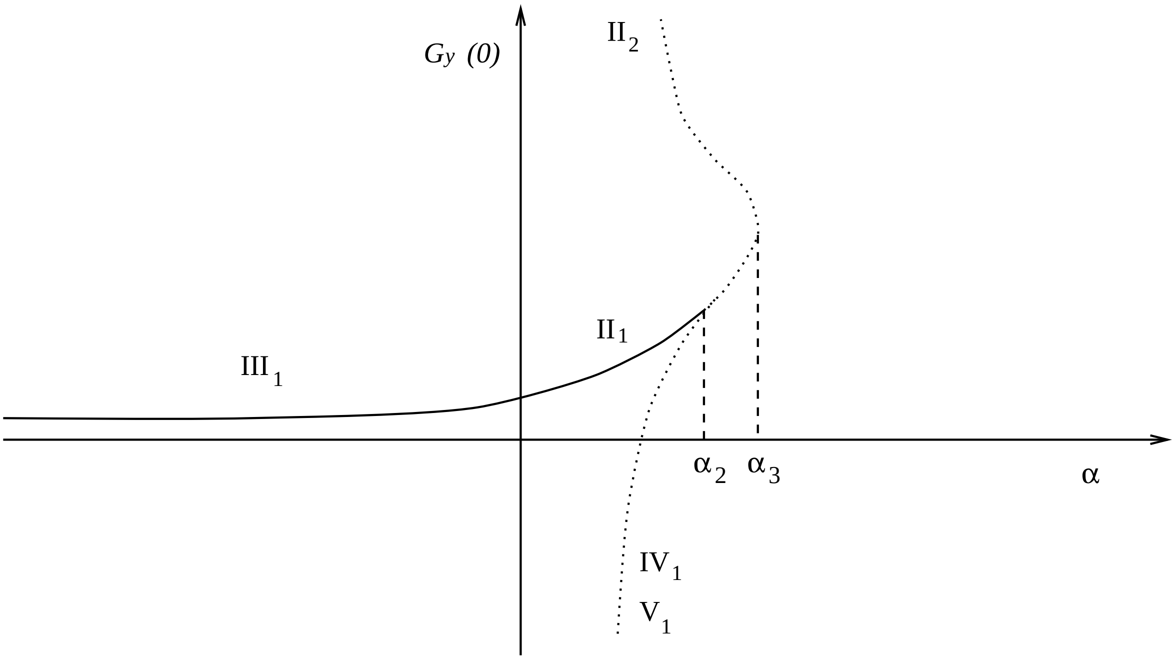

Figure 6.5: A typical bifurcation diagram for Jeffery–Hamel flow (for fixed R).

Consider taking a fixed Reynolds number and slowly increasing the semi-angle α (move vertically upwards in figure 6.3). Take as the state variable the velocity of the central streamline (i.e. $G_y(0)$). A sketch of the bifurcation diagram found is shown in figure 6.5 (from [12], p. 64).

For $\alpha < 0$ the flow is of type III_1. Note that flows of type III_1 exist if $\alpha R < 0$ (see (6.7)) and hence III_1 is valid for $R > 0$ as long as $\alpha < 0$. Then as α passes through zero there is a smooth continuous change to type I or II_1. (This change will only be continuous if $R > 0$ for type III_1.)

At the boundary $\alpha = \alpha_2(R)$ a subcritical pitchfork bifurcation occurs. The unstable branches for solutions of type IV_1 and V_1 appear to coincide in figure 6.5, but, the sketch is a sideways view and the two prongs actually extend out from and into the page in a third dimension with the state variable $G_{yy}(0)$.

Recalling figure 6.2; the sketch is in the shape of a subcritical pitchfork bifurcation and the marginal stability curve (c) occurs where $\alpha = \alpha_2(R)$ when the flow is on the verge of separating at the walls, (i.e. $G_{yy} = 0$ at $y = \pm 1$).

There is a further bifurcation at $\alpha = \alpha_3(R)$ which is a turning point. It may be seen from figure 6.5 that for $\alpha > \alpha_3(R)$ there is no continuous extension of the flow. As $\alpha \to \alpha_2(R)$ or $R \to R_2(\alpha)$ (from below) the principle of exchange of stabilities is valid and the steady, primary Jeffery–Hamel flow bifurcates to a steady, unstable secondary flow. The primary Jeffery–Hamel flow is hence marginally stable to a 'Dean mode' as $\alpha \to \alpha_2(R)$.

The mechanism for instability of Jeffery–Hamel flow may be simply described as follows. The vorticity equation (6.2) is invariant under the transformation $\theta \mapsto \theta + \delta$. Hence, if $\Psi(\theta)$ is a solution of (6.2) then so is $\Psi(\theta + \delta)$. Now let $\delta \to 0$ and expand Ψ as a Taylor series

$$\Psi(\theta + \delta) = \Psi(\theta) + \delta \Psi_\theta(\theta) + O(\delta^2) \quad \text{as} \quad \delta \to 0\,. \tag{6.23}$$

In order that (6.23) satisfies the boundary conditions (6.6) it is required that $\Psi_{\theta\theta} = 0$ in addition to $\Psi = \Psi_\theta = 0$ at $\theta = \pm\alpha$. However, $\Psi(\theta)$ is the stream function of the basic flow and hence any small rotation of the profile leads to an unstable profile with a perturbation stream function of the form $\psi' = \delta \Psi_\theta$, (compare (6.23) with (6.9)). Therefore the profile with $\Psi = \Psi_\theta = \Psi_{\theta\theta} = 0$ at $\theta = \pm\alpha$ is that of marginal stability (i.e. figure 6.2 (c)). The mechanism of instability of Jeffery–Hamel flow to 'Dean modes' is thus a small rotation of the profile about the line source ($r = 0$).

6.1.6 Bifurcation of other channel flows

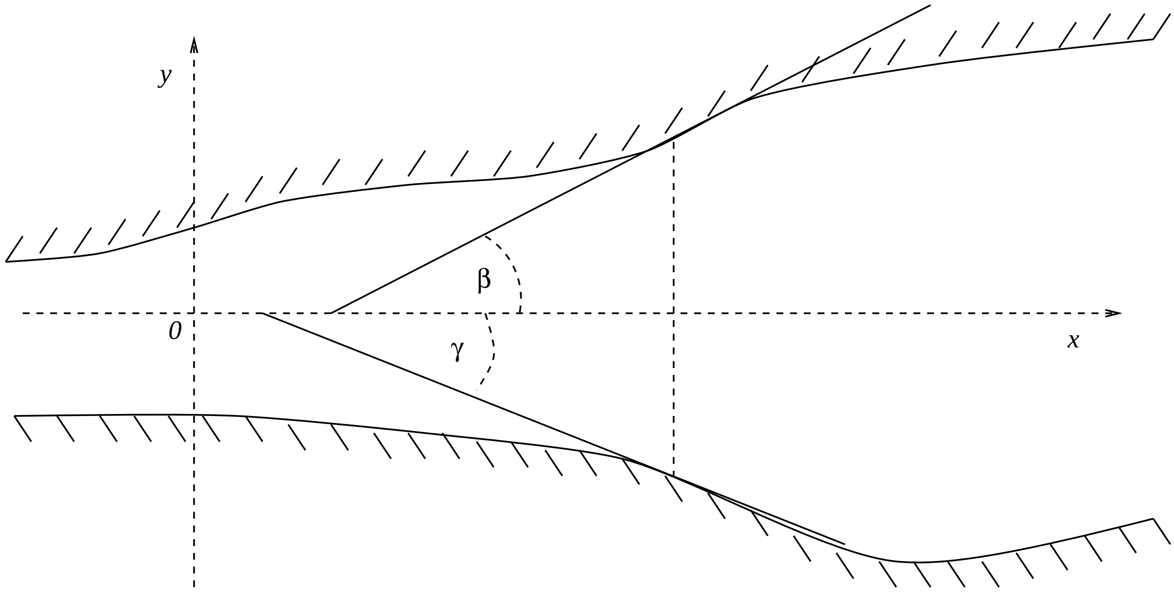

Figure 6.6: Sketch of a channel of small curvature approximated locally by a Jeffery–Hamel flow

As well as for Jeffery–Hamel flow the stability of other channel flows (symmetric and asymmetric) has been investigated and in several cases related to Jeffery–Hamel flow.

If the curvature of the walls is not too great then channel flow may be approximated locally at fixed stations to a Jeffery–Hamel flow with semi-angle $\alpha = \frac{1}{2}(\beta + \gamma)$ (see figure 6.6) with R determined by the flux along the channel and the viscosity of the fluid.

In 1986 Sobey & Drazin conjectured that flow in the channel would be stable if the local Jeffery–Hamel flow was stable at each station along the channel. In other words let α_m be defined as the maximum value of $\frac{1}{2}(\beta + \gamma)$ for all stations along the channel and then the flow will be stable if $\alpha_m < \alpha_2(R)$.

However, numerical studies of symmetric channels have all shown the first pitchfork bifurcation to be supercritical. Hamadiche et al. [21] considered the flow in a symmetric diverging channel over a finite domain (i.e. $a \leq r \leq b$) and indeed found the bifurcation to be supercritical.

Thus we have the paradox that Jeffery–Hamel flow solutions have a subcritical pitchfork bifurcation whereas the pitchfork bifurcation will be supercritical for channel flows. Modelling a channel flow as a series of Jeffery–Hamel flows may lead to a value of α_m such that the flow is predicted to be unstable when in fact the first bifurcation has led to another stable flow.

6.2 Temporal stability far downstream

From §6.1.5 the primary Jeffery–Hamel flow is unstable when $R > R_2(\alpha)$ to a 'Dean mode'. However, as $\alpha \to 0$ the flow becomes the well known plane Poiseuille flow for which the primary flow is known to become unstable when $R > R_c \approx 3848$. At $R_c \approx 3848$ there is a subcritical Hopf bifurcation as an oscillatory instability sets in. R_c is $\frac{2}{3}$ times the 'usual' value of 5772 for plane Poiseuille flow because of the scaling chosen here. (Note that as $\alpha \to 0$ then $R = Q/2\nu$ will equal the Reynolds number for plane Poiseuille flow in a channel defined as $R = UL/\nu$, where U is the central streamline velocity and L half the width of the channel.)

This mode of instability is referred to as an Orr–Sommerfeld mode because the disturbance is generated through the Tollmien–Schlichting instability mechanism, namely through the transfer of energy from critical layers in the fluid (near the walls) to the disturbance.

The value of $R_c \approx 5772$ is well known for plane Poiseuille flow with a profile $U(y) = 1 - y^2$. For the Jeffery–Hamel flow as $\alpha \to 0$ then the profile becomes $\frac{3}{2}(1 - y^2)$ and hence R_c is actually found to be 3848 for Orr–Sommerfeld modes of disturbance (that is $\frac{2}{3}$ times 5772).

When $\alpha = 0$ the primary flow is marginally stable when $R = 3848$ to an Orr–Sommerfeld mode. However, when $R = 3848$ the primary flow will be marginally stable to a 'Dean mode' for a semi-angle $\alpha \approx 4.712/3848 = 0.00122$ radians, i.e. 0.07 degrees. These two modes are associated with very different mechanisms of instability.

This work is motivated by the investigation of the roles played by the alternative mechanisms of instability in the flow between two nearly parallel walls.

In equation (6.10) the variables r and t are not both separable. Tam [43] considers the linear stability of a two-dimensional jet and he approximates separated variables far downstream. The spirit of Tam's method was to scale time with some power of the distance downstream such that far downstream there would be a valid asymptotic solution. Following Tam's method it was recognized by McAlpine & Drazin [31] that introducing a new time variable $\tau \propto t/r^2$ would allow the terms $\nabla^4\psi'$ and $(\nabla^2\psi')_t$ in (6.10) to be of the same order of magnitude as $r \to \infty$ and hence it would be possible to separate the variables r and τ far downstream.

6.2.1 Calculation of temporal stability characteristics

Firstly define the change of variables,

$$(r, \theta, t) \mapsto (r, y = \theta/\alpha, \tau = Rt/\alpha^2 r^2) \, , \tag{6.24}$$

and assume that as $r \to \infty$ for fixed y and τ, the solution may be resolved into a superposition of modes of the form

$$\psi'(r, y, \tau) = \Re \left\{ \exp[i(k\alpha^{-1}\ln r - \omega\tau)] f(y) \right\} \, , \tag{6.25}$$

for complex frequency ω and real wavenumber k.

Now substitute (6.25) into (6.10) and the leading terms as $r \to \infty$ are found to be

$$\begin{aligned}
(\nabla^2\psi')_t &\sim -\frac{i\omega R}{\alpha^4 r^4} \left\{ f'' - (k + 2i\alpha)^2 f \right\} \exp[i(k\alpha^{-1}\ln r - \omega\tau)] \, , && (6.26)\\
(\nabla^2\psi')_r &\sim \frac{i(k + 2i\alpha)}{\alpha^3 r^3} \left\{ f'' - k^2 f \right\} \exp[i(k\alpha^{-1}\ln r - \omega\tau)] \, , && (6.27)\\
\psi'_r &\sim \frac{ik}{\alpha r} f \exp[i(k\alpha^{-1}\ln r - \omega\tau)] \, , && (6.28)\\
\psi'_\theta &\sim \frac{1}{\alpha} f' \exp[i(k\alpha^{-1}\ln r - \omega\tau)] \, , && (6.29)\\
\nabla^4\psi' &\sim \frac{1}{\alpha^4 r^4} \left\{ f^{iv} - [k^2 + (k + 2i\alpha)^2] f'' + \right. \\
&\quad \left. k^2 (k + 2i\alpha)^2 f \right\} \exp[i(k\alpha^{-1}\ln r - \omega\tau)] \, , && (6.30)
\end{aligned}$$

for the quantities involving ψ' required in (6.10).

Substituting (6.26), (6.27), (6.28), (6.29) and (6.30) into (6.10) reveals each term of (6.10) to be of $O(1/r^{4-ik/\alpha})$ and hence multiplying through by $\alpha^4 r^4 \exp[-i(k\alpha^{-1}\ln r - \omega\tau)]$ gives in the limit as $r \to \infty$,

$$f^{iv} - [k^2 + (k+2i\alpha)^2]f'' + k^2(k+2i\alpha)^2 f = -i\omega R[f'' - (k+2i\alpha)^2 f] \\ + iR(k+2i\alpha)G_y(f'' - k^2 f) - ikRG_{yyy}f - 2\alpha RG_{yy}f' \,, \tag{6.31}$$

with boundary conditions

$$f = f' = 0 \quad \text{at} \quad y = \pm 1 \,. \tag{6.32}$$

(6.31) together with (6.32) is a fourth-order eigenvalue problem which describes the development of the flow to infinitesimal disturbances far downstream.

Letting the velocity profile $G_y(y) = U(y)$, then equation (6.31) in the limit as $\alpha \to 0$ reduces to

$$f^{iv} - 2k^2 f'' + k^4 f = ikR[(U - c)(f'' - k^2 f) - U'' f] \,, \tag{6.33}$$

where $c = \omega/k$. This is the familiar Orr–Sommerfeld equation for the stability of a parallel flow to infinitesimal disturbances in a bounded channel. Note that the variable τ had a constant of proportionality R/α^2 to ensure that (6.31) would reduce in the limit $\alpha \to 0$ to the familiar form of the Orr–Sommerfeld equation (6.33).

Further, by setting $\omega = 0$ and $\lambda = ik/\alpha$ equation (6.31) reduces to

$$f^{iv} + \alpha^2[\lambda^2 + (\lambda-2)^2]f'' + \alpha^4\lambda^2(\lambda-2)^2 f = \alpha R[(\lambda-2)U(f'' + \alpha^2\lambda^2 f) - \lambda U'' f - 2U'f'] \,, \tag{6.34}$$

the Dean equation (§6.1.4, (6.17)) for steady, spatial disturbances.

After considering the limits as $\omega \to 0$ and $\alpha \to 0$, it may be seen that the eigenvalue problem (6.31), (6.32) bridges the gap between the two distinct stability mechanisms, namely the subcritical pitchfork bifurcation of Jeffery–Hamel flow to 'Dean modes' and the subcritical Hopf bifurcation associated with Orr–Sommerfeld modes.

As $r \to \infty$, (6.25) is assumed to be the leading order term of an asymptotic solution of (6.10). In McAlpine & Drazin [31], appendix A by Dr. R.R. Kerswell and Prof. P.G. Drazin discusses the validity of this assumption. A simplified model problem is considered, namely the diffusion equation in two dimensions. A solution is sought for large r following the method in this chapter. However, for this model problem an exact solution is also found because the variables y and τ are separable. A comparison of the two solutions suggests an asymptotic expansion for the solution of the diffusion equation, with a leading term similar to (6.25) as $r \to \infty$. The form of the asymptotic solution appears admissible as a solution of the linearized vorticity equation (6.10).

6.2.2 Calculation of the energy transfer from the basic flow to the perturbation

As was noted in §6.1.2 and §6.1.5 the primary basic flow does not exist for $R > R_3(\alpha)$ and therefore the problem (6.31), (6.32) has no meaning for $R > R_3(\alpha)$. As a result it makes little sense to look at the limit as $R \to \infty$ in (6.31) to consider the inviscid problem (as in the case of the Orr–Sommerfeld equation which reduces to the Rayleigh stability equation in the limit as $R \to \infty$). However, for small α a Jeffery–Hamel flow exists for fairly large values of R. Numerical results for large values of R may be obtained by using asymptotics in the limit as $R \to \infty$.

In Chapter 3 the energy equation (3.97) was introduced which described the energy transfer between perturbations and the basic flow. Energy is transferred from the basic flow to the perturbation via the product of the velocity gradient and the Reynolds stress. Phase differences between the velocity perturbations contribute to the Reynolds stress. Viscous forces may produce this phase shift in the components of the perturbation velocity. Contributions to the Reynolds stress are thus significant in two regions of the basic flow, namely the viscous wall layer and the critical layer. As R increases the majority of the energy transfer from the basic flow to the perturbation is via the Reynolds stress in the critical layer.

The critical layer occurs where the inviscid stability equation is singular. After considering (6.31) as $R \to \infty$, note that the coefficient of f'' vanishes where $i(k + 2i\alpha)U = i\omega$. The critical layer is thus defined as the point y_c where,

$$U(y_c) = \frac{\omega}{k + 2i\alpha}\,, \tag{6.35}$$

which will be *complex* at marginal stability when $\alpha \neq 0$. (For the computations y_c is taken to be at the point where U is equal to the real part of the RHS of (6.35).)

From the energy equation (3.97), the term I_2 (3.99) gives the rate of transfer of energy from the basic flow to the perturbation via the Reynolds stress. The term $(\partial u_i/\partial x_j)(u_i'u_j')$ in I_2 is more readily written in terms of the rate-of-strain tensor, d_{ij}, as $d_{ij}u_i'u_j'$. For two-dimensional motion and plane polar coordinates,

$$\begin{bmatrix} d_{rr} & d_{r\theta} \\ d_{\theta r} & d_{\theta\theta} \end{bmatrix} = (2\alpha^2 r^2)^{-1} \begin{bmatrix} -2\alpha U & U' \\ U' & 2\alpha U \end{bmatrix} , \tag{6.36}$$

and $u_r' = \partial\psi'/r\partial\theta$, $u_\theta' = -\partial\psi'/\partial r$.

From (6.25), the modes have 'wavelength' $2\pi\alpha/k$ in $\ln r$ space. As $r \to \infty$ and for *small* $2\pi\alpha/k$, the variation in $1/r^2$ will be negligible compared with $\ln r$ over $2\pi\alpha/k$. After noting that $r\mathrm{d}r\mathrm{d}\theta = \alpha r^2 \mathrm{d}(\ln r)\mathrm{d}y$, the local rate of energy transfer, for $y =$ constant, will be,

$$\sigma(y) = -\frac{k}{2\pi\alpha}\int_0^{2\pi\alpha/k} r^2 d_{ij}u_i'u_j' \,\mathrm{d}(\ln r) , \tag{6.37}$$

on averaging over a 'wavelength' in the radial direction. Neglecting small terms as $r \to \infty$ and holding r constant while averaging over variations in $\ln r$ reduces (6.37) to approximately,

$$\sigma(y) = -\frac{1}{4\alpha^4 r^4}\exp(2\omega_i Rt/\alpha^2 r^2)\left\{ikU'(f^\star f' - ff^{\star'}) - 2\alpha U(|f'|^2 - k^2|f|^2\right\} , \tag{6.38}$$

where $\star$ denotes a complex conjugate quantity. In the limit as $\alpha \to \infty$, $\sigma(y)$ reduces to the energy transfer expression obtained from the Orr–Sommerfeld problem, (the similarity between (6.38) and the Reynolds stress (3.90) from the Orr–Sommerfeld problem may be observed).

In §6.4 the quantity,

$$S(y) = -\left\{ikU'(f^\star f' - ff^{\star'}) - 2\alpha U(|f'|^2 - k^2|f|^2\right\} , \tag{6.39}$$

is normalized and plotted to represent the energy transfer from the basic flow to the perturbations far downstream.

6.3 The method of orthonormalization

The solution to the Orr–Sommerfeld problem (6.33) on a semi-infinite domain $[0, \infty)$ has already been discussed in §3.4 by using the method of compound matrices. An asymptotic solution of the Orr–Sommerfeld equation is known far outside of the boundary layer. This solution is required when using the method of compound matrices. However the form of the solution of the Orr–Sommerfeld equation on a bounded domain is not clear and a superior method to use in this case is the method of orthonormalization which makes no assumption about the form of the eigenfunctions.

The method may be found in Davey [8] and is suitable for two-point boundary-value problems of similar character to the Orr–Sommerfeld problem. The Orr–Sommerfeld equation is a stiff equation. Let it be written as a homogeneous equation

$$L[\phi] = 0 \,, \tag{6.40}$$

where the operator L is defined as

$$L = \left\{D^2 - \alpha^2 - i\alpha R(U - c)\right\} \left\{D^2 - \alpha^2\right\} + i\alpha R U'' \,. \tag{6.41}$$

Then solving the characteristic equation for (6.40) reveals the characteristic values of the operator L to be $O(\pm\alpha)$ and $O(\pm\sqrt{\alpha R})$ as $R \to \infty$. The eigenfunctions ϕ will then (for large R) vary greatly in size and the solution will be dominated by one set of the characteristic values. Care must be taken to ensure all the solutions are found.

The details of the method for a model fourth-order problem are now briefly given (following Davey [8]). Consider the homogeneous, fourth-order problem,

$$L[\phi] = 0 \,, \quad \phi = D\phi = 0 \quad \text{at} \quad x = 0, 1 \,. \tag{6.42}$$

Divide the domain $[0, 1]$ into m equal intervals of length $h = 1/m$. Now let $\mathbf{y}_i$ denote the four-dimensional vector value of

$$\mathbf{y} = \left(\phi, D\phi, D^2\phi, D^3\phi\right) \,, \tag{6.43}$$

at $x = ih$ for $0 \leq i \leq m$.

Recall that the solution of

$$\dot{\mathbf{y}} = A(t)\mathbf{y} \, , \tag{6.44}$$

a system of n first order linear ordinary differential equations, may be expressed in terms of a fundamental matrix $F(t)$. $F(t)$ is an $n \times n$ matrix of any n linearly independent solutions of (6.44). Then $F(t)$ will span the solution space of (6.44) and every solution will be of the form

$$\mathbf{y}(t) = F(t)\mathbf{c} \, , \tag{6.45}$$

where $\mathbf{c}$ is a constant vector. If the solution is known at $t = t_0$, say $\mathbf{y}(t_0) = \mathbf{a}$, then $\mathbf{c} = F^{-1}(t_0)\mathbf{a}$ and the solution of the initial value problem will be,

$$\mathbf{y}(t) = F(t)F^{-1}(t_0)\mathbf{a} \, . \tag{6.46}$$

Now define A^{i+1} to be a 4×4 transfer matrix such that

$$\mathbf{y}_{i+1} = A^{i+1}\mathbf{y}_i \, . \tag{6.47}$$

A^{i+1} is determined by letting $\mathbf{y}_i$ in turn be $(1,0,0,0)$, $(0,1,0,0)$, $(0,0,1,0)$ and $(0,0,0,1)$ and then integrating from $x = ih$ to $(i+1)h$. The transfer matrices show how neighbouring values of $\mathbf{y}$ may be found from each other.

The relationship between $\mathbf{y}_0$ and $\mathbf{y}_m$ will be

$$\mathbf{y}_m = B\mathbf{y}_0 \, , \tag{6.48}$$

where $B = A^m A^{m-1} \ldots A^2 A^1$. Write (6.48) out in full (implementing the boundary conditions given in (6.42)) to find,

$$\begin{pmatrix} 0 \\ 0 \\ D^2\phi \\ D^3\phi \end{pmatrix}_{x=1} = \begin{pmatrix} \star & \star & B_{13} & B_{14} \\ \star & \star & B_{23} & B_{24} \\ \star & \star & \star & \star \\ \star & \star & \star & \star \end{pmatrix} \begin{pmatrix} 0 \\ 0 \\ D^2\phi \\ D^3\phi \end{pmatrix}_{x=0} . \tag{6.49}$$

Let $u = D^2\phi$ and $v = D^3\phi$ evaluated at $x = 0$ and then (taking the upper right hand quarter of B) deduce

$$\begin{pmatrix} 0 \\ 0 \end{pmatrix} = \begin{pmatrix} B_{13} & B_{14} \\ B_{23} & B_{24} \end{pmatrix} \begin{pmatrix} u \\ v \end{pmatrix} . \tag{6.50}$$

To ensure that (u, v) is a non-null solution we require,

$$\det \begin{pmatrix} B_{13} & B_{14} \\ B_{23} & B_{24} \end{pmatrix} = 0 \, . \tag{6.51}$$

The influence of the most rapidly growing solution may modify B such that it does not fully span the solution space. Let the number of integration steps be $m = pq$ where $p, q \in \mathbb{N}$. To ensure B fully spans the solution space for (6.44), let $B = B^p B^{p-1} \dots B^2 B^1$ where B^1 is the left product of the first q transfer matrices, B^2 the left product of the next q transfer matrices and so on. Now take B^1 and add a multiple of the third column to the fourth column such that they are now orthogonal. Then normalize all four columns before left-multiplying by B^2. Repeat this process of orthonormalization before left-multiplying by B^3 and so on until a modified B^p is obtained.

The essential idea here is that as you integrate from 0 to 1 you adjust the solutions to ensure they do not become nearly parallel. This ensures the span of the solution space is maintained and the orthonormalization will not affect the value of the determinant in (6.51) (because a matrix determinant is unchanged after elementary row operations).

In practice an initial guess for the eigenvalue, say c, is required. The modified matrix B is calculated using typically a fourth-order Runge–Kutta integration scheme with a Gram–Schmidt orthogonalization routine to orthogonalize the third and fourth columns of B^i.

The value of the determinant in (6.51) is then sought and this (for fixed values of all other parameters in (6.42)) will be a function of c only. A standard iterative scheme may then be used to find the exact eigenvalue c. A suitable scheme was found to be the ‘regula falsi’ method which is essentially Newton’s method with an approximate expression used for the derivative.

Having evaluated the eigenvalue c, the corresponding eigenfunction ϕ may be calculated. Some extra computational work is required to calculate ϕ although all the necessary ‘information’ will have been obtained during the calculation of c. The disadvantage of the method of orthonormalization is that ϕ is not readily obtained during the calculation of c. The matrices B^i must be stored and then following the procedure described by Davey [9], pp. 496–498, the eigenfunction ϕ may be calculated.

When integrating the Orr–Sommerfeld equation over $[0, 1]$, using $m = 1000$ and $p = 10$, eigenvalues accurate to six decimal places were obtained. (This is based on the results for plane Poiseuille flow compared with published results.)

6.4 Results

Using the method of orthogonalization described in §6.3, equation (6.31) was solved for various values of fixed α. To simplify the problem (or rather to reduce the computational load), only even eigenfunctions were considered. As a result (6.31) was only integrated over half the domain, i.e. $0 \leq y \leq 1$. The restriction to an even mode is permissible for the following reasons. It is well known that for plane Poiseuille flow the most unstable mode will be the first even eigenfunction. Also, at the boundary $R_2(\alpha)$ a Jeffery–Hamel flow bifurcates from a stable, symmetric flow (II_1) to an unstable, symmetric flow (II_2) and so symmetry is preserved. In both mechanisms the initial instability will have an even eigenfunction.

As in the Orr–Sommerfeld calculations (e.g. Chapter 3) marginal curves in the (R, k)-plane were computed for fixed semi-angles α. However, for Jeffery–Hamel flow the basic velocity profile varies with R (and is recalculated at each point on the marginal curve), although $G_y(y) \to \frac{3}{2}(1 - y^2)$ as $\alpha \to 0$ giving plane Poiseuille flow, which is independent of R.

At each point in the (R, k)-plane the least stable mode was calculated. Although there are presumably two countably infinite families of modes, there appears to be at most one unstable mode for each fixed R, k and α.

Several of the marginal stability curves are shown in figure 6.7. As mentioned in §6.1.5, the convention taken for a Jeffery–Hamel flow with $\alpha < 0, R > 0$ is that the flow is into a line sink (i.e. a flow of type III_1). Note that solving (6.31) for negative R is the same as solving it for negative α, ω and k, which explains the negative wavenumber axis in figure 6.7(a).

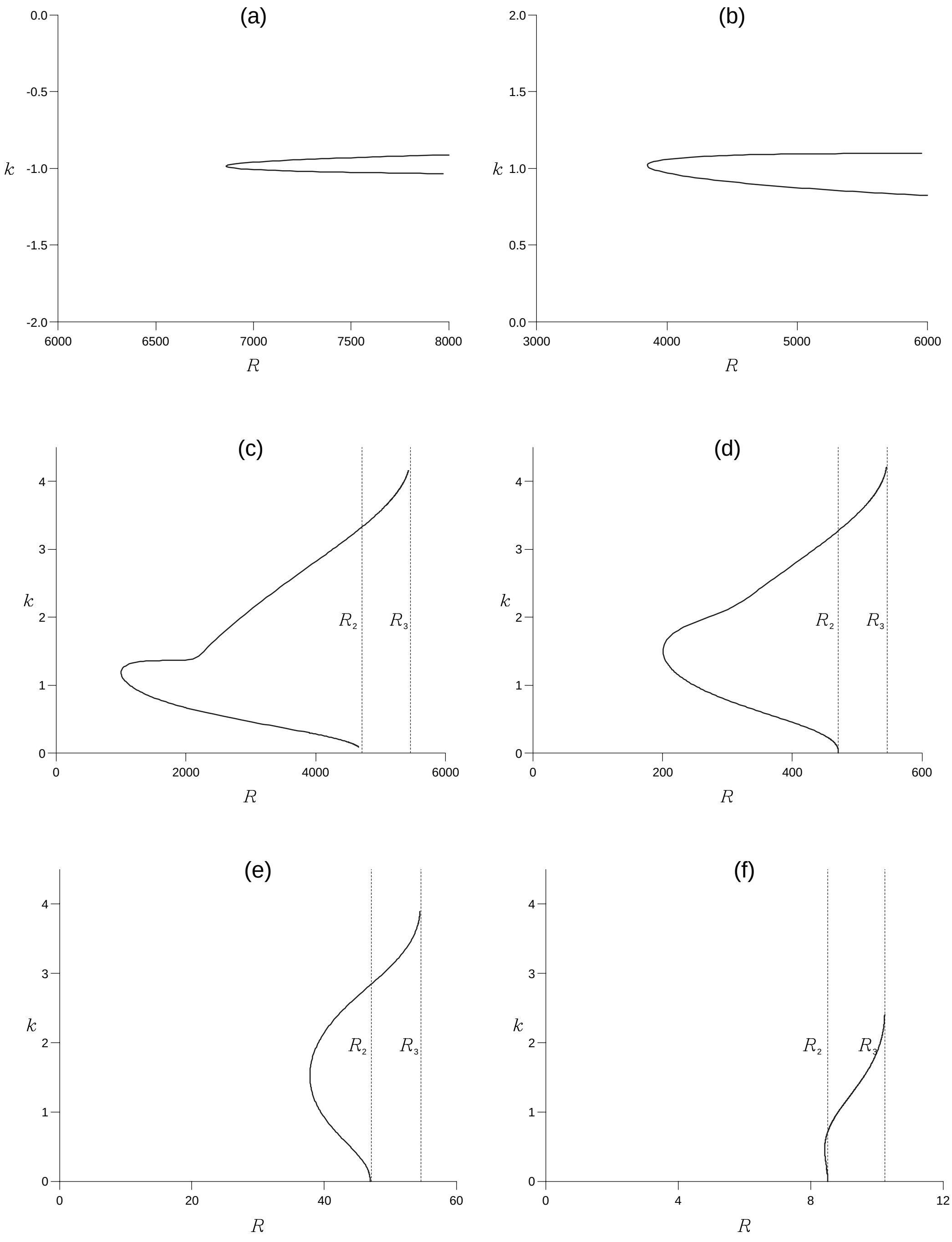

Figure 6.7: Marginal curves in the (R, k)-plane for varying α. (a) $\alpha = -0.0001$, (b) $\alpha = 0$, (c) $\alpha = 0.001$, (d) $\alpha = 0.01$, (e) $\alpha = 0.1$ and (f) $\alpha = 0.5$. (Note the different scales).

On each curve the values of $R_2(\alpha)$ and $R_3(\alpha)$ are shown by the vertical dashed lines. Recall from §6.1.4 that on $R_2(\alpha)$ there are four known exact solutions to the Dean problem (6.17). These correspond to $\lambda = 0, 2, -1$, and -1 or alternatively $k = 0, -2i\alpha, i\alpha$, and $i\alpha$. The three Dean solutions giving imaginary wave numbers were used as a check of the computer program. Each marginal curve (for $\alpha > 0$) as $k \to 0$ approaches $R = R_2(\alpha)$ corresponding to the Dean eigensolution, $\lambda = 0, \phi = G_y$. Note that on the marginal curves $\omega \to 0$ as $k \to 0$ thereby verifying that the curves do indeed tend to the *steady* 'Dean modes' on $R_2(\alpha)$. The marginal curve represents both instability mechanisms for 'Dean' and Orr–Sommerfeld modes.

Define $R_c(\alpha)$ to be the critical Reynolds number for a particular semi-angle α. $R_c(\alpha)$ was calculated and compared with $R_2(\alpha)$. From figure 6.7(b), $R_c(0) = 3848$, the value for plane Poiseuille flow. The value of $R_c(\alpha)$ on the marginal curves then changes very rapidly with a small increase or decrease of α from zero (as will be seen later in figure 6.8).

Now define k_c as the value of k at $R_c(\alpha)$, (i.e. the critical wavenumber) and k_3 as the value of k at $R_3(\alpha)$. Note that the analogous value k_2 is always zero. Observe that as α increases slowly from zero k_c first of all increases before decreasing, whereas k_3 just decreases. However the changes are small and, $k_c \approx 1$ and $k_3 \approx 4$.

Also as the marginal curves tend to the line $R = R_3(\alpha)$ their gradients become steeper and appear to become infinite at $R = R_3(\alpha)$. Recall the bifurcation diagram figure 6.6 for Jeffery–Hamel flow where there is a turning point at $R = R_3(\alpha)$. If the marginal curve were continued then it may bend back on itself giving another unstable region for larger values of k. At present the marginal curves have only been calculated up to the turning point at $R_3(\alpha)$ and not for the II_2 solution branch after the turning point.

The graphs of $R_c(\alpha)$ and $R_2(\alpha)$ are shown in figure 6.8. Due to the range of R, the graph has been split into three with the two small insets showing the behaviour in greater detail for low Reynolds numbers and very small semi-angles.

In all the calculations it seems that $R_2(\alpha) > R_c(\alpha)$ and $R_c(\alpha) \sim R_2(\alpha)$ as $R \to 0$.

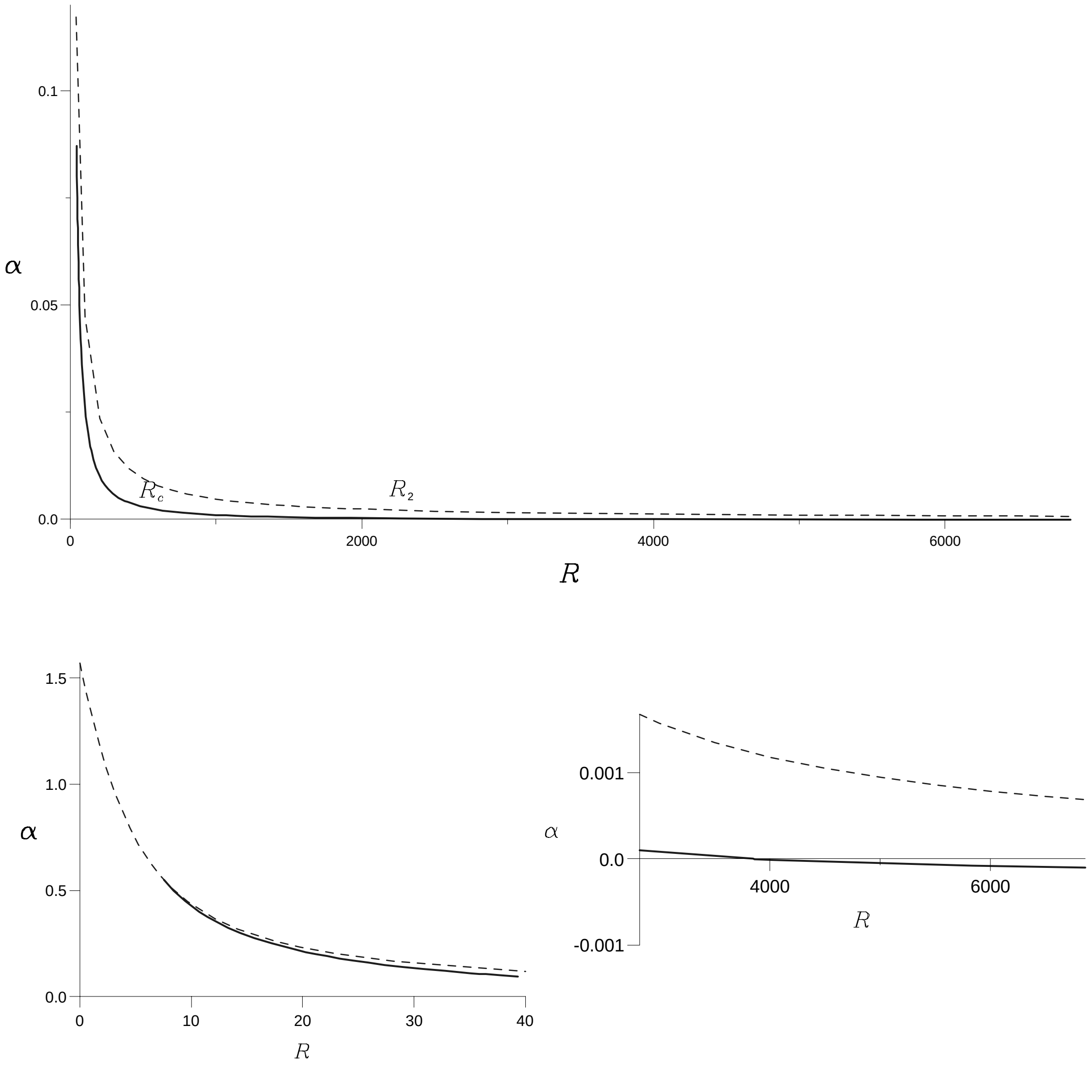

Figure 6.8: Graph of $R_c(\alpha)$ and $R_2(\alpha)$ with insets for small R and small α.

For $\alpha \approx 0.5$ the two curves are virtually indistinguishable with $R_c(\alpha) \approx R_2(\alpha)$.

Also observe the rapid change of $R_c(\alpha)$ for small perturbations about $\alpha = 0$. The linear theory predicts that a small divergence of the walls has a strong destabilizing effect on the plane Poiseuille flow and a small convergence leads to an even stronger stabilizing effect.

The values of $R_c(\alpha)$ become surprisingly small (i.e. lower than 10), and $R_c(\alpha)$ never crosses $R_2(\alpha)$. Observations from experiments would suggest Hopf bifurcations do not appear until the Reynolds number is at least of the order of a hundred in the majority of channel flows.

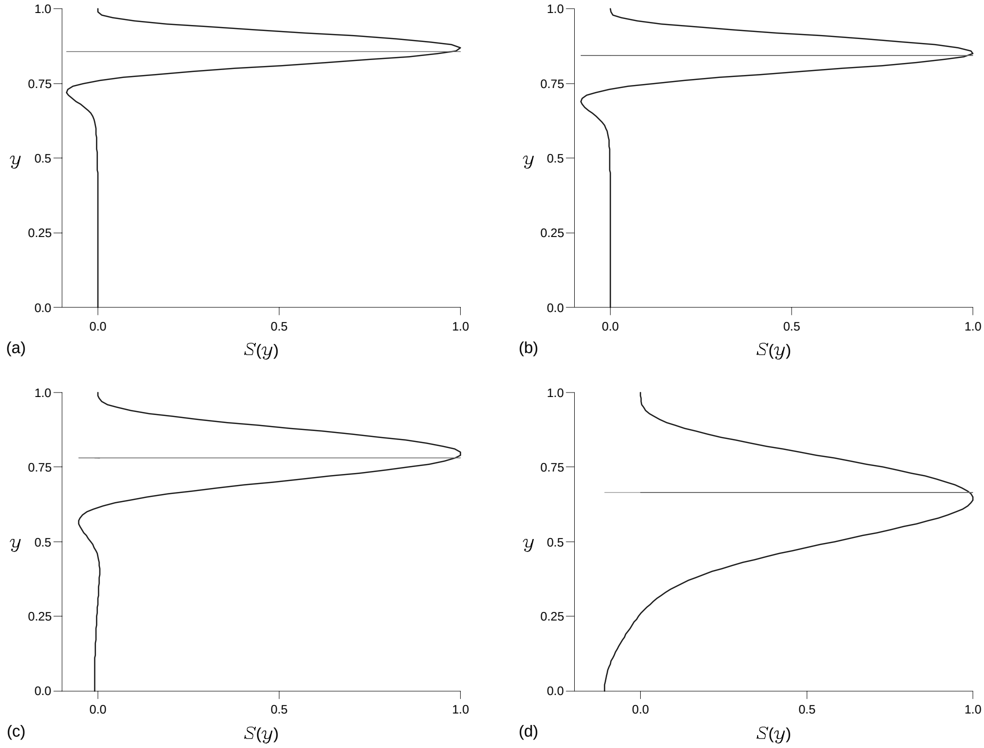

Figure 6.9: Local energy transfer $S(y)$ from the basic flow to the perturbation, at the 'nose' of the marginal curve. (a) $\alpha = 0$, $R = R_c = 3848.2$; (b) $\alpha = 0.0001$, $R = R_c = 2822.4$; (c) $\alpha = 0.001$, $R = R_c = 999.1$; (d) $\alpha = 0.01$, $R = R_c = 200.7$.

Figures 6.9 and 6.10 examine the rate of transfer of energy from the basic flow to the perturbation via the Reynolds stress. Figure 6.9 plots $S(y)$ where $R = R_c$ on the marginal curve for Jeffery–Hamel flow with semi-angle $\alpha = 0,\ 0.0001,\ 0.001,$ and 0.01. Figure 6.10 plots $S(y)$ at a point on the lower branch of the marginal curve for the same values of α.

Figure 6.8 demonstrates that a small divergence of the flow may have a strong destabilizing influence. Figures 6.9 and 6.10 show the effect of a small divergence of the flow on the energy transfer mechanism. The solid horizontal line on each graph is y_c, the critical point defined by (6.35).

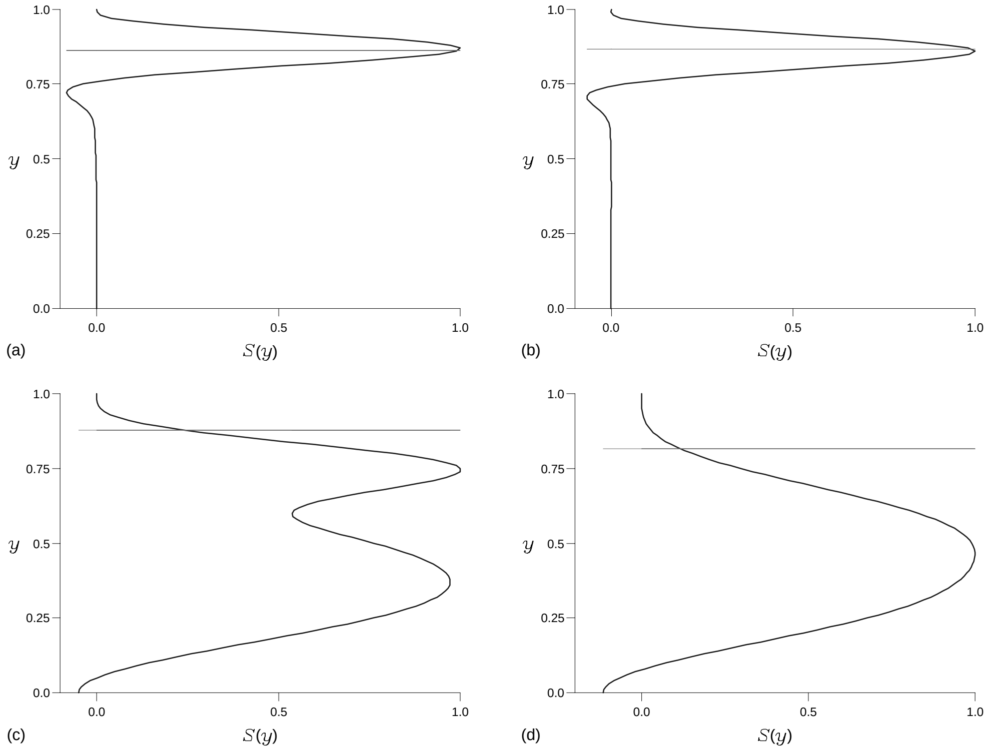

Figure 6.10: Local energy transfer $S(y)$ from the basic flow to the perturbation, at a point on the lower branch of the marginal curve. (a) $\alpha = 0$, $R = 4000$; (b) $\alpha = 0.0001$, $R = 4000$; (c) $\alpha = 0.001$, $R = 4000$; (d) $\alpha = 0.01$, $R = 400$.

In figure 6.9, at the 'nose' of each marginal curve the energy transfer is seen to be dominated by the critical layer mechanism. On increasing α the critical layer is seen to move slightly further away from the boundary.

In figure 6.10, the energy transfer is still dominated by the critical layer mechanism for very small semi-angles α, (figures 6.10(a) and (b)). However, on increasing α the Tollmien–Schlichting instability mechanism described by the Orr–Sommerfeld problem is seen to be modified (figures 6.10(c) and (d)). For a small divergence of the flow, the predominant energy transfer is no longer confined to the critical layer region.

Figure 6.11 plots the basic velocity profiles at the points on the lower branch of the marginal curve in figure 6.10. The main difference between the profiles 6.11(a), (b) and

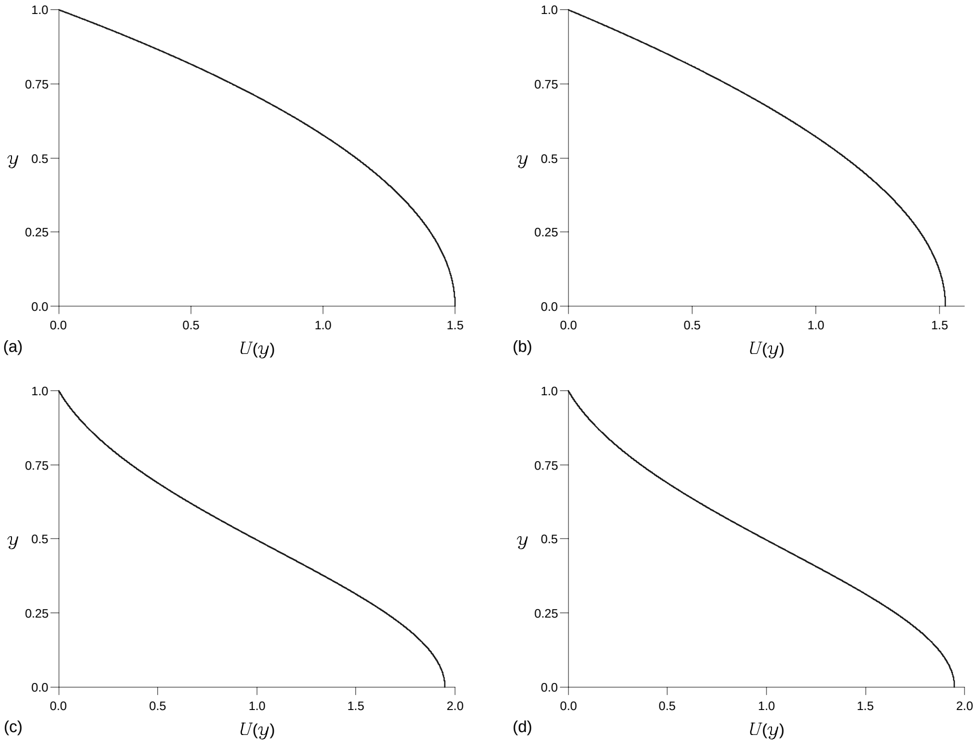

Figure 6.11: Jeffery–Hamel basic velocity profile $U(y) = G_y(y)$, at a point on the lower branch of the marginal curve. (a) $\alpha = 0$, $R = 4000$; (b) $\alpha = 0.0001$, $R = 4000$; (c) $\alpha = 0.001$, $R = 4000$; (d) $\alpha = 0.01$, $R = 400$.

6.11(c), (d) is that the magnitude of U' is a maximum at the boundary for 6.11(a), (b) whereas for 6.11(c), (d) U' is a maximum at $y \approx 0.5$. Recall that the energy transfer $S(y)$ is dependent on both $U(y)$ and $U'(y)$. The energy transfer mechanism described by the Orr–Sommerfeld problem is only proportional to $U'(y)$.

6.5 Conclusions

The primary motivation for this work was to provide a simple technique for studying the linear stability of Jeffery–Hamel flows. Solutions to (6.10) are difficult to calculate because the variables r and t are not separable. However by scaling the time t, with the square of the radial distance r^2, the problem may be reduced to considering individual modes of the form (6.25) far downstream. It is anticipated that any linear disturbance may be expressed in terms of a superposition of modes of the form of (6.25) for large enough r.

When t is of order r^2 then the approximation is invalid and the domain of validity may be too far away to be of practical importance (i.e. too far downstream to be relevant to any practical example or experiment).

The results obtained show qualitative agreement with the CFD calculations in Hamadiche et al. [21], figure 1, p. 77. Hamadiche et al. solved the full linearized vorticity equation for the Jeffery–Hamel flow with inlet and outlet conditions. Hence the results given by Hamadiche et al. are not suitable to permit detailed comparison because they were obtained on a bounded domain.

The work has also attempted to link the entirely separate mechanisms of instability present in channel flow, i.e. 'Dean modes' associated with a subcritical pitchfork bifurcation at $R_2(\alpha)$ for a Jeffery–Hamel flow and Orr–Sommerfeld modes associated with a subcritical Hopf bifurcation at $R_c(\alpha)$.

The result that $R_2(\alpha) > R_c(\alpha)$ offers an explanation to part of the paradox in §6.1.6 but poses a further problem. If $R_c(\alpha) < R_2(\alpha)$ then the subcritical pitchfork bifurcation of Jeffery–Hamel flows is irrelevant when considering the stability of the flow in a symmetric channel of small curvature. A Hopf bifurcation will occur *before* the Jeffery–Hamel pitchfork bifurcation as the Reynolds number is slowly increased from zero. The Jeffery–Hamel subcritical pitchfork bifurcation would not be observed in a channel flow as a Hopf bifurcation would occur at a lower Reynolds number. However, observations show that a supercritical pitchfork bifurcation is observed in symmetric channel flows from one steady flow to another. This is not compatible with the calculations in §6.4. The calculations suggest that at fairly low Reynolds numbers the flow will become unstable and bifurcate to an unsteady, periodic flow. I have at present no explanation of this.

Carrying out a weakly nonlinear stability analysis would give either a sub- or supercritical Hopf bifurcation at R_c and hence not resolve the paradox that a supercritical pitchfork bifurcation is actually observed.

Perhaps the most surprising result of this work was the remarkably strong influence on the stability of the flow exerted by small changes in the semi-angle between the planes. The critical Reynolds number for plane Poiseuille flow was reduced from 3848 to 1000 after inclining the walls by an angle of 0.001 radians (0.057 degrees) for diverging flow. Conversely, inclining the walls by an angle of 0.0001 radians (0.0057 degrees) for converging flow raised the critical Reynolds number to nearly 7000! The tolerances when constructing a channel in a machine shop will be of a similar order to the magnitude of the angles mentioned here. These results further show how small changes to a parallel flow may disturb the delicate balance between stabilizing and destabilizing mechanisms described by the Orr–Sommerfeld problem.

For *small* α equation (6.31) compared with the Orr–Sommerfeld equation (6.32) is similar apart from the 'extra' term $-2\alpha R G_{yy} f'$ on the RHS of (6.31). On increasing α from zero the destabilizing effect on the flow may be significant when the magnitude of $-2\alpha R G_{yy} f'$ is the same as the terms on the LHS of (6.31). This occurs when the magnitude of αR is $O(1)$. For $R = R_c = 3848$, then αR will be $O(1)$ when $\alpha \approx 1/R_c = 0.00026$. The sensitivity of the instability to a small convergence or divergence of the flow may depend on αR, not α. For $R = 3848$ and $\alpha \geq 0.00026$ then $\alpha R = O(1)$ and the nature of the stability mechanism may be modified from the Orr–Sommerfeld mechanism for a parallel flow.

Figure 6.7(c) is the marginal curve for a flow with $\alpha = 0.001$, i.e. a very small divergence. The shape of the marginal curve around the 'nose' is similar to 6.7(b) for plane Poiseuille flow except for the reduction in R_c. However the lower and upper branches of the marginal curve for $\alpha = 0.001$ are observed to diverge when R is sufficiently greater than R_c. The small divergence of the flow leads to a wider band of unstable perturbation wavelengths. Recall that for plane Poiseuille flow the lower and upper branches of the marginal curve converge for R sufficiently greater than R_c.

Figure 6.9 shows that the energetics of the instability for $R \approx R_c$ appear to be the same, even for 6.9(d) when $\alpha R = O(1)$. The instability appears to be governed by the critical layer mechanism, as in the case of a bounded, parallel flow. In figure 6.10, the energetics of the instability for R greater than R_c appear to depend on the values of α and R. Figures 6.10(a), (b) clearly show the transfer of energy to be controlled by the critical layer. The product αR remains small at these points on their respective marginal curves. However, figures 6.10(c), (d) show the transfer of energy is no longer confined to the critical layer. In both cases the product $\alpha R = O(1)$ and the transfer of energy (particularly 6.10(d)) appears to be unrelated to the position of the critical layer.

It is concluded that for $R \approx R_c$ and also for $\alpha R < O(1)$ instabilities appear to be governed by the same mechanisms described by the Orr–Sommerfeld problem for a parallel flow. The Orr–Sommerfeld instability mechanism appears to be substantially modified by a small convergence or divergence of the flow when $R > R_c$ and $\alpha R = O(1)$. It is assumed that the divergence of the flow leads to additional mechanisms through which positive Reynolds stresses are generated, no longer confining the energy transfer mechanism to the critical layer region.

The first term of $S(y)$, defined in equation (6.39), is the familiar transport term from the Orr–Sommerfeld problem whereby contributions are mainly through the phase difference between f and f' across the critical layer. The second term of $S(y)$ is proportional to αU and presumably the size of the second term is no longer negligible compared with the first term in figures 6.10(c), (d). It is suggested that in figure 6.10(c) the peak close to the critical layer is due to the remaining influence of the critical layer. The lower peak of similar magnitude is thus due to the additional transfer of energy described by the second term of $S(y)$. As the size of the two terms in $S(y)$ become more comparable then the two-peaked profile merges into the one-peaked profile seen in figure 6.10(d). These results provide further evidence of the delicacy of the mechanisms controlling the stability of a convergent or divergent flow for small α.

In experiments plane Poiseuille flow is typically *observed* to become unstable at Reynolds numbers of the order of one thousand. The value of the critical Reynolds number observed in experiments compared with $R_c \approx 3848$ obtained from linear theory is significantly different. The difference may be attributed to nonlinearity, with a subcritical instability. Also for plane Poiseuille flow it has been calculated that the energy of some temporally stable modes actually increases substantially for a short time before decaying. This is another explanation for the low critical Reynolds number observed experimentally. This work by no means offers an alternative explanation *but* does indicate that large changes in the stability characteristics may come about from very small changes in the flow conditions.

Finally, the stability of a basic flow is conventionally concerned with its development in time. A flow is defined to be asymptotically stable if the amplitude of every perturbation decays to zero as $t \to \infty$. However in this chapter the development of small-amplitude perturbations is considered in the limit as $r \to \infty$ and $\tau \propto t/r^2 \to 0$. The method is only valid as $t \to \infty$ if $r \to \infty$ fast enough to ensure that $\tau \to 0$.

Appendix A

Data for tonal cases 1, 2 and 3

In Chapter 3, calculations of the linear amplification of boundary-layer instability waves over the aerofoil is presented, using experimental data obtained from wind-tunnel experiments. As discussed in §2.3.4, some of the data used was obtained using a prediction code, reducing the amount of experimental measurements which were required.

Examples of the predicted and measured data obtained are listed in the following spreadsheets. The data used for cases 1, 2 and 3 is presented. Details of the spreadsheet columns are listed below:

station - station number where measurements were taken.

$\boldsymbol{x/c}$ - location of each station as a fraction of chord length (c), measured from the leading edge of the aerofoil.

data type - states whether the data are 'predicted' or 'measured'.

$\boldsymbol{\delta}$ - boundary-layer displacement thickness (m), defined by (3.33).

$\boldsymbol{\theta}$ - boundary-layer momentum thickness (m), defined by (3.34).

$\boldsymbol{H}$ - boundary layer shape factor, defined by (3.35).

$\mathbf{d}\boldsymbol{p}/\mathbf{d}\boldsymbol{x}$ - boundary-layer pressure gradient ($\mathrm{kg\,m^{-2}\,s^{-2}}$). Only predicted data were available.

$\boldsymbol{\omega}$ - non-dimensional frequency of the tone, defined in §3.2.2.

$\boldsymbol{R}$ - Reynolds number based on displacement thickness, defined in §3.2.2.

$\boldsymbol{\beta}$ - parameter of Falkner–Skan equation (3.25).

$\boldsymbol{H}$ - Falkner–Skan boundary-layer shape factor defined by (3.35), calculated using (3.33) and (3.34).

$\mathbf{d}\boldsymbol{p}/\mathbf{d}\boldsymbol{x}$ - Falkner–Skan boundary-layer pressure gradient, calculated using (3.20).

% error - relative error between the predicted aerofoil boundary layer, and Falkner–Skan boundary layer, pressure gradients.

At each station on the aerofoil the boundary layer was modelled by a Falkner–Skan profile, by choosing a profile with the same shape factor H. The shape factors matched by at least 2 s.f. .

As a further comparison between experiment and theory, pressure gradients of the Falkner–Skan profiles were compared with predicted pressure gradients of the flow (before separation) on a NACA 0012 aerofoil. For cases 1, 2 and 3 the relative error downstream of station 2 was approximately 20–30%. In each case, the relative error at station 2 is large. The pressure gradient at station 2 is small. The relative error is large because the comparable pressure gradients have opposite signs.

Conclusions from the comparison between the predicted and theoretical pressure gradients are difficult because the pressure gradients could not be measured. Therefore the accuracy of the predicted pressure gradients is unknown. On matching the shape factor of the theory to the measured shape factor of the experiment, downstream of station 2, the pressure gradient predicted theoretically seems to be consistent with the experiment.

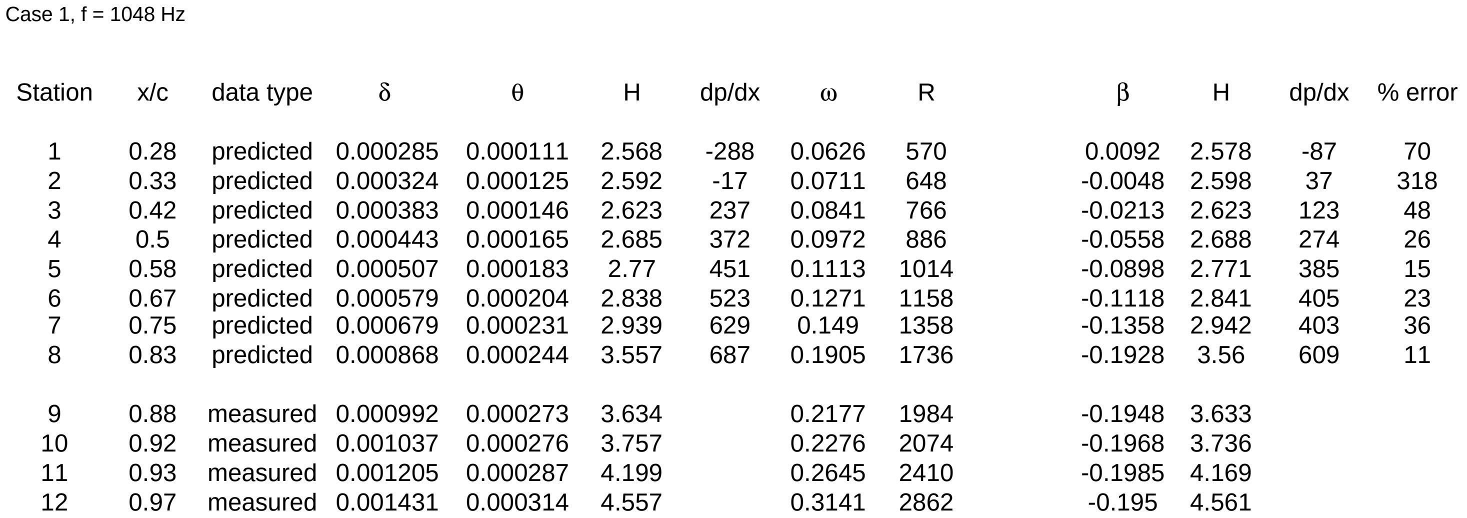

Case 1, f = 1048 Hz

Station	x/c	data type	δ	θ	H	dp/dx	ω	R	β	H	dp/dx	% error
1	0.28	predicted	0.000285	0.000111	2.568	-288	0.0626	570	0.0092	2.578	-87	70
2	0.33	predicted	0.000324	0.000125	2.592	-17	0.0711	648	-0.0048	2.598	37	318
3	0.42	predicted	0.000383	0.000146	2.623	237	0.0841	766	-0.0213	2.623	123	48
4	0.5	predicted	0.000443	0.000165	2.685	372	0.0972	886	-0.0558	2.688	274	26
5	0.58	predicted	0.000507	0.000183	2.77	451	0.1113	1014	-0.0898	2.771	385	15
6	0.67	predicted	0.000579	0.000204	2.838	523	0.1271	1158	-0.1118	2.841	405	23
7	0.75	predicted	0.000679	0.000231	2.939	629	0.149	1358	-0.1358	2.942	403	36
8	0.83	predicted	0.000868	0.000244	3.557	687	0.1905	1736	-0.1928	3.56	609	11
9	0.88	measured	0.000992	0.000273	3.634		0.2177	1984	-0.1948	3.633		
10	0.92	measured	0.001037	0.000276	3.757		0.2276	2074	-0.1968	3.736		
11	0.93	measured	0.001205	0.000287	4.199		0.2645	2410	-0.1985	4.169		
12	0.97	measured	0.001431	0.000314	4.557		0.3141	2862	-0.195	4.561		

Figure A.1: Case 1, $U_\infty = 30\,\mathrm{ms}^{-1}$, $f = 1048\,\mathrm{Hz}$.

Case 2, f = 1280 Hz

Station	x/c	data type	δ	θ	H	dp/dx	ω	R	β	H	dp/dx	% error
1	0.28	predicted	0.000254	9.9E-05	2.566	-453	0.0538	643	0.0087	2.579	-130	71
2	0.33	predicted	0.000287	0.00011	2.609	-26	0.0607	727	-0.0083	2.603	103	496
3	0.42	predicted	0.000342	0.000129	2.651	373	0.0724	866	-0.0338	2.645	323	13
4	0.5	predicted	0.000396	0.000147	2.694	585	0.0838	1003	-0.0558	2.688	429	27
5	0.58	predicted	0.000452	0.000165	2.739	708	0.0957	1145	-0.0783	2.74	503	29
6	0.67	predicted	0.000518	0.000183	2.831	823	0.1096	1312	-0.1063	2.822	587	29
7	0.75	predicted	0.00061	0.000203	3.005	990	0.1291	1545	-0.1483	3.01	743	25
8	0.93	measured	0.000997	0.000254	3.925		0.211	2526	-0.1986	3.922		
9	0.95	measured	0.001073	0.000263	4.08		0.2271	2718	-0.1987	4.085		
10	0.97	measured	0.001108	0.000271	4.089		0.2345	2807	-0.1988	4.075		
11	0.98	measured	0.001144	0.000294	3.891		0.2421	2898	-0.1984	3.885		
12	0.998	measured	0.001113	0.000334	3.332		0.2356	2820	-0.1824	3.332		

Figure A.2: Case 2, $U_\infty = 38\,\mathrm{ms}^{-1}$, $f = 1280\,\mathrm{Hz}$.

Case 3, f = 1420 Hz

Station	x/c	data type	δ	θ	H	dp/dx	ω	R	β	H	dp/dx	% error
1	0.28	predicted	0.000235	9.1E-05	2.582	-618	0.0477	689	0.0087	2.579	-176	72
2	0.33	predicted	0.000265	0.000102	2.598	-36	0.0537	777	-0.0083	2.603	141	492
3	0.42	predicted	0.000324	0.000122	2.656	509	0.0657	950	-0.0373	2.651	470	8
4	0.5	predicted	0.000367	0.000137	2.679	798	0.0744	1077	-0.0558	2.688	585	27
5	0.58	predicted	0.000419	0.000153	2.739	967	0.085	1229	-0.0783	2.74	684	29
6	0.67	predicted	0.00045	0.00016	2.813	1123	0.0912	1320	-0.1063	2.822	911	19
7	0.75	predicted	0.000561	0.000187	3	1351	0.1138	1646	-0.1463	2.998	1000	26
8	0.9	measured	0.000689	0.000222	3.104		0.1397	2021	-0.1628	3.113		
9	0.92	measured	0.000728	0.00023	3.165		0.1476	2135	-0.1683	3.162		
10	0.93	measured	0.000819	0.000236	3.47		0.1661	2402	-0.1898	3.476		
11	0.95	measured	0.000821	0.000229	3.585		0.1665	2408	-0.1933	3.576		
12	0.97	measured	0.001005	0.000238	4.223		0.2038	2948	-0.1982	4.225		

Figure A.3: Case 3, $U_\infty = 44\,\mathrm{ms}^{-1}$, $f = 1420\,\mathrm{Hz}$.

Bibliography

[1] L.B. Aizin. Sound generation by a Tollmien–Schlichting wave at the end of a plate in a flow. *Translated from Prikladnaya Mekhanika; Tekhnicheskaya Fizika*, 3:50–57, 1992.

[2] J.D. Anderson. *Fundamentals of Aerodynamics.* McGraw–Hill, Inc., second edition, 1984.

[3] H. Arbey and J. Bataille. Noise generated by airfoil profiles placed in a uniform laminar flow. *J. Fluid Mech.*, 134:33–47, 1983.

[4] W.H.H. Banks, P.G. Drazin, and M.B. Zaturska. On perturbations of Jeffery–Hamel flow. *J. Fluid Mech.*, 186:559–581, 1988.

[5] R.J. Bodonyi and F.T. Smith. The upper branch stability of the Blasius boundary layer, including non-parallel flow effects. *Proc. R. Soc. Lond. A*, 375:65–92, 1981.

[6] M. Bouthier. Stabilité linéaire des écoulements presque parallèles, (premiére partie). *Journal de Mécanique*, 11(4):599–621, 1972.

[7] T.F. Brooks, D.S. Pope, and M.A. Marcolini. Airfoil self-noise and prediction. *NASA RP 1218*, 1989.

[8] A. Davey. A simple numerical method for solving Orr–Sommerfeld problems. *Q. J. Mech. Appl. Math.*, XXVI, Pt. 4:401–411, 1973.

[9] A. Davey. Numerical methods for the solution of linear differential eigenvalue problems. *Rotating Fluids in Geophysics, ed. P.H. Roberts and A.M. Soward*, 1978.

[10] A. Davey. On the numerical solution of difficult boundary value problems. *J. Comp. Physics*, 35(1), 1980.

[11] A.V. Dovgal and V.V. Kozlov. Influence of acoustic perturbations on the flow structure in a boundary layer with adverse pressure gradient. *Fluid Dynamics*, 18:205–209, 1983.

[12] P.G. Drazin. Stability of flow in a diverging channel. *Propagation in Fluids and Solids ed. G.P. Galdi (Wien: Springer–Verlag)*, pages 39–65, 1995.

[13] P.G. Drazin and W.H. Reid. *Hydrodynamic Stability.* Cambridge University Press, 1981.

[14] A.V. Dovgal et al. Laminar boundary layer separation: instability and associated phenomena. *Prog. Aerospace Sci.*, 30:61–94, 1994.

[15] D.G.Crighton et al. *Modern methods in analytical acoustics.* Springer, 1992.

[16] R.W. Paterson et al. Vortex noise of isolated airfoils. *J. Aircraft*, 10(5), 1973.

[17] J.E. Ffowcs-Williams and L.H. Hall. Aerodynamic sound generation by a turbulent flow in the vicinity of a scattering half plane. *J. Fluid Mech.*, 40:657–670, 1970.

[18] M.R. Fink. Fine structure of airfoil tone frequency. *Paper H3, presented at the 95th meeting of the Acoustical Society of America*, 1978.

[19] M. Gaster. A note on the relation between temporally-increasing and spatially-increasing disturbances in hydrodynamic stability. *J. Fluid Mech.*, 14:222–224, 1962.

[20] M. Gaster and I. Grant. An experimental investigation of the formation and development of a wave packet in a laminar boundary layer. *Proc. Roy. Soc. Lond. A*, 347:253–269, 1975.

[21] M. Hamadiche, J. Scott, and D. Jeandel. Temporal stability of Jeffery–Hamel flow. *J. Fluid Mech.*, 268:71–88, 1994.

[22] J.J. Healey. Characterizing boundary layer instability at finite Reynolds numbers. Submitted to J. Fluid Mech., Jan. 1996.

[23] A.S. Hersh and R.E. Hayden. Aerodynamic sound radiation from lifting surfaces with and without leading-edge serrations. *NASA CR 114370*, 1971.

[24] N. Itoh. Spatial growth of finite wave disturbances in parallel and nearly parallel flows Part 1. The theoretical analysis and the numerical results for plane Poiseuille flow. *Trans. Japan Soc. Aero. Space Sci.*, 17(38):160–174, 1974.

[25] N. Itoh. Spatial growth of finite wave disturbances in parallel and nearly parallel flows Part 2. The numerical results for the flat plate boundary layer. *Trans. Japan Soc. Aero. Space Sci.*, 17(38):175–186, 1974.

[26] E.J. Kerschen. Boundary layer receptivity. *AIAA Paper No. 89-1109*, 1989.

[27] C.C. Lin. On the stability of two-dimensional parallel flows. *Quart. Appl. Math.*, 3, 1945.

[28] R.E. Longhouse. Vortex shedding noise of low tip speed, axial flow fans. *J. Sound Vibr.*, 53(1):25–46, 1977.

[29] M.V. Lowson, S.P. Fiddes, and E.C. Nash. Laminar boundary layer aeroacoustic instabilities. *AIAA 94-0358 32nd Aerospace sciences meeting and exhibit, Reno*, 1994.

[30] L.M. Mack. A numerical study of the temporal eigenvalue spectrum of the Blasius boundary layer. *J. Fluid Mech.*, 73:497–520, 1976.

[31] A. McAlpine and P.G. Drazin. On the spatio-temporal development of small perturbations of Jeffery–Hamel Flows.
Submitted to Fluid Dynamics Research.

[32] A.F. Messiter. Boundary layer flow near the trailing edge of a flat plate. *SIAM J. Appl. Math.*, 18:241–257, 1970.

[33] E.C. Nash. *Boundary layer instability noise on aerofoils.* PhD thesis, University of Bristol, Department of Aerospace Engineering, 1996.

[34] E.C. Nash and M.V. Lowson. Noise due to boundary layer instabilities. *First joint aero-acoustics conference AIAA/CEAS, Munich*, 1995.

[35] V.Ya. Neiland. Theory of laminar boundary separation in supersonic flow. *Fluid Dyn.*, 4(4):33–35, 1969.

[36] B.S. Ng and W.H. Reid. An initial value method for eigenvalue problems using compound matrices. *J. Comp. Physics*, 30(1), 1979.

[37] R. Parker. Resonance effects in wake shedding from parallel plates: some experimental observations. *J. Sound Vibr.*, 4:62–72, 1966.

[38] R. Parker. Resonance effects in wake shedding from parallel plates: calculation of resonant frequencies. *J. Sound Vibr.*, 5:330–343, 1967.

[39] R. Parker and S.A.T. Stoneman. The excitation and consequences of acoustic resonances in enclosed fluid flow around solid bodies. *Proc. Instn. Mech. Engrs.*, 203, 1989.

[40] F.T. Smith. On the non-parallel flow stability of the Blasius boundary layer. *Proc. R. Soc. Lond. A*, 366:91–109, 1979.

[41] K. Stewartson and P.G. Williams. Self-induced separation. *Proc. R. Soc. Lond. A*, 312:181–206, 1969.

[42] C.K.W. Tam. Discrete tones of isolated airfoils. *J. Acoust. Soc. Am.*, 55(6), 1974.

[43] K.K. Tam. Linear stability of the non-parallel Bickley jet. *Canadian Appl. Math. Quart.*, 3:99–110, 1996.

[44] S.E. Wright. The acoustic spectrum of axial flow machines. *J. Sound Vibr.*, 45(2):165–223, 1976.